POLITECNICO
MILANO 1863

Department of Energy
Doctoral Program in Energy and Nuclear Science and Technology

COMBUSTOR-TURBINE INTERACTION IN GAS TURBINES

Doctoral dissertation of:
Andrea Notaristefano

Supervisor:
Prof. Paolo Gaetani

Tutor:
Prof. Vincenzo Dossena

The Chair of the Doctoral Program:
Prof. Vincenzo Dossena

July 2023– Cycle XXXV

ACKNOWLEDGEMENTS

Sono passati quasi quattro anni da quando ho intrapreso il percorso del dottorato di ricerca, una strada impegnativa, ma ricca di tantissime soddisfazioni, che giunge ora alla conclusione con questa tesi. Questo percorso mi ha permesso di crescere, sia sotto l'aspetto tecnico che sotto quello personale. Desidero ringraziare tutte le persone che hanno reso possibile raggiungere questo importante traguardo.

Innanzitutto, ringrazio il mio supervisore prof. Paolo Gaetani. Mi hai trasmesso tutta la tua conoscenza e passione per il tuo lavoro. La fiducia che hai riposto in me mi ha motivato a dare sempre il massimo. Grazie per la tua preziosa guida e supporto in questi anni. Un ringraziamento speciale va anche a tutti gli altri professori e tecnici del gruppo LFM: grazie per i vostri consigli, per la vostra disponibilità e per il vostro aiuto. Grazie anche a tutti i ragazzi dell'ufficio, anche loro preziosi per il sostegno e i consigli che ci siamo scambiati lungo questo percorso.

Un ringraziamento particolare va anche a tutti i ragazzi che ho avuto l'onore di supervisionare durante le loro tesi magistrali. Parte di questi risultati è merito anche vostro.

Un grandissimo grazie anche ai colleghi della UniFi per le loro simulazioni CFD. Le vostre conferme CFD hanno aumentato il valore delle nostre prove sperimentali. Il premio vinto insieme è una testimonianza di ciò.

A big thank you to my reviewers for taking the time to review my thesis and for providing insightful feedback and constructive comments.

I would also like to express my gratitude to the DLR group in Berlin for hosting me. I have learned a great deal from that experience, and my time at DLR will always hold a special place in my memories.

Non possono mancare, ora, i ringraziamenti personali. Dedico questa tesi a mia madre. La tua assenza sarà pesantissima per me, ma so che saresti stata estremamente orgogliosa di questo mio ulteriore traguardo. Sei stata sempre la persona che ha creduto in me più di ogni altra. Il secondo pensiero è per mio padre: anche tu, come mamma, hai sempre dimostrato una grande fiducia in me. Sarai sempre un riferimento per me. I vostri sacrifici e il vostro amore nei miei confronti sono stati determinanti per il mio successo e ve ne sarò sempre grato. Ringrazio anche i miei fratelli, Ilaria e Vittorio su cui so posso sempre contare. Il nostro legame non fa altro che rafforzarsi sempre di più.

Un ringraziamento va anche alla mia famiglia allargata di zii e cugini, sempre pronti ad offrirmi il loro supporto.

Ringrazio tutte le persone, compresi gli amici dei miei genitori, che mi sono state vicine, specialmente durante i momenti difficili degli ultimi anni, questo risultato è anche merito vostro. Grazie per il coraggio, la forza e la fiducia che mi avete dimostrato. Un ringraziamento speciale va ai miei amici di lunga data: rappresentate ancora oggi un punto di riferimento fondamentale per me. Grazie anche a tutto il gruppo di amici di Milano, mi avete accolto nella vostra famiglia e fatto sentire a casa, nonostante la distanza da Bari.

A mia madre

SUMMARY

In order to reduce pollutant emissions in gas-turbines, complex combustion systems are used, which generate aerodynamic and thermal flow perturbations. These perturbations, such as steady and unsteady temperature hot-spots, increased vorticity, and turbulence levels, persist at the turbine inlet and impact the turbine aerodynamics. They also interact with cooling flows and generate indirect combustion noise. While several studies have addressed the topic of combustor-turbine interaction in the literature by studying each combustor non-uniformity in isolation, only a few have combined all the combustor-released features. Furthermore, only a handful of studies have investigated this interaction through experimental campaigns, which are challenging due to the harsh and hot environment in a real gas-turbine that restrict the use of classical turbomachinery measuring techniques. Therefore, experiments are generally performed on non-reactive turbine test benches by simulating combustor features using a combustor simulator. In this research, a similar approach is followed by placing a combustor simulator that generates a swirl profile in isolation and a combined swirl profile and steady/unsteady temperature perturbation on a turbine test rig. Novel cases are studied by injecting a combined swirl profile and entropy waves and compared with other injection cases that are more common, such as the swirl profile in isolation and the combination of swirl with a hot-streak. Different injection positions are also studied, and the turbine is operated at different operating conditions.

The main objective of this research is to provide significant insights into the effect of combustor non-uniformities on a turbine's first stage aerodynamics by thoroughly analyzing the aero-thermal flow field measured. To achieve this goal, advancements in measuring techniques are required, and key analyses are highlighted to provide guidelines for carrying out similar investigations. The CFD analysis conducted to support the experimental findings by UniFi addresses noise emissions. The extensive dataset generated will also enable CFD validation, including high-fidelity simulations, that could be used to simulate more complex phenomena. Additionally, simplified models are developed to fully characterize the aerodynamic flow field at the stator outlet in its span-wise distribution, as well as the downstream transport and shape of the temperature disturbance. For the rotor, a simple correlation is developed that links non-dimensional coefficients with temperature perturbation decay and radial transport through the blade. The development of simplified models presented in this research can provide useful insights for turbine designers during the preliminary design phase, enabling them to predict the impact of combustor non-uniformities on the first turbine stage. These models, and generally the extended dataset, can help identify the injection conditions that may lead to increased aerodynamic and thermal perturbations, allowing designers to optimize the combustor-turbine system for improved turbine performance and reduced emissions.

The thesis is divided into four main sections. The first section (chapters 2 and 3) describes the experimental and numerical methods used, as well as the definition of the tested conditions, highlighting the novel experimental elaboration procedures.

In the second section (chapter 4), the flow field generated by the combustor is analyzed. This characterization is also supported by a detailed investigation in a wind tunnel where turbulence measurements are carried out, and CFD simulations are conducted. This analysis revealed the

main transport and decay of the perturbations released by the combustor simulator, providing all necessary input information for high-fidelity CFD simulations.

In the third section (chapters 5 and 6), the aero-thermal flow field at the stator is analyzed, and the main features introduced by the perturbations are discussed. A change in stator performance is found, depending mainly on the injection position. However, no significant differences are observed in the aerodynamics flow field for the different injection cases. The thermal flow field depends on both the injection position and injection case. Simplified models are developed to predict the impact of the injected perturbations on the stator flow field.

Finally, the fourth section (chapter 7) examines the rotor outlet flow field through steady and unsteady analysis. Interesting features are observed for the operating condition that exhibits the highest blade load. However, no significant differences are observed for the other operating conditions, indicating that the rotor aerodynamics is still dominated by the secondary flows. The injected perturbation has a slight impact on the rotor flow field, regardless of the injection case and position. The development of simplified models for the rotor is limited due to the strong secondary flows, but a simple correlation for temperature disturbance transport and decay is established.

CONTENTS

CHAPTER 1

INTRODUCTION

1.1 Research motivation

In 1903, Orville e Wilbur Wright revolutionized the way the world is interconnected. Air transportation has made a profound impact on people's daily lives, allowing for the availability of fresh products from every corner of the world and shortening travel time to even the most remote destinations. In the last years, passenger and cargo transportation demand is increasing as a consequence of economic growth, technological advancements, and market liberation. According to the International Air Transport Association (2019), the number of flight passengers is expected to increase significantly by 2050. In 2019, the estimate is that already in 2037 passengers will double the numbers in 2018. However, the COVID-19 pandemic has temporarily impacted air travel, and the exact rate of growth beyond 2023 is difficult to predict at this time. Nevertheless, the pandemic seems to have just slowed the aforementioned growth that will restart with the previously forecasted pace.

This exceptionally high growth rate and the increasing concern for the environment grow the pressure on manufacturers to produce engines that are more environmentally friendly reducing their impact on air quality and noise pollution. Therefore, the aviation industry has started a new path towards cleaner and more silent aero-engines. Companies are pursuing the objective of the UN Race to Zero and UN Business Ambition for 1.5°C campaigns, meaning that they have the target to achieve net zero greenhouse gas emissions operations and facilities by 2030, excluding product test emissions; by 2050, they aim to mitigate these remaining emissions, to become a carbon neutral business. In particular, the European air transport system has agreed on a common vision for aviation. The Flightpath 2050 (European Commission, Directorate-General for Mobility and Transport, Directorate-General for Research and Innovation, 2011) fixes the targets for 2050 as a 75% reduction in CO_2 emissions per passenger kilometers, and a 90% reduction in nitrogen oxide emissions. Furthermore, noise emissions from aircraft should be reduced by 65%. These percentages are relative to the capabilities of aircraft manufactured in 2000.

The technology that offered the highest potential to achieve the ambitious targets set by European Commission and Directorate-General for Research and Innovation (2002) for 2020 was the lean burn technology (International Civil Aviation Organization, 2010), Mongia (2003). Successful applications of this combustor are the Rolls-Royce lean-burn combustor described by Lazik *et al.* (2008) and the General Electric TAPS combustor shown by Foust *et al.* (2012). However, this kind of combustor introduces challenges to the coupling between the combustor and the turbine. Fuel-to-air ratios are low and a highly swirling flow is imposed on the mainstream to maintain a stable flame Lazik *et al.* (2008). A significant drawback of lean premixed combustion is its increased burning unsteadiness (Dowling & Stow, 2003). Furthermore, burning by a diffusion flame makes each portion of fluid burn at a different mixture ratio which would require a large distance downstream of the flame zone to make uniform the flow field due to molecular and turbulent mixing (Strahle, 1978). In real gas turbines, this distance is not available and the combustion at spatially and temporally varying mixture ratio generates hot spots (or cold spots) which persist to the turbine inlet. The same applies to vorticity perturbations generated by the unsteady shear in combustion (Chu & Kovásznay, 1958). The turbulent mixing maintains the necessary fuel-to-air ratio to sustain combustion and it is generated by flow recirculation and jets-in-crossflow cooling. Part of the compressor air enters the combustion region through holes placed on the annulus that inject the flow in a perpendicular direction with respect to the mainstream one. This generates the necessary turbulence intensity to sustain the combustion.

Therefore, the flow field at turbine first stage can not be treated as uniform and it is characterized by a complex flow field. Its main features are a residual swirl profile, high turbulence, vorticity and temperature perturbations. This flow field impacts the turbine performance, cooling and generate indirect combustion noise. The literature review is divided into two sections:

- Section 1.1.1 examines the available data at the outlet of real gas turbine combustors, which is essential for designing combustor simulators and validating CFD calculations. For simplicity, the effects of combustor perturbation on a turbine stage are studied decoupling the two components. A full numerical study of both components would be extremely challenging and time-consuming, and conducting experiments within a real gas turbine would be difficult due to the high temperatures and limited accessibility.

- Section 1.1.2 aims at providing a literature review of the experimental and numerical studies carried out on the topic. The main issues on the turbine aerodynamics and cooling are discussed. It will be divided into subsections discussing the impact of swirl profile and turbulence 1.1.2.1, temperature disturbance 1.1.2.2, and the combination of swirl profile and temperature disturbances 1.1.2.3. Finally, entropy waves are discussed 1.1.2.4.

1.1.1 Flow-field characterization downstream of real combustors

There are two main types of combustion systems employed in gas turbines: lean burn combustors and rich burn combustors. In lean burn combustors, the fuel is combusted with an excess of air. The use of lean burn fuel injectors significantly impacts the temperature and velocity distribution at the combustor exit, as these injectors allow a substantial portion of the total flow to pass through. This is in contrast to rich burn technology. Consequently, the flow released by the injectors dominates the flow field at the combustor exit. Downstream of the fuel injector, no mixing jets interacts with the combusting flow, but the latter interacts with cooling flows (Schroll *et al.* (2016)). Rich burn combustors utilize a rich primary combustion zone to stabilize the flame, along with sizable dilution jets to regulate the emissions of NOx and smoke. Approximately one third of the compressor flow enters the combustion nozzles, while the remaining two-thirds are injected into dilution jets perpendicular to the streamwise direction, as shown in Fig. 1.1 of McGuirk (2014). Overall, the combustion is still lean (Cha *et al.* (2012*a*)). The flow field at the exit is predominantly influenced by the dilution jets, which induce significant turbulence and dissipate the flow generated by combustor nozzles.

In the following, attempts to characterize the aero-thermal flow field downstream of the two kind of combustors are discussed. However, measurements downstream of real combustors are very challenging due to the high temperature and pressures. Actually, the measurements are restricted to intrusive emission sampling and temperature measurements, carried out in non-reacting flows. Typical measurements are based on thermocouples, hot wires, multi-hole probes, tracer techniques and PIV Schroll *et al.* (2016). Moss & Oldfield (1991) compared combusting and non-combusting combustion chambers and showed that the turbulence is mainly generated by the combustion chamber geometry and the combustion does not change the turbulence intensity and length-scales. Moss & Oldfield (1991) findings support other studies based on non-combusting environments as Zimmerman (1979), Heitor & Whitelaw (1986) and the (Cha *et al.*, 2012*a*), (Cha *et al.*, 2012*b*). However, the approach of considering non-reacting environment is questionable in presence of strong swirling flows. The turbulence intensity at the outlet of the combustor investigated by (Goldstein *et al.*, 1983) reduces of 30-50% in case of combustion. (Goebel *et al.*, 1993) discovered that the combustion process reduces the swirl strength and subsequently decreases the turbulence intensity, as swirl was found to be a major contributor to turbulence generation. Other limitations to measurements in real combustors regard the measuring techniques: optical techniques can be carried out only at atmospheric pressure to not break the glass window; gas path probes have access limitations and can be used for a few seconds to avoid thermal degradation. (Lubbock & Oldfield, 2018) provided a review of all the measurement techniques available and listed the turbulence intensities measured by several studies. Overall, the review suggests that the turbulence intensity at the combustor outlet exceeds 10%. Therefore, it can be concluded that turbulence cannot be

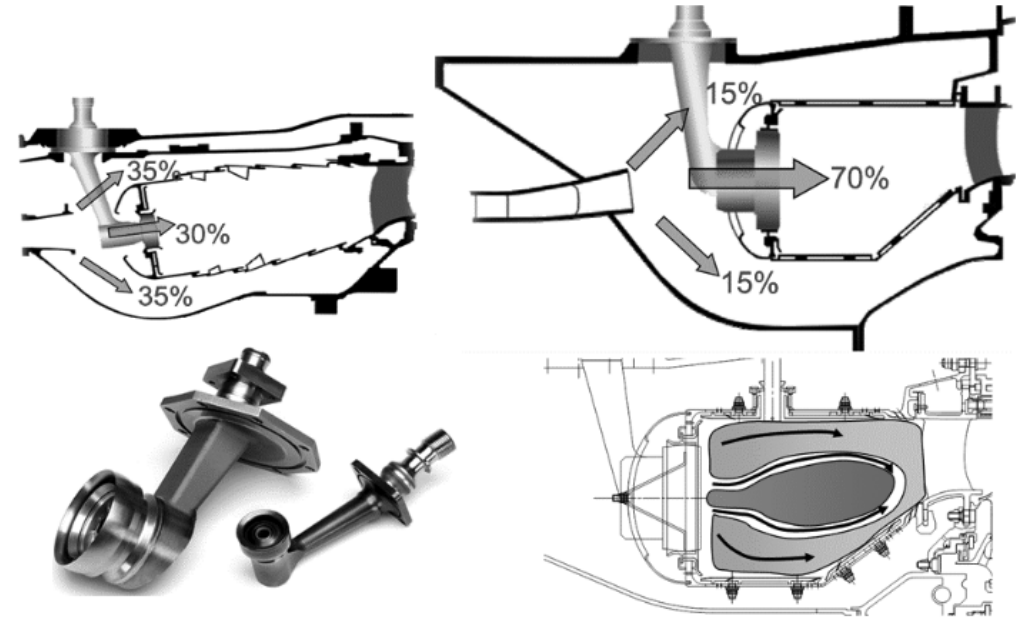

FIGURE 1.1. Comparison of rich burn (top-left) and lean (right) burn combustor architectures. McGuirk (2014).

generated using a grid that only achieves turbulence intensity levels between 1% to 4%.

Attempts to measure the aerothermal flow field experimentally downstream of a combustor are documented in a few papers. Schroll *et al.* (2016) show the potentiality of filtered Rayleigh scattering o make measurements at the combustor outlet. In their experimental study, authors show a significant swirl profile that persists at the turbine inlet. Cha *et al.* (2012*a*) use a miniature pneumatic five-hole probe and CO_2 measurements. The value of RTDF is ~0.15 at the turbine inlet plane. This value is consistent with the data of combustors Lefebvre (1983), which also reports a value of OTDF ~0.3. Cha *et al.* (2012*a*) case is a rich-burn combustor, therefore a less intense swirl is imposed to the combustion air. Greifenstein *et al.* (2020) measured the temperature profile that exhibited strong inhomogeneities and temporal fluctuation especially for low frequencies, i.e. lower than 500 Hz. Kampmann *et al.* (1993) used two-dimensional laser Rayleigh scattering to perform quantitative measurements of the temperature field. Authors identified incomplete premixed regions as possible causes of higher temperature than the adiabatic one. Furthermore, the regions of high appearance probability of the flame front are characterized by the highest RMS temperature distributions. Considering the difficulties in conducting experimental results, a common approach to investigate the combustor-turbine interface is to perform high-fidelity CFD. Medic *et al.* (2007) performed a full gas-turbine CFD simulation incorporating all the components. Their results show the presence of temperature hot-streaks at the flame locations that persist at the turbine inlet. Another approach is to study the coupling of combustor-turbine by means of LES or hybrid LES-RANS. RANS equations are capable of reproducing the steady-state flow field but fail in capturing the combustion detailed dynamics (Gicquel *et al.*, 2012). Gicquel *et al.* (2012) divided CFD LES simulations into two main categories: laboratory-scale combustors which allow to have advanced measurements and real combustion chambers of engines operating at realistic operating conditions. In the latter case, the only available measurements are the temperature profiles at

the combustor outlet which matches with a good agreement with the LES outcomes as shown by James *et al.* (2006), Moin & Apte (2006) and Boudier *et al.* (2007). The previous literature review underlines the challenges of studying the combustor-turbine interaction issues on a real engine. Therefore, the academic research focuses on combustor simulators, devices that are able to reproduce the main features of the flow-filed released by the combustor. The literature review on this topic continues in the next section where the main combustor simulators are introduced. These could be non-reactive combustors or even simpler devices.

1.1.2 Combustor-turbine interaction studies with combustor simulators

The previous chapter based on the data relative to real combustors has shown that the flow field downstream of the combustor is unsteady and characterized by temperature non-uniformities and a strong swirl motion. The aim of combustor simulators is to reproduce these features and study their impact on turbine stages by means of experimental and numerical studies. In this section a review of the combustor simulators available in the literature is discussed and their impact on the turbine is analyzed. The majority of the studies focus on the effects of swirl profile and turbulence (section 1.1.2.1) or steady (section 1.1.2.2) or unsteady (section 1.1.2.4) temperature perturbations. Only in the last years, swirl profile and steady temperature disturbances have been considered coupled (section 1.1.2.3). Furthermore, there are researches that dealt with the turbulence increase at the combustor outlet. In the next sub-sections, the different cases are discussed.

1.1.2.1 Swirl profile and turbulence

The effects of a swirl profile on a first turbine stage have been investigated experimentally on several facilities, imposing a uniform total temperature profile. All these studies have equipped the turbine facility with a lean-burn combustor swirl profile simulator. For its nature, a swirl profile increase/decrease the vane incidence angle at different span-wise positions. The first experimental analysis on a rotating turbine was carried out by Qureshi *et al.* (2013) using the swirler generator described in Qureshi & Povey (2011) and showed in Fig. 1.2. Authors set target swirl angles of minimum 40°. In this pioneering study, the swirl profile acting as a source of off-design vane incidence altered the vane loading distribution, deformed the LE stagnation lines, modified the secondary flows and increased/decreased the pressure losses in span-wise direction, accordingly to the increased/decreased loading associated with the off-design incidence. The impact was significantly higher for the vane blade which LE was aligned with the core of the swirl profile. The aforementioned aspects introduce significant challenges for the aero-thermal design of a vane blade, in particular for the cooling design system which has to consider the great alteration of streamlines. Further analysis on the Oxford turbine has been carried out by Qureshi *et al.* (2012) to study the impact of the residual swirl profile at the vane exit on the rotor aerodynamics. The strong acceleration that the swirl profile undergoes through the turbine vane reduced the strength of the swirl profile, thus the relative incidence angle on the rotor was significantly lower than the off-design incidence experienced by the stator. Overall, the residual swirl profile impacted the rotor modifying the surface streamline pattern, changing the blade loading distribution and the tip clearance leakage vortex. However, these differences were smaller than the ones experienced by the vane. This aspect was confirmed by Beard *et al.* (2014) that measured an efficiency penalty of 1.22% in the presence of inlet swirl. The increased loss in the stationary vane was identified as the main cause of the performance penalty.

In another experimental test case, Jacobi *et al.* (2017) carried out experimental measurements on a high-speed linear cascade with two can combustors and four nozzle guide vanes. The vane surfaces are affected by the coherent structures produced by the swirl profile, which oscillate harmonically in the spanwise direction and have a significant impact on heat transfer. Additionally,

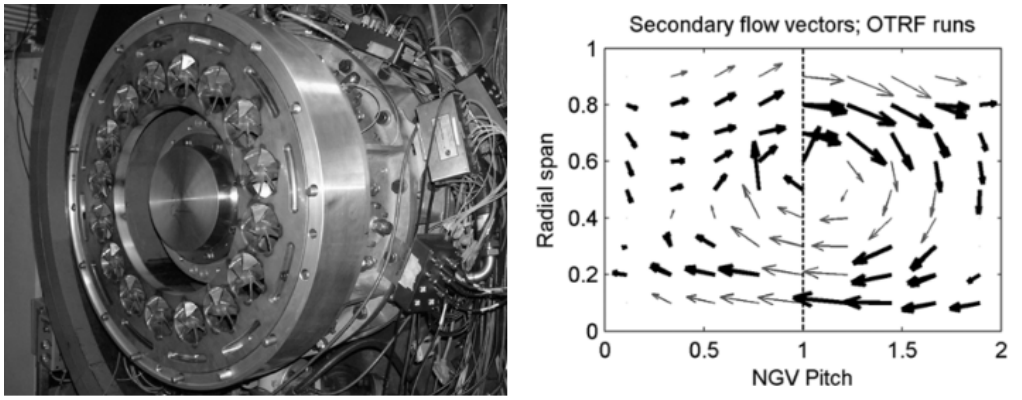

FIGURE 1.2. Left: inlet swirl generation system installed in the Oxford Turbine Research Facility with the turbine module removed. Right: measured secondary flow vectors profile. Qureshi & Povey (2011)

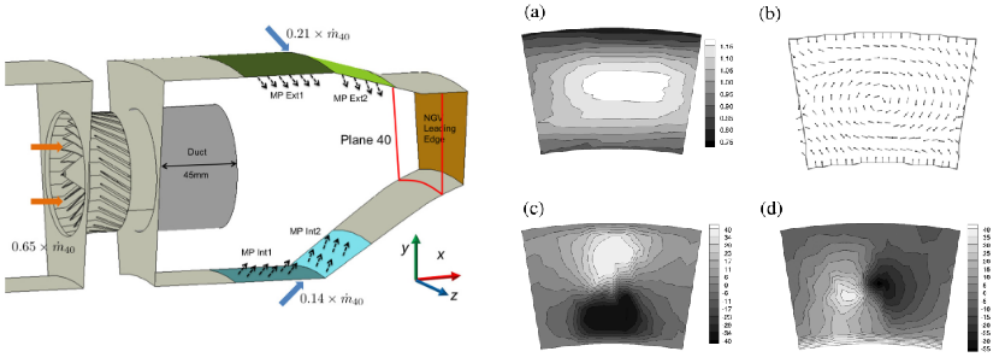

FIGURE 1.3. Left: schematic of the combustor simulator in University of Florence. Right: Target fields in plane 40 (view from upstream), (a) temperature made non-dimensional to the mean value, (b) velocity vectors, (c) swirl angle (deg), and (d) pitch angle (deg). Koupper *et al.* (2014)

the authors noted a periodic spanwise oscillation of vorticity around the vane leading edge, which interacts with the swirl core and vane potential field.

At the University of Florence, the combustor simulator described by Koupper *et al.* (2014) has been used with a uniform inlet total temperature profile generating a realistic swirl profile at the vane inlet (Fig. 1.3). Bacci *et al.* (2019) showed the significant impact of the swirl on the blade cooling effectiveness. The position of the swirler and vane in relation to each other plays a crucial role in determining the distribution of film effectiveness. Additionally, the location of the stagnation line between the central and lateral vanes is crucial for the optimal performance of the leading-edge film cooling system. The key factors affecting the film cooling performance due to the swirling flow are the nonuniform pressure, the alteration of the stagnation line, and the modification of the streamlines on both the pressure and suction sides.

Further investigations on the impact of a swirl profile on the blade cooling effectiveness were carried out on the Large-Scale Turbine Rig at the Darmstadt University, that is a cooled 1.5-stage axial turbine (Fig. 1.4). Werschnik *et al.* (2017*a*) studied the injection of a swirling flow aligned with the center of the blade vane passage. The measurements indicate that, in comparison to the axial inflow, there was an increase in the Nusselt numbers and a reduction in the film-cooling

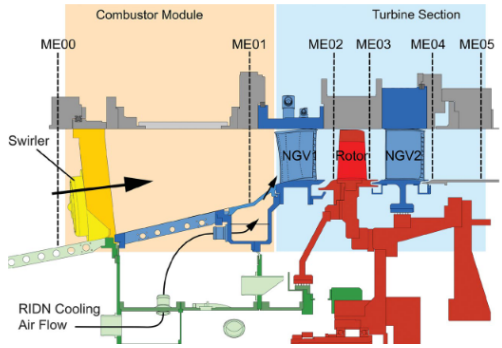

FIGURE 1.4. Test rig sectional view at Darmstadt University. Werschnik *et al.* (2017*a*)

effectiveness. As a result of the vane-swirl interaction, significant sections of the end wall remained uncooled.

The aerodynamics of the vane blade is also impacted by the swirl profile. Werschnik *et al.* (2017*b*) showed that pressure loss increases from 5.4% to 6.5% (7.3%) in NGV exit flow aligning the swirl profile to the center of the blade passage (LE). Additional losses were observed in addition to the stator wake that are more likely to stem from the interaction between the swirler outflow and the vane row, rather than from any interaction with the coolant flow.

The effect of the turbulence intensity on turbine performance has been investigated by Folk *et al.* (2020). A representation of different turbulent intensities is shown in Fig. 1.5 for the combustor turbulence intensity is 10% and the grid turbulence intensity is 1.3% at the turbine inlet. At the vane inlet, the turbulence is nearly isotropic and infiltrates deeply into the boundary layer, decreasing its shape factor. The mean shear of the boundary layer causes the turbulence to stretch, resulting in an increase of turbulent kinetic energy production within the boundary layer. As a result, in zero pressure gradient conditions, the presence of combustor turbulence causes a 22% rise in the dissipation coefficient. In turbine cascades, the presence of combustor turbulence results in a 47% increase in total loss, which is attributed to a 37% rise in profile loss and a 47% rise in endwall loss. Applying these loss mechanisms to the vane from a high-pressure stage representative of an engine results in a 1.3% reduction in stage efficiency, a significant figure that underscores the importance of incorporating this new mechanism into turbine design systems.

In summary, the aerodynamic flow field generated by a combustor is expected to have the following effects:

- **Vane** The flow field from the combustor alters the loading distribution, deforms the leading edge stagnation lines, modifies the secondary flows, and causes variations in pressure losses in the span-wise direction. These changes significantly impact the aerodynamics of the vane.
- **Vane cooling** The design of the vane cooling system needs to account for the significant alteration of streamlines resulting from the flow field.
- **Rotor** The residual swirl profile change the blade loading distribution and the tip clearance leakage vortex. However, the impact on the rotor is generally smaller compared to the vane due to the attenuation of the swirl profile as it passes through the stator.

1.1.2.2 Hot-streaks

Munk & Prim (1947) demonstrated theoretically that steady temperature disturbances, labeled hot-streak (HS), do not alter the inviscid streamline pattern in a stationary blade row, given an

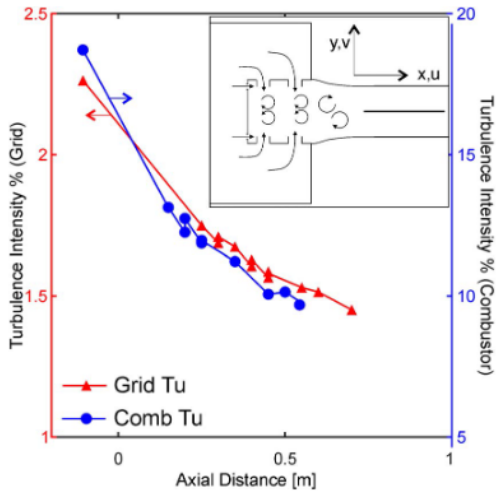

FIGURE 1.5. Axial development of freestream turbulence measured over the flat plate. Folk *et al.* (2020)

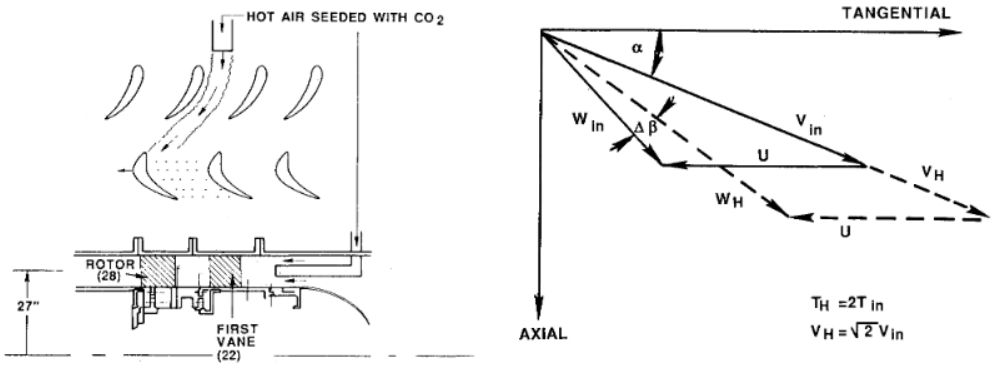

FIGURE 1.6. Left: experimental apparatus. Right: velocity triangles for hot and cold fluid. Butler *et al.* (1989)

unaltered inlet total pressure distribution. The impact on the rotor is not negligible because the inlet temperature profile generates secondary flow in a rotating blade. Resulting as a normal component of the relative vorticity at the rotor entrance, the inlet temperature distribution is converted to streamwise vorticity through the rotor. This secondary flow analysis has been developed by Hawthorne (1951) and extended to rotating blades by Lakshminarayana & Horlock (1973). Furthermore, a non-uniform inlet temperature leads to a segregation of hot and cold air in the rotor caused by a difference in the rotor inlet flow angle depending on the flow temperature. This effect was firstly investigated both theoretically and experimentally by Kerrebrock & Mikolajczak (1970) in an axial flow compressor. The pioneering experimental study of Butler *et al.* (1989) demonstrated the previous introduced theories, as shown in Fig. 1.6. Authors injected a temperature distortion in the inlet of a large-scale research turbine, seeding CO_2 to determine the temperature distortion migration through the turbine by sensing CO_2 concentration.

Other significant effects of HS on the rotor are related to the radial migration of the temperature perturbation that is driven by two main causes. First, Shang & Epstein (1997) described an inviscid

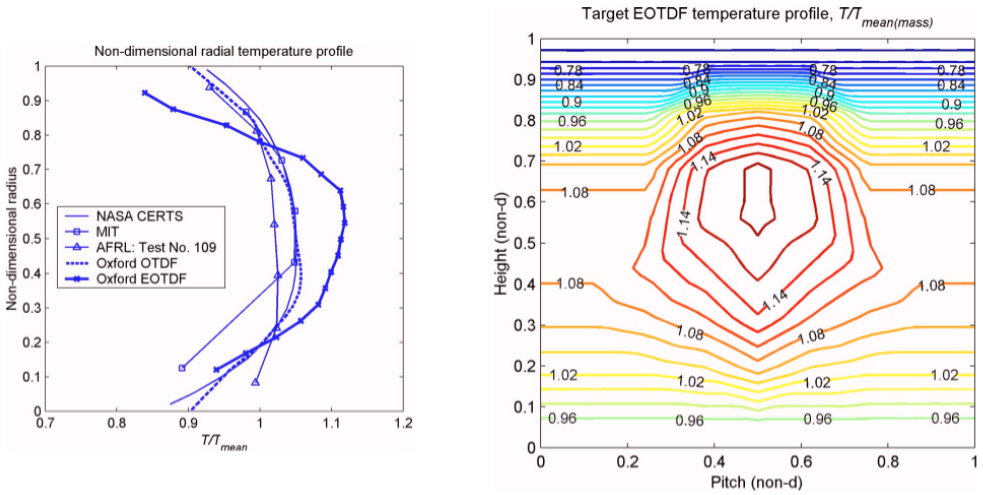

FIGURE 1.7. Left: comparison of simulated temperature profiles. Right: target profile. Povey & Qureshi (2009)

effect where buoyancy forces in the rotor cause the HS to radially migrate towards the hub. In viscous flows, a second aspect driven by the gradient-driven secondary flow must also be taken into account that makes the HS move towards the casing, as described by Prasad & Hendricks (2000).

These studies have laid the foundation for understanding HS physics. In recent years, there has been a growing interest in the topic. Povey & Qureshi (2009) provided a review of six existing HS generators and showed the combustor temperature measurements from the open literature (Fig. 1.7). Povey *et al.* (2005) measured the effect of engine-representative inlet temperature distribution taken from a military engine. Authors tested two different injection positions and demonstrated the large impact of HS on the vane and end wall heat transfer. Simone *et al.* (2011) studied both experimentally and numerically the effect of HS within the stage and in the downstream component. Furthermore, they found a beneficial effect of combustor cooling on the rotor casing and tip. In one of the most recent works of the Oxford group on HS, Beard *et al.* (2013) measured a reduction in the stage efficiency of 0.88%. Losses in the rotor increased because of the rotor off-design incidence and stronger gradients in relative total pressure and density.

He *et al.* (2004) investigated the effect of HS count and observed its effect on the blade wall temperature and aero-mechanics. With an NGV/HS ratio of 1, the wall temperature has a local difference of 8% in the rotor with respect to uniform inlet conditions but blade forces are unaffected. Reducing the number of HS, the temperature on the pressure surface reduces than the ratio 1, however the unsteady temperature and unsteady forcing increase. Jenkins *et al.* (2004) and Jenkins & Bogard (2005) tested the HS in different mainstream turbulence intensities, i.e. 5% and 20%, and observed an attenuation 20% larger of the temperature peak in the case of the highest turbulence intensity. Ong & Miller (2012) developed a novel cooling configuration under the influence of a HS, reducing the amount of cooling mass flow by a sixth. Authors found that coolant injected from an upstream row could potentially be used as secondary cooling in a downstream row. Liu *et al.* (2014) focused their numerical study on the effect of tip clearance height on the HS migration. The higher the tip gap, the wider the hot fluid spread on the blade tip. Gaetani & Persico (2017) tested in a rotating turbine facility the injection of HS at four different clocking positions with respect to the stator vane and made detailed measurements of the flow-field in the inter-row. Numerical calculations of this case are shown by Gaetani *et al.* (2020). Barigozzi *et al.* (2017) studied

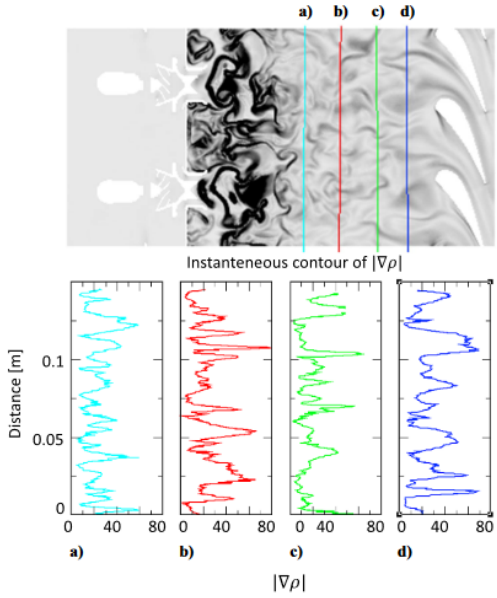

FIGURE 1.8. Instantaneous contour of the density gradient magnitude (top) and profiles of density gradient at different axial locations (bottom). Miki *et al.* (2022)

numerically and experimentally HS migration in a vane cascade with film cooling. In the cooled case, the HS attenuation was observed to be moderate compared to the uncooled vane, but the vane surface temperature at the leading edge significantly benefited from the coolant. Badžek *et al.* (2022) showed a new test setup to investigate the HS transport on a representative turbine center frame geometry. In their experimental study, the HS migrated radially outwards due to the pressure gradient established in the first bend of the turbine center frame. Miki *et al.* (2022) performed a full coupled simulation of the combustor and turbine. They observed temporal fluctuations in temperature (Fig. 1.8) at the combustor exit which result in an efficiency fluctuation too.

In conclusion, the effect of the hot-streak can be summarized as follows:

- **Vane** From an aerodynamic perspective, no significant impact is expected on the vane. However, the presence of the hot-streak poses challenges in the design of cooling systems for the vane.

- **Rotor** The hot-streak at the stator outlet results in an increase in the rotor incidence angle. It also undergoes a conversion to streamwise vorticity as it passes through the rotor. A segregation of hot and cold air within the rotor takes place. The hot-streak is radially transported within the rotor due to gradients in secondary flows and buoyancy forces.

1.1.2.3 Hot-streaks and swirl profile

The first studies of the effect of a combined injection of HS and swirl on a turbine stage were carried out numerically. Khanal *et al.* (2013) concluded that the combined swirl and hot-streak injection impacts significantly the aerodynamics and heat-transfer and the effects are nonlinear, thus modeling them by a superposition of the two in isolation could lead to misleading results. Khanal *et al.* (2013) found that the established concept of hot-streak migration in cases where only hot-streaks are present no longer holds true when the hot-streak is combined with swirl. For

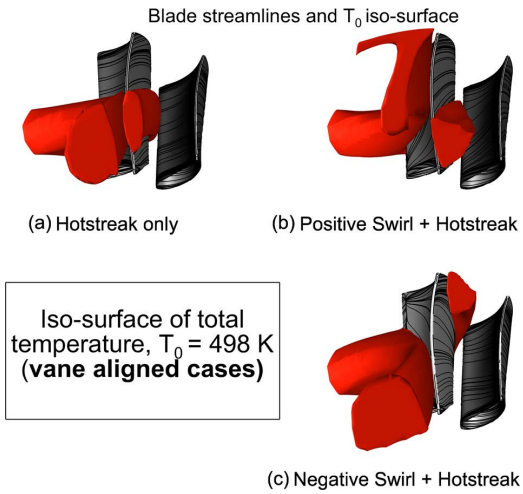

FIGURE 1.9. Convection of hot fluid, upstream view from nozzle guide vane exit. Khanal *et al.* (2013)

example, they demonstrated that clocking the hot-streaks in phase with the vanes does not lead to a decrease in heat on the blade pressure side surface. Furthermore, the unsteady single-passage simulations result in a higher variation of the performance parameter than steady simulations, highlighting the importance of the unsteady interaction between the swirl and the temperature streak. An example of the different transport of the isolate HS or combined with the swirl profile is shown in Fig. 1.9. In their simulations, Rahim & He (2015) compared a case with the isolate HS with the combined injection of swirl and HS. The HS radially transport through the vane is altered by the swirl resulting in a flatter spanwise temperature profile at the NGV exit and modifying the blade heat transfer features.

One of the first experimental campaigns combining the injection of a swirl profile with a temperature disturbance was developed at the University of Florence (Koupper *et al.*, 2014; Bacci *et al.*, 2015*a*). In particular, Bacci *et al.* (2019) investigated the HS migration through a NGV cascade of the three-sector invested by a temperature distortion combined with an aggressive swirl. The combustor simulator was aligned with respect to the vane LE. The turbulence intensity was also high Bacci *et al.* (2015*b*) making the inlet flow field engine-representative. The swirling flow significantly impacted the pressure losses and secondary flows, influencing the HS migration and interaction with the coolant flows, that was different from the documented cases with the only hot-streak injected. Furthermore, the injected combustor-representative pattern impacts the blade aerodynamics and the coolant migration differently on the blade aligned or misaligned with the combustor simulator. Bacci *et al.* (2023) used a non-reactive combustor simulator coupling a swirl profile and hot-streak to investigate the heat transfer coefficient on three uncooled NGV passages. Altering the stagnation line, the swirl profile was the main driver of the heat transfer coefficient distribution. Furthermore, the inlet swirl changes the radial movement of the hot streak. The development of the latter on PS and SS changes due to the different flow momentum. Lastly, Tomasello *et al.* (2022) showed that to fully characterize the behavior of film cooling and to accurately predict the adiabatic effectiveness, high-fidelity turbulence approaches are recommended because RANS could overestimate the interaction between film cooling and the vane.

The first experimental campaign on a rotating turbine was carried out by Adams *et al.* (2021), implementing the combustor simulator designed on the basis of Hall *et al.* (2014) and commissioned by Adams *et al.* (2020) into the Oxford turbine research facility (Fig. 1.11). The facility is a 1.5-stage film-cooled turbine with 40 vanes, 60 unshrouded rotor blades and 20 IP vanes. Experiments

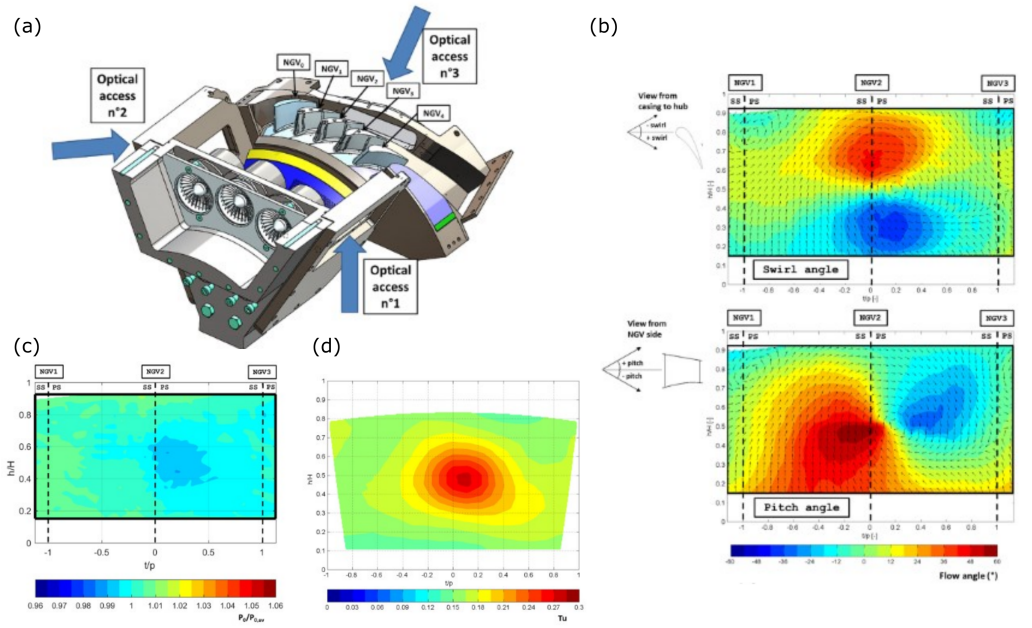

FIGURE 1.10. Trisector rig layout at University of Florence (a). Flow angles (b), scaled total pressure (c) and turbulence level (d) measured at stator inlet. Bacci *et al.* (2019)

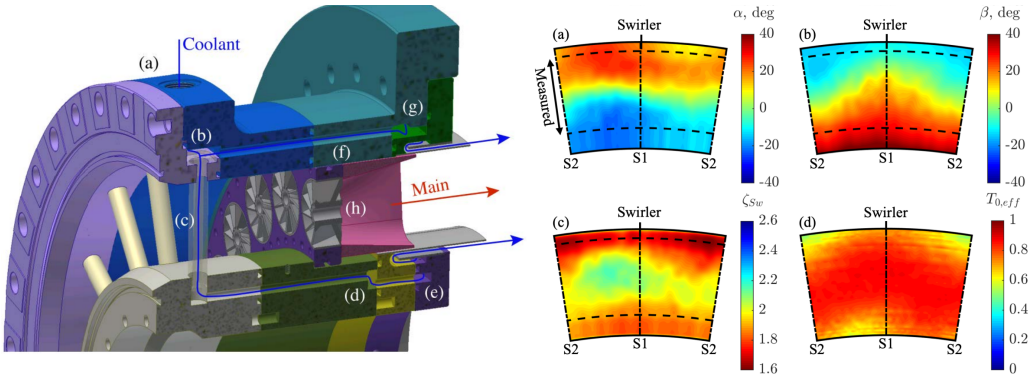

FIGURE 1.11. Left: CAD model of the lean-burn combustor simulator at Oxford University. Right: combustor simulator exit profiles measured in the atmospheric test facility: (a) yaw angle, (b) pitch angle (c) total pressure loss coefficient, (d) total temperature effectiveness. All contours are plotted as viewed from downstream. Adams *et al.* (2020)

were carried out at transonic conditions. The results showed that the HP vane aerodynamics was impacted primary by the swirl profile, the changes in the rotor aerodynamics by the HS. Furthermore, the swirl profile redistributes the film coolant accumulating it in some regions and reducing it in others. The swirl profile was dissipated due to the vane acceleration, thus the residual swirl at vane exit did not impact the rotor aerodynamics significantly, which is mainly modified by the vane outlet radial temperature profile which caused a reduction of rotor incidence angle up to -12.7° near the endwalls. At mid-span the temperature was not enough to produce a off-design incidence such as the one at endwalls.

Few other numerical works have been developed in recent years on the topic. Mansouri & Jefferson-Loveday (2022) investigated the effects of three hot-streaks shapes combined with a swirl profile on a rotating turbine stage. Authors found that, in the case of the absence of the swirl, the different HS remained almost unaltered at the vane exit, whereas the superposition of the swirl increased the mixing altering the morphology of each HS at the vane outlet. Furthermore, the swirl altered the radial transport of the HS through the vane increasing the thermal gradient on the shroud. Wang *et al.* (2018) studied a film-cooled vane under different setups combining HS and swirl profile. Due to the swirl, authors demonstrated an increase in the vane surface thermal load and a worsening of the coolant flow attachments. Wang *et al.* (2021) performed heat transfer simulations on a film-cooled turbine stage comparing a uniform inlet case, an isolate HS case and the superimposition of the HS with both swirl orientations. Combining the HS and the swirl, authors found a reduction of the film cooling effectiveness on both rotor surfaces. Lastly, Zhang *et al.* (2022) investigated the impact of different swirl intensities combined with HS on a vane. The positive swirl intensifies heat transfer in the hub region of the suction side and weakens it on the pressure side, whereas the opposite is true for the negative swirl. These trends are further amplified by higher swirl intensities.

The literature review conducted indicates that in the presence of a combined swirl profile and temperature disturbance, the following observations can be made:

- **Vane** The swirl profile primarily affects the aerodynamics of the stator. The presence of both disturbances complicates the design of cooling systems. The swirl profile alters the evolution of hot-spots through the vane.
- **Rotor** The swirl profile attenuates as it passes through the stator, resulting in the temperature disturbance having a more pronounced impact on the rotor aerodynamics. This is due to changes in the incidence angle caused by the temperature disturbance. Additionally, the effectiveness of film cooling on both rotor surfaces is reduced.
- **Superimposition?** The superimposition of the two disturbances is not feasible, as the presence of a swirl profile significantly alters the transport of the temperature disturbance.

1.1.2.4 Entropy waves

As discussed in the previous sections, the flow field at the combustor chamber outlet is strongly unsteady resulting in temperature fluctuations, generally referred to as Entropy Waves (EWs). EWs are considered one of the main causes of indirect combustion noise generation. Typically, as described by Dowling & Mahmoudi (2015), combustion noise is divided into direct and indirect combustion noise. The former is produced by the fluctuation of heat release rate associated with the chemical reaction. The latter, identified for the first time by Morfey (1973) and Marble & Candel (1977), generates when vorticity, temperature, and mixture-composition fluctuations are accelerated through nozzle guide vanes. In particular, the indirect combustion noise produced due to acceleration of temperature non-uniformities is called entropy noise. In recent years, Bake *et al.* (2009) built an Entropy Wave Generator (EWG) to study experimentally the indirect combustion noise showing that small temperature non-uniformities can generate significant noise when accelerated through a nozzle. The entropy wave was characterized by a pulse duration of 100 ms and a maximum temperature increase of 13.4 K. These experiments generated great interest and the scientific community was intended to explain the Bake *et al.* (2009) results. The generated sound pressure increases linearly with the temperature fluctuations, confirming the Marble & Candel (1977) theory. Furthermore, the sound pressure increases non-linearly with the nozzle Mach number, but after a certain amount, it starts to decrease. Leyko *et al.* (2009) predicted a higher contribution of indirect combustion noise than direct one for engine-representative conditions.

After the flame generates EWs, temperature disturbances are carried by a highly turbulent flow that is strongly non-uniform, thus the residence time of the EW varies across the cross-section (Sattelmayer, 2003). Furthermore, the flow turbulence can diffuse temperature disturbances. Both these effects reduce the EW potential for sound generation, reducing temperature fluctuations. According to Dowling & Hubbard (2000), turbulent fluctuations can diffuse the EW, especially when these disturbances have a small wavelength compared with the turbulent length scale. Below a few hundred Hz, the wavelength is large enough making turbulence negligible in EW diffusion. Furthermore, the magnitude of these amplitudes could potentially exceed the threshold for entering the nonlinear range, which usually occurs at temperatures above 100 K with a background temperature in the combustion chamber equal to 1000 K (Huet & Giauque (2013)).

Few models have been developed to account for this dissipation. Morgans *et al.* (2013) carried out one of the few attempts, performing a DNS on a turbulent channel-flow imposing Gaussian temperature perturbation. One of their main outcomes was that the EW dissipation was negligible between the flame position and the end of the combustor. The differential convection due to a nonuniform flow was the main cause of the entropy dissipation. Giusti *et al.* (2017) developed a further model based on CFD and experimental data. Authors developed a small-scale entropy rig generating EWs at a frequency of 10.7 Hz. The amplitude of EWs decreases as a function of both the frequency and the mean residence time of the wave. Given as input only the mean velocity profile, their model predicts both the magnitude and phase of the entropy transfer function. This applies very well for low/intermediate Helmholtz numbers because for its high values the turbulent mixing and diffusion could also further increase the EW attenuation. Christodoulou *et al.* (2020) developed a model which accurately predicted the EW non-uniform evolution in both position and amplitude using a nonlinear differential equation. The model case-specific parameters can be estimated from limited data and its equations can be analytically solved, making it suitable for integration into active control systems.

In recent years, the European Project RECORD has enabled researchers at the Politecnico di Milano to study, for the first time, the evolution and generation of indirect combustion noise caused by the injection of EW in a turbine stage, which frequency was at maximum 90 Hz. Gaetani & Persico (2019) showed the experimental results that were compared with numerical simulations by Pinelli *et al.* (2021). Experiments and simulations showed considerable attenuation of the temperature perturbation at stator outlet. The EW morphology at the stator exit depended on the azimuthal position of the injection. Leading edge injection induced the highest alteration in the EW shape and is expected to be more critical than other clocking positions. At the rotor exit, the presence of the EW produces significant alterations in both temperature and flow fields. The unsteady interaction of the temperature disturbance with the rotor blade is the main cause of EW distortion in the rotor row. Bake *et al.* (2016) investigated two different operating conditions comparing the entropy and vorticity noise to reference cases. The parametric study shows a strong increment of total power due to accelerated vorticity fluctuations. The entropy wave excitation generates significant additional acoustic power. In the upstream section, the noise generation by pulsating cold EW jets exceeds the heated EW noise for all investigated conditions. In the downstream section, the clean entropy generated sound power reveals a linear behavior with respect to the squared temperature amplitudes of the perturbation. In a further work of Knobloch *et al.* (2017), the analysis revealed an increase in broadband noise downstream of the stage. Only a small part of the acoustic energy is transmitted for the investigated frequency range. There is a strong reflection of incoming waves. The direct noise is highly attenuated by the HP turbine rows. For unsteady disturbances, a strong increase in total power was observed when analyzed with respect to the excitation frequency. In the upstream section, the reflected noise generated by pulsating cold EW jets exceeds the heated EW noise. Pinelli *et al.* (2022) conducted a numerical investigation on the effect of clocking on entropy noise generation in an aeronautical high pressure turbine stage.

The main sources of entropy noise were located in the stator channel and depended on the clocking position of the temperature spots. When the EW was injected at the blade leading edge, it generated an entropy noise 5 dB higher than other injection positions where the EW did not interact with the blades. This increase in entropy noise was due to both the acceleration of the EW and an unsteady load on the blade that was twice as high in the leading edge injection case compared to others.

Further numerical studies were carried out on the PoliMi turbine. Bach *et al.* (2021) investigated the effect of film cooling on entropy noise generation in a stator blade using a URANS simulation. Results showed that the EW amplitude is only minimally attenuated by the injection of a cooling flow. However, the added mass flow rate changes the velocity field and leads to an increase in the reflected and transmitted acoustic transfer function. The low-order model of Cumpsty and Marble was extended to incorporate the effect of film cooling flows and showed that increasing the temperature difference between the main and coolant flows further attenuated the EW. Huet & Geiger (2022) developed a non-compact model for evaluating indirect combustion noise generated through a stator. The model builds on the compact model of Cumpsty *et al.* (1977) and is extended to higher frequencies by taking into account the flow evolution in the inter-blade channel.

Cumpsty *et al.* (1977) model is the most used to predict entropy noise using the compact disk assumption but its validity is limited to low frequencies. Among its most recent improvements, the Guzmán-Iñigo *et al.* (2021) extended the model to airfoils beyond the limits of thin-airfoil theory. Brind & Pullan (2021) replicated the blade camber dividing the blade into multiple elements and taking into account the mean flow evolution, as then also proposed by Huet & Geiger (2022).

The study of EW transport within the first turbine stage is crucial due to the following reasons:

- They are responsible for indirect combustion noise generation.
- At first turbine stage outlet, the presence of the EW produces alterations in both temperature and flow fields.
- Regarding the frequencies of interest, they are below few hundred Hz because the EW wavelength and the turbulence scales do not match and the EW is not dissipated.

1.2 Research objectives and outcomes

As outlined in section 1.1, the increasing complexity of new combustion systems in gas turbines leads to unsteady combustor outlet flow fields and introduces temperature non-uniformities, making the study of combustor-turbine interaction more challenging. While most studies in the literature rely on CFD simulations, there are few experimental investigations. Although LES calculations are becoming increasingly common and affordable, it remains essential to validate these codes against complex experimental studies. Therefore, the goal of this PhD project is to enhance the understanding of combustor-turbine interaction by conducting a comprehensive experimental campaign using a non-reactive, uncooled one-stage turbine test rig equipped with a combustor simulator. Through a detailed analysis of the aero-thermal flow field downstream of the stator and rotor, this study aims to provide guidance for future experimental campaigns and generate a large dataset for validating numerical codes. Overall, this study wants to represent an important step forward in the quest to fully comprehend the intricate physics of combustor-turbine interaction.

The uniqueness of the combustor simulator lies in its capability to impose different perturbations at the stator inlet, which includes:

- A swirl profile
- A superimposition of a swirl profile and a steady temperature perturbation

- A superimposition of a swirl profile and an unsteady temperature perturbation at different frequencies

Notably, the last case has never been explored in previous turbine test rig studies. According to the discussion about combustor simulators detailed in section 1.1, the target profiles of the combustor simulator are: local swirl angles of ± 40°, a swirl number of 0.6, a local temperature peak that exceeds at least of 1.1 the mainstream temperature, temperature disturbance frequency higher than 100 Hz and inlet turbulence of approximately 10% at turbine inlet. The combustor simulator can be moved in circumferential direction with respect to the stator blades allowing to study different combustor simulator-stator vanes positions. These injection cases are then compared against a uniform inlet condition, which is the typical inlet condition in turbine test rigs without any inlet disturbances.

In addition to the combustor simulator flexibility, the test rig can operate at various operating conditions, enabling the investigation of the impact of off-design conditions on the combustor-turbine interaction problem.

The complexity of the test case necessitates advancements in measuring techniques, which are thoroughly discussed in this thesis. Novel methods are developed to utilize typical turbomachinery measuring devices in such a challenging environment. To better characterize the turbulence associated with the combustor simulator disturbances, a dedicated test campaign is carried out on an atmospheric wind tunnel. This campaign is complemented with CFD simulations for a more comprehensive understanding of the flow field.

One interesting new feature presented in this thesis, developed through a research collaboration with UniFi, is the assessment of the noise generated by the turbine as a result of the swirling EW injection at the stator inlet.

To conclude, the extensive data-set gathered in this study is utilized to develop simplified models that can predict the effects of combustor non-uniformities on the aero-thermal flow field at stator outlet. This includes a complete resolution of the uniform aerodynamic flow field in a span-wise distribution, as well as the perturbed cases. A loss breakdown is performed to highlight the contribution of the disturbances to losses. The temperature disturbance position and shape at the stator outlet are also fully reproduced. For the rotor, a straightforward correlation based on non-dimensional coefficients provides information on the decay and radial displacement of the EW/HS.

1.3 Outline of the thesis

The thesis is structured as follows.

Chapter 2 presents the test rig, combustor simulator and calibration facilities. In this section the tested cases are discussed specifying which parameters are modified.

Chapter 3 explains the experimental and numerical methods used and developed for the analysis carried out in this thesis. For each measuring probe the novelties in data elaboration are underlined. The traversing probes are a 5-hole probe, a fast response pressure probe, a fast-thermocouple and a hot-wire anemometer. The procedure to calculate the measurement uncertainties is discussed. Finally, the numerical setups are shown used for turbine test case and hot-wire characterization.

Chapter 4 characterizes the flow perturbations generated by the combustor simulator. The aero-thermal flow field released by this device is deeply investigated. Parallel to the turbine test rig characterization, hot-wire measurements downstream of the combustor simulator are carried out on a dedicated atmospheric wind tunnel and CFD simulations are carried out to support the understanding of the experimental findings.

Chapter 5 shows the aero-thermal characterization downstream of the stator. This analysis is carried out regarding the steady aerodynamics by means of 5-hole probe and supported by unsteady aerodynamic measurements to detect the unsteadiness produced by the EW-stator vane interaction. Finally, a fast-thermocouple is traversed. Some of the tested cases have been simulated through CFD.

Chapter 6 aims at developing simplified models to predict the impact of combustor non-uniformities on the stator outlet aero-thermal flow field. For this purpose, correlations available in the literature are used and supported by experimental evidences. The model is able to reconstruct the uniform and perturbed cases span-wise aerodynamics distribution and to predict the temperature perturbation and shape at the stator outlet.

Chapter 7 is the last chapter and discusses the rotor outlet flow field. It is characterized by means of time-averaged and unsteady analysis. Furthermore, the different blade loading is studied by means of CFD simulations. In this section, the generation of indirect combustion noise due to the swirling EW injection is presented. A simple correlation is developed to correlate the EW decay rate and radial displacement with non-dimensional parameters.

Chapter 8 summarizes conclusions and draws recommendations for future research activities.

CHAPTER 2

TEST RIG, COMBUSTOR SIMULATOR AND CALIBRATION FACILITIES

This chapter shows the facility and methods used for the analysis discussed in this thesis. The PoliMi turbine test rig is described, including its working principle and main components, as well as the design and commissioning of the combustor simulator used to generate an engine-representative perturbation at the turbine inlet. This device produces a combination of a steady/unsteady temperature disturbance with a swirl profile. Furthermore, the facilities used to calibrate probes are briefly illustrated. Finally, the experimental and numerical methods used are discussed to provide clarity on the determination of the results presented in the next chapters.

Some contents of this chapter are also discussed in:

Notaristefano, A., Gaetani, P., (2020) Design and Commissioning of a Combustor Simulator Combining Swirl and Entropy Wave Generation, *International Journal of Turbomachinery, Propulsion and Power*, vol. 5(2):6, doi:10.3390/ijtpp5040027

Notaristefano, A., Gaetani, P., (2023) The Role of Turbine Operating Conditions on Combustor–Turbine Interaction—Part I: Change in Expansion Ratio, *ASME Journal of Turbomachinery*, vol. 145(5):051001, doi:10.1115/1.4055642

Notaristefano, A., Gaetani, P., (2023) The Role of Turbine Operating Conditions on Combustor–Turbine Interaction—Part II: Loading Effects, *ASME Journal of Turbomachinery*, vol. 145(5):051002, doi:10.1115/1.4055643

Notaristefano, A., Persico, G., Gaetani, P., (2023) Turbulence Measurements Downstream of a Combustor Simulator Designed For Studies on the Combustor-Turbine Interaction, *European Turbomachinery Conference 15*, Budapest, Hungary

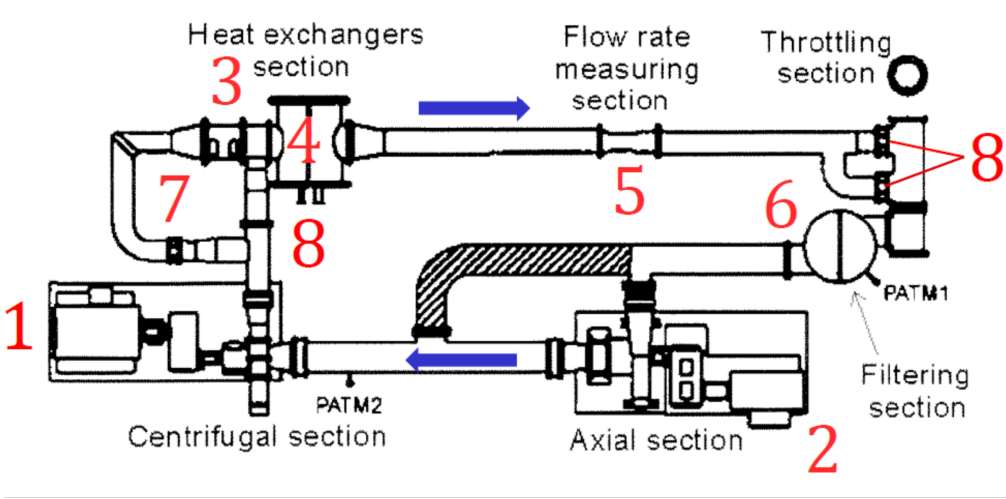

FIGURE 2.1. Air circuit and components.

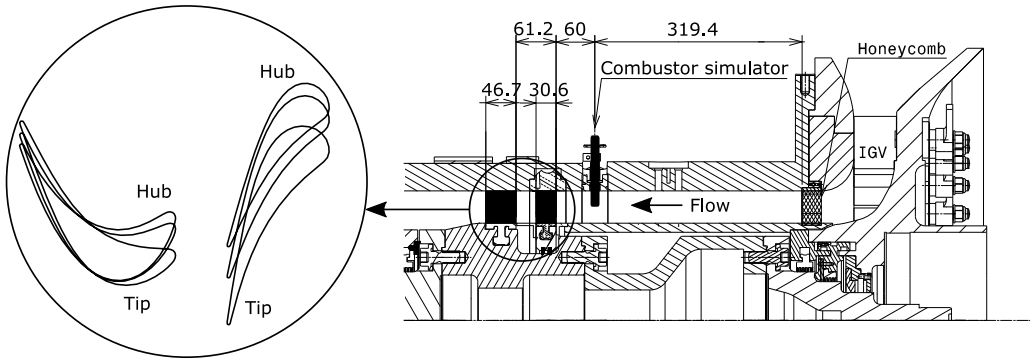

FIGURE 2.2. Turbine meridional plane and blade geometry detail. Dimensions are expressed in millimeters.

2.1 Turbine test rig

The PoliMi turbine test rig is a closed-loop non-reactive facility designed to test different axial turbines and centrifugal compressors. The research capabilities of the facility include studying the operating characteristics of these machines by exploiting the property of similarity and conducting three-dimensional fluid dynamics measurements. The air circuit schematic is shown in Fig. 2.1.

The facility is continuously fed by a centrifugal compressor, that is component 1 in Fig. 2.1. It is a single-stage machine composed of an aluminum impeller and diffuser, both enclosed in a carbon steel case. The impeller has 16 backward curved blades without splitter blades and an external diameter of 400 mm. The vaned diffuser is equipped with 19 blades and is preceded by a 20 mm vaneless diffuser. The centrifugal compressor is powered by an electrical motor with a rated power of 800 KW and voltage of 600 V.

The turbine section (component 2 Fig. 2.1) features a single-stage un-cooled axial turbine that is representative of a highly-loaded and low aspect ratio high-pressure turbine stage. The meridional view of the test section is shown in Fig. 2.2. An inlet guide vane is placed upstream of the stage to pre-orient the flow, thereby reducing total pressure losses through the honeycomb. The

TABLE 2.1. Turbine geometry parameters.

Geometry	h [mm]	t_c/h	D_m [mm]	$Gap/c_{x,V}$
	50	0.02	350	1.0
Blade rows	Blade number	Solidity	AR	Blade deflection [°]
Vane	22	1.2	0.83	75.2
Rotor	25	1.25	0.91	115.3

flow at the turbine inlet is uniform, and there is room to place a combustor simulator approximately 60 mm upstream of the stator blade leading edge.

The turbine can operate in subsonic or transonic conditions and has a blade height of 50 mm, constant through the stage, and an inner diameter of 300 mm. The stator row has 22 stationary leaned blades and the rotor has 25 rotating bowed blades. The vane blades are designed with a lean angle of 12°. The radial evolution of the blades is shown in Fig. 2.2 and further geometrical details are listed in Tab. 2.1. The rotor is connected to an electric motor with a nominal power of 400 kW and a supplied voltage of 600 V, which can operate as either a brake or a motor. During experiments, the stator blades are connected to a ring gear that moves the vanes in the circumferential direction while the traversing probes remain fixed.

The other components highlighted in Fig. 2.1 are:

- Secondary (3) and primary (4) air-water heat exchanger.
- Venturi nozzle (5).
- Filtering section (6).
- Throttle valves (7 and 8).

The components listed are necessary for regulating the facility. The temperature at the turbine inlet is controlled by acting on the heat exchangers (3) and (4), while the mass flow, measured using (5), is regulated by means of the throttling valves (8).

From a thermodynamic point of view, the working fluid is air that can be assumed as a perfect gas. The static pressure at the compressor inlet is regulated acting on the pressure tap PATM2 in Fig. 2.1. The second controlled thermodynamic point is the inlet temperature at the turbine inlet by means of the heat exchangers. The desired operating condition is determined acting on the turbine and compressor rotational speed, as well as imposing the desired mass flow rate by the valves. Each operating point (OP) is sufficiently stable to perform time-resolved analysis. During the timespan of a few hours required to complete a test, the temperature drift is of ±0.25°C, the rotational speed changes of ±10 rpm and the expansion ratio of ±0.001.

2.1.1 Definition of the operating conditions

In this research, four operating points are studied. Two different expansion ratios are set and, with one expansion ratio fixed, three rotational speeds are considered. The design condition at a low expansion ratio is labeled OP3. Changing the rotational speed of OP3, the rotor incidence angle varies, as shown in Fig. 2.3. The purpose of varying the rotational speed is to investigate the influence of off-design conditions on the interaction between combustor non-uniformities and the turbine stage. The unloaded condition OP3U runs at 8240 rpm and experiences an average negative incidence of -10° along the blade span, resulting in reduced blade loading. The loaded operating

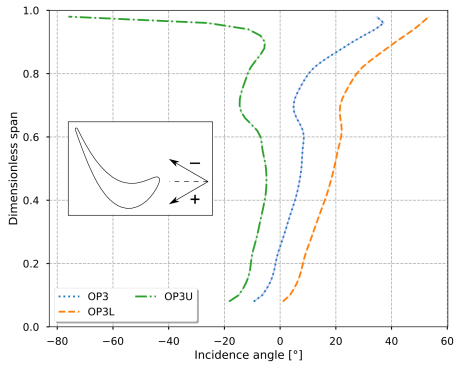

FIGURE 2.3. Rotor incidence angle for the OP3, OP3U and OP3L cases.

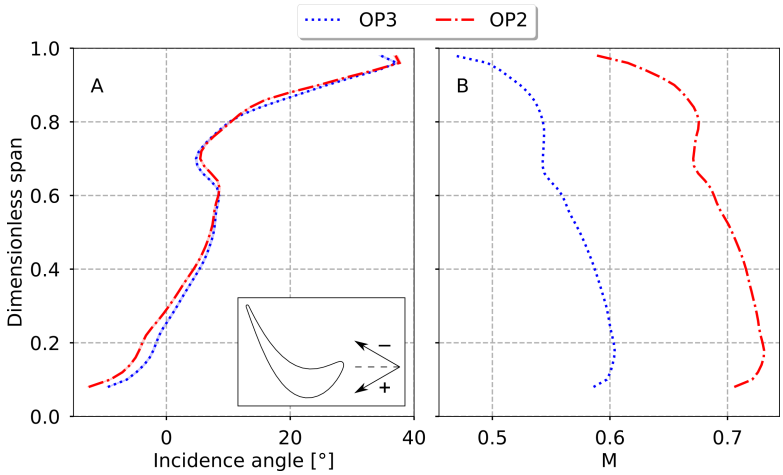

FIGURE 2.4. Rotor incidence angle (A) and M (B) for the OP3 and OP2 cases.

point OP3L operates at 5000 rpm and has the largest incidence angle, ranging from close to 0° at the hub to +20° at mid-span and +45° at the tip. Measurements downstream of the stator show a constant pattern in terms of angles and total pressure losses among the three OP3 cases, while the reaction degree slightly changes, affecting static pressure and Mach number. On average, with respect to OP3, Mach number increases by 0.015 in OP3L and reduces by 0.01 in OP3U. This is a consequence of the change in static pressure, which is 15 mbar higher in OP3L and 10 mbar lower in OP3U than in OP3.

The fourth operating point, OP2, features the highest expansion ratio and speed. OP2 has been chosen to achieve the same mid-span velocity triangle at the stator outlet/rotor inlet as OP3 (Fig. 2.4 A). This condition is representative of a transonic condition, providing a basis for comparison with the OP3 condition. The increase in expansion ratio and Mach number also results in an increase in Reynolds number, which slightly affects losses and performance. In particular, Fig. 2.4 B shows an increase in Mach number of approximately 20% in OP2 compared to OP3.

Table 2.2 lists the main thermodynamic and cycle properties, as well as the main non-dimensional coefficients.

TABLE 2.2. Operating points parameters. M and Re computed at plane T3 are based on the relative velocity.

	OP3		OP3U		OP3L		OP2	
$T_{t,1}$ [°C]	40		40		40		50	
β	1.4		1.4		1.4		1.76	
$\dot{m}$ [kgs]	3.85		3.82		3.92		5.30	
$n\,[rpm]$	7000		8240		5000		8740	
u/v_1	0.65		0.77		0.46		0.66	
$v_{1,a}/u$	0.38		0.31		0.54		0.37	
λ	1.75		1.26		3.43		1.88	
	T2	T3	T2	T3	T2	T3	T2	T3
$Re/10^5$	8.7	4.4	8.6	4.5	8.8	4.1	12.1	6.0
M	0.57	0.34	0.57	0.35	0.59	0.32	0.71	0.47

2.2 Combustor simulator

The turbine test rig, described in section 2.1, can accommodate a combustor simulator as shown in Fig. 2.2. The turbine geometry allows for the installation of one combustor simulator for every two stator vanes. This device was designed from scratch and is an updated version of the EW/HS generator described by Persico *et al.* (2017). One of the main innovations of this device is the ability to superimpose a steady or unsteady temperature disturbance with a swirl profile. As discussed in 1.1.2.3, while there are a few combustor simulators capable of combining a swirl profile with a steady temperature disturbance, to the best of the author's knowledge, none can combine a swirl profile with an unsteady temperature disturbance.

The layout of the combustor simulator is shown in Fig. 2.6, which should be referred to for the labels of the components used in its description. The combustor simulator is supplied with compressed air sourced from the laboratory reservoir described in section 2.3, which operates at a pressure of 180 bar. To heat the compressed air, an "electric heater" with a maximum power of 600 W is utilized. The air temperature is regulated by a power regulator that controls the outlet temperature measured by a K-thermocouple. This device has a constraint on the outlet temperature, which cannot exceed an increase of 400°C compared to the inlet temperature. Depending on the desired temperature disturbance, either the "valves dispenser" is activated to produce EW or the "by-pass valve" is opened to generate HS. While the HS generation is straightforward, the EW production requires a more detailed description. The "valves dispenser" is a set of automotive fuel injectors for methane-fueled engines that can operate at a maximum frequency of 110 Hz. These devices are driven by pulse width modulation (PWM), specifically built in-house. Each PWM circuit requires two relays (S1 and S2 as shown in Fig. 2.5) that are controlled by an Arduino board. The valve frequency can be set by the operator at the beginning of each test. The two relays are controlled to provide a current peak needed to open the valve (when both S1 and S2 are closed) and a lower current (when S1 is closed and S2 is open) that maintains the valve opened. Each valve has its own circuit, so by opening or closing relay S1, the hot and cold branches are opened. Different valve duty cycles can also be imposed using the Arduino board. The fuel injectors ("hot valve" and "cold valve") alternatively feed two different ducts, both with installed electric heaters. The "main hot duct" has its heater switched on, while the "main cold duct" has its heater switched off. This configuration ensures the same pressure losses. The two main ducts are then coupled at the head of an injector into two tubes angled at 2° with respect to the injector axis and with a diameter of 0.3 mm. The EW/HS enters in a larger volume that is reduced as much as possible to

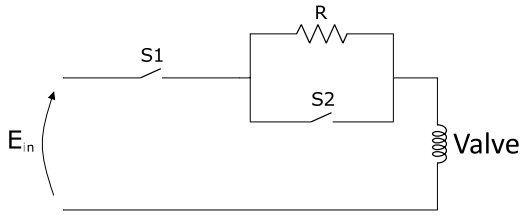

FIGURE 2.5. Valve control circuit.

minimize mixing between the hot and cold spots in the EW case. Finally, the EW/HS is injected in the turbine streamwise direction and forced through a swirler generator. This device acts on both the mainstream air coming from the turbine and partially on the EW/HS, according to the schematic shown in Fig. 2.7, generating a clockwise vortex if viewed from upstream of the injector (Fig. 2.8 A). The central region of the swirler generator (4 mm diameter), fed by the EW/HS, is not swirled to minimize the risk of generating instabilities (Hall *et al.* (2014)). The entire injector is manufactured using 3D printing technology, specifically chrome-cobalt material. The thinnest section of the injector measures 0.5 mm, while the smallest diameter is 3 mm. Both of these values exceed the manufacturer's suggested limits. The injector stem is elliptical in shape, with dimensions of 10 mm and 13 mm, where the longest dimension is aligned axially. The inner case of the swirler measures 15.4 mm. The surface roughness of the device is approximately 1 m. The blade is designed with an inlet angle of 20° and an outlet angle of 40°. Among various geometries considered, this particular swirler generator was chosen for its ability to provide the most uniform and intense swirl profile.

Figure 2.8 B shows the full integration of the combustor simulator into the turbine test rig, with the main geometric distances highlighted. Furthermore, Fig. 2.8 B shows the traversing planes:

- **T1** Located downstream of the combustor simulator and upstream of the stator row.
- **T2** Located in the inter-stage gap at 67% of the vane axial chord downstream of its trailing edge.
- **T3** Located downstream of the rotor at 32% of the rotor axial chord downstream of its trailing edge.

The combustor simulator is fully instrumented. The supply air temperature is measured by a T-type thermocouple and its total pressure by a Kulite XT190 pressure transducer (full-scale 50 psi). A calibrated nozzle is used to measure the mass flow rate, with its pressure drop measured by a Kulite XT190 transducer (full-scale 10 psi). Downstream of the electric heater, a K-type thermocouple controls the power supply of the heater. The pressure difference between the heater inlet and the turbine static pressure is measured by a Kulite XT190 (full-scale 50 psi) and used as a safety control; if this pressure difference is negative, the heater is switched off. A Kulite XT190 transducer, with a full scale of 10 psi, measures the pressure in the cold duct which is used as a trigger signal to phase-average unsteady measurements. The trigger signal in this study demonstrates a high level of repeatability, which has been carefully verified through various acquisitions by analyzing its Fourier transform. Upon valve opening, a rapid and substantial increase in the pressure signal is recorded, as shown in Fig. 2.9, and the maximum value of this signal is utilized for phase-averaging the measurements.

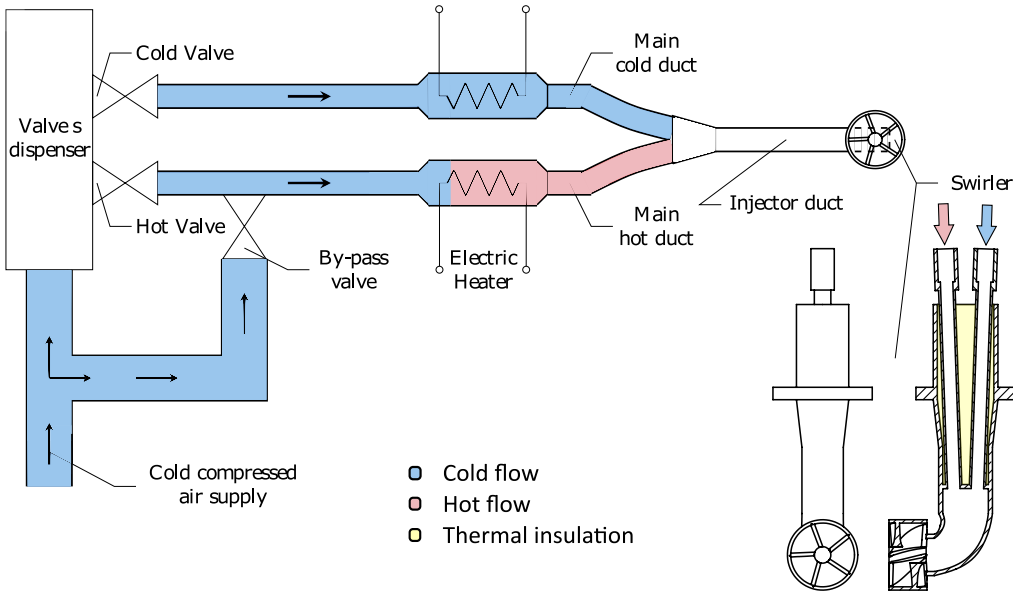

FIGURE 2.6. Combustor simulator schematic.

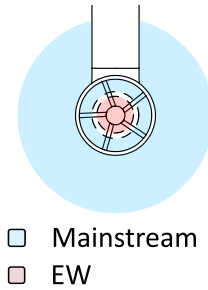

FIGURE 2.7. Downstream view of the combustor simulator.

2.2.1 Definition of the injection cases

The flexibility of both the turbine test rig and the combustor simulator allows testing different injection cases:

- **"Clean"** The combustor simulator is removed, resulting in a uniform flow at the turbine inlet.
- **"EWG off"** The combustor simulator is in place but the air supply is switched off, so the injector duct is not fed. In this case, only a swirl profile is imposed at the turbine inlet by swirling the mainstream air into the swirler generator.
- **"HS"** The combustor simulator is in place, the by-pass valve is opened, the valves dispenser is switched off and the electric heater of the hot duct is switched on. This results in the generation of a continuous steady hot temperature streak superimposed to a swirl profile.
- **"10 Hz" and "110 Hz"** The combustor simulator is in place, the by-pass valve is closed, the valves dispenser is switched on at 10 Hz or 110 Hz, and the electric heater of the hot duct

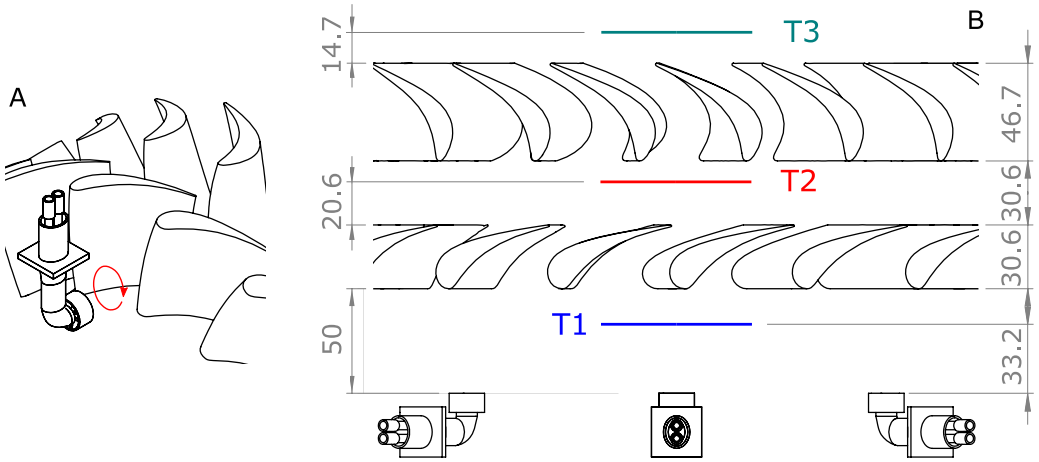

FIGURE 2.8. (A) Swirl profile generated at the turbine inlet. (B) Combustor simulator and turbine geometries. Dimensions are expressed in millimeters.

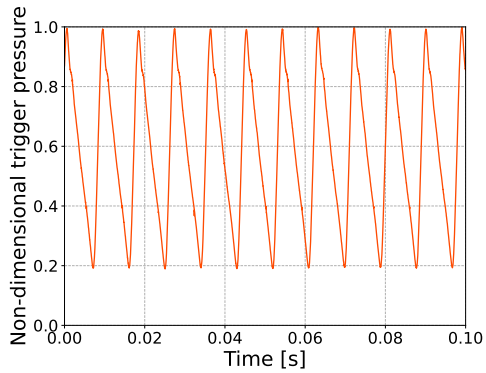

FIGURE 2.9. Example of the pressure trigger signal on the cold duct for 110 Hz, made non-dimensional on the peak value.

is switched on. This results in the generation of an unsteady hot/cold temperature streak superimposed to a swirl profile.

- **"Cold 10 Hz"** The combustor simulator is in place, the by-pass valve is closed, the valves dispenser is switched on at 10 Hz, and the electric heater of the hot duct is switched off. This results in the generation of an unsteady cold/cold temperature streak superimposed to a swirl profile.

Furthermore, for OP3 30 Hz, 50 Hz and 75 Hz are tested. The main parameters of the EW/HS generator are listed in Tab. 2.3. The first number in the "Duty cycle" row refers to the hot period, while the second refers to the cold injection time. Therefore, the valves are modulated to have a longer cold injection time than hot. The feeding pressure is the pressure difference between the inlet of the electric heater in the hot duct and the static pressure at turbine inlet. For each injection case, the best combination of feeding pressure, valve duty cycle, and heater power is chosen to maximize EW/HS peak-to-trough temperature difference while avoiding the formation of a pronounced jet, which would generate a region of high total pressure. These parameters are

TABLE 2.3. Combustor simulator main parameters.

Injection case		HS	10 Hz	110 Hz	Cold 10 Hz
Frequency [Hz]		0	10	110	10
Duty cycle		0-0	40-60	35-65	40-60
Feeding pressure [bar_G]	OP3	0.7	1.2	0.7	1.2
	OP2	0.9	1.5	0.9	
Heater power [W]		600	600	600	0

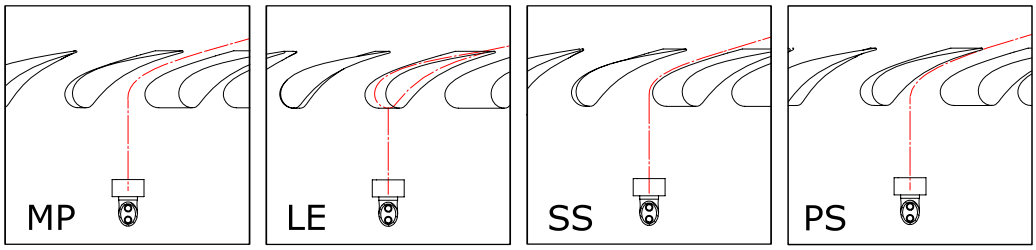

FIGURE 2.10. Injection positions.

tuned in OP3, while the feeding pressure in OP2 is calculated based on the different expansion ratios between OP3 and OP2.

The test rig flexibility allows for testing different alignments between the combustor simulator and the stator vanes. As discussed in section 2.1, the traversing probes are fixed, while the stator and the combustor simulator are mounted on two separate annuli that move synchronously in the circumferential direction to measure the full measuring grid, covering about 32.5° to exploit the combustor simulator full periodicity. The relative position between the combustor simulator and the stator vanes can be set at the start of testing. Four different injection cases are considered, as schematized in Fig. 2.10:

- **LE** The combustor simulator is aligned with the leading edge of the stator vane.
- **MP** The combustor simulator is aligned with the mid-pitch of the stator vane.
- **PS** The combustor simulator is aligned with a point at 1/3 of the pitch from the leading edge close to the pressure side.
- **SS** The combustor simulator is aligned with a point at 1/3 of the pitch from the leading edge close to the suction side.

The position of the LE injection case was carefully chosen based on geometric measurements and verified by tracking the temperature disturbance downstream of the stator while changing slightly the initial positioning of the combustor simulator.

2.2.2 List of test cases

Overall, Tab. 2.4 lists all the combinations among the possible parameters tested during the experimental campaign. Considering the different injection cases, injection positions, and OPs, 56 different test cases are experimentally studied in this research. OP3 is the most studied operating condition and was the first to be assessed. After its evaluation, it was decided to focus on a smaller number of test conditions for the other OPs that were found to be the most representative in order

to reduce the required testing time. Even in OP3, some cases were only evaluated at the stator outlet because they were found to be very similar to others that had already been tested.

2.3 Calibration facilities

Two further experimental calibration facilities have been used to calibrate probes. Both facilities are blow-down wind tunnels that are fed by a reservoir of compressed air with a maximum pressure of 180 bar. The test pressure is set at the inlet of the wind tunnels using a series of throttling valves. To prevent ice formation inside the pipes due to the temperature drop caused by expansion, air is heated before reaching the throttling valve using a heat exchanger fed by hot oil. The maximum air mass available for the tests is 3200 kg, which allows for complete calibration at low Mach number. However, at transonic conditions, the need for more mass flow can only be satisfied by splitting the calibration into two parts.

The wind tunnel used for aerodynamic calibrations of pressure probes is shown in Fig. 2.11. It generates a stable flow field at a fixed Mach number throughout the calibration process. Before reaching the nozzle, compressed air passes through a stagnation chamber and a honeycomb to dampen vibrations and make the flow more uniform. In the convergent section of the wind tunnel, a Pitot tube measures the reference total pressure. It is positioned far enough upstream from the probe under calibration to prevent any disturbance to the measurement. The generated flow exits the nozzle in a rectangular section where the probe under calibration and the reference static pressure tap are placed. The probe tip and static pressure tap are positioned at the same streamwise cross-section for reliable Mach number definition. Additionally, the tip of the probe under calibration is placed in the center of the cross-section, which can be considered isentropic with good approximation, so that it is not influenced by the boundary layer at the nozzle walls. Given the small section occupied by the probe, static pressure is assumed constant across the entire nozzle exit area. Typically, the probe is mounted on two motors that allow probe rotations according to the schematic shown in Fig. 2.11. For all the calibrations, the yaw angle is defined as the angle around the probe axis, the pitch angle is the angle of inclination of the probe axis with respect to the main flow direction.

The second calibration wind tunnel (Fig. 2.12) operates similarly to the previous one, but with the added capability of two additional linear motions in a plane perpendicular to the streamwise direction. This allows for the characterization of a full 2D measuring grid. This calibration wind tunnel is used to measure the turbulence generated by the combustor simulator, as it is not feasible to do so in the turbine test rig due to geometric constraints. To achieve this, the combustor simulator is mounted on the wind tunnel, as shown in the photo on the right side of Fig. 2.12. This blow-down wind tunnel replicates turbine inlet conditions by imposing the same Mach number. However, due to density effects, Reynolds number is 30% lower than in the turbine test rig. Table 2.5 shows the mainstream properties. Three Reynolds numbers are given: Re_{duct} is based on the duct size, $Re_{c,s\omega irler}$ on the chord of the swirler generator blades and $Re_{d,injector}$ on the injector diameter. The calibrated nozzle has a square exit section of 0.08 m side and retains a wall-bounded character for an axial distance of two jet widths downstream of the nozzle according to the nozzle calibration performed by Persico *et al.* (2010). The combustor simulator is placed within a straight prolongation added downstream of the exit section, as shown in Fig. 2.12. Probes are traversed downstream of the device at two planes, one representative of the plane where measurements are carried out upstream of the turbine stage, that is approximately one chord of the swirl generator blade downstream of the device itself, and the second at a position coincident with the turbine vane LE (in the turbine experiments). Both planes are inside the axial extension of two jet widths.

TABLE 2.4. Combustor simulator main parameters. Bold names indicate that the case is fully characterized, non-bold names indicate that the characterization is limited to the aero-thermal measurements at the stator outlet, italicized names are limited to temperature measurements at the stator outlet.

	Operating points				Injection case									Injection position			
Name	OP3	OP3U	OP3L	OP2	Clean	EWG off	10 Hz	30 Hz	50 Hz	75 Hz	110 Hz	Cold 10 Hz	HS	MP	LE	PS	SS
Clean OP3	X				X												
OP3 EWG off MP	X					X								X			
OP3 EWG off LE	X					X									X		
OP3 EWG off PS	X					X										X	
OP3 EWG off SS	X					X											X
OP3 10 Hz MP	X						X							X			
OP3 10 Hz LE	X						X								X		
OP3 10 Hz PS	X						X									X	
OP3 10 Hz SS	X						X										X
OP3 30 Hz MP	X							X						X			
OP3 30 Hz LE	X							X							X		
OP3 30 Hz PS	X							X								X	
OP3 30 Hz SS	X							X									X
OP3 50 Hz MP	X								X					X			
OP3 50 Hz LE	X								X						X		
OP3 50 Hz SS	X								X								X
OP3 75 Hz MP	X									X				X			
OP3 75 Hz LE	X									X					X		
OP3 75 Hz SS	X									X							X
OP3 110 Hz MP	X										X			X			
OP3 110 Hz LE	X										X				X		
OP3 110 Hz PS	X										X					X	
OP3 110 Hz SS	X										X						X
OP3 Cold 10 Hz MP	X											X		X			
OP3 Cold 10 Hz LE	X											X			X		
OP3 HS MP	X												X	X			
OP3 HS LE	X												X		X		
OP3 HS PS	X												X			X	
OP3 HS SS	X												X				X
OP3U Clean		X			X												
OP3U EWG off MP		X				X								X			
OP3U EWG off LE		X				X									X		
OP3U 10 Hz MP		X					X							X			
OP3U 10 Hz LE		X					X								X		
OP3U 110 Hz MP		X									X			X			
OP3U 110 Hz LE		X									X				X		
OP3U HS MP		X											X	X			
OP3U HS LE		X											X		X		
OP3L Clean			X		X												
OP3L EWG off MP			X			X								X			
OP3L EWG off LE			X			X									X		
OP3L 10 Hz MP			X				X							X			
OP3L 10 Hz LE			X				X								X		
OP3L 110 Hz MP			X								X			X			
OP3L 110 Hz LE			X								X				X		
OP3L HS MP			X										X	X			
OP3L HS LE			X										X		X		
OP2 Clean				X	X												
OP2 EWG off MP				X		X								X			
OP2 EWG off LE				X		X									X		
OP2 10 Hz MP				X			X							X			
OP2 10 Hz LE				X			X								X		
OP2 110 Hz MP				X							X			X			
OP2 110 Hz LE				X							X				X		
OP2 HS MP				X									X	X			
OP2 HS LE				X									X		X		

TABLE 2.5. Mainstream properties for combustor simulator turbulence characterization.

Re_{duct}	$Re_{c,sirler}$	$Re_{d,injector}$	M	T_t [K]
$2.35x10^5$	$3.5x10^4$	$3.8x10^4$	0.13	303

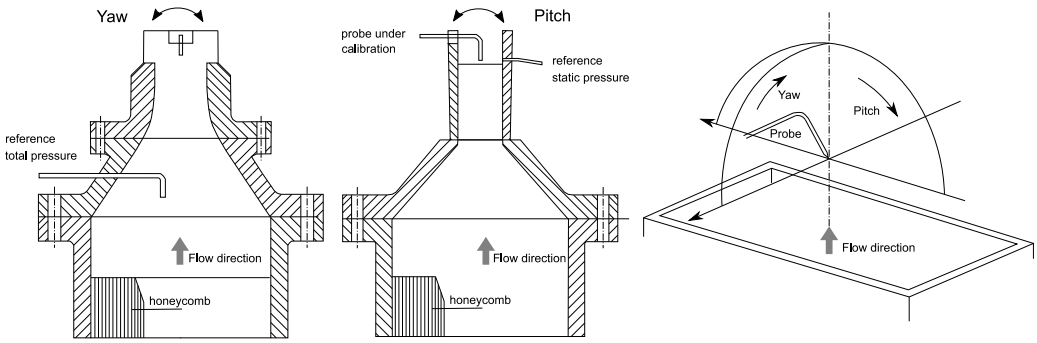

FIGURE 2.11. Schematic of the nozzle used for calibrating aerodynamic probes.

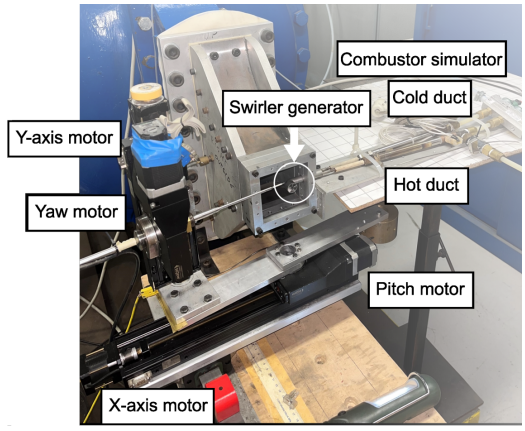

FIGURE 2.12. Wind tunnel layout for measuring the turbulence generated by the combustor simulator.

CHAPTER 3

EXPERIMENTAL AND NUMERICAL METHODS

This section presents a detailed discussion of the measuring and numerical techniques used in this thesis work, highlighting the novelties proposed for data elaboration, which are briefly summarized in this introduction. The angle calibration range of 5-hole probe is extended to angles larger than ±44° to fully characterize the highly swirled flow released by the combustor simulator. A fast response pressure probe is used to characterize the flow unsteadiness and, for the first time, resolve the phase-average at the EW frequency. A μ-thermocouple measures the temperature disturbance at each measuring plane, but it is not fast enough to capture the rotor thermal field. A single-wire slanted hot-wire is used to assess the turbulence flow field downstream of the combustor simulator. Guidelines for improving the calibration process are described. Finally, the numerical methods are presented.

Some contents of this chapter are also discussed in:

Notaristefano, A., Gaetani, P., (2020) Design and Commissioning of a Combustor Simulator Combining Swirl and Entropy Wave Generation, *International Journal of Turbomachinery, Propulsion and Power*, vol. 5(2):6, doi:doi.org/10.3390/ijtpp5040027

Notaristefano, A., Gaetani, P., (2021) Uncertainty Evaluation on Multi-Hole Aerodynamic Pressure Probes, *ASME Journal of Turbomachinery*, vol. 143(9):091001, doi:10.1115/1.4050452

Pinelli, L., Marconcini, M., Pacciani, R., Notaristefano, A., and Gaetani, P. (2023) The Effects of Swirling Flows in Entropy Wave Convection Through High-Pressure Turbine Stage, *ASME Journal of Turbomachinery*, vol. 145(3): 031004, doi:10.1115/1.4055613

Notaristefano, A., Persico, G., Gaetani, P., (2023) Turbulence Measurements Downstream of a Combustor Simulator Designed For Studies on the Combustor-Turbine Interaction, *European Turbomachinery Conference 15*, Budapest, Hungary

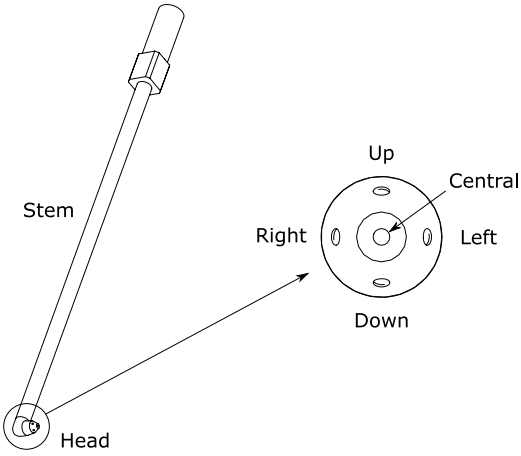

FIGURE 3.1. 5-hole probe schematic.

TABLE 3.1. Pressure transducers uncertainties for 5-hole calibration.

	Quantity	Uncertainty [Pa]
5-hole	p_c	60
	p_l	37
	p_r	34
	p_u	27
	p_d	28
Jet	p_t	45
	p_s	62

3.1 5-hole pressure probe

5-hole pressure probes are used to measure the steady aerodynamic flow field at planes T1 and T2. These probes have a main body and a conical head with five holes: one central and four lateral. Two lateral are on the pitch plane, which contains the probe stem axis and head. The other two holes lie on the yaw plane, perpendicular to the pitch one. Holes are labeled according to the schematic shown in Fig. 3.1.

Two different 5-hole probes are used in this research. At plane T1, the probe has a 5 mm head overhang due to geometric constraints in the turbine test rig, while at T2 it is 15 mm. Both probes have a 2.2 mm head diameter and are small enough to not perturb the flow field.

3.1.1 Calibration and application

During the calibration process, the probe is placed in the wind tunnel described in section 2.3 and exposed to a known flow field. The total and static pressures of the mainstream flow are measured. The flow angles are imposed by moving the 5-hole probe with motors. Each pressure tap on the probe head is pneumatically connected to a pressure scanner (Pressure Systems 9116). Table 3.1 lists the uncertainty values of the pressure scanner. Furthermore, there are additional sources of uncertainty that should be considered, including factors such as the readiness and repeatability of the equipment, as well as the motor precision, which has an accuracy of 0.1°.

The object of the calibration is to obtain calibration matrices at different Mach numbers, selected according to the flow conditions of the test rig where the probe will be used. Values for intermediate Mach numbers are obtained by interpolating the calibration matrices. 5-hole probes are typically calibrated within an angular range of ±22° to avoid stall on the downwind hole. The 5-hole probe used at plane T2 is calibrated with this approach. During calibration, the Mach number is fixed and the probe is moved to different angles relative to the mainstream using motors. At each position, the pressure measured from the five taps is combined into four non-dimensional pressure coefficients relative to the dynamic pressure (Eqs. 3.1, 3.2, 3.3 and 3.4).

$$K_y = \frac{p_l - p_r}{p_t - p_s} \tag{3.1}$$

$$K_p = \frac{p_u - p_d}{p_t - p_s} \tag{3.2}$$

$$K_{p_t} = \frac{p_t - p_c}{p_t - p_s} \tag{3.3}$$

$$K_{p_s} = \frac{p_s - \frac{p_l + p_r + p_u + p_d}{4}}{p_t - p_s} \tag{3.4}$$

Where:

- p_t Mainstream total pressure.
- p_s Mainstream static pressure.
- p_c Central tap pressure.
- p_l Left tap pressure.
- p_r Right tap pressure.
- p_u Up tap pressure.
- p_d Down tap pressure.

When the probe is used in an unknown pressure field, only the five pressure readings are known. An iterative process is required to determine flow angles and pressures. The first step is to guess initial values for total and static pressures. The total pressure is set equal to p_c and static pressure is the average of the four lateral taps pressures. The yaw and pitch coefficients are then calculated. Assuming isentropic flow and perfect gas, the Mach number is known. Flow angles can be computed using bilinear interpolation of the calibration matrices with the known Mach number, K_y, and K_p. These angles are used to interpolate the calibration matrices to derive K_{p_t} and K_{p_s}, which are used to update p_t and p_s. The process is repeated until convergence on Mach number and flow angles is reached.

3.1.2 Extended angular calibration range

The swirl profile generated by the combustor simulator is characterized by high flow angles of around ±40°. This requires calibrating the probe used at plane T1 within a range of ±44°. However, as previously discussed, when flow angles exceed ±22°, stall may occur on the downwind hole. If this happens, calibration coefficients defined by Eqs. 3.1, 3.2, 3.3 and 3.4 are not unique (see Fig. 3.2) and the iterative process described in section 3.1.1 does not converge.

TABLE 3.2. 5-hole probe coefficients for the extended angular calibration range.

Sub-range	Yaw [°]	Pitch [°]	K_y	K_p	K_{p_t}	K_{p_s}
L	-46 → -16	-14 → 16	$-\frac{p_r - p_c}{p_t - p_{mean}}$	$\frac{p_u - p_c}{p_t - p_s}$	$\frac{p_t - p_r}{p_t - p_s}$	
C	-22 → 26	-24 → 16	$\frac{p_l - p_r}{p_t - p_s}$	$\frac{p_u - p_d}{p_t - p_s}$	$\frac{p_t - p_c}{p_t - p_s}$	
R	16 → 46	-14 → 16	$\frac{p_l - p_c}{p_t - p_{mean}}$	$\frac{p_u - p_c}{p_t - p_s}$	$\frac{p_t - p_l}{p_t - p_s}$	
LD	-46 → -10	14 → 42	$\frac{p_c - p_r \frac{p_{mean}}{p_c}}{p_t - p_s}$	$\frac{p_u \frac{p_{mean}}{p_c} - p_c}{p_t - p_s}$	$\frac{p_t - p_u}{p_t - p_s}$	
D	-12 → 10	10 → 42	$\frac{p_l - p_r}{p_t - p_s}$	$\frac{p_u - p_c}{p_t - p_{mean}}$	$\frac{p_t - p_u}{p_t - p_s}$	$\frac{p_s - p_{mean}}{p_t - p_s}$
RD	8 → 46	10 → 42	$\frac{p_l \frac{p_{mean}}{p_c} - p_c}{p_t - p_s}$	$\frac{p_u \frac{p_{mean}}{p_c} - p_c}{p_t - p_s}$	$\frac{p_t - p_u}{p_t - p_s}$	
LU	-46 → -8	-42 → -12	$\frac{p_c - p_r}{p_t - p_s}$	$\frac{p_c - p_d}{p_t - p_s}$	$\frac{p_t - p_d}{p_t - p_s}$	
U	-10 → 10	-42 → -12	$\frac{p_l - p_r}{p_t - p_s}$	$\frac{p_c - p_d}{p_t - p_s}$	$\frac{p_t - p_d}{p_t - p_s}$	
RU	6 → 46	-46 → -12	$\frac{p_l - p_c}{p_t - p_s}$	$\frac{p_c - p_d}{p_t - p_s}$	$\frac{p_t - p_d}{p_t - p_s}$	

To overcome this limitation, new calibration coefficients are defined dividing the angular range into 9 sub-ranges, as listed in Tab. 3.2. Excluding the sub-range called "C", the other sub-ranges are named with the stalled pressure tap name. The pressure information from the leeward tap is ignored in favor of a combination of non-stalled pressures. Only the pressure called p_{mean} is computed using stalled taps, as it is the average of p_l, p_r, p_u and p_d. Figure 3.3 shows the nine K_y and K_p calibration matrices obtained for a Mach number of 0.2. The horizontal and vertical grid lines represent increments of 2° in yaw and pitch angles, respectively.

The reconstruction procedure begins by guessing that the flow meets the conditions of the central sub-range and uses its coefficients definitions. The iterative cycle is resolved as explained in 3.1.1. Since the interpolating functions allow extrapolation, if the flow angle values fall within the defined range for the central matrix, the flow field reconstruction is considered complete. However, if the angular values lie within a different zonal matrix, the flow field reconstruction is repeated using the appropriate set of calibration coefficients. Finally, the obtained flow angles are checked again to ensure they fall within the used sub-range. If not, the iterative cycle is repeated updating the sub-range. To prevent bouncing between the sub-ranges at each iteration, angular boundaries overlap among adjacent sub-range values.

Although the use of stalled pressure taps is limited to calculating p_{mean}, which is not expected to have a significant influence, an investigation into the effect of Reynolds number should be conducted. This is because the pressure probe will operate in a higher Reynolds number flow when placed on the turbine test rig. Unfortunately, this type of investigation cannot be carried out on the wind tunnel in its current layout. Therefore, an analytical analysis was conducted by assuming that

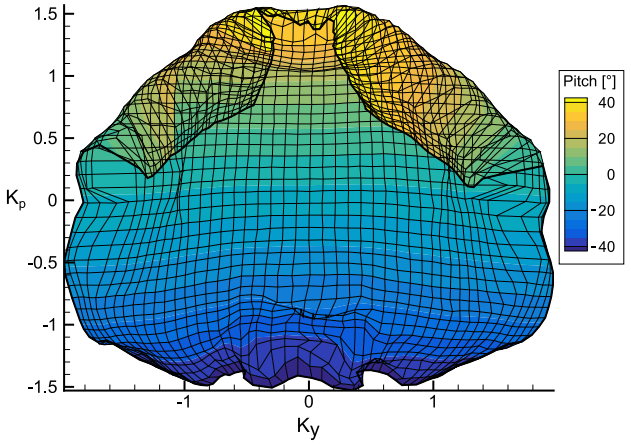

FIGURE 3.2. Calibration matrix of the probe used at plane T1 using Eqs. 3.1 and 3.2.

the flow around the five-hole head is equivalent to the cross-flow around a circular cylinder. This allows for the calculation of pressure in a higher Re number flow.

Fixed the lowest Mach number of the calibration process 0.2, the Reynolds number based on the probe head diameter increases from 9.7×10^3 in the calibration wind tunnel to 1.34×10^4 in the turbine test rig. Using data from Cheng *et al.* (2017), the pressure values of the five holes are updated to account for the different Reynolds numbers. Considering each hole is placed at an angular location of 45° from the central tap, if the flow yaw angle is -45°, the left tap is aligned with the flow, the central tap is at |45°| and the right one is at |90°|. The updated pressure is calculated as shown in Eq. 3.5, where the left pressure is computed at a yaw angle of -45°.

$$p_{Re_{turbine}} = p_{Re_{calibration}} + (c_{p_{Re_{turbine}}}(90°) - c_{p_{Re_{calibration}}}(90°))\frac{1}{2}\rho V^2 \tag{3.5}$$

With the updated pressures, the flow reconstruction is performed. In the worst case, for matrices LD and RD where the stalled pressure is used the most, there is a difference of 0.4° in angles and 0.7 mbar in pressures compared to the calibration outcomes. These values are within the measurement uncertainties. This investigation shows that Reynolds effect is very limited and flow field reconstruction performance is not expected to change. This is consistent with the Re threshold value of $1.1\text{x}10^4$ found by Passmann *et al.* (2021). Above this value, the probe can be used without significant loss of accuracy.

3.2 Fast thermocouple

A fast-response micro-thermocouple is traversed at planes T1, T2 and T3 to characterize the thermal flow field and study the EW/HS transport through the stage. Figure 3.4 shows the used thermocouple that is an S-type with a diameter of 25 μm and an exposed junction. This allows for a quick response from the probe but limits its capability to withstand severe aerodynamic loads. For this reason, this probe is not used downstream of the stator for OP2 cases because it broke after the first test.

Thermocouples are composed of two dissimilar metals joined at both ends. When the temperature at one of the ends changes, it induces an electric current in the circuit. If this circuit is broken at the center, the open-circuit voltage depends on the temperature gradient between the two

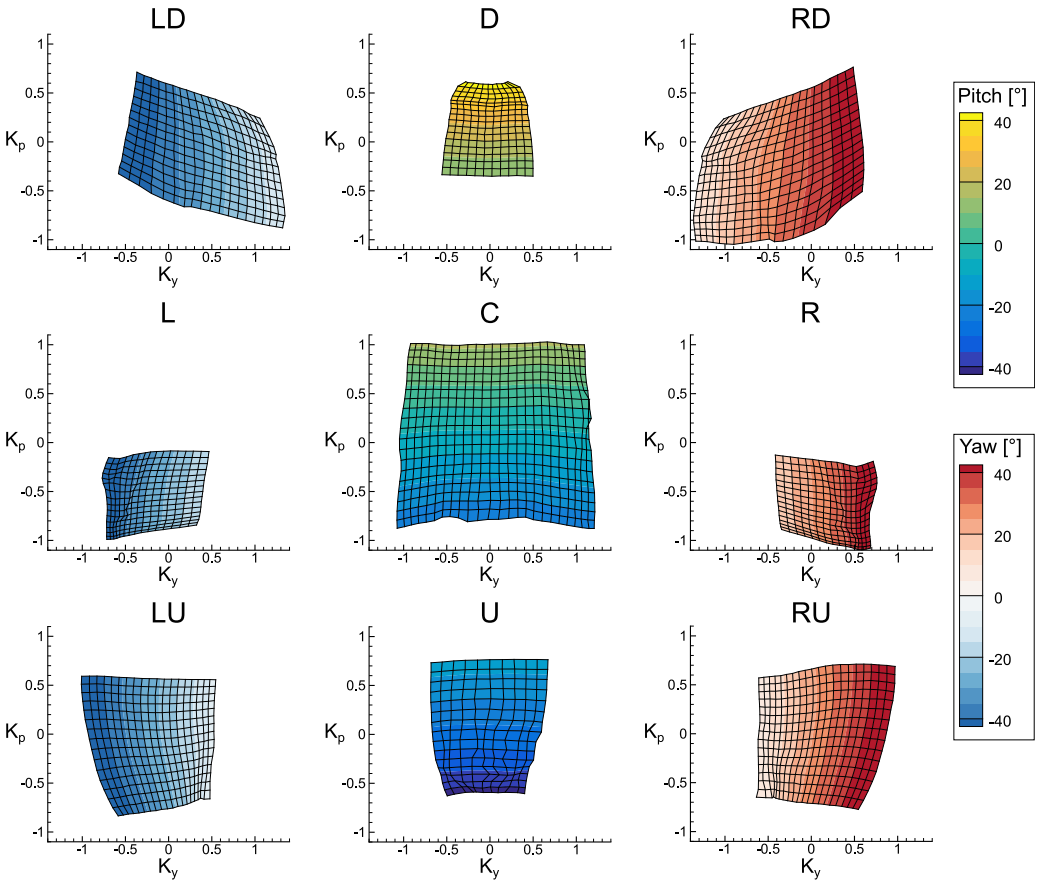

FIGURE 3.3. Calibration matrices of the probe used at plane T1 using coefficients defined in Tab. 3.2.

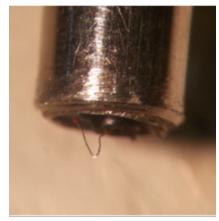

FIGURE 3.4. Picture of the fast thermocouple junction.

junctions. Therefore, it is possible to correlate the junction temperature with the produced voltage. This is typically done through a static calibration in an oven.

To characterize the frequency response of the probe, a dynamic calibration is performed in a shock tube, described by Persico *et al.* (2005). Typically, the frequency response of this probe is similar to that of a first-order linear system. Therefore, if the initial and final states, as well as the time constant, are experimentally determined, the transfer function is known. The outcomes of the shock tube test are shown in Fig. 3.5. Using shock equations, the ideal shock temperature can be calculated (black line in Fig. 3.5). The experimentally measured temperature is interpolated using a 4^{th}-order polynomial and the time constant is defined as the time that it takes for the interpolated

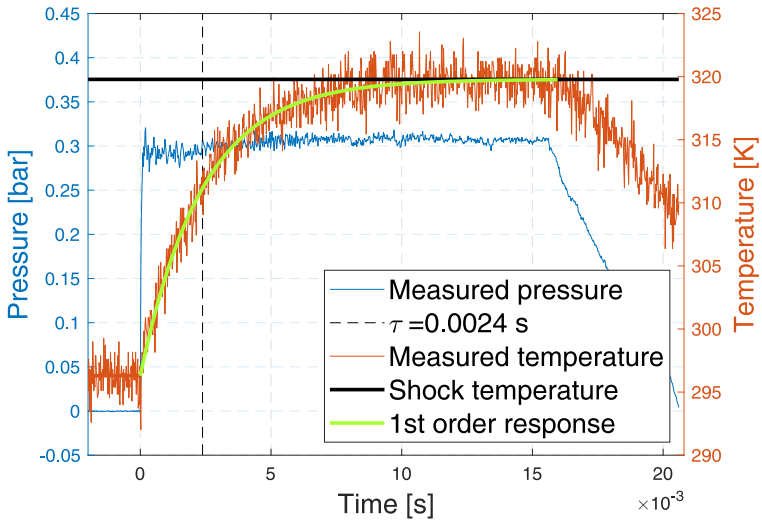

FIGURE 3.5. Dynamic calibration of the fast thermocouple.

line to reach 63.2% of the step shock temperature. Its value of 2.4 ms, coupled with frequency compensation, allows for extending the instrument frequency range up to about 500 Hz. This frequency range is sufficient to characterize the EW, which has a maximum frequency of 110 Hz, but it is not fast enough to resolve the rotor thermal flow field, which has a minimum blade passing frequency of about 2000 Hz in OP3L.

3.3 Fast response pressure probe

A single-hole fast response cylindrical pressure probe (FRAPP) is used during measurements on the turbine test rig. Its main geometrical parameters are shown in Fig. 3.6. The probe is traversed at planes T2 and T3 to reconstruct the flow field where the flow is inherently unsteady due to the rotor passage. Furthermore, this type of probe can analyze the unsteadiness related to the EW frequency.

The cylindrical shape of the probe makes it suitable for measuring flow direction in a plane perpendicular to the cylinder axis (yaw angle), as well as total and static pressures. However, it has a low sensitivity to the flow components parallel to the axis (pitch angle). The probe is considered insensitive to pitch angle values within ±10°, as determined by a dedicated test campaign. In the turbine test rig, pitch angles fall within this limitation, allowing for FRAPP accurate measurements.

The probe is designed for miniaturization with a main dimension of 2 mm and contains a single sensor. It operates as a virtual 3-hole probe by measuring pressures at different rotations around its axis. The lack of simultaneous measurements is not a significant limitation for unsteady measurements since the periodic component of the flow unsteadiness is typically of interest. This component can be extracted using ensemble averages locked on a key-phasor. If measurements are to be phase-averaged based on rotor frequency, a key-phasor placed on the rotor wheel is used. If the focus is on studying the EW, the key-phasor is the trigger pressure measured on the combustor simulator, as described in section 2.2.

The virtual operation precludes direct turbulence measurements. However, an estimate of the turbulence intensity can be obtained by considering the signal acquired by the probe at its angular

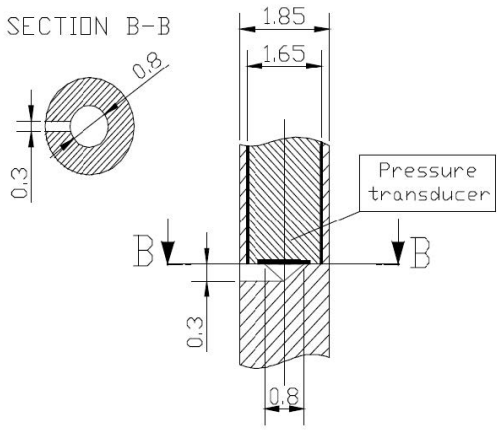

FIGURE 3.6. Schematic of the FRAPP.

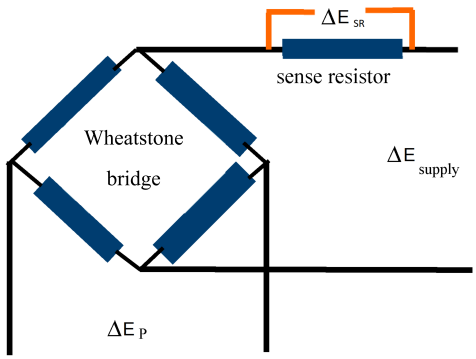

FIGURE 3.7. Electrical scheme for the pressure and temperature calibration.

position aligned with the phase-averaged flow direction when the unresolved flow angle fluctuations are sufficiently low (±9°), as discussed by Persico *et al.* (2008).

A dynamic calibration was performed in a shock tube to determine the promptness of the FRAPP, which was found to be about 80 kHz. This value is high enough to meet the specifications of all FRAPP applications considered in this research. The transfer function is similar to a second-order linear system, with a peak at about 35 kHz representing the resonance of the probe line-cavity system. The discovered transfer function is used to compensate the measured signals.

Due to the sensor sensitivity to temperature, a calibration in both pressure and temperature is required before performing aerodynamic and dynamic calibrations. The sensor sensitivity to temperature is measured by applying an additional resistance called sense resistance (see Fig. 3.7). The voltage drop across this resistance (ΔE_{SR}) is primarily a function of the current flowing through the bridge, which depends on the bridge temperature.

During the static calibration, FRAPP is inserted into an oven which allows for setting the temperature. After steady thermal conditions have been established, a static pressure calibration ramp with both positive and negative slopes is applied over the range foreseen for the tests. As a result, slope (S_{p_i}) and intercepts (Q_{p_i}) for the $i-th$ temperature level are determined using linear interpolation with respect to the voltage difference across the bridge ΔE_p. Once the pressure

calibration is completed, the oven temperature is changed and the previous calibration is repeated.

Finally, S_{p_i} and Q_{p_i} are interpolated using a parabolic function with respect to ΔE_{SR}. Equations 3.6, 3.7 and 3.8 can be used during application to reconstruct the pressure readings of the FRAPP.

$$p_{FRAPP} = S_p \Delta V_p + Q_p \tag{3.6}$$

$$S_p = a_s \Delta E_{SR}^2 + b_s \Delta E_{SR} + c_s \tag{3.7}$$

$$Q_p = a_q \Delta E_{SR}^2 + b_q \Delta E_{SR} + c_q \tag{3.8}$$

Once the probe is statically calibrated, it can undergo aerodynamic calibration in the wind tunnel described in section 2.3. For its application on the turbine test rig, the FRAPP is calibrated over an angular range of ±22° and from Mach numbers ranging from 0.2 to 0.8. As previously mentioned, the probe operates as a virtual three-hole probe, with p_l and p_r obtained by rotating the probe around its axis from the central position by ±45°. This allows for defining three coefficients, as shown in Eqs. 3.9, 3.10 and 3.11.

$$K_y = \frac{p_l - p_r}{p_t - p_s} \tag{3.9}$$

$$K_{p_t} = \frac{p_t - p_c}{p_t - p_{atm}} \tag{3.10}$$

$$K_{p_s} = \frac{p_s - \dfrac{p_l + p_r}{2}}{p_t - p_s} \tag{3.11}$$

Using the defined coefficients, the probe can be applied to an unknown flow field using an approach similar to that described for 5-hole probes in section 3.1.1. For the FRAPP, the absence of K_p simplifies the interpolation, reducing it to only K_y.

3.4 Hot-wire

A slanted single-wire hot-wire probe is used to characterize the turbulence content of the flow released by the combustor simulator. This probe has a slanting angle χ of 45° and is connected to a DISA55M system. The hot-wire is calibrated in the wind tunnel described in section 2.3, which schematic is shown in Fig. 3.8. Figure 3.8 shows also two different reference systems: one relative to the wind tunnel and one to the hot-wire. The former is composed of 2 that is the axial component, 1 is parallel to the combustor simulator injector stem axis and 3 is perpendicular to it. The hot-wire reference system is composed by a component normal n and binormal b to the wire, and by a component which lies on the wire direction t. The probe is mounted on four stepping motors (Fig. 2.12): two of them control the traversing position, one controls the yaw angle (φ in Fig. 2.3) and the last controls the pitch angle (Π). The thin wire of approximately 5 μm guarantees a very high dynamic response (30 kHz) in the constant temperature configuration. To keep the wire temperature constant in presence of an incoming flow, the hot-wire Wheatstone bridge regulates the supply voltage. This well-established response relationship is described by the King's law (Eq. 3.12).

$$\bar{E}_{corr}^2 = A + BQ^n \tag{3.12}$$

Where:

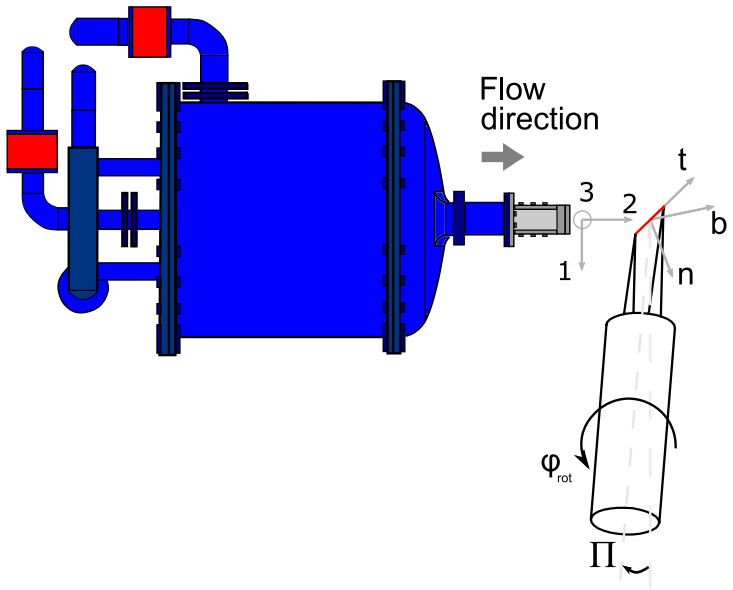

FIGURE 3.8. Calibration nozzle viewed from above and calibration reference systems.

- $\bar{E}_{corr}$ is the mean average of the supply voltage, corrected to account for temperature drifts (Eq. 3.15).
- Q is the cooling velocity.
- A, B and n are calibration constants.

The calibration constants are obtained after a least square regression of the calibration data. The King's law is obtained aligning the hot-wire perpendicularly to the main flow. In such a way, the cooling velocity Q corresponds to the flow velocity V. For a slanted single-wire probe, the pitch angle has to be imposed at -45° and the yaw angle to 0°, according to the reference system shown in Fig. 3.8. Therefore, the cooling velocity depends only on the velocity normal component to the hot-wire U_n, as possible to derive resorting to the change in the reference system highlighted by Eq. 3.13.

$$\begin{cases} V_n = V(cos\Pi cos\varphi sin\chi - sin\Pi cos\chi) \\ V_t = V(cos\Pi cos\varphi cos\chi + sin\Pi sin\chi) \\ V_b = -V cos\Pi sin\varphi \end{cases} \tag{3.13}$$

In the other positions of the hot-wire with respect to the mainstream flow, the angular sensitivity of the probe with respect to the other components must be known but it is unknown at this stage of the calibration. A further constraint to determine the King's law is that the turbulence intensity of the calibration jet is below 5% or the velocity component will depend also on the Reynolds tensor components. This condition is satisfied in the calibration facility used.

To improve the results reliability of the King's law, it is split into three different voltage ranges, as shown in Fig. 3.9. Furthermore, the anemometer output voltage E is corrected to account for possible temperature drifts during the calibration, using the Eq. 3.14 suggested by Bruun (1995).

$$E_{corr}^2 = E^2 \frac{T_\omega - T_0}{T_\omega - T_{flo\omega}} - E_0^2 \tag{3.14}$$

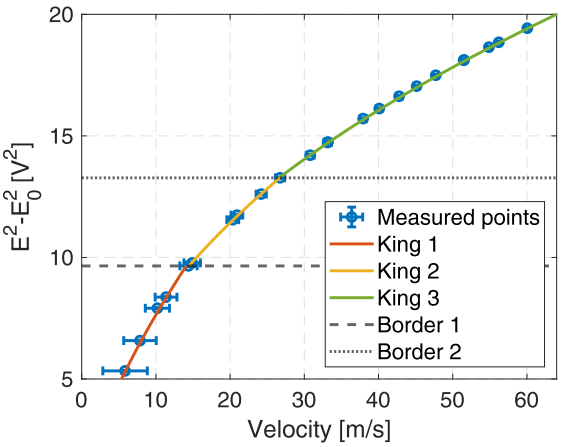

FIGURE 3.9. King's law.

Where:

- T is the constant temperature of the wire (set at 493 K).
- E_0 is the voltage at rest conditions.
- T_0 is the temperature at which E_0 is measured.
- $T_{flo\omega}$ is the temperature of the incoming air.

The fluctuating component of the cooling velocity can be derived by decomposing the King's law as suggested by Perdichizzi *et al.* (1990) and depends on the King's coefficient and the mean velocity:

$$\overline{q^2} = \left[\frac{2\bar{E}^2_{corr}}{nB\bar{Q}^{n-1}}\right]^2 \overline{e^2} \tag{3.15}$$

Where:

- q is the fluctuating velocity component.
- e is the root mean square of the hot-wire voltage measurements.

In real applications, the velocity could have different components than the normal one. The impact of the other velocity components on the hot-wire cooling velocity is non-linear and could be well-described by the Eq. 3.16 or Jorgensen's law (Perdichizzi *et al.* (1990)).

$$Q^2 = V_n^2 + k^2 V_t^2 + h^2 V_b^2 \tag{3.16}$$

k^2 and h^2 are two angular calibration coefficients to be defined through an aerodynamic calibration. First, the coefficient k^2 is defined by setting the yaw angle to 0° and varying the pitch angle on the calibration range of ±45 every 5°. In such a way, $\varphi = 0°$, $V_b = 0$ and k^2 can be computed as shown in Eq. 3.17.

$$k^2 = \frac{\dfrac{Q^2}{V^2} - (cos\Pi sin\chi - sin\Pi cos\chi)^2}{(cos\Pi cos\chi + sin\Pi sin\chi)^2} \tag{3.17}$$

Finally, the aerodynamic calibration can be completed defining the last coefficient of the Jorgensen's law h^2 by means of Eq. 3.18. This is obtained by changing yaw and pitch angles in the calibration range, which for the yaw angle is ±120° every 5°.

$$h^2 = \frac{\frac{Q^2}{V^2} - (cos\Pi cos\varphi sin\chi - sin\Pi cos\chi)^2 - k^2(cos\Pi cos\varphi cos\chi + sin\Pi sin\chi)^2}{cos\Pi cos\chi + sin\Pi sin\chi} \tag{3.18}$$

Defined the calibration coefficients, the probe can be applied in an unknown flow field and the velocity and turbulence content reconstructed. Labeled the rotation of the yaw motor φ_{rot}, the velocity components in the calibration wind tunnel can be related to the ones of the hot-wire by means of Eqs. 3.19.

$$\begin{cases} V_n = V_1 cos\chi + V_2 cos\varphi_{rot} sin\chi + V_3 sin\varphi_{rot} sin\chi \\ V_t = -V_1 sin\chi + V_2 cos\varphi_{rot} cos\chi + V_3 sin\varphi_{rot} sin\chi \\ V_b = V_2 sin\varphi_{rot} - V_3 cos\varphi_{rot} \end{cases} \tag{3.19}$$

Replacing Eqs. 3.19 into Eq. 3.16, the cooling velocity can be written as a function of the velocity components in the nozzle reference system (Eq. 3.20).

$$Q^2 = A_{11}V_1^2 + A_{22}V_2^2 + A_{33}V_3^2 + A_{12}V_1V_2 + A_{23}V_2V_3 + A_{13}V_1V_3 \tag{3.20}$$

The coefficients A_ij are a function of the yaw angular position, the slanted angle and the calibration coefficients h^2 and k^2. However, one single equation is not enough to solve the flow field which has three unknowns. The system is overdetermined with 13 equations obtained by changing the probe yaw angle in the range ±120° every 20°. This set of angles is chosen after optimization of the procedure in terms of computational costs and results reliability considering different ranges and steps. The first guess of the velocity is evaluated as Q computed by King's law (Eq. 3.12) with only an axial component ($V = V_2 = Q$). The outcome of this overdetermined system is the velocity with its three components. However, the effective cooling velocity depends also on the velocity fluctuating components, making the previous approach valid only for low turbulence intensity flows. Expressing each velocity component in terms of mean (denoted with upper case letters) and fluctuating (denote lower case letters) components, and calculating the mean value (denote with an overline), Eq. 3.20 can be written as Eq. 3.21. In this equation, time mean and Reynolds stress components can not be separated.

$$\overline{Q^2} = A_{11}(\bar{V}_1^2+\overline{v_1^2})+A_{22}(\bar{V}_2^2+\overline{v_2^2})+A_{33}(\bar{V}_3^2+\overline{v_3^2})+A_{12}(\bar{V}_1\bar{V}_2+\overline{v_1v_2}+A_{23}(\bar{V}_2\bar{V}_3+\overline{v_2v_3})+A_{13}(\bar{V}_1\bar{V}_3+\overline{v_1v_3}) \tag{3.21}$$

Equation 3.21 can be rewritten considering the largest velocity components as the axial one V_2 as done in Eq. 3.22.

$$\begin{aligned} Q = A_{22}^{1/2}\bar{V}_2 \Bigg\{ & 1 + 2\frac{v_2}{\bar{V}_2} + \left[\frac{v_2}{\bar{V}_2}\right]^2 + \frac{A_{11}}{A_{22}}\left[\frac{\bar{V}_1 + v_1}{\bar{V}_2}\right]^2 + \frac{A_{33}}{A_{22}}\left[\frac{\bar{V}_3 + v_3}{\bar{V}_2}\right]^2 + \frac{A_{12}}{A_{22}} \\ & \left[1 + \frac{v_2}{\bar{V}_2}\right]\left[\frac{\bar{V}_1 + v_1}{\bar{V}_2}\right] + \frac{A_{23}}{A_{22}}\left[1 + \frac{v_2}{\bar{V}_2}\right]\left[\frac{\bar{V}_3 + v_3}{\bar{V}_2}\right] + \frac{A_{13}}{A_{22}}\left[\frac{\bar{V}_1 + v_1}{\bar{V}_2}\right]\left[\frac{\bar{V}_3 + v_3}{\bar{V}_2}\right] \Bigg\}^{1/2} \end{aligned} \tag{3.22}$$

The mean velocity and the mean of the fluctuating component can be calculated after approximating at first order Eq. 3.22. Furthermore, series expansion can be applied if all the other

components are assumed much lower than $\bar{V}_2$. Neglecting third order terms or greater, the mean effective cooling velocity is computed by means of Eq. 3.23 as described by Buresti & Di Cocco (1987).

$$\bar{Q} = R_2\bar{V}_2 + R_1\bar{V}_1 + R_3\bar{V}_3 + R_4\frac{\bar{V}_1^2}{\bar{V}_2} + R_5\frac{\bar{V}_3^2}{\bar{V}_2} + R_6\frac{\bar{V}_1\bar{V}_3}{\bar{V}_2} + R_4\frac{\bar{v}_1^2}{\bar{V}_2} + R_5\frac{\bar{v}_3^2}{\bar{V}_2} + R_6\frac{\bar{v}_1\bar{v}_3}{\bar{V}_2} \tag{3.23}$$

Finally, considering that $\overline{q^2} = \overline{Q^2} - \bar{Q}^2$, by subtracting Eq. 3.21 to the square of Eq. 3.23, neglecting third-order terms Eq. 3.24 is obtained. This equation can be used if turbulence intensity is lower than 20%, thus Eqs. 3.22 and 3.23 are consistent.

$$\begin{aligned}\overline{q^2} = Z_1\overline{v_2^2} + \left[Z_2 + 2Z_{10}\frac{\bar{V}_1}{\bar{V}_2} + Z_{12}\frac{\bar{V}_3}{\bar{V}_2}\right]\overline{v_1^2} + \left[Z_3 + Z_{13}\frac{\bar{V}_1}{\bar{V}_2} + 2Z_{15}\frac{\bar{V}_3}{\bar{V}_2}\right]\overline{v_3^2} + \left[Z_4 + 2Z_7\frac{\bar{V}_1}{\bar{V}_2} + \right.\\ \left. + 2Z_8\frac{\bar{V}_3}{\bar{V}_2}\right]\overline{v_1v_2} + \left[Z_5 + Z_8\frac{\bar{V}_1}{\bar{V}_2} + 2Z_9\frac{\bar{V}_3}{\bar{V}_2}\right]\overline{v_2v_3} + \left[Z_6 + Z_{11}\frac{\bar{V}_1}{\bar{V}_2} + Z_{14}\frac{\bar{V}_3}{\bar{V}_2}\right]\overline{v_1v_3}\end{aligned} \tag{3.24}$$

The coefficients A_i, R_i and Z_i are adapted to the used reference system starting from the definition given by Buresti & Di Cocco (1987) and Fitouri *et al.* (1995). Since the flow under study is significantly swirled, the hypothesis of V_2 the dominant component does not hold true on the whole measuring grid, especially in the vortex core. If the tangential velocity V_3 is dominant, the reference system can be rotated but this requires acquiring measurements on a wider rotational range than ±120°, that is chosen at ±160° considering that the maximum/minimum angles expected are ±40°. Therefore, after having resolved the over-determined system of equations considering V_2 the main velocity component, if $\|\varphi\|$ is greater than 10°, then the central hot-wire rotation is updated to the actual velocity direction and V_2 is again the main velocity component, considering the rotation of the coordinate system 1-2-3.

If V_1 is the dominant component, the equations are derived considering this has the main component starting from Eq. 3.22.

The flow chart shown in Fig. 3.10 synthesizes the steps necessary to apply the hot-wire.

Finally, the hot-wire is used to characterize the power spectrum and the turbulence length scale. Roach (1987) proposed a method to compute the integral length scale based on the integration of the autocorrelation of the velocity $R(T)$. By means of Taylor's hypothesis the integral time scale can be converted to the integral length scale. In the case of noisy signals, the autocorrelation can be integrated until it reaches a value of 1/e, to mitigate issues arising from random noise that might delay the autocorrelation crossing zero, as explained by Flay & Stevenson (1986). Taking into account the above, the computation of the integral length scale follows Eq. 3.25.

$$\lambda = V\int_0^{1/e} R(T)dT \tag{3.25}$$

3.5 Uncertainties quantification

Uncertainty quantification is carried out for each used probe to provide results with their uncertainties. This is mandatory when experimental campaigns are under study to make results and comparisons with CFD more reliable.

Considering the complex measurement chain, uncertainties quantification is carried out by means of a Monte Carlo method. To apply this method, the inputs have to be considered with their

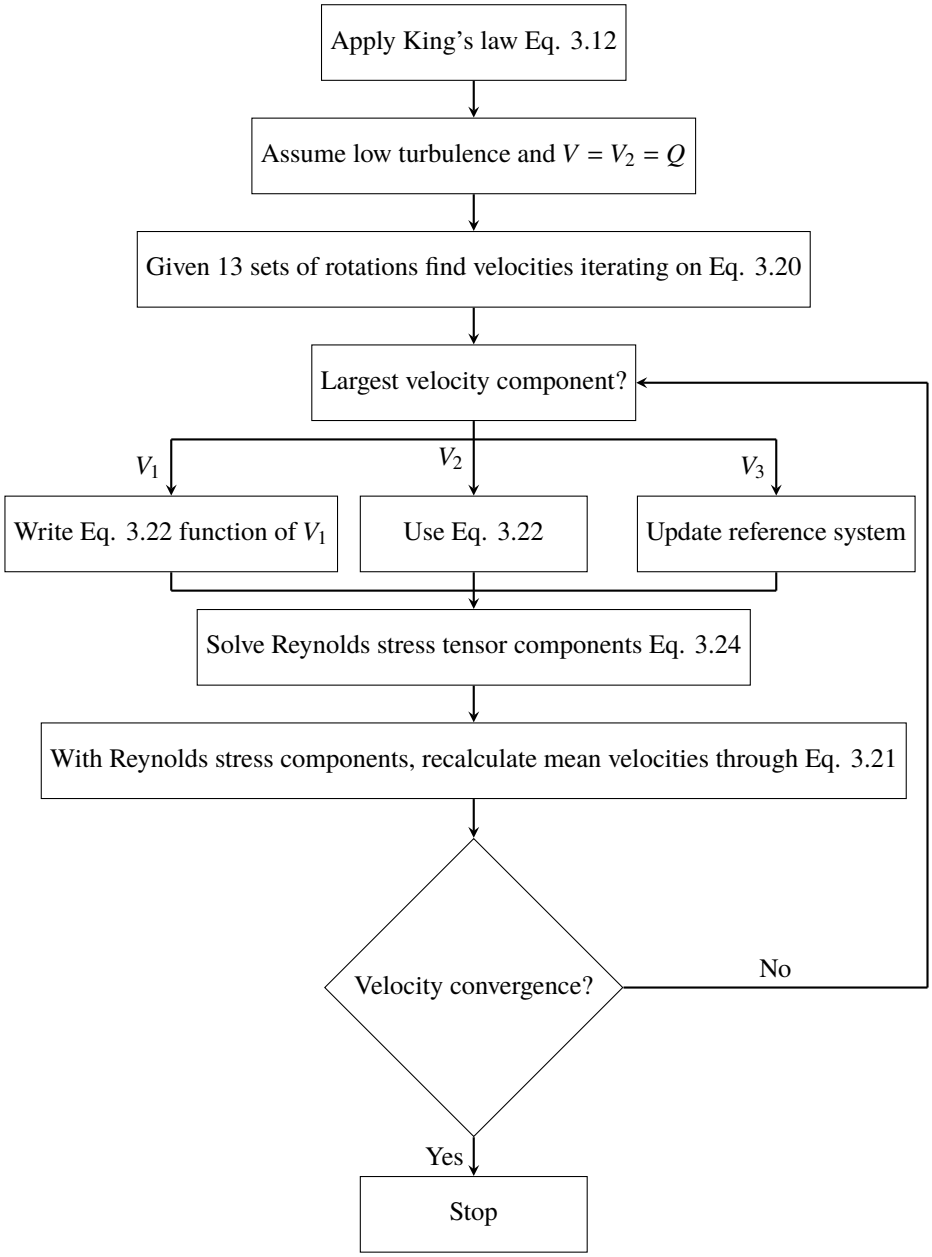

FIGURE 3.10. Flow chart for hot-wire data elaboration.

statistical distribution, that is typically a normal or rectangular one. With each input mean, standard deviation and probability distribution, new data are randomly generated for each parameter and then used to apply the probe's calibration or application processes. This operation is repeated as many times as reasonably sufficient to get a statistically significant output distribution, as suggested by JCGM (2008), at affordable computational cost. The number of iterations is set to 10^4 which guarantees a consistent statistical data set and a converged error. The Monte Carlo method gives

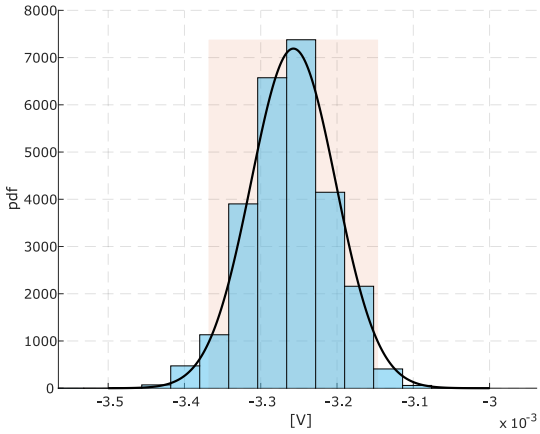

FIGURE 3.11. PDF of one of the pressure transducers used.

TABLE 3.3. Average extended uncertainties of the traversed probes.

Turbine test rig	Pressures	Angles [°]
5-hole probe @ T1	50 [Pa]	0.5
5-hole probe @ T2	80 [Pa]	0.15
FRAPP	0.5% kinetic head	0.25

Hot-wire campaign	T_i [%]	V [m/s]	V_3 [m/s]	λ [m]
Mainstream	0.07	0.5	1	$2.6\text{x}10^{-4}$
Perturbed region	5	4.8	8	$8\text{x}10^{-5}$

as output 10^4 samples of the output quantities, thus its statistical distribution, mean and standard deviation are known. With respect to the classical uncertainty propagation method, the Monte Carlo method is robust and allows to avoid simplifications in the relations among the different quantities and it can handle correlations between inputs. Its main drawback is the great computational effort required to run simulations; however, some tools can help to reduce the computational cost (McKay *et al.* (1979)), even though they are not used in this paper.

The hypothesis of Gaussian distribution for the input quantities is verified on one pressure transducer. The probability density function (PDF) of its distribution is shown in Fig. 3.11, where the blue bars, which represent the PDF of the measured quantities, match with the PDF of a normal distribution with mean and standard deviation computed by the population (black line). The orange region represents the 2σ confidence interval. Skewness and kurtosis are -0.08 and 3.13, respectively, values close to a normal distribution. Therefore, the assumption of Gaussian distribution is considered to be correct.

All the uncertainty outcomes refer to an expanded uncertainty $\pm 2\sigma$ which means a 95% confidence interval, according to the 3-sigma rule. The main uncertainties of the traversing probes are listed in Tab. 3.3. Furthermore, each line plot will be accompanied with the uncertainties bars.

3.6 Numerical calculations setup

The experimental test case has been further studied by means of numerical simulations with the objective to support the experimental measurements to understand the complete flow features.

Three are the numerical campaign carried out:

- By means of a collaboration with the University of Florence, simulations on the turbine test rig have been carried out and compared with experimental data. These simulations provide also data on the acoustic issue.
- During a research stay at DLR in Germany, the acoustic issue has been further investigated. CFD simulations using a Harmonic Balance method on the turbine test rig were performed.
- The experiments of the hot-wire campaign have been simulated. Cases that cannot be studied experimentally are investigated by means of CFD.

Considering that the main goal of this thesis is the experimental characterization, few CFD results are shown and are only limited to the aspects that experimentally cannot be assessed.

The main numerical setups are discussed in the following, with the exclusion of the CFD campaign conducted at DLR using their Harmonic Balance code, which has not yet yielded significant results regarding aero-acoustics - the focus of the analysis. The acoustic post-processing tool utilized by DLR assumes a uniform flow at the plane of application. However, downstream of the rotor, the flow is not uniform enough, which can lead to misleading results. Specifically, the downstream running pressure waves display an undefined trend at different axial positions. Other possible causes of this trend are an energy scattering between radial modes and reflections at the outlet plane, despite the implementation of a buffer zone.

3.6.1 Full-annulus CFD

The unsteady Reynolds-averaged Navier-Stokes (URANS) TRAF code has been used which is capable of simulating HS transport (Gaetani *et al.* (2020)) and EW evolution (Pinelli *et al.* (2021) and Pinelli *et al.* (2022)) through the PoliMi turbine test rig. For this research, the additional challenge is the addition of a swirl profile. The code solves the unsteady, three-dimensional RANS equations in the finite volume formulation on multi-block structured grids. Convective fluxes are discretized by a second order TVD-MUSCL strategy build on the Roe's upwind scheme. A central difference scheme is used for viscous fluxes and a Wilcox $k-\omega$ model in its high-Reynolds formulation is used for turbulence closure. Time-accurate calculations are performed by means of dual-time stepping approach and the coupling between stator and rotor is handled by sliding interfaces that use phantom cells which lie on the adjacent blade passage. For this type of analyses, a time-varying 2D inlet is implemented to impose EW as boundary conditions. Moreover, a run-time Fourier transformation in time of the flow quantities implemented for aeroacoustics studies (Burberi *et al.* (2018)) has been employed to filter the low-frequency content associated with the EW spots: the EW amplitude and 3D shape can be extracted by means of a dedicated post-processing tool (fully described by Pinelli *et al.* (2022)) from the complex Fourier coefficients for comparison purposes.

The computational domain includes the whole experimental domain starting from the measuring plane T1. At the outlet, the domain extends for 4 rotor axial chords downstream of the plane T3 and a buffer zone is included to avoid spurious wave reflections and used as a non-reflecting boundary condition. Any domain tangential reduction is possible given the blade count of 22/25, thus the entire stage is simulated and shown in Fig. 3.12. O-type mesh is used around the blades to obtain a y^+<1.5 and H-shape blocks in the other regions. The mesh density ensures at least 30/40 cells

for the shorter wavelength among the acoustic, vorticity and entropy waves. The overall domain contains about 250 Mcells. The clearance present at both the hub trailing edge of the stator vane and at the tip of the rotor blade have not been discretized, but rather only modeled. The model used involves the transfer of flows from the pressure side to the suction side of the vane, without resolving the flow in the tip gap.

Regarding the boundary conditions, at the inlet the yaw and pitch angles, as well as the inlet total pressure and temperature are imposed, equal to the measured ones, as 2D non-reflecting boundary conditions. Freestream turbulence is 2.5% at the turbine inlet as accurately measured, the turbulence intensity is increased to 8% in the whole region of the combustor simulator perturbation, where the turbulence length scale is imposed equal to the characteristic dimension of the injector. At the outlet the static pressure is set. No slip and adiabatic conditions are applied to all the wall surfaces.

The time discretization is selected to solve up to the second rotor passing frequency that leads to a time step of 0.014 ms in OP3, ensuring a CFL (Courant–Friedrichs–Lewy) number of approximately 0.8. Frequencies of the EW are slightly modified to match the rotor frequencies. For instance, in OP3 the 10 Hz frequency is reduced to 9.72 Hz so that it corresponds to 12 rotor revolutions. Three EW pulsations are fully simulated and convergence is checked in terms of blade lift fluctuations, the mean performance quantities and acoustic emission that must have the same time history between successive revolutions.

By means of this set-up the following cases are studied:

- OP3 10 Hz MP
- OP3 110 Hz MP
- OP3 10 Hz LE
- OP3 110 Hz LE
- OP3 110 Hz MP reversed swirl
- OP3 110 Hz LE reversed swirl
- OP3L 10 Hz MP
- OP3L 10 Hz LE
- OP3U 10 Hz MP
- OP3U 10 Hz LE

3.6.2 Hot-wire characterization CFD

The experimental campaign on the wind tunnel to assess the turbulence levels generated by the combustor simulator is supported by CFD calculations. For this purpose, a dedicated fully-3D URANS computational model was developed in ANSYS-Fluent, considering the injector of the combustor simulator immersed in the nozzle airflow. The same combustor simulator described in section 2.2 is used. Figure 3.13 left shows computational domain. The inlet boundary is placed at the nozzle outlet section. Two further inlet conditions are placed at the head of the injector where steady/unsteady boundary conditions are set to simulate the operation of the combustor simulator in HS/EW mode. Inlet boundary conditions include temperature and velocity magnitude, while the static pressure is specified at the outlet. The injector surfaces are modeled as no-slip walls, and the domain four lateral surfaces, i.e. the lateral surfaces of the jet, are modeled as slip

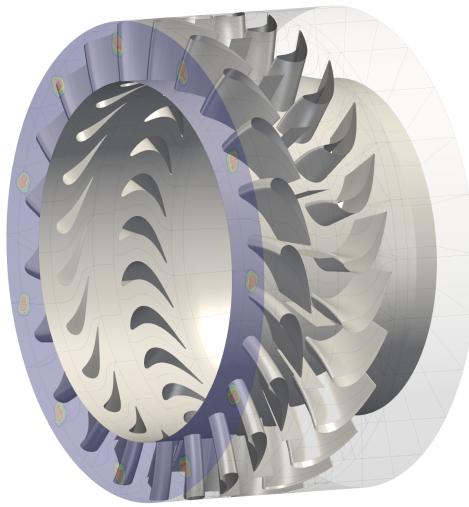

FIGURE 3.12. Computational domain UniFi.

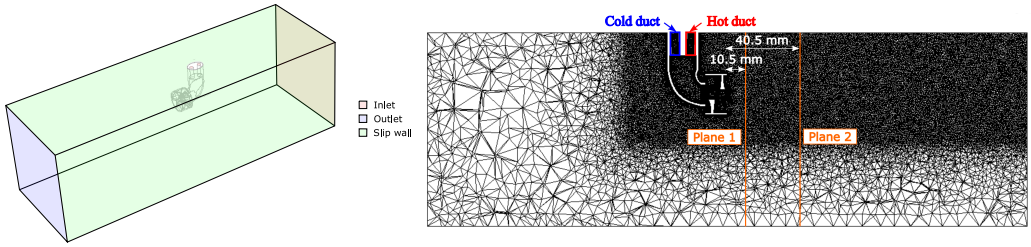

FIGURE 3.13. Hot-wire campaign: CFD computational domain (left); numerical mesh and main measuring distances (right)

walls. According to measurements, at the inlet the turbulence intensity is assigned equal to 1%, the turbulence length scale is also assigned at 10% of the relevant inlet boundary scale.

Unsteady RANS CFD simulations are carried out also in steady injection cases to simulate the vortex shedding downstream of the injector stem, that would play a significant role in the decay of the main properties of the perturbation generated by the simulator. After having performed a fast Fourier transform on the instantaneous mass-flow average at the outlet section, the main periodicity of the problem was identified and the period was discretized into 40 time steps.

Figure 3.13 right shows a cut of the unstructured 3D mesh. Two meshes were tested and the results of a grid-independence analysis are shown in Tab. 3.4. The two meshes feature the same boundary layer resolution, characterized by 20 layers and a y^+<1. Among the two tested meshes, the one with 6 million cells is used, considering the small differences in the outcomes of the grid-independence analysis.

The Fluent pressure-based coupled solver is selected, using the k-ω SST turbulence model and ideal gas as a thermodynamic fluid model. High resolution in the numerical solution is achieved by adopting second-order upwind schemes for the advective fluxes, second-order central differences for the viscous terms, and second-order implicit discretization for the unsteady term.

In this numerical campaign, some cases are tested that are not experimentally investigated. The experimental cases are limited to cold injections because the hot temperature can burn the thin wire and can also modify the hot-wire working principle, since it changes the heat transfer

TABLE 3.4. Hot-wire campaign: grid independence analysis.

	Coarse	Fine	Difference
Number of cells	$6x10^6$	$12x10^6$	
$(p_{t_{inlet}} - p_{t_{outlet}})/(p_{t_{inlet}} - p_{s_{outlet}})$	0.038	0.034	0.49%
$T_{t_{outlet}} - T_{t_{inlet}}$ [K]	0.79	0.76	0.03

TABLE 3.5. Hot-wire campaign: studied cases.

		Cold duct			Hot duct				
Case name	Frequency [Hz]	Feed?	CFD plane treatment	T_t [K]	Feed?	CFD plane treatment	T_t [K]	Exp.	CFD
HS	0	No	Wall		Yes	Inlet	670		X
CS	0	No	Wall		Yes	Inlet	303	X	X
110 Hz	110	Yes	Inlet	303	Yes	Inlet	670		X
110 Hz cold	110	Yes	Inlet	303	Yes	Inlet	303	X	X

coefficient, requiring a dedicated calibration. For this reason, experiments are carried out at ambient temperature switching off the electric heater. Hot cases are limited to a CFD study. Therefore, the case equal to the HS, as described in section 2.2.1, but with the electric heater switched off is called "cold-streak" (CS), the unsteady injection of two cold streaks similar to the EW case is called with the valve frequency followed by "cold-streak". Table 3.5 lists the experimental and numerical tests performed.

Two different traversing planes are studied, as shown in Fig. 3.13 right:

- **Plane 1** It is representative of the plane T1 (section 2.2) where probes are traversed in the turbine test rig to characterize the flow field released by the combustor simulator. It is approximately one chord of the swirl generator blade downstream to the blade TE of the device.
- **Plane 2** This plane is coincident with the turbine vane LE in the turbine experiments.

CHAPTER 4

FLOW FIELD CHARACTERIZATION AT PLANE T1

This chapter introduces the discussion on the experimental data focusing on the results at plane T1. The flow field is characterized in terms of steady and unsteady aerodynamics, temperature flow field, and turbulence properties. Both OP3 and OP2 results are discussed, as well as all the injection cases.

Some contents of this chapter are also discussed in:

Notaristefano, A., Gaetani, P., (2020) Design and Commissioning of a Combustor Simulator Combining Swirl and Entropy Wave Generation, *International Journal of Turbomachinery, Propulsion and Power*, vol. 5(2):6, doi:doi.org/10.3390/ijtpp5040027

Notaristefano, A., Gaetani, P., (2022), Impact of Swirling Entropy Waves on a High Pressure Turbine, *ASME Journal of Turbomachinery*, vol. 144(3): 031010, doi:10.1115/1.4052353

Notaristefano, A., Gaetani, P., (2023), The Role of Turbine Operating Conditions on Combustor–Turbine Interaction—Part I: Change in Expansion Ratio, *ASME Journal of Turbomachinery*, vol. 145(5): 051001, doi:10.1115/1.4055642

Notaristefano, A., Persico, G., Gaetani, P., (2023) Turbulence Measurements Downstream of a Combustor Simulator Designed For Studies on the Combustor-Turbine Interaction, *European Turbomachinery Conference 15*, Budapest, Hungary

4.1 Characterization in the turbine test rig

This section presents the measurements downstream of the combustor simulator, specifically at plane T1 (Fig. 2.8), for the different injection cases in the turbine tests. The measuring instrumentation used includes a 5-hole probe with an overhang of 5 mm and a fast-response thermocouple, both of which are described in detail in Chapter 3, as well as a fast-pitot tube to capture pressure fluctuations resulting from the EW.

To facilitate understanding of the results, a mask is used to highlight the blade height radially and the stator blade periodicity circumferentially.

Most of the results are shown for the OP3 case, as the flow physics and features do not change significantly for OP2.

4.1.1 Aerodynamic flow field

The 5-hole probe is traversed to assess the total pressure field perturbations at the turbine inlet caused by the combustor simulator. Although efforts were made during design to limit total temperature non-uniformities, the generated swirl profile pattern unavoidably creates some non-uniformities. Figure 4.1 shows the steady total pressure 5-hole probe measurements in the OP3 *10 Hz* case overlapped with velocity vectors. To save testing time, measurements are limited to the disturbed region only, as other regions remain undisturbed. The total pressure pattern is characterized by a high swirled flow with a core of low total pressure which is recovered moving radially outward. Furthermore, the presence of the stem wake generates a region of low total pressure above the swirl profile and until the upper casing. The boundary layer close to the casing generates another region of low total pressure which extends circumferentially across the entire measuring grid. Two regions of high total pressure, due to the pressure of the hot/cold EW streaks, are highlighted by two circles in Fig. 4.1. The swirling vortex is not placed at mid-span, which is highlighted in Fig. 4.1 with a dashed line. The swirl center is located at the radial position highlighted with a point in Fig. 4.1, which corresponds approximately to 54% of the blade span where the swirler generator center is geometrically placed. This match between the centers of the swirl profile generator and the measured vortex indicates that no precessing vortex instability is taking place.

The structure of the vortex can be further analyzed by examining the mass-weighted average velocity profile along the radial coordinate in a cylindrical reference system centered at the vortex core (the point highlighted in Fig. 4.1). This analysis is presented in Fig. 4.2. The axial velocity profile, as shown in Fig. 4.2 A, is lowest at the vortex core (R = 0) and increases linearly up to R = 6 mm, where it plateaus. In this region, the injector stem wake has an influence on and modifies the axial velocity. Then, the contribution of the wake diminishes in terms of percentage weight, and the axial velocity recovers the value of the free-stream flow. In terms of the tangential velocity profile shown in Fig. 4.2 B, it follows a common vortex pattern characterized by zero velocity at the core, an abrupt increase up to a radius of 3 mm following a forced vortex trend, and then a slow decrease until zero following a free vortex trend.

The flow angles in the blade-to-blade plane are shown in Fig. 4.3 A-B for OP3 and E-F for OP2, considering as injection cases *EWG off* (frames A and E) *10 Hz* (B and F). The *10 Hz* case is representative of *110 Hz* and *HS* cases. The top left corner of the figure indicates the blade-to-blade angle convention used, where a negative flow angle corresponds to positive incidence on the stator. Flow angles achieve values larger than ±40°, which indicates the presence of an intense swirl structure. A swirl number SN (Eq. 4.1) of 0.6 is computed based on the experimental data in the swirl profile region for all the injection cases.

The injection of the EW/HS strengthens the vortex since the swirl generator acts on both mainstream air and EW. Furthermore, the EW fills, and thus stabilizes, the core of the swirl profile. Although some differences are observed among the injection cases, they are not significant. The

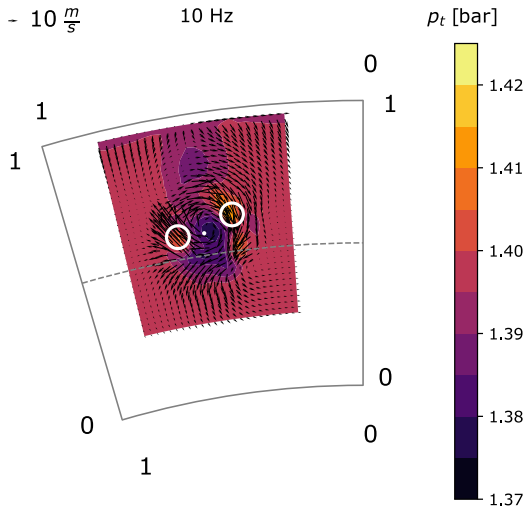

FIGURE 4.1. Total pressure measurements at plane T1 for the case 10 Hz OP3. White circles highlight the EW hot-cold branches, the white point the center of the vortex.

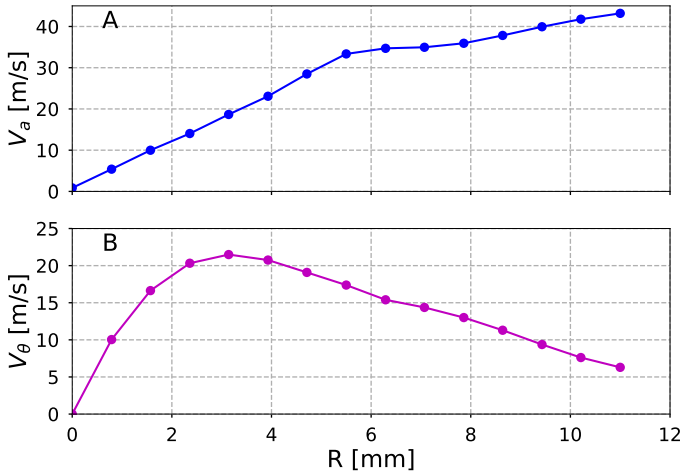

FIGURE 4.2. Velocities mass-averaged in the swirl cylindrical reference system for 10 Hz OP3 case. (A) axial velocity, (B) tangential velocity.

total pressure contours (C-D and G-H of 4.3) show slight variations between *EWG off* cases and *10 Hz* cases, with the latter displaying high total pressure regions corresponding to the EW/HS jets identified in Fig. 4.1. These regions are absent in *EWG off* cases.

The change from OP3 to OP2 increases the inlet pressure and, thus, the Reynolds number. This leads to a better mixing between the temperature streak and the mainstream in OP2, resulting in EW/HS peaks closer to the mainstream pressure. Additionally, the wake region is wider in OP2 than in OP3 due to the higher kinetic energy. In the vortex region, the flow is faster in OP2 than in

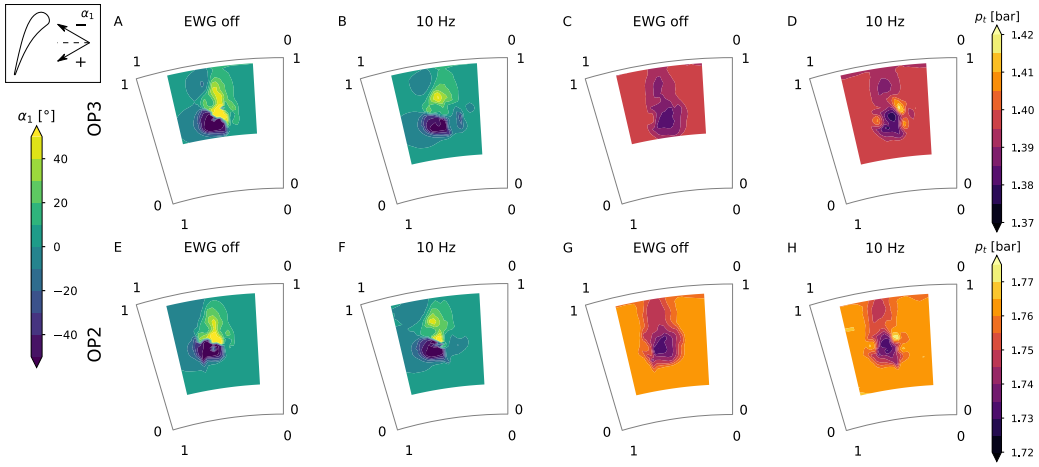

FIGURE 4.3. Blade-to-blade angle (frames A-B and E-F) and total pressure (frames C-D and G-H) contours at plane T1 for 10 Hz and EWG off cases. First row OP3, second OP2.

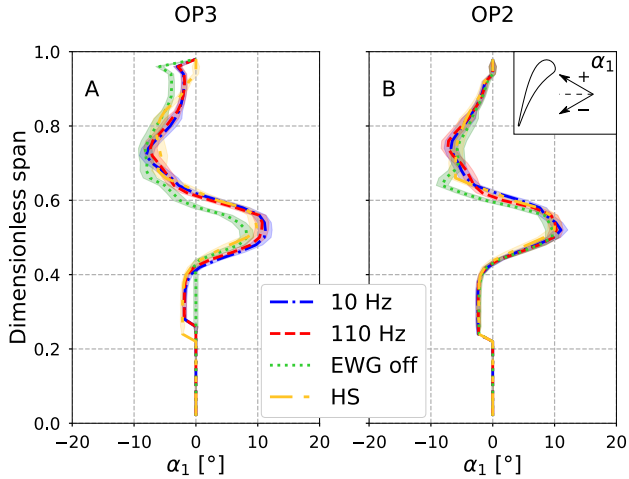

FIGURE 4.4. Pitch-wise area averaged flow angle at plane T1 for OP3 (A) and OP2 (B).

OP3, and the central recirculation is magnified.

$$SN = \frac{\int \rho V_a V_\vartheta r dA}{R \int \rho V_a^2 dA} \tag{4.1}$$

Figure 4.4 shows a pitch-wise area-average of the inlet blade-to-blade angle over one stator pitch for each injection case. Area-averaging is employed to effectively weigh the results at the vortex core, which has a significant mass flow deficit. The *Clean* case is not included in the figure, as it has a blade angle of 0°, over the entire span. As expected, the only injection case that differs from the rest is the *EWG off* case since it lacks any feeding in the injector. The center of the vortex, where α_1 is zero, is located at approximately 60% of the blade span.

4.1.2 Thermal flow field

The fast thermocouple is traversed for the EW/HS cases. In EW cases, the peak-to-trough temperature value ΔT results are obtained phase-averaging the temperature measurement at the EW frequency and calculating the difference between its maximum and minimum values. For HS cases, the ΔT is the difference between the measured local temperature and the mainstream value. The outcomes of these measurements are shown in Fig. 4.5 for each injection case and both OP3 and OP2. The inlet conditions of OP3L and OP3U are identical to those of OP3. The peak-to-trough temperature values are larger in OP3 than OP2. This difference has several potential contributing factors. First, the higher flow velocity in OP2 increases the Reynolds number and promotes the heat exchange and mixing. Second, the mainstream temperature in OP2 is increased to 50° to prevent humidity condensation at the turbine outlet. Third, the EW/HS mass flow in OP2 is larger due to the higher pressure ratio across the combustor simulator valves and a more pressurized turbine compared to OP3. To keep the hot EW/HS temperature constant, a higher air heater power would be required, which is not available. Therefore, both OPs operate at maximum heater power, resulting in a heater outlet temperature lower in OP2 than in OP3.

At plane T1, the maximum measured temperature to mainstream temperature ratios are 1.21 for OP2 and 1.26 for OP3 at *10 Hz*, 1.15 for OP2 and 1.18 for OP3 at *110 Hz* and 1.14 for OP2 and 1.20 for OP3 at *HS*.

Based on the results obtained, the penalty due to the aforementioned issues in OP2 is not particularly significant. The higher mainstream temperature in OP2 is likely the most influential factor. If 10 K are subtracted from the trough temperature of OP2, the two OPs would have a closer match in Fig. 4.5. Any remaining differences between OP2 and OP3 are likely due to variations in the flow physics.

Regarding the effect of the different injection cases, the peak-to-trough temperature values are higher at *10 Hz* than *110 Hz*, since higher frequencies lead to more severe mixing between the hot and cold EW branches. Additionally, the HS case has a higher hot mass flow due to the continuous nature of the streak injection, resulting in a lower ΔT at plane T1. However, the increased thermal power introduced by the higher mass flow makes the HS spot larger, as a result of heat transfer and mixing with the surrounding air.

The combustor non-uniformities are found at 60-70% of the channel height, despite the combustor simulator being designed to inject perturbations at 54% of the channel span. This behavior can be attributed to the swirl profile, which pushes the disturbance upwards.

In order to further investigate the behavior of the injected unsteady flow field, the unsteady pressure field and its correlation with the temperature field are studied. Figure 4.6 shows for the OP3 *10 Hz* case. In frame A, the peak-to-trough pressure values phase-averaged at the EW frequency are shown. In frame B, the pressure and temperature time signals acquired at their respective peak positions are plotted during the EW period. Their locations on the flow field are highlighted on the contour of frame A with the relative color circles. Signals in Fig. 4.6 B are made non-dimensional on their peak value and their phase is referenced to the trigger maximum pressure.

Figure 4.6 B reveals a mismatch between the peaks of the temperature and pressure signals, exactly half a period apart. When the hot flow is injected, the measured pressure is minimum, whereas when the temperature is at its valley, the pressure is maximum. This observation highlights the dynamic nature of the EW: the hot flow generated by the combustor has the highest temperature but a pressure similar to the mainstream flow, whereas the cold jet has the minimum temperature but exploits a higher pressure. Despite the feeding pressure being the same for both the hot and cold flows, the total pressure reduction of the hot stream is the result of a density effect.

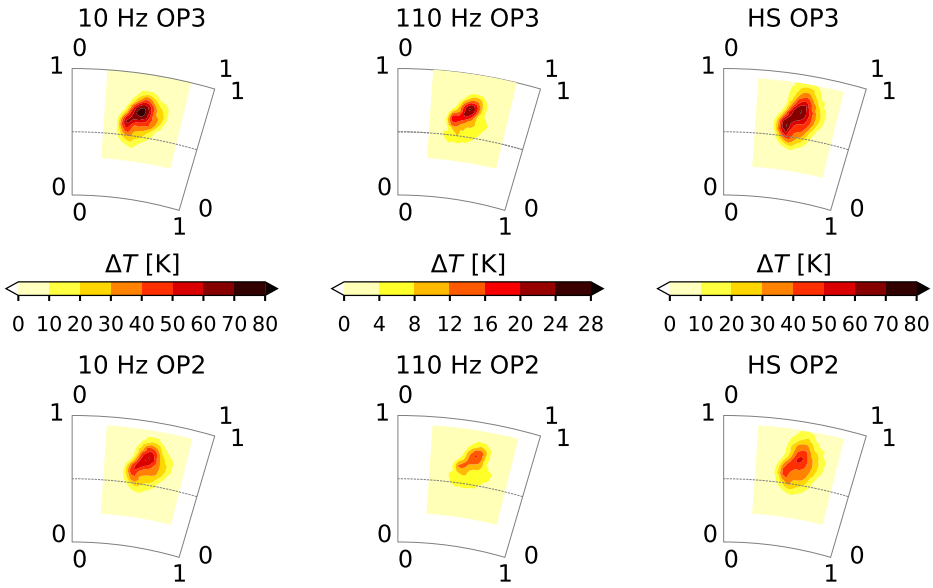

FIGURE 4.5. Peak-to-trough temperature values. First row OP3, second row OP2.

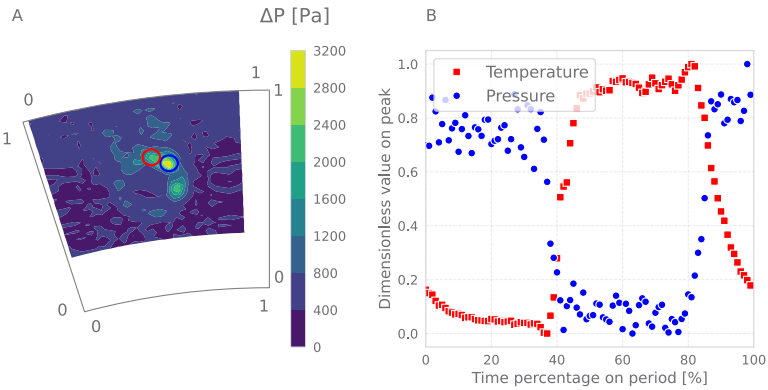

FIGURE 4.6. (A) Peak-to-trough pressure values. (B) Temperature and pressure time signals in their respective peak positions highlighted in (A). All the signals are phase-averaged at the EW frequency (10 Hz).

4.2 Characterization in the calibration wind tunnel

The aero-thermal flow field generated by the combustor simulator has been described in section 4.1 that showed the results of the test campaign in the turbine test rig at plane T1. However, that campaign did not allow for the assessment of the turbulence content of the generated perturbation. Therefore, a dedicated test campaign is conducted in the calibration wind tunnel described in section 2.3. This allows for the simplification of the hot-wire application. In the wind tunnel, there are no geometrical constraints that limit the hot-wire yaw and pitch rotations, the probe can be traversed in more axial planes, and the lowered aerodynamic load on the wire reduces the risk of wire breakage. Most importantly, applying the hot-wire in the same calibration environment allows for maintaining the same temperature and Reynolds number of its calibration. This is essential because the working principle of the hot-wire is based on the heat transfer between the flow and

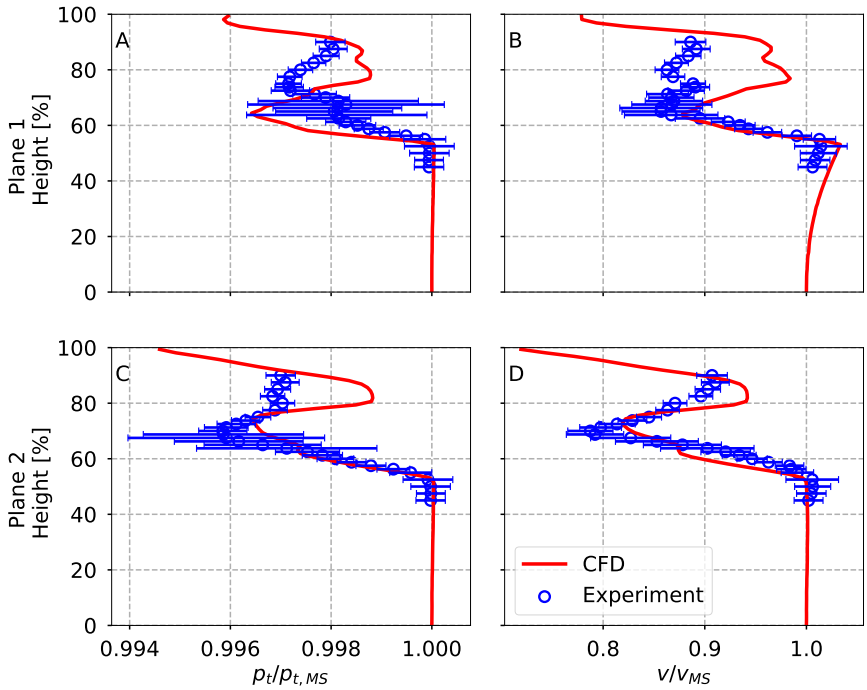

FIGURE 4.7. (A) Peak-to-trough pressure values. (B) Temperature and pressure time signals in their respective peak positions highlighted in (A). All the signals are phase-averaged at the EW frequency (10 Hz).

the wire, and any deviation from the calibration conditions can result in misleading results, if not properly accounted for.

The calibration wind tunnel campaign considered planes 1 and 2, which refer to plane T1 and the stator LE plane, respectively, as described in section 3.6.2.

To validate the CFD model described in section 3.6.2, a comparison is made in Fig. 4.7 between the mass flow average on the direction 1 (Fig. 3.8) of the 5-hole probe and CFD, in terms of total pressure (frames A and C) and flow velocity (frames B and D), both non-dimensional with respect to the mainstream (MS) value. A and B refer to plane 1, C and D to plane 2. CFD effectively captures the evolution of the swirl profile but the agreement reduces in the stem wake region, particularly at plane 1. The poor prediction of the CFD model of the stream-wise evolution of the vortexes shed by the injector stem may be the main potential cause of this difference.

4.2.1 Plane 1

The investigation of the flow field phenomena is conducted by analyzing contour plots generated with the perspective of an observer positioned downstream of the traversing plane. The results discussed are time-averaged, with the CFD simulations being time-averaged on the periodicity of the problem, which was also used to calibrate the time step, as explained in section 3.6.2. In the swirl core region, both hot-wire and 5-hole probes operate near the limits of their angular calibration range, leading to increased measurement uncertainty.

Figure 4.8 shows the absolute velocity of the flow field, which exhibits a good agreement between the measurements and CFD in terms of velocity magnitude and flow morphology. Two main flow structures are identified: the first is the stem wake released by the injector stem,

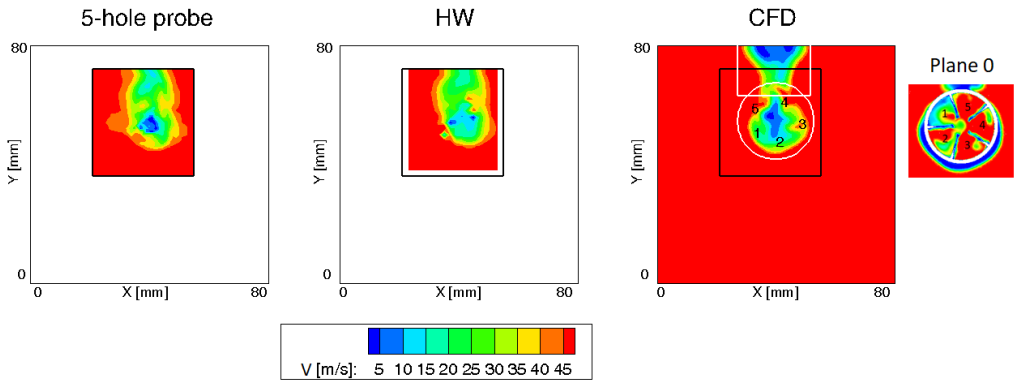

FIGURE 4.8. Hot-wire campaign, absolute velocity contours at Plane 1 for cold streak case. Plane 0 refers to a plane at the swirler generator trailing edge. Numbers 1-5 highlights the flow in the five swirler generator channels and rotate between the two planes due to the swirl.

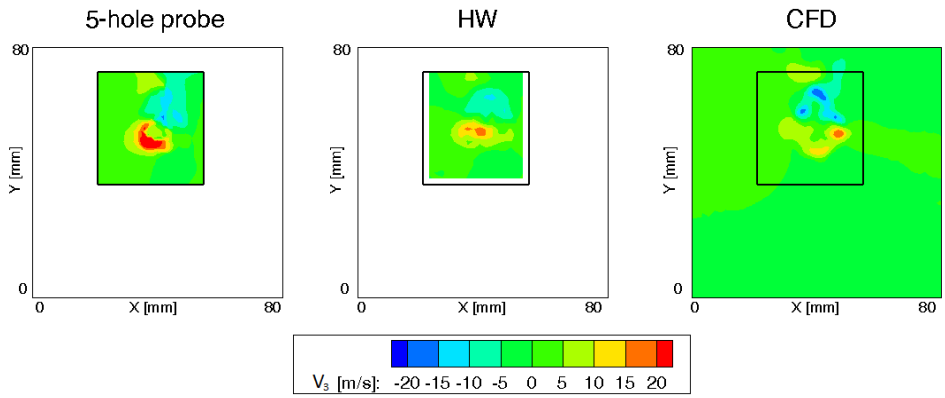

FIGURE 4.9. Hot-wire campaign, tangential velocity contours at Plane 1 for cold streak case.

highlighted with a white box in the CFD frame, and the second is the swirl profile, identified by a white circle.

Defined the Plane 0 as the plane placed at the swirler generator blades trailing edge, the different five channels are numbered in Fig. 4.8 Plane 0 from 1 to 5. Channels 1-2 collect the flow from the injector stem wake, resulting in low velocities. The swirler generator vanes 3 to 5 act on the mainstream and are the channels where the CS is mainly swirled, as confirmed by the streamlines plot of the CS in Fig. 4.9. As a result, high velocities are observed in regions 3-5 at Plane 1, while low velocities are detected in regions 1-2. The presence of velocity peaks is attributed to the fact that the flow structures are not yet fully mixed, with the first measuring plane located approximately 10 mm downstream of the swirler generator. While both 5-hole and hot-wire probes record the three regions labeled 3-5, the measured velocity peak is lower than that predicted by the CFD. This discrepancy could be related to a limitation of RANS in predicting the mixing process.

For the same reasons, the tangential velocity contours (Fig. 4.10) show the lowest absolute magnitudes on the left part of the swirl profile, which corresponds to swirler generator channels 1-2. The differences between simulations and experiments are mainly quantitative, since the trends are highly similar. Both in simulations and experiments, a reduction of high positive/negative tangential velocities is observed during the circumferential evolution, which is caused by the wakes

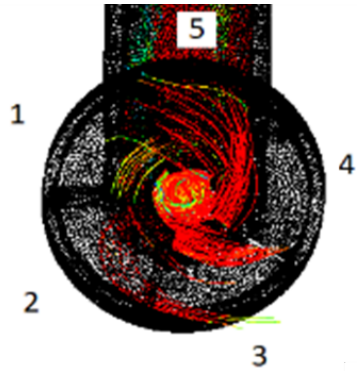

FIGURE 4.10. Hot-wire campaign, tangential velocity contours at Plane 1 for cold streak case.

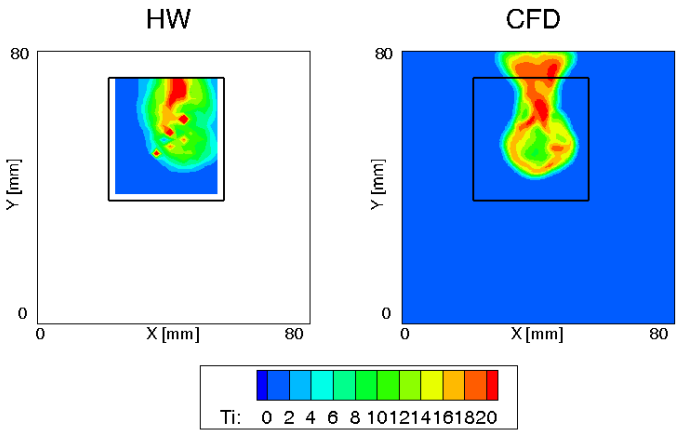

FIGURE 4.11. Hot-wire campaign, turbulence intensity [%] contours at Plane 1 for cold streak case.

of the swirler generator blades.

The comparison between CFD and hot-wire measurements of the turbulence intensity shows a good agreement (Fig. 4.11). The turbulence intensity is defined as the ratio of the root-mean-square of the turbulent velocity fluctuations and the mean velocity. The area-averaged turbulence intensity is found to be 7.2% in CFD and 6.1% in the experimental measurements, which confirms the choice of setting 8% of turbulence intensity at the inlet plane of the turbine CFD simulations, as described in section 3.6.1.

At plane 1, the injector stem wake and the swirl profile are the primary sources of turbulence generation. The former exhibits the highest turbulence intensity and a very good agreement is obtained between CFD and experimental measurements. However, in the swirling region, some grid points do not converge because the hot-wire operates close to or above its angular calibration limit of the pitch angle. In CFD, the shear layer formed at the boundary between the flow released by the swirler generator and the free-stream produces high turbulence in an annular zone contouring the swirl core, which is not measured experimentally. This discrepancy may be attributed to the underestimation of the mixing process in CFD, which in experiments nullifies the contribution. Furthermore, the high velocities zones 3-5 of Fig. 4.8 feature low turbulence levels, which are mainly produced by boundary layers on the injector walls. Overall, the turbulence intensity levels in the swirl core match well between CFD and experiments.

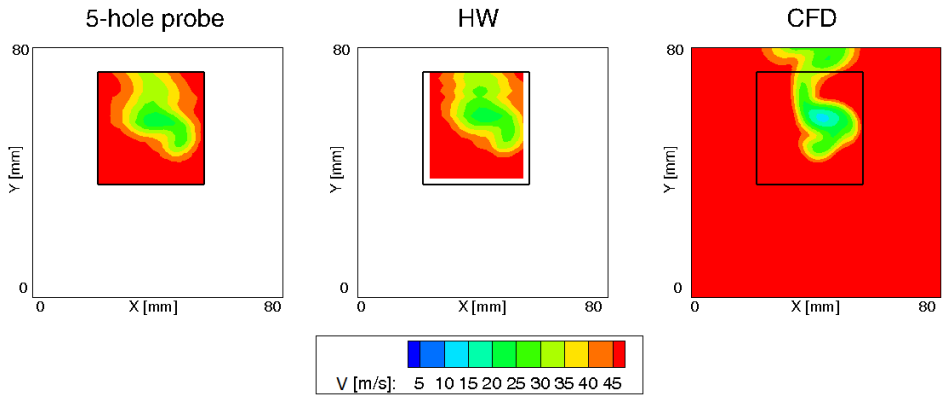

FIGURE 4.12. Hot-wire campaign, absolute velocity contours at Plane 2 for cold streak case.

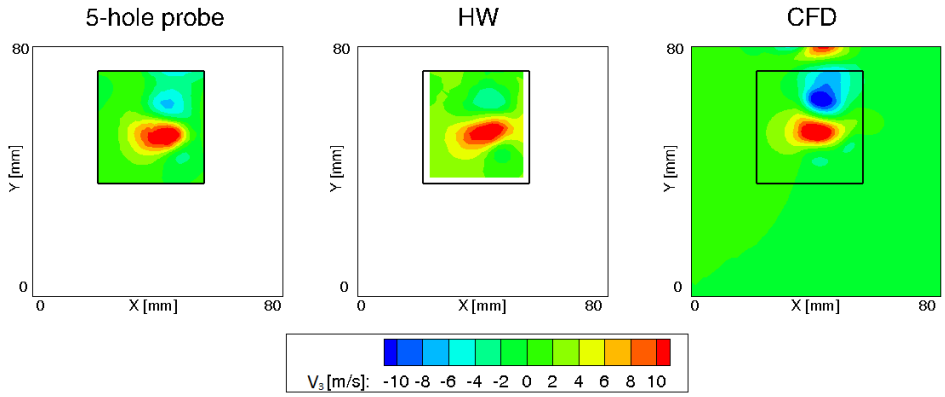

FIGURE 4.13. Hot-wire campaign, tangential velocity contours at Plane 2 for cold streak case.

4.2.2 Plane 2

Plane 2 is representative of the plane containing the stator vane leading edge. This analysis is useful to understand the swirl decay and its interaction with the surrounding flow. In particular, the two high momentum flow regions identified with 4 and 5 in Fig. 4.8 break the pattern of the swirl profile and elongate the swirl profile in the X-axis direction and generate a tail at the bottom of the swirl profile, as observed in Fig. 4.12. This feature is measured and correctly predicted by numerical calculations, with the only difference being the X-axis position of the tail. This difference can be potentially related to possible manufacturing differences in the 3D printed injector device. In fact, the CS and its interaction with the swirl profile dominate flow regions 4 and 5, both of which are sensitive to injector geometries. Finally, the lower velocity in the swirl core in CFD simulations than in experiments can be attributed to an underestimation of the mixing process.

The shear interaction between the swirl profile and the boundary layer on the outer casing of the swirler generator produces a counter-rotating vortex in the bottom-right part of the swirl profile, as shown in the tangential velocity contours of Fig. 4.13.

Turbulence intensity is slightly overestimated by simulations as shown in Fig. 4.14. The area-average CFD value is 6.6% higher than the experimental value of 5.9%, even though the numerical wake is thinner. Turbulence intensity is similar at the swirl core between CFD and hot-wire measurements but numerical outcomes predict a larger T_i in an annular region contouring

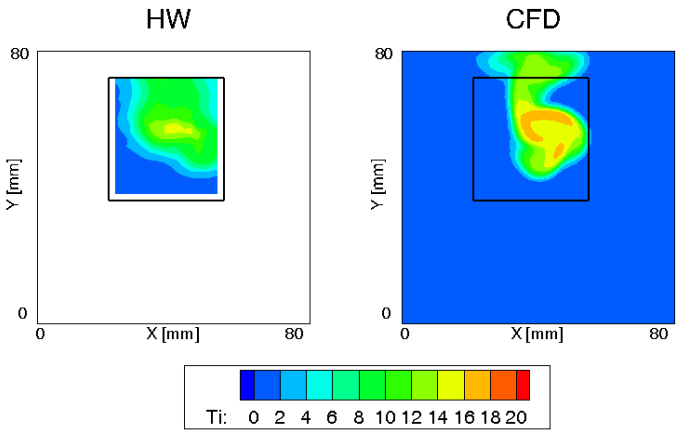

FIGURE 4.14. Hot-wire campaign, turbulence intensity [%] contours at Plane 2 for cold streak case.

the center of the vortex. This is possibly due to the shear interaction between the regions 3-4-5 and the surrounding fluid, while zones 1-2 are completely mixed.

4.2.3 Decay of turbulence and SN

CFD simulations allow to investigate the decay rate of each flow parameter in the axial direction. In this section, the reduction of the turbulence intensity and the SN are studied.

In order to study the decay of the turbulence intensity on the different measuring points, its CFD values are area-averaged at different axial positions and the results are shown in Fig. 4.15. This plot is compared to a cross-section of the numerical domain cut on a plane containing the injector and nozzle axes. The plot reveals the presence of four primary mechanisms that generate turbulence due to shear flow interaction. These include:

- The injector stem wake.
- The boundary layer developing around the outer casing of the swirler generator.
- The generation of the swirl profile.
- The injection of the streak inside the injector.

Along the axial direction, five different regions of turbulence generation/decay can be identified. According to the numeration of Fig. 4.15, these are:

1. Generation by the four aforementioned mechanisms.
2. Decay in the regions of the injector stem wake and the boundary layer around the swirler generator casing, generation in the swirler core. Overall, turbulence reduces.
3. Generation in the swirl region, decay in the other ones. The turbulence slightly increases.
4. Decay in all the regions. Some shear interactions between the different zones are still present, altering the decay rate.
5. Generation of new turbulence at the interface between the injector stem wake and the swirl regions. After the generation, it again starts to decay.

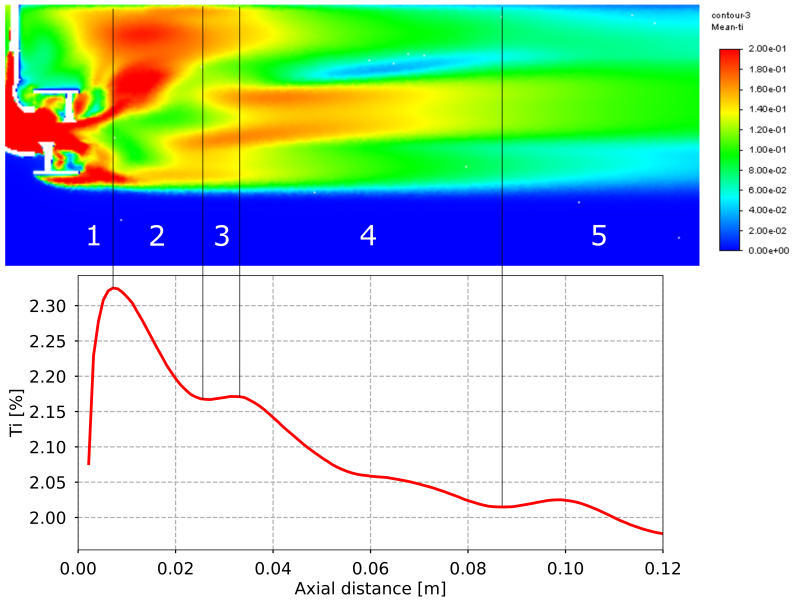

FIGURE 4.15. Hot-wire campaign, cut of a plane containing axis 1-2 (upper frame) and area-average turbulence intensity decay (lower frame).

Regarding the SN (Eq. 4.1), it is computed on a cylindrical reference system centered in the swirler generator center. In this analysis, SN is computed using 5-hole probe results and the integration area of CFD predictions is limited to the area investigated experimentally with the 5-hole. The value of the SN at different axial positions z is shown in Fig. 4.16. CFD predictions are the solid line, points are the experimental values and the dashed line represents an interpolation of the CFD data with a power law, described by Eq. 4.2. The agreement is good between numerical predictions and measurements in Fig. 4.16. The swirl profile is almost fully developed at an axial distance of approximately one swirler generator blade chord, which corresponds closely to the location of the first measuring point. The swirl profile stabilizes and starts decaying after approximately two swirler generator blade chords.

$$SN = 0.0154 z^{-0.477} \tag{4.2}$$

The SN computed on CFD data and on the influence area of the swirl profile is 0.61, very similar to the experimental value calculated based on the 5-hole probe measurements at the turbine inlet (section 4.1.1).

4.2.4 Turbulence length scales

The last important information to provide is the integral length scale of the turbulence and its energy spectra. These will enable the setup of high-fidelity CFD simulations on the turbine test section. For this purpose, the integral length scale is computed applying the Taylor's hypothesis to the autocorrelation of the velocity, see Eq. 3.25. This equation is applied for each grid point on the velocity signal measured by the hot-wire at its rotation the closest to the actual flow angle. The integral length scale is shown in Fig. 4.17. Its highest values are in the mainstream region, intermediate magnitudes are in the wake zone, the lowest in the swirl region. This trend is consistent

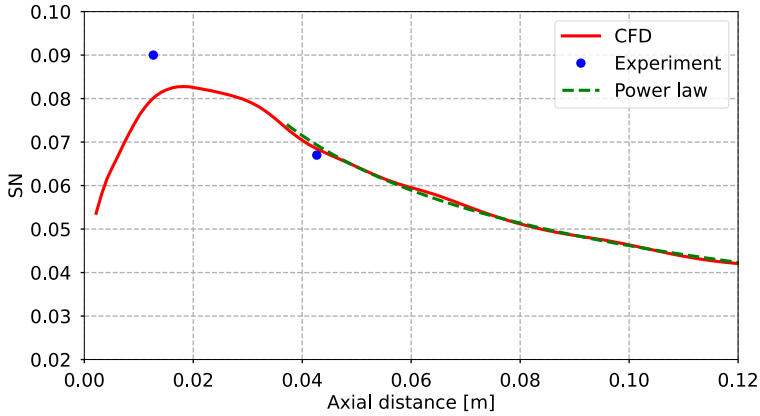

FIGURE 4.16. Hot-wire campaign, SN decay.

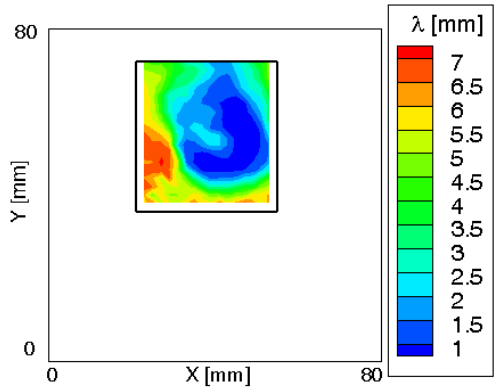

FIGURE 4.17. Hot-wire campaign, integral length scale at plane 1.

with the low velocities in the region of injector stem wake and swirl profile that reduce the turbulent kinetic energy content. The turbulence length scale in the mainstream region is approximately 10% of the main wind tunnel size, that is the channel height, as imposed at the CFD inlet domain (section 3.6.2).

To provide a better understanding of the turbulence length scales, the energy spectrum in the mainstream and perturbed regions is shown in Fig. 4.18. The energy is computed as the Fourier transform of the velocity autocorrelation, as described by Kundu & Dowling (2012). The spectra clearly show an inertial region following the -5/3 power law. The energy associated with the point in the perturbed region has lower turbulent kinetic energy due to the lower velocity than the mainstream one. This analysis indicates that nearly isotropic turbulence is generated by the combustor simulator.

4.2.5 110 Hz cold

The analysis of the unsteady case involves studying each time-instant of the disturbance frequency. The time-mean features do not differ significantly from the CS case. The hot-wire data require a

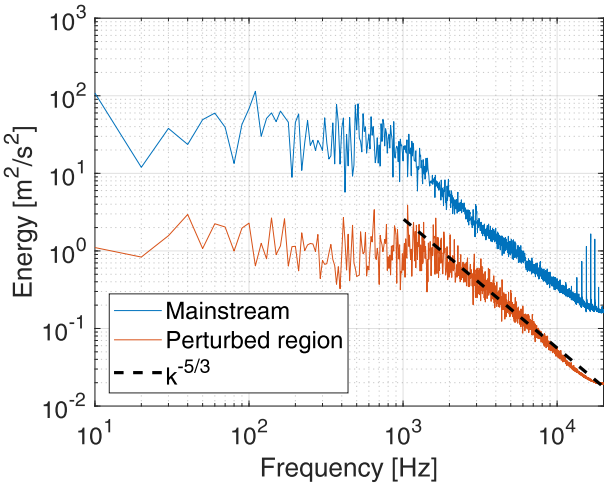

FIGURE 4.18. Hot-wire campaign, energy spectrum at plane 1.

particular post-processing of the measurements based on the trigger pressure signal, which is used to re-phase each measurement. To obtain converged statistics, each time period of the disturbance is divided into 20 intervals. Given a number of samples of 40000, an acquisition frequency of 40000 Hz and a disturbance frequency of 110 Hz, each interval has only about 18 samples, which are not sufficient to compute E and e reliably. Therefore, given the periodicity of the phenomena and its good repeatability, the calculations of E and e are performed on more than one period, including all the periods in the acquisition time (1 second). As a result, a voltage supply array of 2000 points is generated, ensuring a reliable statistical analysis. However, this procedure reduces the highest frequency that can be encoded from 20000 Hz to 1100 Hz, due to the Nyquist limit. Nonetheless, this frequency range is well above the range of interest.

Experimental and CFD results are shown in Fig. 4.19 and 4.20, respectively. Only 6 phases are reported that correspond to 0, 15, 30, 45, 60 and 80% of the disturbance period. The phases for the hot-wire measurements are selected from the 20 intervals on which the disturbance period is divided, following the previously described procedure. The CFD outcomes are plotted at each time-instant, while the hot-wire results are derived through the discussed procedure that, involving averaging, reduces the available frequency content. This explains why CFD data (Fig. 4.20) experiences a significant time-dependence, not fully captured by the measurements (Fig. 4.19). The main causes of unsteadiness are the vortex shedding in the wake of the injector stem and the alternative feeding of combustor simulator hot and cold ducts (see Fig. 3.13 for ducts label definition). Each of these two streams interacts differently with the swirler generator changing the generation of the swirl profile. The air injected through the hot duct is more dissipated inside the injector because it must significantly turn inside the device. Conversely, the air through the cold duct follows the shape of the injector and exhibits lower mixing. Therefore, the turbulence intensity is higher during the injection period when the hot duct is fed (phases 1-3). The SN calculated in each time step on the hot-wire measuring grid is also higher during the cold duct feeding period (phases 4-6) than during the hot one (phases 1-3) in both CFD and measurements, as demonstrated in Tab. 4.1. Both methodologies predict a more compacted shape of the combustor-representative disturbance in phases 4-6 than 1-3. The reason is that the two generated streaks interact differently with the swirler generator and the tail generation identified in the bottom part of the swirl profile in Fig. 4.8 is less intense during the injection of the cold duct than during that of the hot one.

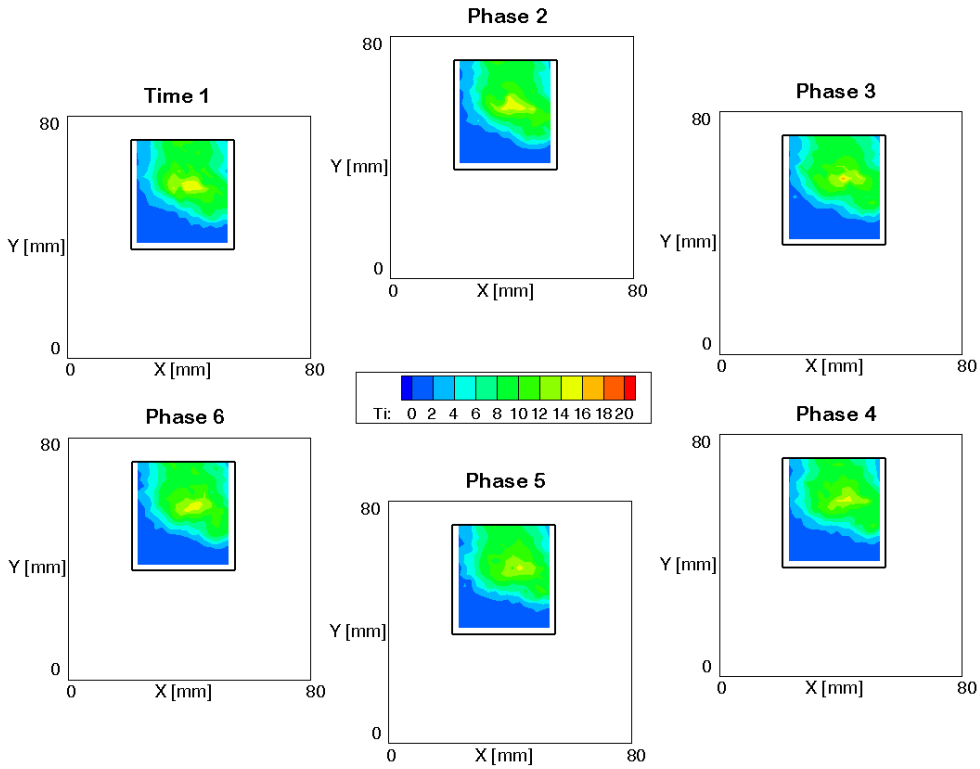

FIGURE 4.19. Hot-wire campaign, turbulence intensity snapshots measured at Plane 2.

TABLE 4.1. Hot-wire campaign, SN at Plane 2 time evolution for 110 Hz cold case.

	Phase	CFD	Hot-wire
Hot duct fed	1	0.087	0.088
	2	0.084	0.088
	3	0.096	0.092
Cold duct fed	4	0.101	0.094
	5	0.108	0.093
	6	0.114	0.092

4.2.6 Temperature effect

The primary objective of validating the numerical scheme is to use CFD to investigate the impact of temperature on turbulence generation, which cannot be achieved experimentally due to the risk of hot-wire bursts and the need for a more complex calibration that accounts for temperature.

The validity of conducting experiments without heating the streak flowing in the hot duct is verified by the results presented in Table 4.2, which provides the time-averaged and area-averaged values of SN and turbulence intensity on the hot-wire measuring grid. The CFD results are time-averaged over the main flow periodicity, and experimental results are averaged over the entire acquisition period. The turbulence intensity appears to be minimally impacted by temperature, with similar turbulence intensities observed for both electric heater on and off conditions. Since

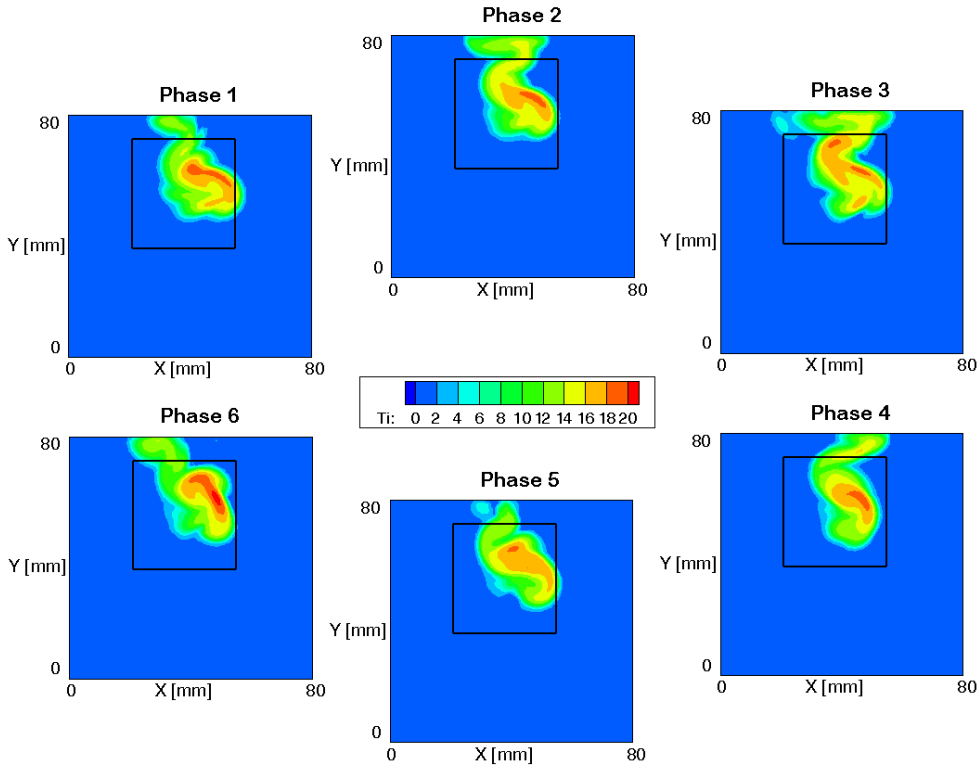

FIGURE 4.20. Hot-wire campaign, CFD turbulence intensity snapshots calculated at Plane 2.

cross-flows and shear interactions are the primary drivers of turbulence generation, temperature could influence these phenomena by affecting the kinematic viscosity. Despite the air temperature at the combustor simulator exit increasing by approximately 400 K, it is unlikely to significantly affect the turbulent diffusion.

The increase in temperature results in a faster flow due to the density effect, which in turn increases turbulence generation due to shear interaction. However, the overall aerodynamics remains largely unaltered, as evidenced by the unchanged SN.

Lastly, by comparing the steady and unsteady cases, it can be observed that the time-mean values of the unsteady cases are very similar to the steady cases, extending the notion that EW can be treated as a series of HS, as previously discussed by Gaetani & Persico (2019), also in swirling environments.

4.3 Representativity of the combustor simulator

This section focuses on quantifying the differences between the flow field generated by the utilized combustor simulator and that of a real gas-turbine combustor. The target profiles of the combustor simulator, as described in Section 1.1, are successfully achieved. These target profiles include local swirl angles of ± 40°, a swirl number of 0.6, a local temperature peak surpassing the mean temperature by at least 1.1 times, temperature disturbance frequency higher than 100 Hz, and inlet turbulence of approximately 10% at the turbine inlet. The generated flow pattern, specifically the swirl velocities and local intensities of the swirl angles, closely align with the data presented in

TABLE 4.2. Hot-wire campaign, SN and time-average area-average turbulence intensity for different injection cases.

		SN				T_i [%]			
		110 Hz cold	110 Hz	CS	HS	110 Hz cold	110 Hz	CS	HS
Plane 1	Exp	0.12		0.09		6.5		6.1	
	CFD	0.12	0.11	0.10	0.10	7.2	7.3	7.2	7.4
Plane 2	Exp	0.09		0.09		5.9		5.9	
	CFD	0.09	0.08	0.08	0.08	6.4	6.4	6.4	6.9

section 1.1.2.1 where other simulators and data engine representative are reported. This applies also for the turbulence intensity, that is expected to exceed 10% in real gas turbine combustor outlet, as outlined in section 1.1.1. Furthermore, the peak temperature achieved by the combustor simulator reaches approximately 1.18 times the mainstream value, demonstrating a good match with the target values presented in Fig. 1.7 of Povey & Qureshi (2009). In terms of magnitudes and frequencies of the EW, the experimental values obtained in this study surpass those reported in previous research, such as the work by Bake *et al.* (2009).

The primary distinction between the combustor simulator used in this study and other simulators described in the literature lies in the region affected by the imposed disturbance. The dimensions of the combustor simulator are constrained by the geometry of the turbine test facility, thereby limiting its size and affected area. As a result, the generated disturbances only impact one-third of the span and half of the stator pitch. It is important to note that this constrained region reduces the amplification of combustor non-uniformities on the turbine stage, which would have been more pronounced if the disturbance area were larger.

If the swirling EW/HS impacts the entire span and stator pitch, stator losses are expected to increase. As it will be detailed in the following, in particular in chapter 6, the stator pressure losses are heavily influenced by the stator incidence angle. Expanding the impact area of the swirl profile would lead to at least a doubling of these pressure losses,considering that in the present configuration one vane out of two is undisturbed.

The presence of a larger temperature spot would result in an more elevated temperature at the stator outlet, subsequently leading to a higher increase in the rotor incidence angle. This, in turn, could amplify the impact on the rotor aerodynamics, that is limited in the present configuration. Additionally, an expanded region affected by the temperature streak would make more challenging the cooling system design. However, it should be noted that this thesis does not address the investigation of cooling system issues. From an aerodynamic standpoint, the expected impact on the stator remains negligible, as will be elaborated upon in subsequent discussions.

An elevation in turbulence levels will certainly have an impact on the stator aerodynamics, leading to increased losses. However, it will also have a beneficial effect on the dissipation of the temperature spot, promoting better mixing and dispersion.

In summary, all the anticipated effects outlined in Section 1.1.2 are documented in this study, as will be elaborated upon in the subsequent chapters. This serves to highlight the accuracy of the generated flow field at the combustor outlet, despite the limited area impacted by its perturbations.

CHAPTER 5

FLOW FIELD CHARACTERIZATION AT PLANE T2

This chapter discusses the impact of combustor simulator disturbances on the stator outlet flow field. The flow field is characterized in terms of steady and unsteady aerodynamics, as well as temperature. The analysis focuses on all operating conditions and injection cases, with particular emphasis on the MP and LE injection positions. Some results are also presented for the PS and SS positions.

Some contents of this chapter are also discussed in:

Notaristefano, A., Gaetani, P., (2021) Transport of Swirling Entropy Waves through an Axial Turbine Stator, *International Journal of Turbomachinery, Propulsion and Power*, vol. 6(4):45, doi:10.3390/ijtpp6040045

Notaristefano, A., Gaetani, P., (2022), Impact of Swirling Entropy Waves on a High Pressure Turbine, *ASME Journal of Turbomachinery*, vol. 144(3): 031010, doi:10.1115/1.4052353

Pinelli, L., Marconcini, M., Pacciani, R., Notaristefano, A., and Gaetani, P., (2023), The Effects of Swirling Flows in Entropy Wave Convection Through High-Pressure Turbine Stage, *ASME Journal of Turbomachinery*, vol. 145(3): 031004, doi:10.1115/1.4055613

Notaristefano, A., Gaetani, P., (2023), The Role of Turbine Operating Conditions on Combustor–Turbine Interaction—Part I: Change in Expansion Ratio, *ASME Journal of Turbomachinery*, vol. 145(5): 051001, doi:10.1115/1.4055642

Notaristefano, A., Gaetani, P., (2023), The Role of Turbine Operating Conditions on Combustor–Turbine Interaction—Part II: Loading Effects, *ASME Journal of Turbomachinery*, vol. 145(5): 051002, doi:10.1115/1.4055643

Notaristefano, A., Gaetani, P., (2023), Modelling of Combustor Non-Uniformities Evolution through a High-Pressure Turbine Stage, *ASME Turbo Expo 2023*, GT2023-102601, Boston, Massachusetts, United States

5.1 Aerodynamic flow field

The stator blade outlet flow field is mainly influenced by the secondary vortexes and the pressure field resulting from its leaned geometry. Fig. 5.1 displays the total pressure coefficient Y_2, defined by Eq. 5.1, for the *Clean* case in the first row, *LE 10 Hz* in the second row, and *MP 10 Hz* for the last one. The first and second columns correspond to OP3 and OP2, respectively.

$$Y = \frac{p_{t_1,ref} - p_{t_2}}{p_{t_2} - p_{s_2}} \tag{5.1}$$

The *Clean* cases provide insight into the flow characteristics of the stator. The boundary layer at the casing causes the highest pressure losses in those regions, while the remaining part of the blade span can be divided into a wake zone and an almost isentropic region. Due to the blade lean geometry, an overturning occurs at the tip and an underturning at the hub. This flow field distorts the blade wake in the azimuthal direction, thus it does not develop only radially. Among the stator secondary structures, the tip passage vortex (TPV), shed vortex (SV), and hub clearance vortex (HCV) most affect the total pressure flow field, as shown in Fig. 5.1 frames A and B. The TPV generates additional losses at 80% of the span close to the top casing, and the viscous interaction between the TPV and the wake generates the SV, further reducing pressure losses in the wake region. The HCV is generated by a clearance slot at the stator blade trailing edge root and introduces a large loss near the bottom casing, not completely measured due to probe geometric constraints.

The injection of the combustor perturbation, that is highlighted in Fig. 5.1 with the vortex labeled IP, perturbs the stator aerodynamics in a different way depending on the injection position.

If the disturbance is injected aligned to the stator passage (5.1 E and F), the swirl profile interacts significantly with the secondary flows and impacts the isentropic zone, resulting in an increase in the total pressure losses compared to the *Clean* case. As the swirl profile has its center at 60% of the span at plane T1 (see Fig. 4.4), the zone of influence of the IP is shifted towards midspan due to the push imposed by the vane's leaned geometry.

In vane-aligned injections, the swirl profile weakens as it impinges on the vane surface and then climbs toward the top casing on the blade suction side. The IP is transported through the stator on the blade suction side, thus interacting to a lesser extent with the secondary structures. Consequently, its impact on the total pressure losses at plane T2 (5.1 C and D) is limited to a smaller portion of the blade span than the MP injection case. The disturbance is positioned at approximately 65% of the blade span, that is the same blade height where it is found upstream of the stator Fig. 4.4). This means that the climb that takes place on the vane leading edge and the lean effect cancel each other out. The total pressure loss contours (5.1 C and D) show that, below midspan, a small portion of the channel remains isentropic. The pressure losses increase in the wake region of the blade where the IP impinges, which is on the wake closest to the azimuthal tick 1. This increase in Y is due to the local severe positive/negative incidence angle that the blade undergoes, leading to increased secondary and profile losses. Furthermore, the transport close to the blade suction side surface inhibits momentum exchange with the mainstream flow, reducing the loss recovery compared to the MP case. All this implies that the losses are higher in LE than MP injection position cases, as demonstrated by the area-averaged results on the measuring grid listed in Tab. 5.1. This will be further discussed in the losses breakdown section (see discussion relative to Fig. 6.6).

In OP2, Re and M effects reduce the total pressure losses in both uniform and perturbed cases with respect to OP3. Furthermore, the intensity of the secondary flows is lower in OP2 than in OP3.

The OP3 campaign includes injection position cases PS and SS, which have intermediate flow aerodynamics between the MP and LE cases. PS results in the highest pressure losses (see Tab. 5.1) due to the high positive/negative incidence generated by the swirl at the blade leading edge,

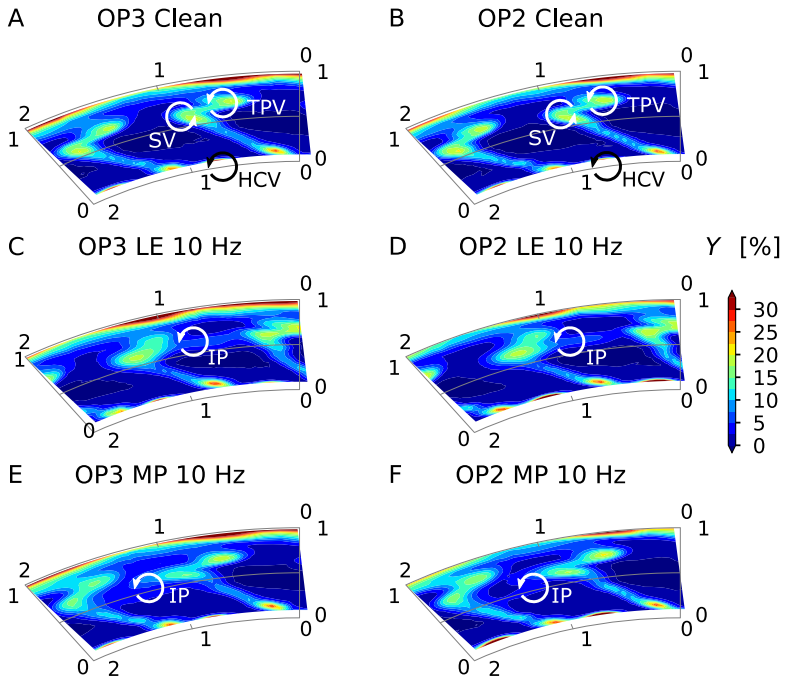

FIGURE 5.1. Total pressure loss coefficient at plane T2 for the case 10 Hz MP and LE, OP3 and OP2. White circular arrows highlight the main vortical structures.

TABLE 5.1. Area average total pressure losses at plane T2. Uncertainties of ± 0.1%

OP	Injection position	Clean	EWG off	10 Hz	110 Hz	HS
OP3	MP	6.3%	6.7%	6.8%	6.8%	6.7
	LE		7.0%	7.1%	7.1%	7.1
	SS		6.5%	6.5%	6.6%	
	PS		7.2%	7.2%	7.2%	
OP2	MP	5.5%	5.9%	5.9%	5.9%	5.9%
	LE		6.1%	6.1%	6.1%	6.2%

which plays a key role in secondary vortex generation. This contribution is stronger in the PS case compared to the LE case, as the swirl in PS impacts the surface where the secondary flows are generated without weakening impinging on the blade surface.

Although total pressure losses are found to be affected by the injection position, they are not significantly affected by the injection cases, as demonstrated in Tab. 5.1 that shows very similar values for different injection cases, given the injection position.

The small differences among the injection cases can be further discussed based on the pitch-wise area-average results at plane T2 for total pressure coefficient (blade-to-blade angle). The outcomes are shown in Figs. 5.2 (5.4) and 5.3 (5.5) that represent the MP and LE cases, respectively. The plots $\widetilde{\Delta}$ are the difference between the perturbed case and the *Clean* one.

Total pressure losses (Figs. 5.3 and 5.2) are higher in OP3 than in OP2, consistent with the different Reynolds numbers. The regions of high total pressure losses identified in Fig. 5.1 can also

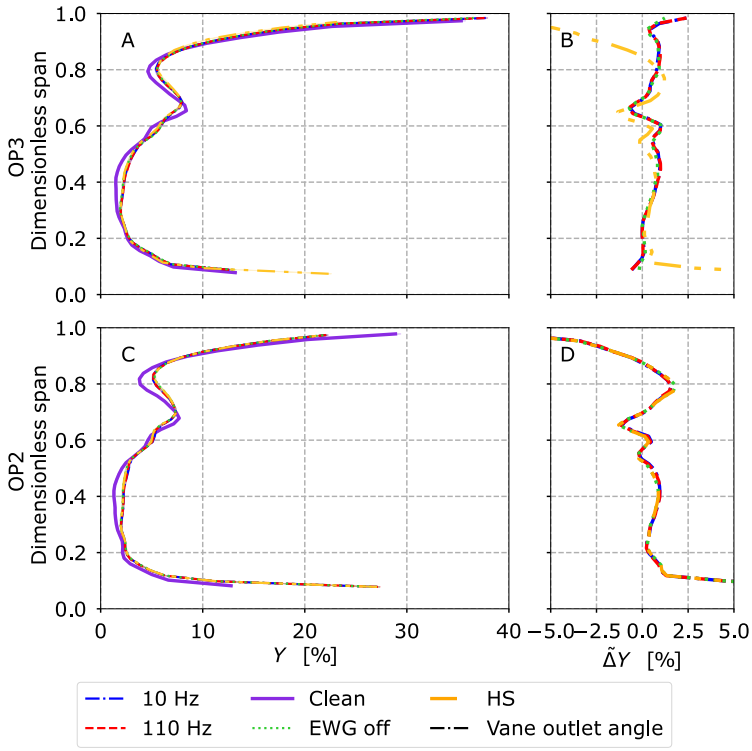

FIGURE 5.2. Pitch-wise area-average total pressure coefficient at plane T2 for injection position MP.

be recognized in the pitch-wise average. Specifically, the regions close to the tip and hub casing are dominated by the casing boundary layer, while at the hub, a clearance slot magnifies losses. At 70% of the span, the SV and TPV produce another region of high losses. From 20% to 50% of the span, an extended isentropic region without secondary structures is detected.

In terms of the effect of injection cases on total pressure losses, the results show that they are almost identical for all injection cases. However, the injection position plays a significant role in determining the differences in pressure losses. Specifically, for the LE case (Fig. 5.3), pressure losses are more concentrated in a region at 60-70% of the span, which corresponds to the core of the residual swirl profile (Fig. 5.5 B and D). In contrast, for the MP case (Fig. 5.2), pressure losses are spread from 40% to 80% of the span, corresponding to the region where the residual swirl is measured. The total pressure loss is higher in LE than in MP, consistent with the findings from Fig. 5.1.

Although PS and SS cases are not reported here, they exhibit a similar trend to the MP case, with the only difference being the magnitude. Table 5.1 shows that injecting the inlet disturbance at MP or LE increases the losses by 0.4-0.5% (0.4%) and 0.7-0.8% (0.6-0.7%) in OP3 (OP2), respectively. The higher Reynolds number and Mach number in OP2 compared to OP3 partially recover the losses caused by the inlet perturbation.

In OP2 the hub is the region of highest pressure loss differences (Fig. 5.2 and 5.3 D). The reason for this is an unavoidable different mounting of the 5-hole probe between perturbed and uniform cases. Measurements are carried out closer to the bottom casing in the case of injected disturbances. Therefore, the HCV is measured to a greater extent (see Fig. 5.1 D and E) increasing its contribution to pressure losses.

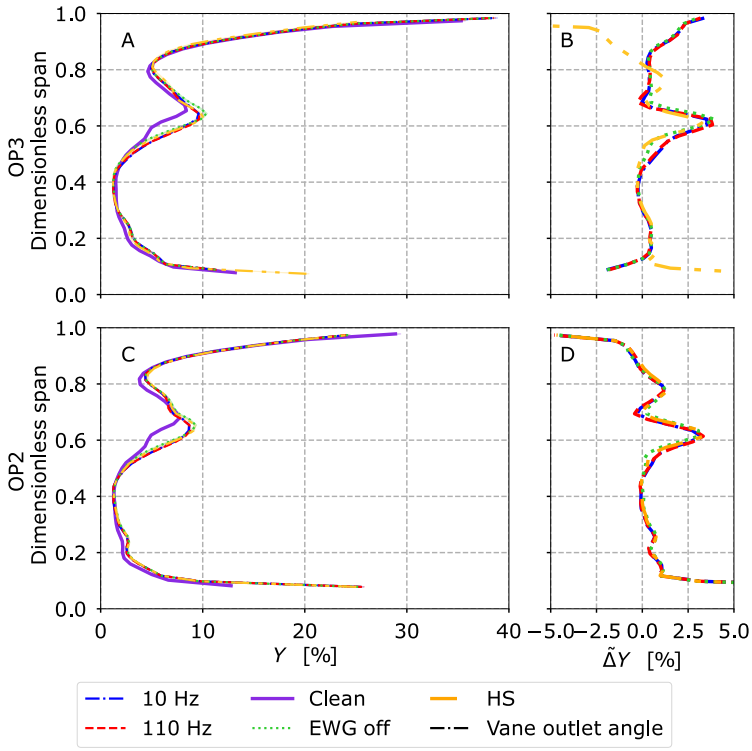

FIGURE 5.3. Pitch-wise area-average total pressure coefficient at plane T2 for injection position LE.

To understand the blade-to-blade angle trends of Figs. 5.4 and 5.5, the *Clean* cases are first discussed. The stator blade has a leaned geometry that produces an overturning at the tip and underturning at the hub, along with a pressure field that pushes downwards and causes secondary vortices to shift towards the hub. The TPV impacts the region at approximately 75%, producing the classical region of overturning/underturning related to secondary flows.

The injection of the non-uniformities at the turbine inlet changes the stator outlet flow field depending on the injection position, as discussed earlier. Downstream of the stator, a residual swirl profile is measured that is centered at approximately mid-span for the MP injection case (Fig. 5.4 B and D) and at 70% of the span for the LE case (Fig. 5.5 B and D). This finding is consistent with the discussion of Fig. 5.1.

The lower branch of the residual swirl profile contributes to underturning, while the upper branch contributes to overturning. To aid in the discussion of blade-to-blade angles, a schematic of the vortex interaction is shown in Fig. 5.6.

In OP2, the injection of the disturbance at the MP position results in a residual swirl profile with higher blade-to-blade angles than OP3 (Fig. 5.4 B and D), while the opposite is observed when the disturbance is injected at LE (Fig. 5.5 B and D). If the disturbance is injected at MP, the interaction of secondary flows with the swirl profile drives the changes in the aerodynamics flow field. The upper branch of the swirl profile opposes the bottom branch of the TPV, resulting in a lower underturning than the *Clean* case (see Fig. 5.6). The swirl profile is approximately centered at mid-span and, according to its turning direction, generates an overturning at 60% of the blade span and underturning at 40%. In OP2, the secondary flows are weakened due to a Reynolds number effect, and the swirl profile upper branch dissipates by a lesser extent because the TPV

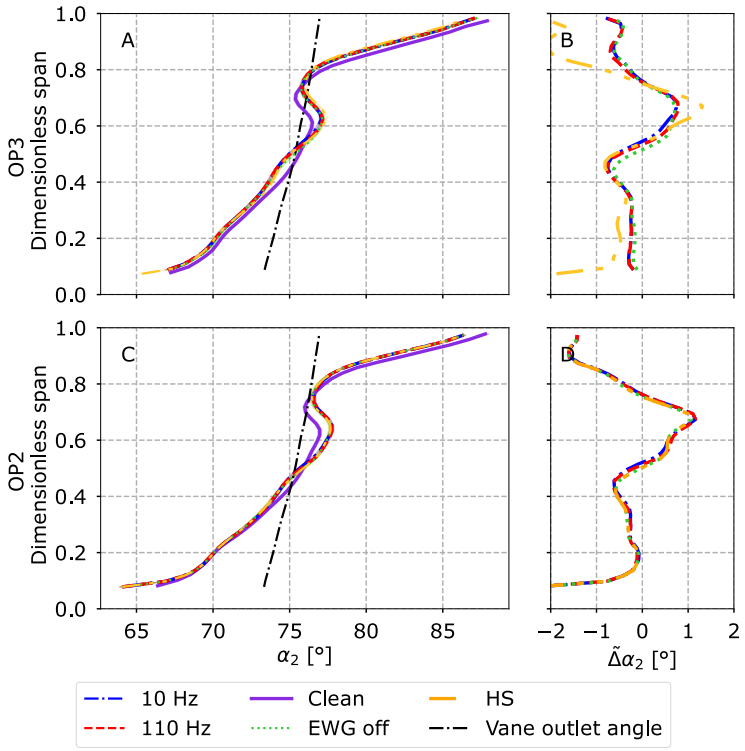

FIGURE 5.4. Pitch-wise area-average blade-to-blade angle at plane T2 for injection position MP.

reduces, and the blade-to-blade angles at 70% of the span are higher than OP3. The lower branch of the swirl profile (from 30% to 50% of the blade span) is not significantly modified because it does not interact with any secondary flow. In this region, the $\widetilde{\Delta\alpha}_2$ is slightly lower in OP2 than OP3 because the flow undergoes a higher acceleration through the stator.

Regarding the LE injection position cases, the swirl profile impinges on the blade leading edge and it is transported close to the blade suction side. In this process, the perturbation climbs on the suction side blade surface moving towards the tip. Consequently, at the stator outlet, the residual swirl core is at a higher radial position than in MP cases. The bottom branch of the swirl profile generates a significant underturning at 60% of the span, and its interaction with the TPV slightly reduces the underturning at 70% of the span because the swirl upper branch weakens the TPV bottom branch. The perturbation is more localized than the MP case because the partial stagnation of the injected disturbance at the vane leading edge causes a weaker and more localized perturbation than the passage-aligned injection. With regard to the OP, the residual swirl in OP2 (Fig. 5.5 D) is weaker than in OP3 (Fig. 5.5 B) due to the higher flow acceleration in OP2 than in OP3, which stretches the swirl and reduces its intensity.

The features discussed apply to each injection case. As shown in Figs. 5.4 and 5.5, the injection cases have nearly identical impacts on the stator outlet aerodynamics. The small differences in $\widetilde{\Delta\alpha}_2$ fall within the measurement uncertainties of approximately 0.3°, which are not shown in the figure to not worsen the readability. The only exceptions are the LE cases that feature a lower intensity swirl profile in the case *EWG off*. This is consistent with the fact that injecting EW/HS changes the swirl generation slightly, as described in chapter 4, because the swirled mass flow increases, thus the swirl intensity. These results indicate that the stator outlet aerodynamics is primarily influenced

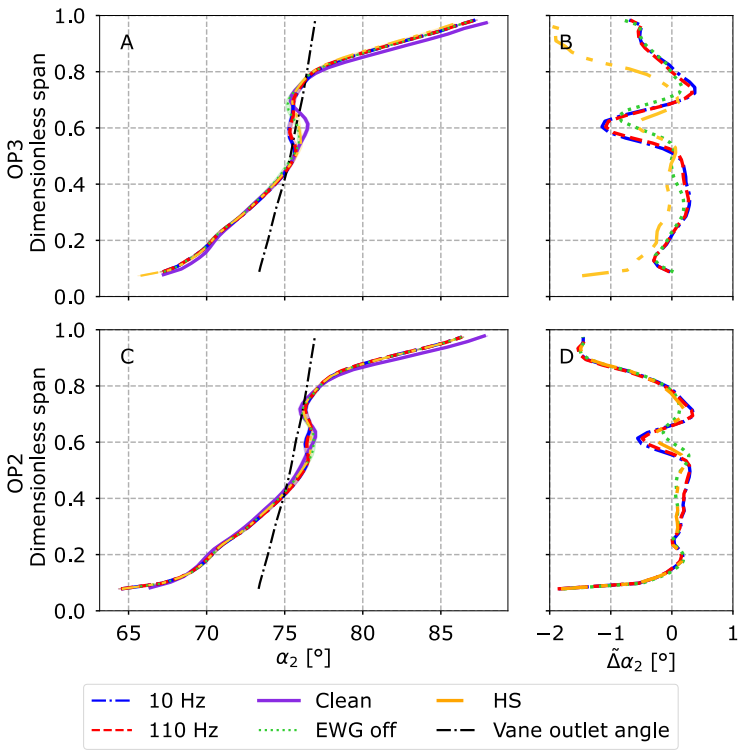

FIGURE 5.5. Pitch-wise area-average blade-to-blade angle at plane T2 for injection position LE.

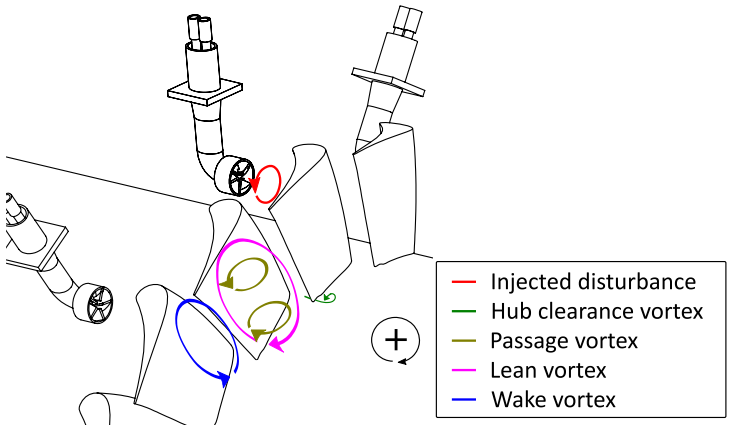

FIGURE 5.6. Schematic of the vortical structures downstream of the stator.

by the swirl profile rather than steady or unsteady (at any frequency) temperature disturbances.

To conclude the aerodynamic flow field analysis, the pitch-wise area-average blade-to-blade angle for PS and SS are shown in Figs. 5.7 and 5.8, respectively. Outcomes show that the blade-to-blade angle flow field is very similar to the case MP, as well as the total pressure coefficient radial distributions, here not shown, that only differ from Fig. 5.2 for some different trends. The

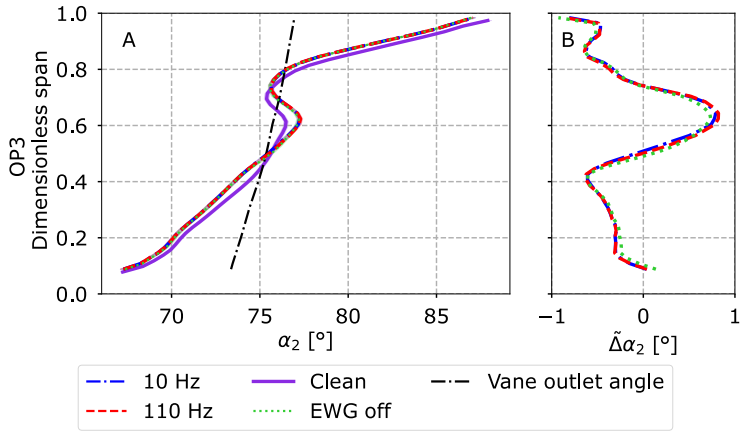

FIGURE 5.7. Pitch-wise area-average blade-to-blade angle at plane T2 for injection position PS.

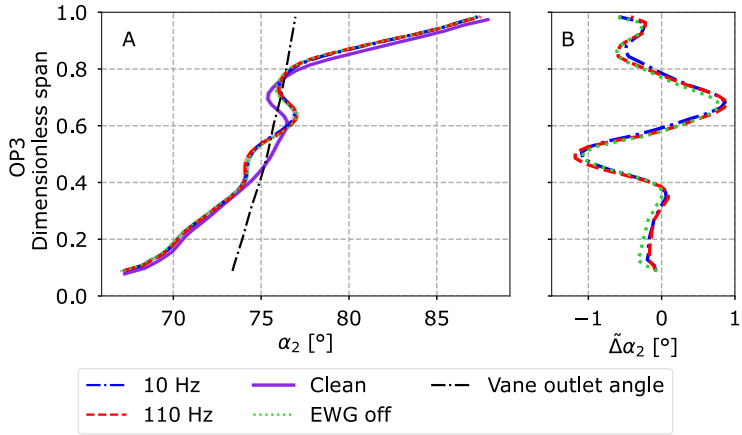

FIGURE 5.8. Pitch-wise area-average blade-to-blade angle at plane T2 for injection position SS.

SS case Fig. 5.8 shows a confined residual swirl around mid-span, while PS and MP influence the blade-to-blade angle until 20% of the span. This is a feature that SS shares with LE case, as well as the residual swirl core radial position, which is closer to the top casing. In the LE case, after the interaction with the vane leading edge, the IP is transported close to the blade suction side, thus SS and LE cases share some flow features.

Figure 5.9 shows the stream-wise vorticity fields for OP3 *10 Hz* cases at the different injection positions. This analysis enables the determination of the circumferential position of the injected perturbation, that is highlighted with a white circle. In Fig. 5.9, the velocity vectors represent the projection of the flow velocity on a plane perpendicular to the local metallic angle. Although these vectors are not secondary velocity vectors, they help in visualizing the vorticity structures. The convention adopted in this study is to assign a positive vorticity to a clockwise vortical structure when viewed from a downstream observer's perspective.

In the *Clean* case (Fig. 5.9 A), the leaned geometry produces the primary positive vorticity field (D'Ippolito *et al.* (2011)). This positive vorticity sums with the HPV and reduces the TPV, being counter-rotating. The interaction between the wake and the positive lean vorticity generates

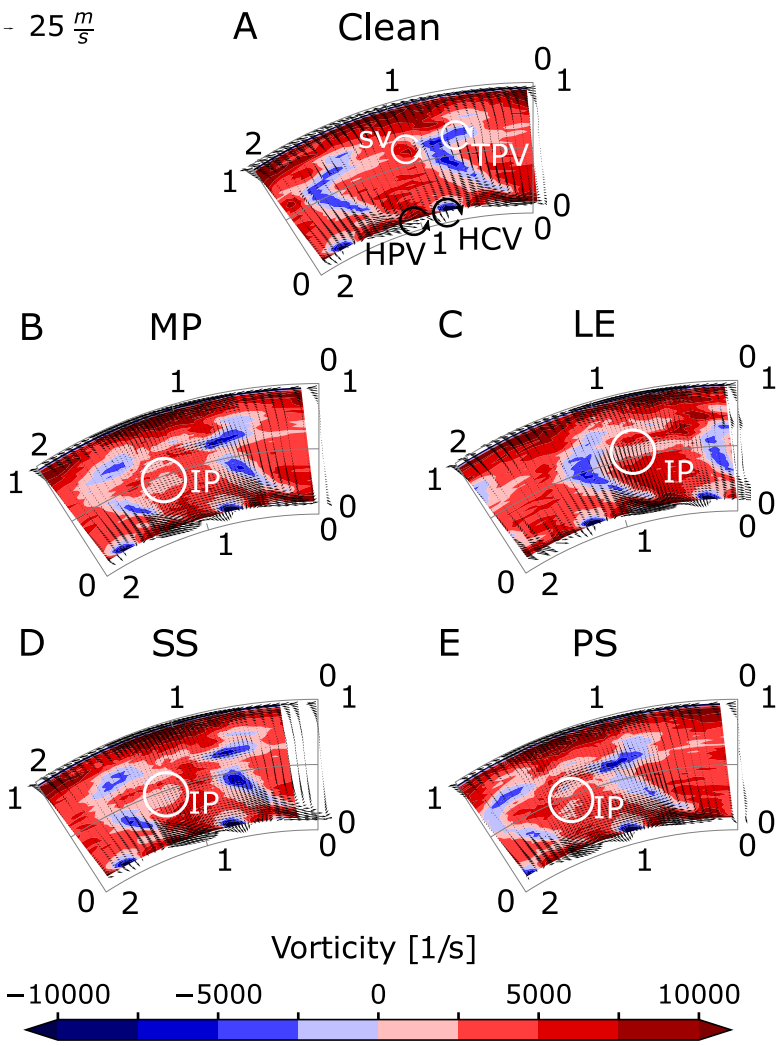

FIGURE 5.9. Stream-wise vorticity at plane T2 for OP3 10 Hz cases.

a negative vorticity in the wake region due to viscous shear. The small clearance at the stator hub results in negative vorticity in the HCV.

When the disturbance is injected, a negative vorticity is introduced, resulting in a reduction of the stream-wise vorticity near the regions highlighted with the white circle IP in each injection position case, as shown in Figure 5.9. The IP is located near the suction side in the LE and SS cases (Fig. 5.9 C and D), at mid-pitch for the MP case (frame B) and slightly shifted towards the pressure side surface in the PS case (frame E). In the LE case, the wake is the widest as a result of its interaction with the swirl profile. In the MP and SS cases, the swirl profile and the wake interact to produce a positive vorticity in the wake, resulting from the generation of counter-rotating viscous structures.

The CFD analysis based on the TRAF code not only confirms some of the previous findings, but also extends the investigation to a scenario with a reversed swirl profile at turbine inlet. Figure 5.10 shows this comparison considering the stream-wise vorticity of OP3 *110 Hz* cases. The counter rotating swirl profile is reported in Fig. 5.11. In both the figures, the temperature spot is highlighted

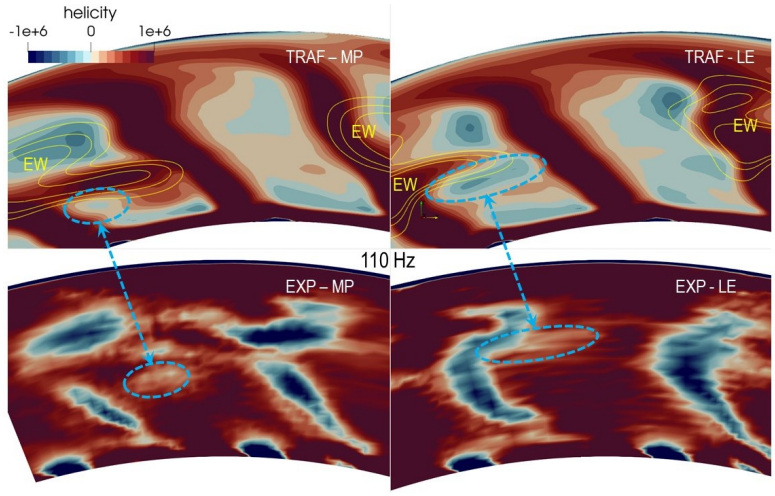

FIGURE 5.10. Stream-wise vorticity at plane T2 for OP3 110 Hz cases, CFD and experiment comparison.

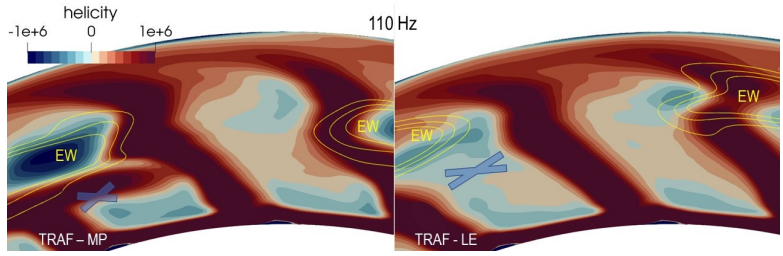

FIGURE 5.11. Stream-wise vorticity at plane T2 for OP3 110 Hz reversed swirl cases, CFD.

by the line contour labeled "EW". CFD (5.10) confirms that the swirl vortex, highlighted with the dashed line, remains close to the blade suction side in the LE injection position case, highly modifying the blade wake. In the MP case, the swirl vortical structure is also close to the blade suction side and generates a high positive vorticity in the above region, affecting the left wake.

In the reversed swirl case (Fig. 5.11), the injection position also has a notable impact on the flow field. In the MP case, the positive vorticity of the reversed swirl profile increases the positive area in the wake region at mid-span, canceling the negative spot identified in Figure 5.10. In the LE case, the channel affected by the disturbance becomes similar to the undisturbed one and the introduced vortex only impacts the region of the EW, close to the tip. As a result, the negative region identified in Figure 5.10 disappears.

5.1.1 Rotor incidence angle for different OP3

As described in section 2.1.1, fixed the expansion ratio of OP3, two different operating conditions are obtained increasing (OP3U) or decreasing (OP3L) the rotor rotational speed. This modification results in a variation of the rotor incidence angle, as illustrated in Fig. 2.3, and a slight modification of the degree of reaction. Specifically, in the *Clean* case, the reaction degree increases (decreases) by 0.015 (0.01) in OP3L (OP3U), compared to OP3, due to the static pressure increase (decrease) of 15 mbar (10 mbar) in OP3L (OP3U). Note that this change in static pressure does not affect the stator pressure losses.

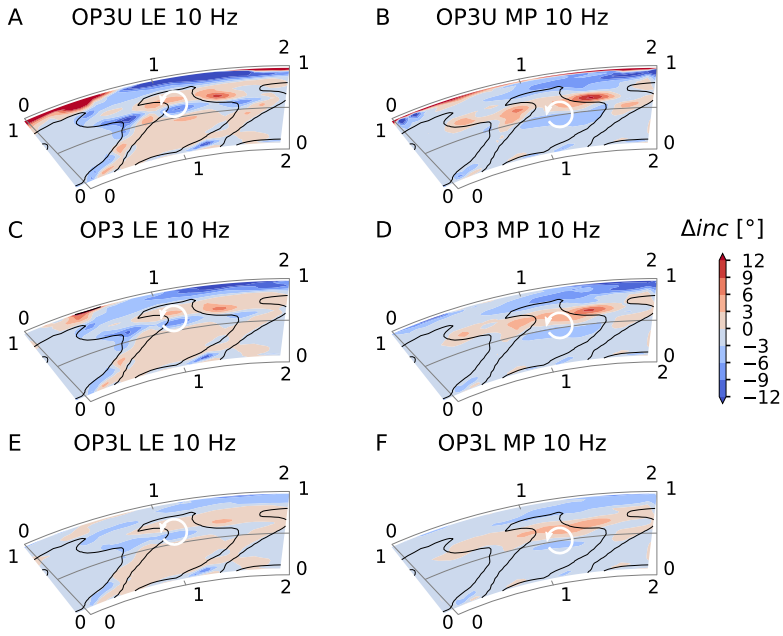

FIGURE 5.12. Rotor incidence angle contours for OP3U, OP3 and OP3L 10 Hz cases. The plots show the difference between the incidence of the perturbed cases and the *Clean*. Line contours show the stator wake.

The impact and transport of the EW/HS in the off-design OP3 remain unaltered. However, the rotor incidence angle requires further investigation for both loaded and unloaded operating points. Figure 5.12 shows the rotor incidence angle of perturbed cases minus the uniform inlet one ($\widetilde{\Delta inc}$) for OP3, OP3L and OP3U. A positive value of the contour corresponds to an increase in the rotor incidence, that is computed considering the mean EW/HS temperature. As the temperature measurements are not available for OP2, its analysis is not included. However, no significant differences are expected in OP2 compared to OP3. The line contour highlights the blade wake. Figure 5.12 shows only the *10 Hz* case, the other injection cases do not differ as previously shown. The residual swirl profile upper branch increases the rotor incidence, while the bottom branch reduces it. OP3U shows the largest incidence increase, and OP3L shows the lowest. All the cases exhibit a negative $\widetilde{\Delta inc}$ close to the top casing possibly due to the injector stem wake. In this region, the flow is slower, resulting in smaller incidence angles than the *Clean* case. This effect could also be attributed to the weakened TPV caused by its interaction with the swirl profile, as discussed earlier.

Anyhow, the change in the incidence angle is not dramatic and slightly affects the rotor aerodynamics in OP3 and OP3U, as it will be shown. However, if the blade is highly loaded as in OP3L, even a small change in the incidence can significantly modify the rotor operation. Therefore, the OP3L case requires further investigations, done in section 5.1.2, especially for the EW case when the rotor could work differently under the EW hot or cold period.

5.1.2 Unsteady analysis

To further investigate the impact of the EW perturbation on the rotor blade, an unsteady analysis is required. The nature of the EW temperature perturbation is inherently unsteady, as discussed in section 4.1.2. Therefore, a time-resolved analysis is necessary to fully characterize the unsteady flow field at the rotor inlet. It should be noted that the lowest blade passing frequency considered

in this study is 2083 Hz in the OP3L case, while the highest EW frequency is 110 Hz. As a result, the injected perturbation can be considered quasi-steady from the perspective of the rotor blades. However, the impact of the perturbation on the overall flow field and the interaction with the rotor blades can still be unsteady, and therefore requires an unsteady analysis.

To characterize the unsteady aerodynamics at plane T2, FRAPP is traversed at plane T2 and signals are phase-averaged on the EW frequency re-phasing the signals on the maximum of the trigger pressure. The peak-to-trough values of total temperature (A), total pressure (C), blade-to-blade absolute (B) and relative (D) angles for MP and LE cases are shown in Figs. 5.13 and 5.14, respectively. The overlapped contour lines show the time-mean values of the corresponding quantities. Total temperature values are measured with the fast-thermocouple and are only shown to identify the location of the EW, which peak temperature is highlighted by a red circle. A deep discussion on the thermal flow field will be done in section 5.2. The injection case considered is the *10 Hz* which exhibits higher fluctuations than *110 Hz*. In the latter frequency, the features differ only in terms of magnitudes that are damped by the higher mixing that is taking place.

Overall, Figs. 5.13 and 5.14 demonstrate that all the quantities examined have a significant frequency content at the EW frequency. Figure 5.14, which corresponds to the LE injection position case, exhibits higher peak-to-trough values for each quantity than Fig. 5.13, representing on the contrary the MP injection position case. This difference can be attributed to the transport psychics through the stator. In the MP case, the injected EW interacts significantly with secondary flows, leading to the diffusion and attenuation of the frequency content. In contrast, the EW injected at the LE position is transported closer to the blade suction side, remains stronger, and is more localized than the EW injected at the MP position. Consequently, close to the EW peak spot, the highest Δ magnitudes are measured in Fig. 5.13, with values of 20 mbar for the total pressure, 4° for the absolute angle and 8° for the relative flow angle, and, hence, the rotor incidence. The measured deviation of the rotor incidence angle from the design value falls within the range of approximately -15° to 5°, which, according to Craig & Cox (1970), is not expected to result in any significant modification of the blade aerodynamics in design OP. The position of peak values of aerodynamics and thermal fields do not overlap perfectly because unsteadiness is also introduced by the swirler generator that acts on the EW, swirling differently its hot and cold branches.

Butler *et al.* (1989) showed that an HS could increase the rotor incidence angle by increasing the flow velocity at a fixed pressure field. Therefore, it is important to understand the effect of the hot branch of the EW on the rotor incidence angle. Considering that the swirler generator introduces a certain unsteadiness on the flow field swirling the EW, it is possible to separate this effect from the temperature effect by comparing the *10 Hz* case with the *10 Hz cold* case. The peak-to-trough relative angle measurements for the *10 Hz cold* case are shown in Fig. 5.15 A, while panel B shows the difference between the peak-to-trough values of the *10 Hz* and *10 Hz cold* cases. The red circles highlight the position of the maximum ΔT of Fig. 5.14 A. The higher velocity associated with the high temperature increases the relative flow angle in the hot case, but the increase is limited to 2° in Fig. 5.15 B. Comparing this to the 8° change induced by the swirling EW (Fig. 5.14) leads to the conclusion that the swirl profile mainly drives the unsteadiness of the relative flow angle.

The unsteady analysis is carried out also for OP2 and results are shown in Fig. 5.16. In frame A OP3 is plotted, in frame B OP2. The white total pressure contour lines highlight the blade wakes. The analysis here reported regards only the LE *10 Hz* case that has been identified as the case with the highest fluctuations, and only the absolute flow angle is analyzed since temperature measurements are not available at OP2, preventing a possible analysis of the incidence angle. The results show that the peak-to-trough variation in absolute flow angle, $\Delta\alpha$, is reduced at OP2 compared to OP3. This is consistent with the outcomes at plane T1 that revealed a reduced peak temperature in OP2. Furthermore, the larger Re in OP2 than in OP3 promotes the mixing and

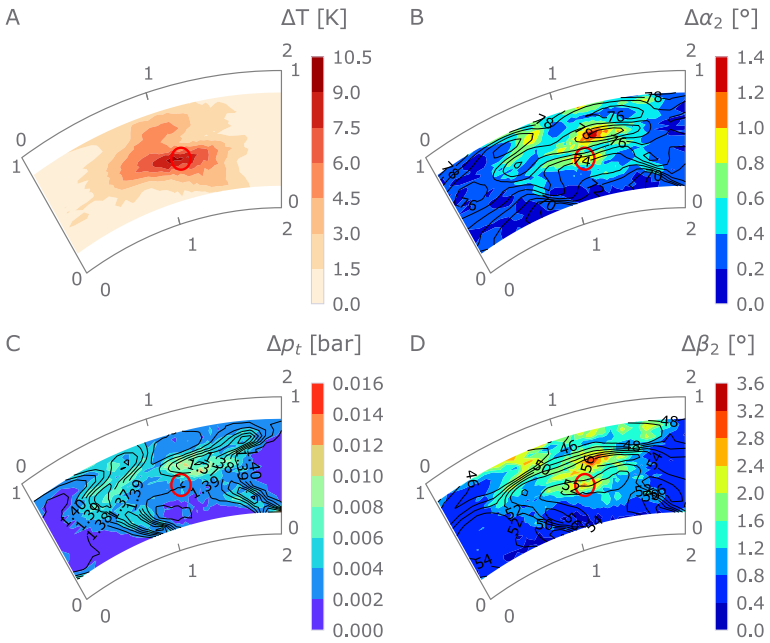

FIGURE 5.13. Peak-to-trough contours measurements at plane T2 for OP3 MP 10 Hz case: (A) temperature, (B) absolute angle, (C) total pressure and (D) relative angle. Contour lines are the corresponding time-mean values.

damping of the pressure fluctuations. Overall, these results suggest that the swirling EW will have less of an impact on the rotor incidence angle in OP2 compared to OP3, where an 8° variation was observed.

To further investigate the temperature effect, Fig. 5.17 shows the time evolution in one EW period of the total temperature and the relative flow angle for the OP3 LE *10 Hz* and OP3 LE *10 Hz cold* cases, both measured at the position where the highest peak-to-trough relative flow angle is measured (Fig. 5.14 D). Both the two variables are significant time-dependent. Despite a small temporal shift, the time peak period is phased with the maximum relative flow angle. Considering that the point under analysis lies in the region where the swirl profile produces an underturning, during the cold period between 0.02 and 0.07 s, the lowest angle is measured in Fig. 5.17 B due to the strengthening of the swirl profile by the cold branch of the EW, which introduces a peak pressure at the stator inlet as shown in Fig. 4.6 A. During the remaining time period, the hot duct is fed and the swirl is weakened, thus the relative flow angle increases. However, the increase in temperature during the hot duct feeding period leads to a larger relative angle for *10 Hz* than *10 Hz cold*, consistent with Fig. 5.15.

The discussion on the rotor incidence in section 5.1.1 highlighted that the OP3L case is highly loaded in the tip region. Therefore, the different incidence angles on the EW period may lead to a different blade operation during the hot or cold periods. This requires performing the unsteady analysis also for OP3L, which outcomes are shown in Fig. 5.18 and 5.19 for the *10 Hz* MP and LE cases, respectively. The two figures show instantaneous values of rotor incidence and total temperature taken from the phase-average of the respective probe at the time of the peak temperature (first row) and a point shifted of half EW period, that is during the cold EW period (second row). The location of the temperature peak is highlighted with a circle. Figures 5.18 and 5.19 show that the hot branch of the EW increases the incidence with respect to the cold period

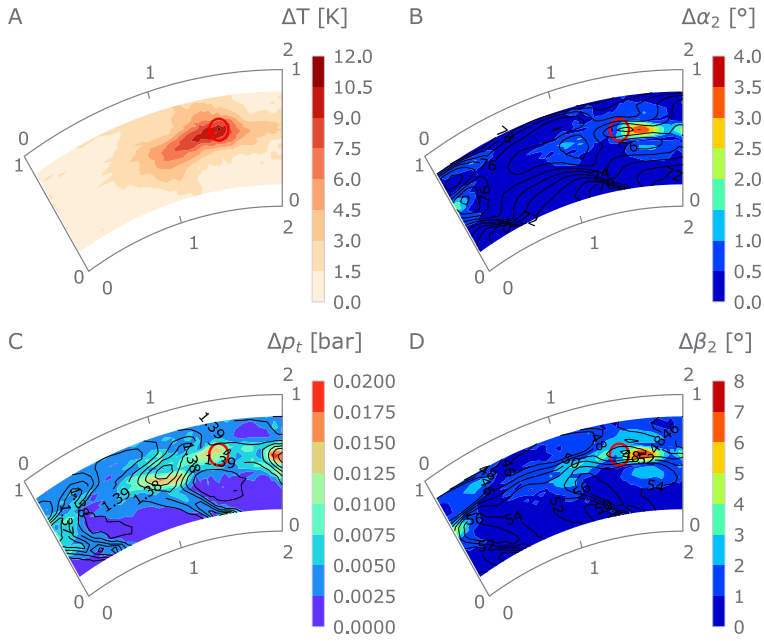

FIGURE 5.14. Peak-to-trough contours measurements at plane T2 for OP3 LE 10 Hz case: (A) temperature, (B) absolute angle, (C) total pressure and (D) relative angle. Contour lines are the corresponding time-mean values.

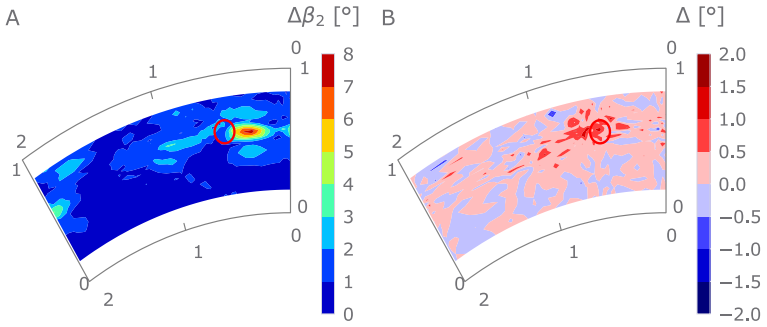

FIGURE 5.15. Peak-to-trough contours of relative flow angle at plane T2 for (A) OP3 LE 10 Hz cold and (B) difference between OP3 LE 10 Hz and OP3 LE 10 Hz cold.

by approximately 4°. This could lead to problems related to the blade stall because the incidence could exceed the positive stalling threshold. Applying Craig & Cox (1970) correlation to the rotor blade, the positive stalling incidence is approximately 25° at mid-span and 30° at 80% of the span. Therefore, in the regions surrounding the red circle, it is expected that the hot and cold branches of the EW will impact the blade operation differently.

Overall, the unsteady analysis has revealed that unsteadiness is present at the stator outlet due to the swirling EW at the stator inlet. The major unsteadiness is related to the inlet unsteady pressure field that affects the swirl magnitude, the EW impacts the incidence angle. The incidence increase is limited considering the temperature attenuation that the temperature perturbation undergoes through the stator, as it will be discussed in section 5.2. However, in the case of OP3L, the different

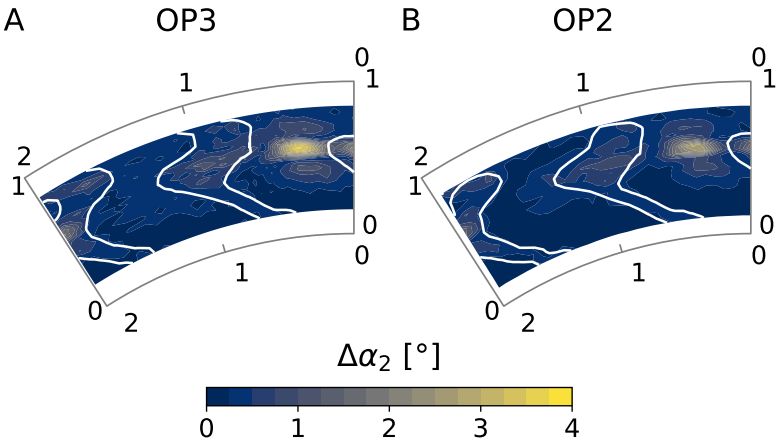

FIGURE 5.16. Peak-to-trough contours of absolute flow angle at plane T2 for (A) OP3 LE 10 Hz and (B) OP2 LE 10 Hz.

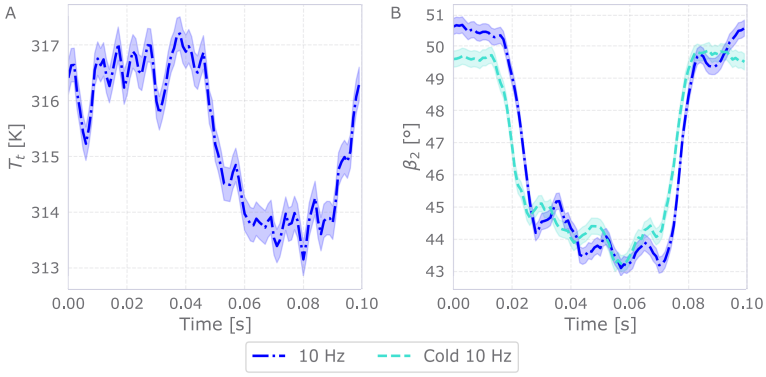

FIGURE 5.17. Time evolution of the (A) total temperature and (B) relative flow angle at plane T2 for OP3 LE 10 Hz and LE 10 Hz cold. Measurements refer to the point of maximum relative flow angle variation.

incidence angles between the hot and cold EW branches may lead to different rotor blade operations during the EW period. The blade operates under severe positive incidence angles, and even a slight modification of the angle could have a significant impact on its operation.

5.2 Thermal flow field

The study of the thermal flow field at the stator outlet for each injection case that features a temperature disturbance focuses on the peak-to-trough temperature value. In the case of EW injections, this is defined as the difference between the peak and trough values of the phase-averaged temperature at the EW frequency. For the HS case, ΔT is calculated as the difference between the measured temperature and the reference mainstream total temperature.

Figures 5.20 and 5.21 show the peak-to-trough contours for each injection position for the two EW cases, *10 Hz* and *110 Hz*, respectively. The line contours are the 5-hole total pressure measurements that are highlighted to identify the EW position at the stator outlet.

For each injection position and injection case, the temperature disturbance perturbs mainly the center of the blade passage, that is the isentropic region in the *Clean* case. The injection position

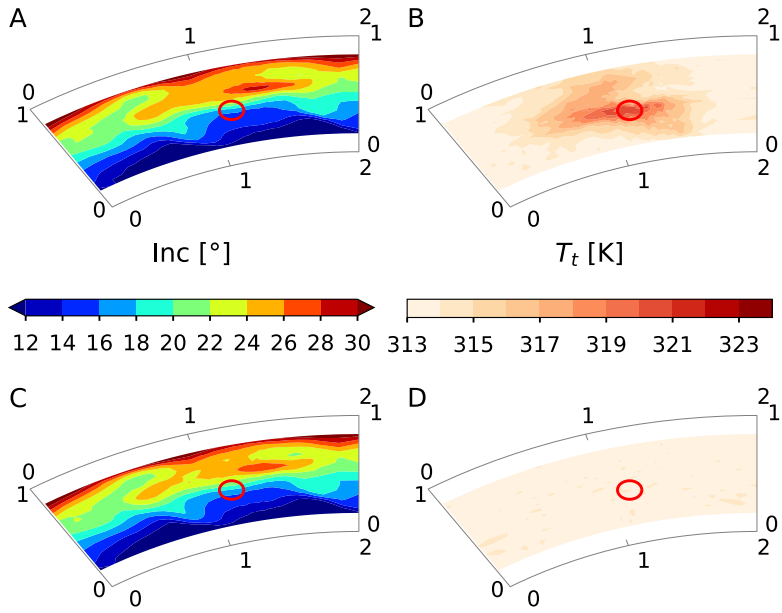

FIGURE 5.18. Phase-averaged rotor incidence (frames A and C) and total temperature (frames B and D) at plane T2 for OP3L MP 10 Hz case. Hot EW branch in the first row, cold branch in the second. The circle shows the location of the hottest spot.

influences the shape and the magnitude, the latter is also impacted by the injection case. The impact of the injection position is discussed with respect to the 10 Hz case of Fig. 5.20, but this can be generalized to the *110 Hz* case shown in Fig. 5.21.

The highest peak-to-trough temperature value is measured for the SS case. For this injection position, the interaction with the stator secondary flows is the lowest. The inlet shape of the temperature disturbance is mainly preserved, it is stretched in the radial direction due to the lean pressure field. The strong interaction with the secondary flows that takes place in MP and PS reduces the peak temperature value promoting the mixing and dissipation. For these injection positions, the temperature disturbance is more spread in the radial direction covering the whole channel. Furthermore, the peak temperature is measured at approximately mid-span despite the EW peak temperature at plane T1 being approximately at 65% of the span. The cause of this downward movement can be attributed to the blade lean pressure field.

Only in the LE case, the temperature disturbance is entrained in the blade wake because it impinges on the blade surface at the stator inlet and interacts significantly with the blade boundary layer, being transported on the suction side surface. In this injection position case, the interaction with secondary flows is lower than MP and PS and a high peak is measured, close to the SS one. All injection cases show a consistent transport of the temperature disturbance in the azimuthal direction towards the channel pressure side, consistent with the direction of the bottom branch of the tip passage vortex.

The observations made for the *10 Hz* case also apply to the *110 Hz* case shown in Fig. 5.21 and to *HS* case, shown in the next chapter (see Fig. 6.11). The shape of the temperature disturbance and its radial and circumferential displacement are similar to the *10 Hz* case. In *110 Hz* the peak-to-trough temperature differences (ΔT) are lower compared to *10 Hz*. This is due to the higher mixing between the hot and cold branches of the EW, which reduces the temperature magnitudes.

Considering the similarity of the cases, the MP and LE are deeply studied being SS and PS two

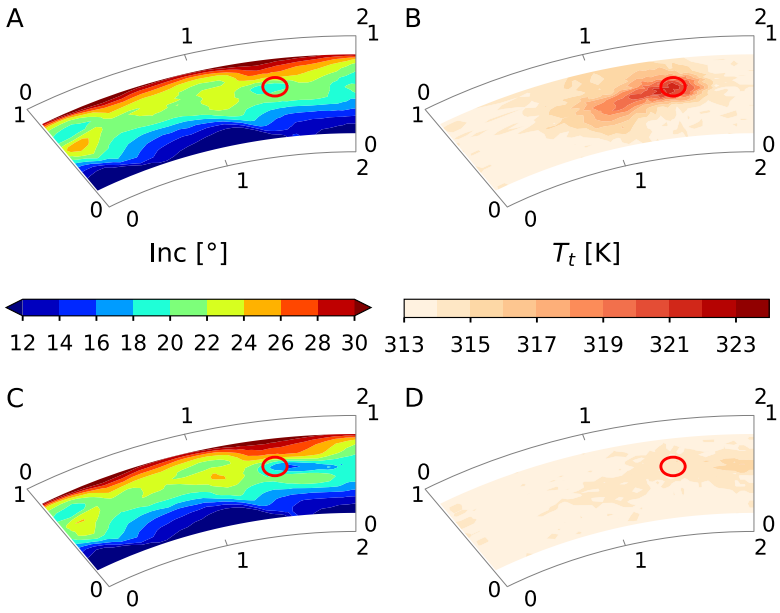

FIGURE 5.19. Phase-averaged rotor incidence (frames A and C) and total temperature (frames B and D) at plane T2 for OP3L LE 10 Hz case. Hot EW branch in the first row, cold branch in the second. The circle shows the location of the hottest spot.

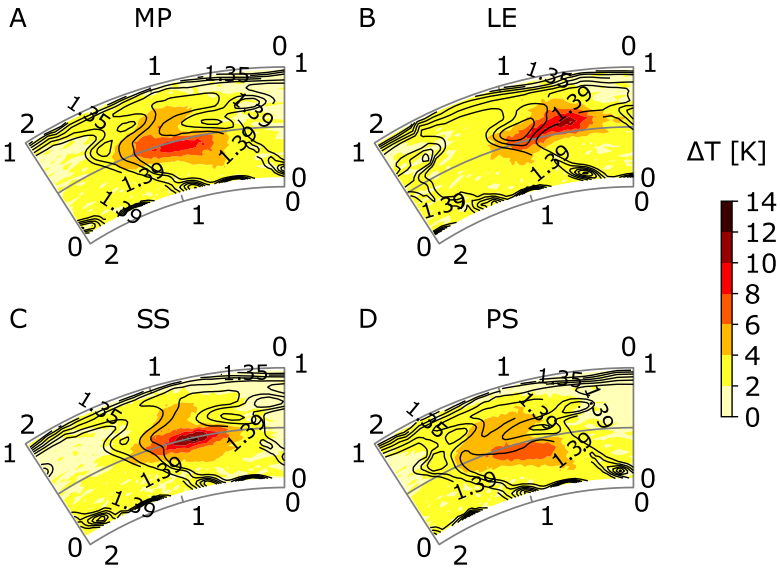

FIGURE 5.20. Peak-to-trough temperature values at plane T2 for OP3 10 Hz.

intermediate cases.

The EW evolution through the vane can be further analyzed by means of CFD. The software validation is shown in Fig. 5.22 and 5.23 for the *10 Hz* and *110 Hz*. The MP case reveals the highest diffusion due to its interaction with the secondary flows. The interaction between the counter-clockwise swirl and the clockwise vorticity generated by the lean geometry blade folds

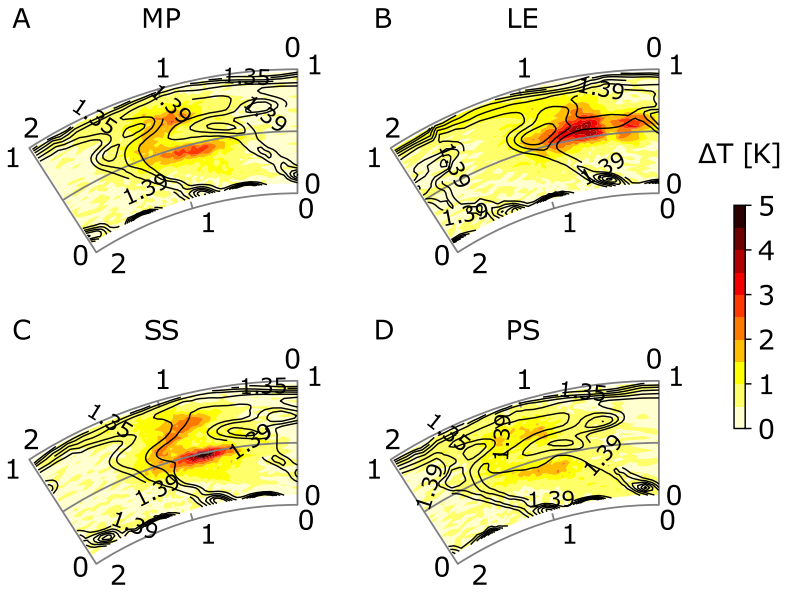

FIGURE 5.21. Peak-to-trough temperature values at plane T2 for OP3 110 Hz.

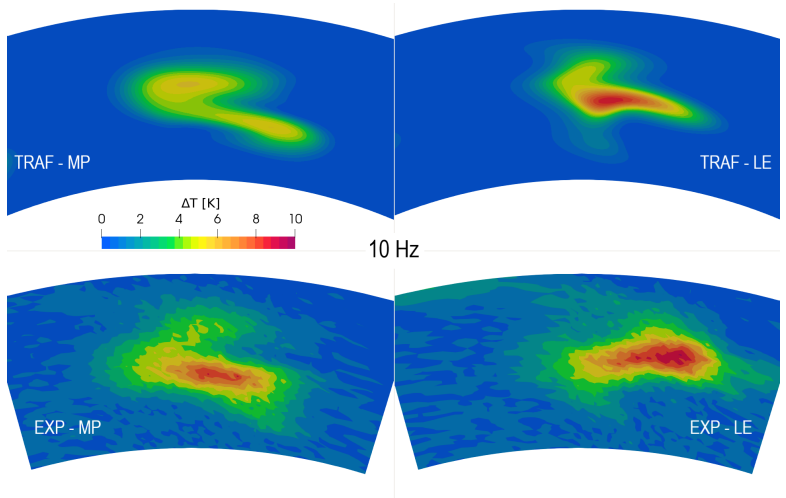

FIGURE 5.22. Peak-to-trough temperature values at plane T2 for OP3 10 Hz cases. Experimental and numerical comparison.

the EW towards the inner channel and produces a C-shape disturbance at the stator outlet. The prevented interaction with the secondary flows makes it possible to maintain a high ΔT value in the LE case. The EW shape between experimental and CFD results differs slightly. This is unavoidable due to the sensitivity of the disturbance transport to small variations in the tangential position of the inlet perturbation, considering its transport physics. Nevertheless, the shape of the EW at the stator outlet is consistent between the *10 Hz* and *110 Hz* cases, with the main difference being the magnitude of the ΔT values.

Isocontours of the ΔT in the LE case for the *10 Hz* injection are presented in Fig. 5.24, which offer insight into the transport behavior of the temperature perturbation through the stator. The

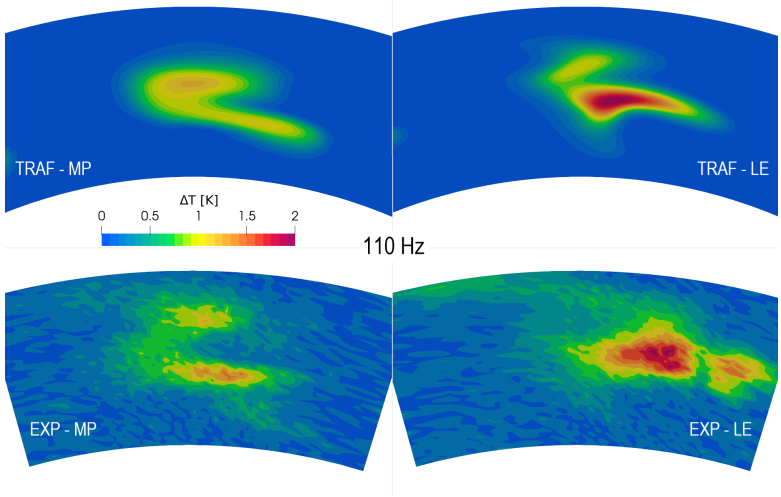

FIGURE 5.23. Peak-to-trough temperature values at plane T2 for OP3 110 Hz cases. Experimental and numerical comparison.

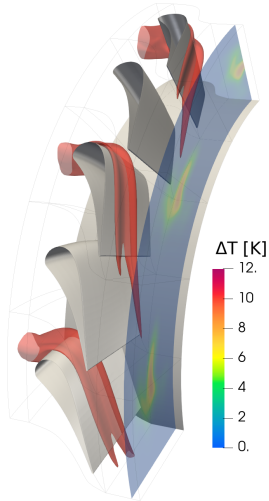

FIGURE 5.24. Evolution of the EW through the stator channel for the OP3 LE 10 Hz case.

CFD results demonstrate that the perturbation impinges on the blade leading edge, with a portion of it climbing towards the top casing and being transported in close proximity to the blade suction side surfaces. These findings corroborate well with the experimental data and demonstrate the validity of the predicted transport behavior.

Finally, the case with reversed swirl is analyzed using only CFD, as shown in Fig. 5.25 for the OP3 *110 Hz* case. In this case, the TPV bottom branch and the swirl profile upper branch share the same direction, and the swirl vorticity is not opposite to the lean one. As a result, the interaction with the secondary flow is reduced. For both the injection positions, the EW maintains its inlet circular shape and the maximum peak-to-trough temperature value is higher than the respective *110 Hz* (Fig. 5.23). In the LE case, the EW is shifted more towards the tip, while in the MP case, the temperature disturbance is located at mid-span.

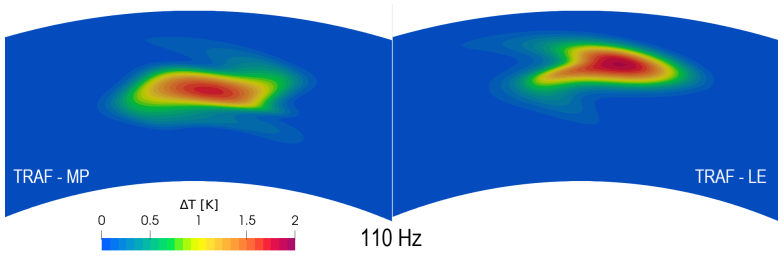

FIGURE 5.25. Peak-to-trough temperature values at plane T2 for OP3 110 Hz reversed swirl cases.

The analysis of the thermal flow field is concluded comparing the results of swirling EW with the axial EW case, studied on the same turbine experimentally by Gaetani & Persico (2019) and numerically by Pinelli *et al.* (2021). Figure 5.26 shows the peak-to-trough temperature value for the different injection positions of an axial EW at 90 Hz (Pinelli *et al.* (2021)), made non-dimensional with respect to the inlet value of 19 K. The first clear difference with respect to the swirling EW case at *110 Hz* (Fig. 5.21), that is the closest frequency, regards the shape of the temperature disturbance. As described previously, the swirl profile, interacting with the secondary flows, causes a shape deformation of the EW.

Considering that in the works of Gaetani & Persico (2019) and Pinelli *et al.* (2021) the axial EW was injected at 70% of the blade span at the turbine inlet, all the cases show a downward movement of the EW toward the hub casing. This effect is due to the blade lean pressure field and takes place also for the swirling EW cases investigated in this thesis, specifically within the MP, SS, and PS injection positions. Another common trend among the swirling and axial EW cases is the maximum measured peak-to-trough value, which is the highest for SS, the lowest for PS, and intermediate for MP.

However, the behavior of the LE case stands out from the trend observed in swirling EW cases due to a unique evolution caused by the blade leading edge. The axial EW spot is split into two branches by the blade leading edge, with one branch evolving on the suction side surface and the other on the pressure side surface. Consequently, the entire wake experiences a temperature increase (see Exp of Fig. 5.26 d). This EW evolution is also sought in the swirling EW case by shifting the EW-stator alignment by 0.1° within the range limited by PS and SS cases. However, this condition was not achieved, indicating that the presence of the swirl profile significantly changes the flow dynamics when the EW impinges on the blade. As discussed in depth, the swirl profile causes the perturbation to climb over the blade towards its suction side.

The last comparison regards the decay rate of the maximum peak-to-trough temperature value, defined as the ratio $\Delta T_{max,2}$ and $\Delta T_{max,1}$. This analysis will be further discussed in section 5.2.1 for the swirling EW cases, where it will be shown that this value is almost independent of the EW frequency. The decay rate is approximately 0.15 for the SS case, 0.15 for LE, 0.12 for MP and 0.09 for PS. Excluding the LE case, which is unique in the axial case, these values are lower than those reported in Fig. 5.26 for the axial case. In the EW axial case, EW dissipation is influenced only by secondary flows and heat exchange with the surrounding flow. In the swirling EW case, the swirl profile further amplifies mixing and dissipation processes, resulting in a higher EW decay.

5.2.1 Temperature decay

The aim of this section is to study the effect of the EW frequency on the maximum peak-to-trough decay between planes T2 and T1, provided that it is influenced by the injection position as discussed in section 5.2. Using an analytical model to predict this number is very challenging because it

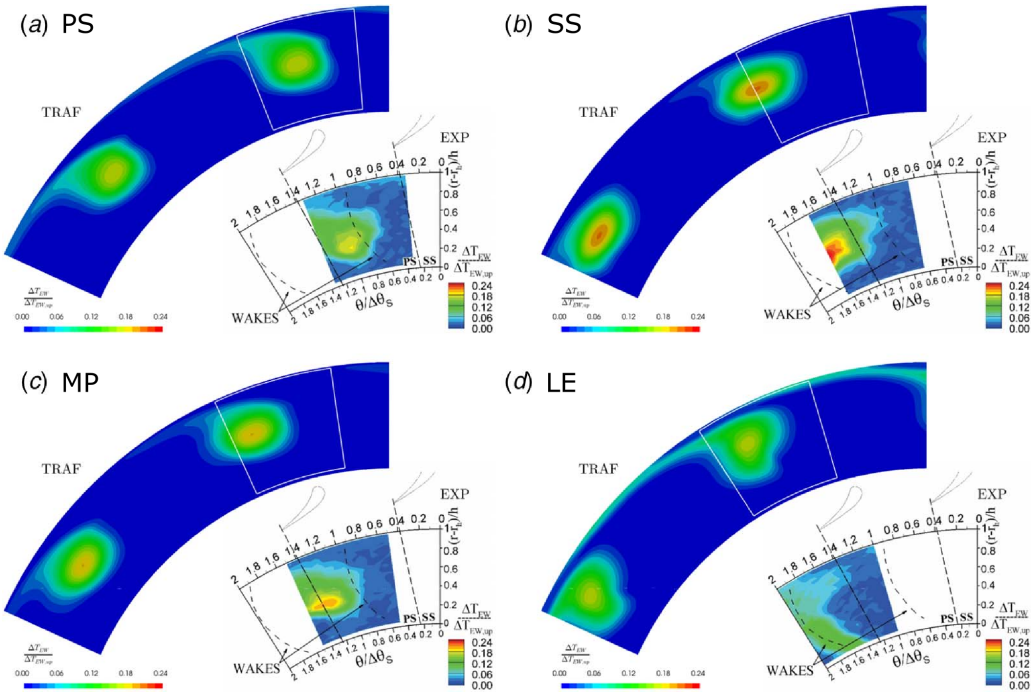

FIGURE 5.26. Peak-to-trough temperature values at plane T2 for axial EW at 90 Hz for different clocking positions: (a) PS, (b) SS, (c) MP, and (d) LE. Pinelli *et al.* (2021)

depends on many parameters, e.g Re, M, secondary flows intensity, inlet swirl profile intensity, EW frequency and injection position. Therefore, the choice is to determine the decay rate based on experimental data. The knowledge of this parameter is of paramount importance to properly design the stage, its film cooling system and to develop simplified models, as it will be shown in section 6.

The decay rate study focuses on five different EW frequencies. The comparison among these different frequencies is possible because the aerodynamic flow field at the stator outlet is not influenced by the EW frequency, as shown in section 5.1 for the highest and lowest EW frequencies. Figure 5.27 shows the ratio between the maximum grid values of the peak-to-trough temperature at plane T2 and the value at plane T1. The injection positions considered are the MP and LE, for which simplified models will be developed. The outcomes show that the LE has a lower reduction of the maximum ΔT than MP, as expected and explained in section 5.2. However, the experimental points do not reveal any clear trend with the frequency. Therefore, given the flatness of the experimental trends, the choice is to consider an average value for each injection position. This choice is supported by the fact that the EW wavelength is at least about five times longer than the axial distance from T1 to T2. Therefore, the main cause of temperature reduction has to be investigated in the interaction of the temperature disturbance with the swirl profile and stator aerodynamic flow field. For this reason, the mixing process between hot and cold branches of the EW plays a secondary role and the decay rate is not significantly affected by the EW frequency.

To provide a complete set of information, the mean decay rate for the PS case is 9% and for the SS case it is 16%.

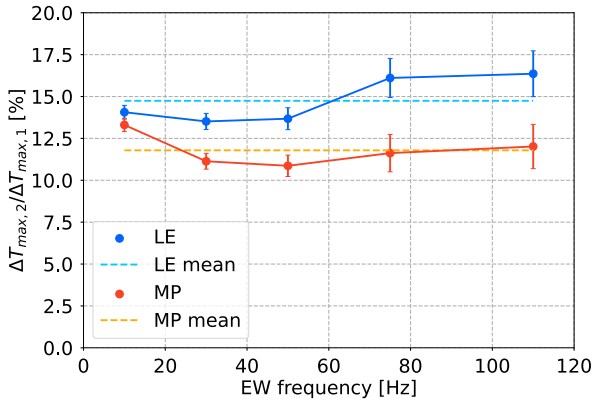

FIGURE 5.27. Decay rate of the maximum peak-to-trough temperature between planes T1 and T2 for OP3.

5.3 Concluding remarks and key findings

This chapter has investigated the effects of combustor non-uniformities on the aerothermal flow field of a turbine stator.

The swirl profile mainly impacts the aerodynamic flow field, increasing the pressure losses at the stator outlet. These losses are mainly impacted by the swirl profile/secondary flows interaction and by the positive/negative incidence imposed by the swirl profile. A residual swirl persists at plane T2 but it is significantly weakened with respect to the inlet one. The aerodynamics depends significantly on the injection position because it changes the interaction between the secondary flows and the swirl profile. In the MP case, the upper branch of the swirl profile interacts with the lower branch of the TPV, resulting in a reduction of the swirl upper branch angle. In the LE case, higher pressure losses are measured because the blade vane undergoes a high positive/negative incidence angle. The swirl profile impinges on the blade leading edge weakening its strength. Then it climbs towards the top casing on the blade suction side surface, close to which it is transported through the stator. SS and PS cases are intermediate with respect to MP and LE. The PS features the highest pressure losses due to the high local incidence angle that is imposed on the vane, similar to the LE case. In the SS case, the swirl profile is transported close to the suction side and it is more confined in the radial direction, as in the LE case. Both SS and PS maintain a swirl intensity at the stator outlet similar to the MP case and share a shift of the vortex core towards the hub, close to mid-span, due to the blade lean pressure field.

The aerodynamic flow field at the stator outlet is not modified changing the injection cases. The only difference regards the *EWG off* case that features a swirl profile with a lower intensity than EW/HS cases because it lacks a central flow in the swirler generator. The lower swirl intensity is consistent with the results shown, i.e. lower total pressure losses and residual swirl.

The effect of the different expansion ratios is to change the stator secondary flows. In OP2, characterized by a higher expansion ratio, Reynolds and Mach numbers are higher, reducing the strength of the secondary flows. This in turn reflects on the swirl impacts on the aerodynamics. The injected disturbance undergoes a higher acceleration through the stator in OP2, thus the swirl is more dissipated. In the MP case, the interaction between the TPV and the swirl reduces and the upper branch of the swirl profile maintains a higher intensity.

The different rotor rotational speeds do not impact significantly the stator aerodynamics but change the rotor incidence angle. In OP3L the incidence angle is very close to the stalling incidence.

The interaction with the TPV is reduced in the reversed swirl case, studied through CFD. This

swirl vorticity adds to the background vorticity generated by the lean geometry. Furthermore, TPV bottom branch and swirl profile upper branch have the same direction and do not dissipate each other.

To conclude the aerodynamics discussion, an unsteady analysis reveals the unsteadiness related to the injection of EWs. Being swirled by the swirler generator, the EWs generate an unsteady flow field that persists at the stator outlet. The hot temperature of the EW produces a further increase in the rotor incidence angle. This incidence increase is limited and is expected to not influence significantly the blade operation in the design cases (OP3 and OP2). This does not apply to OP3L because the different incidences on the hot and cold EW branches could make the rotor work differently on the EW period.

As discussed, the injection of the temperature perturbation as EW/HS does not impact the time-mean aerodynamic flow field but a residual temperature disturbance is present at the stator outlet. This is investigated traversing the fast-response thermocouple and by numerical simulations. The analysis reveals that the injection case influences the results in terms of magnitude. The MP, SS and PS share the same temperature disturbance shape and differ only in magnitude as a result of the different interaction with the secondary flows. In the LE case, the temperature perturbation shape is different and affects the blade wake, consistent with its discussed transport. The MP, SS and PS EW/HS are pushed downwards towards the hub casing by the blade lean pressure field, in the LE case this effect is compensated by the climbing that takes place with the stator leading edge interaction.

The frequency of the EW seems to not affect the decay rate of the temperature disturbance because the EW wavelength is at least about five times longer than the axial distance from T1 to T2. The main causes of the decay are the dissipation and mixing imposed by the secondary flows and swirl profile. The latter plays a significant role because a reduction of the decay rate is measured for swirling EW with respect to the case of axial EW studied by Pinelli *et al.* (2021).

The HS case shares the same features of the EW cases as it will be shown in chapter 6.2.5, where simplified models to predict the aero-thermal flow field will be presented.

CHAPTER 6

SIMPLIFIED MODELS FOR THE AERO-THERMAL PREDICTION AT PLANE T2

This chapter uses the experimental data to develop simplified models to predict the aero-thermal flow field. In particular, it focuses on the MP and LE cases. The object is to develop a model that can predict the aerodynamics of the stator and the impact of combustor non-uniformities, starting from the inlet parameters and the turbine geometrical quantities. This will be an important tool for preliminary turbine design. The analysis starts reconstructing the Clean case for OP2 and OP3 using 1D approaches, thus reconstructing flow quantities in their span-wise distribution. Second, the inlet perturbations are considered and the perturbed 1D radial flow field at the stator outlet is solved. To conclude, the temperature perturbation evolution is addressed.

Some contents of this chapter are also discussed in:

Notaristefano, A., Gaetani, P., (2023), Modelling of Combustor Non-Uniformities Evolution through a High-Pressure Turbine Stage, *ASME Turbo Expo 2023*, GT2023-102601, Boston, Massachusetts, United States

6.1 Flow field reconstruction for Clean case

The primary aim of this investigation is to replicate the 1D span-wise aerodynamic flow field downstream of the stator. The inputs of the models are the vane geometrical parameters and the turbine inlet conditions. The tools for this analysis are correlations available in the open literature plus some considerations based on the experimental results.

The initial state considered is the uniform inlet condition *Clean*. To accomplish this, the domain is divided into several radial subdomains (spaced one millimeter apart), and correlations are applied to each one. The proposed model is based on the assumption that every flow particle retains its radial position as it moves through the stator. For this reason, the experimental data that are shown for model validations are area-averaged. This hypothesis is particularly strong for the current turbine design, which has a lean angle on the pressure side. Nevertheless, to account for the effect of the lean angle, this assumption is relaxed by considering a shift toward the hub casing.

6.1.1 Flow angle

To apply established turbine correlations like Kacker & Okapuu (1982), it is necessary to determine the flow angle at the blade exit. The presented model starting from the definition of the stator blade geometry and inlet conditions calculates the flow angle.

The model neglects the deviation angle, which is predicted to be less than 1° by Aungier (2006) correlation due to the high Mach number at stator discharge (> 0.5) and low gauging angle (arcsin o/s). This term can be neglected if the rotor aerodynamics are not of interest because it will have a larger impact on the rotor incidence angle.

One factor that significantly affects the exit flow angle is the secondary deviation, caused by secondary flows that influence the fluid discharge angle near the hub and tip casing downstream of the stator. While 'classical' secondary flow theory by Hawthorne (1955) and Gregory-Smith (1982) predicts angle variation, it requires significant computational time. To address this, a secondary deviation angle correlation suitable for this model is identified in the work of Massardo & Satta (1985). This correlation involves parameters such as boundary layer thickness at turbine inlet δ (12 mm, estimated from measurements), shape factor H (1.35, typical of turbulent flows Schlichting & Gersten (2017)), velocity ratio v_2/v_1, and flow deflection (Eq. 6.1).

$$\Theta = \alpha_1 - \alpha_2 \tag{6.1}$$

In the current phase of the analysis, the flow angle α_2 remains unknown, as it is the primary target of the model. To address this, the geometrical flow angle is assumed to be equal to the midspan flow angle at the stator outlet. This assumption is supported by the small deviation angle predicted by Aungier (2006) correlation and the nearly isentropic behavior in this region. In order to account for the blade lean angle, the secondary deviation correlation of Massardo & Satta (1985) is adapted by shifting the radial location of the minimum secondary deviation angle (z_{min}) towards the hub casing. Specifically, as shown in Eq. 6.2, the amount of shift is determined by multiplying the tangent of the lean angle Θ by the axial distance between the stator trailing edge and the T2 plane (Δx_{TE-T2}), and subtracting this value from the original minimum radial location, computed using the Massardo & Satta (1985) correlation.

$$z'_{min} = z_{min} - \Delta x_{TE-T2} tan\Theta \tag{6.2}$$

A further contribution to the flow angle is given by the vane lean pressure field which creates vorticity in the secondary plane, resulting in an overturning in the tip region and an underturning in the hub region, as described by D'Ippolito *et al.* (2011). Since to the best author's knowledge there is no prior literature that predicts this source of deviation angle downstream of a turbine blade row,

a simple analytical correlation has been developed based on the data published in D'Ippolito *et al.* (2011). The authors showed the span-wise flow angle distribution of a cascade for various blade lean angles (Θ equal to 10°, 15° and 20°), including the prismatic case, where the lean angle is zero. These distributions are provided at 1.4 axial blade chord downstream of the blade leading edge, which is consistent with the T2 measuring plane (Fig. 2.8), and the blade deflection in the two cases is similar. The correlation is created by determining the differences between span-wise distributions of the leaned vanes and the prismatic one. This reduces the influence of the secondary flow and allows for the applicability of the correlation to other geometries. For each span-wise position, the differences between the three lean cases and the prismatic one are computed and then interpolated using a parabola with the lean angle as the independent variable, as shown in Eq. 6.3, where r is the non-dimensional span.

$$\epsilon_{lean}(r) = a(r)\Theta^2 + b(r)\Theta + c(r) \tag{6.3}$$

Each coefficient (a, b, and c) of Eq. 6.3 is then interpolated through a 10^{th} order polynomial in terms of the non-dimensional radial position, as shown in Eqs. 6.4, 6.5 and 6.6.

$$\begin{aligned} a\,(r) = 51.7r^{10} - 404.9r^9 + 1205.6r^8 - 1880.4r^7 + 1727.4r^6 - \\ + 981.8r^5 + 350.3r^4 - 77.6r^3 + 10.12r^2 - 0.67r + 0.02 \end{aligned} \tag{6.4}$$

$$\begin{aligned} b\,(r) = -9375.1r^{10} + 51067.0r^9 - 118750.9r^8 + 154116.4r^7 - 122569.9r^6 + \\ +61817.3r^5 - 19810.2r^4 + 3932.7r^3 - 451.2r^2 + 24.5r - 0.21 \end{aligned} \tag{6.5}$$

$$\begin{aligned} c\,(r) = 22471.3r^{10} - 125736.7r^9 + 298603.6r^8 - 392646.6r^7 + 313555.8r^6 - \\ + 157738.1r^5 + 50679.3r^4 - 10462.5r^3 + 1368.5r^2 - 102.7r + 3.88 \end{aligned} \tag{6.6}$$

Therefore, the correlation can be applied by following two steps:

1. Determining a(r), b(r), and c(r) given the non-dimensional span r using the Eqs. 6.4, 6.5 and 6.6.
2. Computing $\epsilon_{lean}(r)$ using Eq. 6.3.

The model results are validated by the good agreement between the experiments and the model, as shown in Fig. 6.1 for both the operating points. The figure demonstrates that the developed model is able to capture the position of the TPV and flow angle radial evolution.

The subsequent step is to use the flow angle distribution to determine the pressure losses.

6.1.2 Pressure losses

The pressure losses can be determined by using correlations in the literature, with the flow angle downstream of the stator calculated as described in section 6.1.1. In this study, the correlations developed by Benner *et al.* (1997) and Benner *et al.* (2005) are applied to each radial subdomain to obtain the radial distribution of profile (Y_p) and secondary (Y_s) losses. Neglecting other sources of losses, considered to be negligible, the area-average applied on the correlation outcomes overestimates the losses by around 21% compared to experimental results, mainly due to the lack of experimental data near the casings where the highest pressure losses are expected. The used correlations also lack the lean angle dependency that affects end wall losses, as described by Denton & Xu (1998).

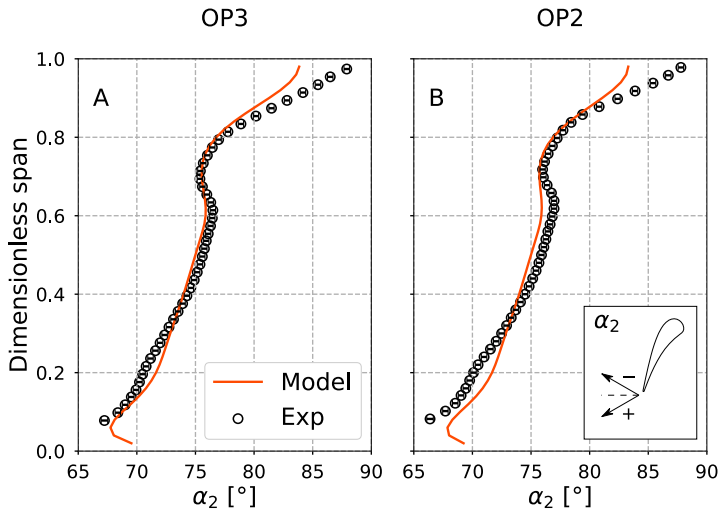

FIGURE 6.1. Experimental and modeled flow angle at plane T2 for the Clean cases.

The described procedure produces a radial distribution of Y_p and Y_s that require further discussions. To not neglect the curvature of the streamlines in a span-wise direction, an area-average of the Y_p on the whole span is assigned to each radial subdomain. Y_s is area-averaged on the whole span and divided into two parts to consider the two loss contributions due to the end walls boundary layer (Y_{BL}) and the secondary kinetic energy loss (Y_{SKE}). This approach follows what suggest by Park & Chung (1992), 88% of Y_s is attributed to Y_{BL}, the remaining portion of 12% to Y_{SKW}. Within the regions of the end walls that are limited by their boundary layer thickness δ, the velocity distribution follows a one-seventh power law $1-(y/\delta)^{(1/7)}$. Therefore, as suggested by Park & Chung (1992), losses can be associated with the velocity deficit and assumed to follow a similar power law, as represented in Eq. 6.7, where y is the span-wise distance from the two walls, thus varies from zero to the half span.

$$Y_{BL} = 0.88Y_s = C_1\left[1-\left(\frac{y}{\delta}\right)^{1/7}\right]^2 \qquad y<\delta \tag{6.7}$$

The losses at other radial positions are influenced by the secondary kinetic energy losses. The Rankine vortex theory suggests that the pressure loss related to a vortex is highest at its core where the velocity gradient is the greatest and the deepest pressure deficit occurs. The principle can be applied to secondary vortices, and their span-wise loss distribution can be expressed as the square of the gradient of the deviation angle, as shown in Eq. 6.8.

$$Y_{SKE} = 0.12Y_s = C_2\nabla\epsilon(y)^2 \qquad \delta<y<0.5h \tag{6.8}$$

The constants C_1 and C_2 can be determined by performing span-wise integrations and reversing Eqs. 6.7 and 6.8. For simplicity, δ_2 is assumed to be equal to δ_1, that is the boundary layer thickness at the stator outlet is the same as the inlet one.

The results of the total pressure loss analysis are presented in Fig. 6.2, which demonstrates that the model accurately predicts the location of the peak secondary losses and the main trends for both the OPs. As previously mentioned, the lack of experimental data in the regions close to the end-walls, particularly the hub region, appears to be the primary reason for the higher predicted area-average losses compared to the measurements.

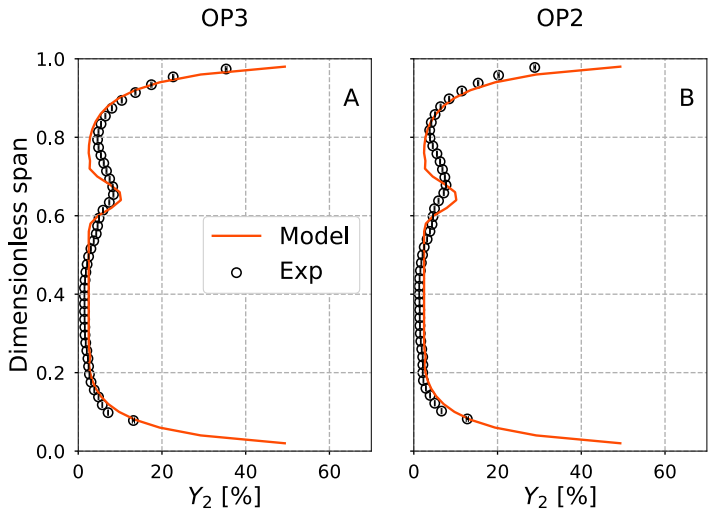

FIGURE 6.2. Experimental and modeled total pressure losses at plane T2 for the Clean cases.

6.1.3 Full reconstruction

To fully characterize the span-wise distribution of flow properties, knowledge of flow angles (section 6.1.1) and pressure losses (6.1.2) downstream the vane row is necessary. At this step of the process, both are known. Solving the radial equilibrium equation, energy equation, equation of state and continuity equation, each flow field quantity is fully characterized for each span-wise position. Few considerations are necessary to simplify the calculation process:

- The total temperature is considered equal to the stator inlet one and remains constant along the blade span.
- The radial equilibrium equation is solved numerically using the mid-span location as the reference point

An iterative loop is then used to obtain the span-wise axial velocity distribution and other flow properties, starting with an initial guess of axial velocity at mid-span. The radial equilibrium equation provides the span-wise distribution of the axial velocity. Using knowledge of flow angles, the absolute velocity is computed and utilized to calculate the other flow quantities exploiting the definition of total pressure losses, total-to-static relationships, and equation of state. The continuity equation is then applied to close the system of equations and provide an updated value for the mid-span axial velocity. This iterative cycle is repeated, recomputing also pressure losses, until convergence on the mass flow is achieved. The model effectiveness in capturing flow quantities is shown in Fig. 6.3 for the axial velocity.

6.2 Flow field reconstruction for perturbed cases

The definition of the *Clean* aerodynamics allows to study the effects of non-uniformities at the stator inlet. This analysis builds upon the procedure outlined in section 6.1 for the uniform inlet case and utilizes its outcomes.

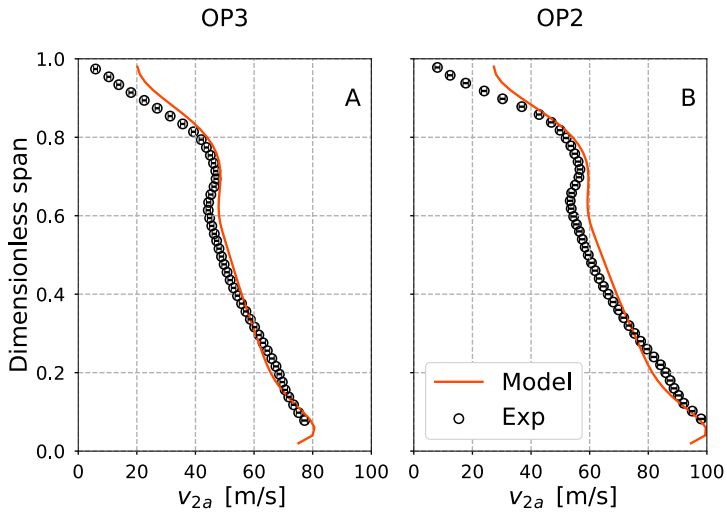

FIGURE 6.3. Experimental and modeled axial velocity at plane T2 for the Clean cases.

The first step is to determine the flow angles at the stator outlet. This information is then used to calculate the total pressure losses, taking into account all possible contributions. Finally, the complete aerodynamics can be reconstructed.

6.2.1 Flow angle

As demonstrated in section 5.1, a residual swirl profile persists at the stator outlet, albeit significantly attenuated compared to its magnitude at the inlet due to acceleration through the vane and interaction with secondary flows.

The model developed to predict the residual swirl profile downstream of the stator is based on the pitch-wise area-average of the tangential velocity at plane T1 calculated on two stator pitches, i.e. combustor simulator periodicity. The model assumes that the inlet swirl profile lies on a plane perpendicular to the stream-wise flow direction at the stator outlet. The transport through the stator stretches and reduces the swirl intensity due to flow acceleration, resulting in a reduction of swirl velocities by a factor equal to the acceleration coefficient K_1 of the Kacker & Okapuu (1982) correlation raised to the power of 0.6, as shown in Eqs. 6.9 and 6.10. This approach assumes that the inlet small non-uniformity in the axial component is fully recovered as a result of acceleration.

As described in section 5.1, the swirl profile changes its radial position depending on the injection position case. Injecting the swirl profile at the leading edge causes the perturbation to climb on the suction side of the blade towards the tip casing, which compensates for the downward movement imposed by the blade lean pressure field, ensuring that the swirl profile does not change its radial position as it progresses through the stator. No corrections are thus applied to the inlet velocity field in this injection case.

In the mid-passage case, the climb does not occur, and the swirl profile is pushed downwards by the lean pressure field. This is accounted for by shifting the radial coordinates of the pitch-wise area-average of the inlet tangential velocity by an amount equal to the axial distance between the stator trailing edge and the T2 plane multiplied by the tangent of the lean angle ($\Delta r = \Delta x_{TE-T2} tan\Theta$).

Drawing on the aforementioned factors, the inlet area-averaged tangential velocity, attenuated by K_1 and properly shifted radially according to the injection position, is decomposed into its tangential and axial components and added to the axial and tangential velocities of the *Clean* case,

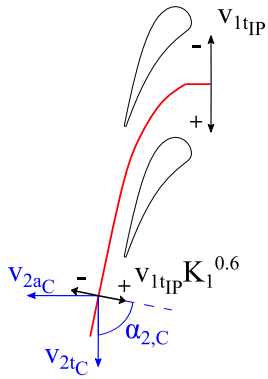

FIGURE 6.4. Schematic of the velocity components.

which are calculated as described in section 6.1.3. The velocities obtained through this process at plane T2 for the perturbed situations (as shown in Eqs. 6.9 and 6.10) are used to determine the flow angle (as expressed in Eq. 6.11). A schematic of the velocity components is shown in Fig. 6.4.

$$\widehat{v_{2t}}_{IP} = \widehat{v_{2t}}_C + \widehat{v_{1t}}_{IP} \, K_1^{0.6} \cos\left(\widehat{\alpha_2}_C\right) \tag{6.9}$$

$$\widehat{v_{2a}}_{IP} = \widehat{v_{2a}}_C - \widehat{v_{1t}}_{IP} \, K_1^{0.6} \sin\left(\widehat{\alpha_2}_C\right) \tag{6.10}$$

$$\widehat{\alpha_2}_{IP} = \arctan\left(\frac{\widehat{v_{2t}}_{IP}}{\widehat{v_{2a}}_{IP}}\right) \tag{6.11}$$

The results of the model for the *10 Hz* MP and LE cases in OP3 and OP2 are presented in Fig. 6.5, which displays the difference between the *10 Hz* and *Clean* cases, that is a picture of the residual swirl at stator outlet. The model exhibits a perfect agreement with the experimental data for the MP OP3 case. However, the upper branch of OP2 shows poor agreement due to the complex interaction with the bottom branch of the TPV, as described in section 5.1, making it challenging to predict accurately. For the LE case, the experimental residual swirl profile is more radially compressed than the calculated one. This is difficult to predict as the swirl profile impinges on the blade LE and its transport through the blade suction side is more intricate than in the MP case. The model correctly predicts the lower intensity of the swirl profile in the LE case in OP2 than OP3 due to the higher acceleration through the vane.

Other injection cases were found to be similar to the *10 Hz* case, as discussed in section 5.1, and hence are not presented in this study.

Although the model needs to consider differences in the development of secondary flows to account for non-zero incidence angles, computations show that these differences are negligible due to the low pitch-wise average incidence angle. However, in cases where the incidence angle is significant, the secondary deviation angle can be determined using the method described in section 6.1.1, which is based on the correlation established by Massardo & Satta (1985).

6.2.2 Pressure losses

The method described in section 6.1.2 allows for the computation of total pressure losses and their radial distribution by defining the flow angle downstream of the stator. The stator incidence angle imposed by the swirl profile impacts the secondary and profile losses of the vane. The incidence angle used in the correlations is computed differently for different injection positions.

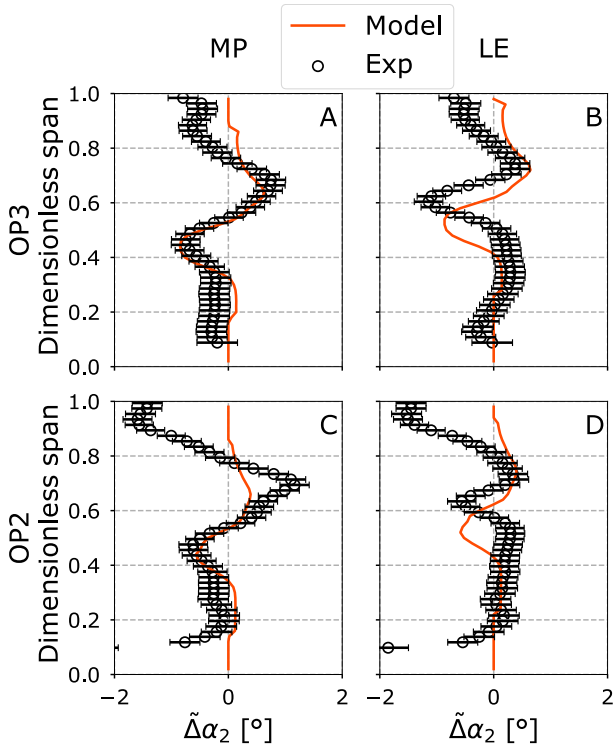

FIGURE 6.5. Experimental and modeled residual swirl at plane T2 for 10 Hz case.

For a passage-aligned combustor disturbance, the incidence angle is determined as the pitch-wise area average on one stator pitch, as shown in Fig. 4.4. For the LE case, a distribution is utilized that represents the local measured swirl angles in the span-wise direction, and it is approximately four times the angles depicted in Fig. 4.4. In both injection cases, one blade passage is affected by the incidence change, while the other remains unaffected and can be considered as the *Clean* case. To calculate the increase of profile losses caused by the combustor-representative disturbance, the Benner *et al.* (1997) correlation is used, while the new secondary losses are estimated using the Benner *et al.* (2005) correlation. After calculating the new profile and secondary pressure losses for each radial subdomain, the results are area-averaged and then distributed radially, following the same procedure as explained for the *Clean* case in section 6.1.2. Finally, the outcome is divided by the stator blades to combustor simulator number ratio, which is two in this study case, to account for the unaffected stator passage.

Another factor that contributes to the losses is the mixing between the swirl profile and the mainstream, referred to as Y_{mix}. This is modeled based on the difference between the kinetic energy coefficients ($\Phi^2 = v_2^2/v_{2,is}^2$) of the uniform inlet and the perturbed one, where the perturbed velocity v_2 is calculated using Eqs. 6.9 and 6.10. Furthermore, the *Clean* isentropic velocity is used in both cases.

The total pressure drop associated with the inlet swirl profile is considered in the calculation of Y_{mix}, where its contribution is estimated as the total pressure loss defined as the second term of Eq.

6.12.

$$
\begin{aligned}
Y_{mix} &= Y(\Phi_C^2 - \Phi_{IP}^2) + \frac{p_{t_1,ref} - p_{t_1,IP}}{p_{t_2,C} - p_{s_2,C}} \\
\Phi_C^2 - \Phi_{IP}^2 &= \frac{v_{2,C}^2}{v_{2,C,is}^2} - \frac{v_{2,IP}^2}{v_{2,C,is}^2}
\end{aligned}
\tag{6.12}
$$

The turbulent component generated by the combustor simulator at the stator inlet is identified as the fourth source of losses. The Reynolds stress tensor is measured for each injection case using a hot-wire to define the turbulent kinetic energy (see section 4.2). The average value of the turbulent kinetic energy in the region of the introduced disturbance (v_{Ti}) is assumed to be fully dissipated at the stator outlet. As a result, the pressure loss coefficient due to the inlet turbulence intensity (Y_{Ti}) is calculated by taking the difference of the kinetic energy coefficient computed on the velocity v_{2_C}-v_{Ti} and the coefficient defined on v_{2_C} (Eq. 6.13).

$$
Y_{Ti} = Y\left(\Phi\left(v_{2_C} - v_{Ti}\right)\right) - Y\left(\Phi\left(v_{2_C}\right)\right) = Y\left(\frac{\left(v_{2_C} - v_{Ti}\right)^2}{v_{2is}^2}\right) - Y\left(\frac{v_{2_C}^2}{v_{2is}^2}\right) \tag{6.13}
$$

To account for the vane blades - combustor simulators ratio, the obtained result is divided by two.

The remaining swirl profile at the stator outlet is negligible, and therefore, the other loss sources are considered to be unaffected.

Figure 6.6 presents the results of the loss breakdown analysis. The figure reveals that the swirl profile mixing losses make a significant contribution to the total losses, taking into account the inlet total pressure loss caused by the swirl profile. The loss attributed to the non-uniform flow at the turbine inlet is lower in OP2 compared to OP3 due to better recovery of flow non-uniformities by the high flow momentum in OP2. In each injection case, secondary and profile losses are higher for the LE case than MP due to a more substantial change in the stator incidence angle. The case with *EWG off* injection exhibits the lowest profile and secondary losses compared to other injection cases, owing to the relatively weaker swirl profile. However, the mixing losses are higher due to the absence of the streak injection, which helps to mitigate total pressure losses at the turbine inlet. Additionally, Reynolds and Mach effects in OP2 cause a reduction in profile and secondary losses. Turbulence losses are slightly lower in OP2 as the inlet turbulence level does not significantly change, while the reference isentropic velocity increases.

The next step involves distributing the total pressure losses obtained to a span-wise distribution. This is done using a method similar to the one outlined in section 6.1.2, along with the implementation of new functions for Y_{Ti} and Y_{mix}. To determine the position with the highest pressure losses at the core of the residual swirl profile, a method similar to the one described for Y_S in section 6.1.2 is used. The two pressure losses are distributed using Eq. 6.14 as a function of the square gradient of $\hat{\Delta}\alpha_2$ (shown in Fig. 6.2.1). The points with a gradient sign opposite to the inlet swirl profile are set to zero.

$$
Y_{T_i} + Y_{mix} = C_3 \nabla \hat{\Delta}\alpha_2 \left(r\right)^2 \tag{6.14}
$$

Figure 6.7 depicts the OP3 and OP2 LE *10 Hz* cases, confirming that the method accurately predicts the experimental data and captures peak positions and main trends. The $\hat{\Delta}Y_2$ model line is obtained by calculating the pressure losses in the *10 Hz* case and subtracting those in the *Clean*, using the method described in this chapter.

Once the pressure loss distribution is known through the method outlined in section 6.1.3, the flow field can be reconstructed completely. However, in cases where EW or HS are involved, it is

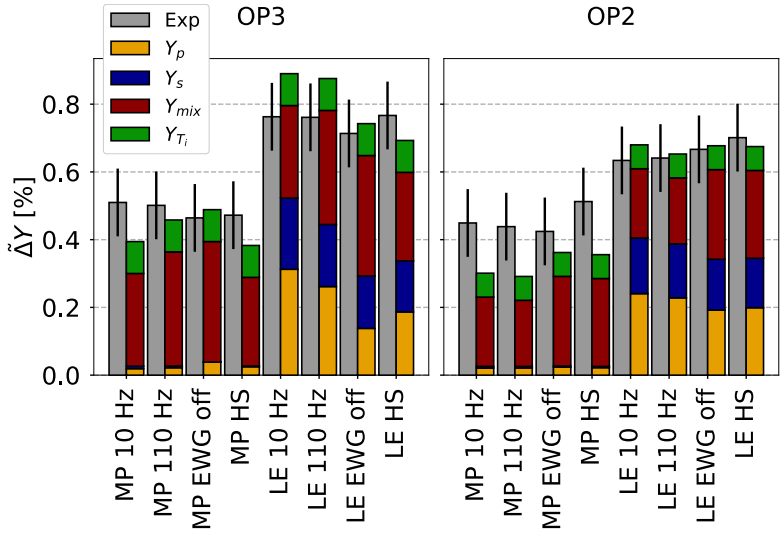

FIGURE 6.6. Losses breakdown downstream of the stator.

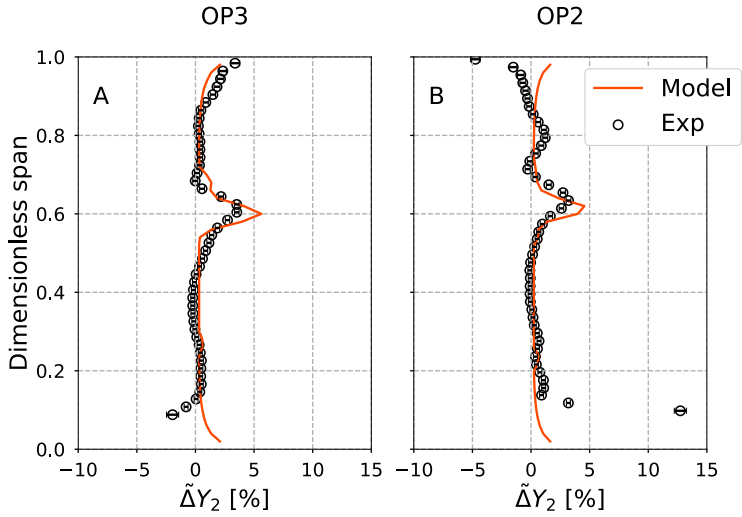

FIGURE 6.7. Experimental and modeled total pressure losses at plane T2 for the LE 10 Hz cases.

not feasible to assume that the total temperature is uniform in the span-wise direction. Nonetheless, the total temperature distribution can be determined by implementing the approach presented in section 6.2.3.

To conclude, the guidelines for applying the aerodynamic model are shown in the flow chart of Fig. 6.8.

6.2.3 Thermal reconstruction

The thermal profile has a negligible effect on stator aerodynamics as discussed in section 5.1, thus simplifying the analysis by decoupling the aerodynamics and thermal analysis. However, this is not

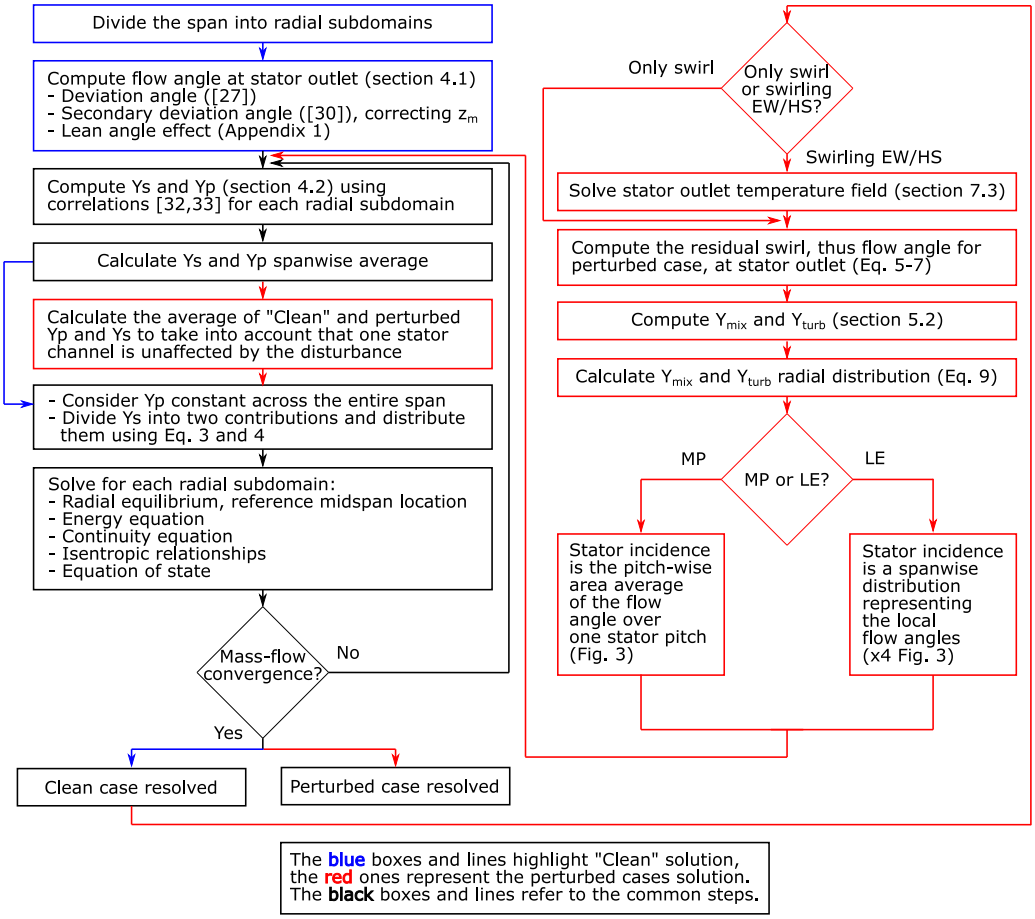

FIGURE 6.8. Flow chart with guidelines for implementing the aerodynamics model.

the case for the rotor, which experiences an increase in incidence angle and the generation of new vorticity (Hawthorne (1951)). Therefore, accurately predicting the thermal flow field at the stator outlet and identifying the position of the temperature disturbance is crucial, as it can significantly affect the rotor aerodynamics and cooling flows.

In this section, an analytical model is proposed to predict the EW/HS evolution through the vanes based on the conservation of thermal power. The model described in this section necessitates two inputs: the maximum peak-to-trough temperature decay (ΔT) between planes T1 and T2 (see section 5.2.1), and the mass flow distribution downstream of the stator for the *Clean* case. This hypothesis simplifies the iterative loops shown in the flow chart of Fig. 6.8, as solving the energy equation is required to determine the mass flow in perturbed cases. The radial total temperature distribution at the stator outlet is determined only at the outset and is not involved in the iterative process.

Furthermore, the model can forecast the displacement of the temperature disturbance in radial and circumferential directions and yield a temperature distribution at plane T2 for the whole sector. While there are some prior attempts to model EW in ducts reported in the literature (e.g. Morgans *et al.* (2013), Giusti *et al.* (2017), Christodoulou *et al.* (2020) and Kaiser *et al.* (2022)), to the best of the author's knowledge, this is the first effort to replicate the downstream evolution of EW

temperature content from a stator blade.

Temperature measurements at the stator outlet for OP2 are not available because the fast-thermocouple is unable to withstand the heavy aerodynamic load downstream of the stator without breaking at this particular operating point.

6.2.4 Displacement of the temperature disturbance

This section details the procedure for predicting the radial and circumferential displacement of the temperature disturbance through the stator. The model is based on the peak temperature position at plane T1.

The peak temperature radial movement is primarily due to the pressure field generated by the blade lean in the channel. In comparison to the MP case, the LE case has a lower downward movement due to the previously discussed swirl-blade interaction. To calculate the radial shifts, Eqs. 6.15 and 6.16 can be used for MP and LE, respectively. These equations correlate the downward movement caused by the blade lean with the tangent of the lean angle.

$$\Delta R_{MP} = (c_x + \Delta x_{TE-T2}) \tan \Theta \tag{6.15}$$

$$\Delta R_{LE} = \Delta x_{TE-T2} \tan \Theta \tag{6.16}$$

To predict the circumferential movement, geometric considerations are taken into account. Specifically, as the temperature disturbance passes through the stator from its leading edge to its trailing edge, it is deflected by an amount equal to the stator vane stagger angle Ψ. Downstream of the stator, the temperature disturbance is assumed to travel in the direction of the blade geometrical angle α_2 from the trailing edge of the vane to plane T2. To calculate the total circumferential displacement, the angles at the center that subtend the chords are computed using the set of equations (Eq. 6.17), with respect to the mid-span radius, based on the geometrical representation shown in Fig. 6.9.

$$\begin{gathered} \Delta\vartheta_{MP} = 2 \arcsin\left(\frac{c_1 + c_2}{2R_m}\right) \\ c_1 = c_x \tan \Psi \quad c_2 = \Delta x_{TE-T2} \tan\ \alpha_{g,2} \end{gathered} \tag{6.17}$$

The LE injection case involves the disturbance impinging on the blade, causing it to climb towards the blade suction side. During this process, there is a tangential shift of almost half the leading edge diameter that needs to be considered, which is achieved by subtracting the displacement c_3 (Eq. 6.18) from c_1 and c_2 (Eq. 6.17).

$$\begin{gathered} \Delta\vartheta_{LE} = 2 \arcsin\left(\frac{c_1 + c_2 - c_3}{2R_m}\right) \\ c_3 = \frac{D_{LE}}{2} \end{gathered} \tag{6.18}$$

6.2.5 Solution of the thermal field

The full solution of the thermal flow field at plane T2 can be obtained by utilizing the decay rate discussed in section 5.2.1 and the temperature disturbance displacements discussed in section 6.2.4. With this information, it is possible to determine the location and maximum value of the

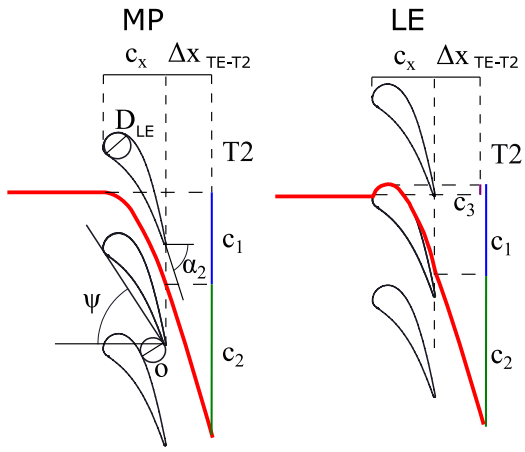

FIGURE 6.9. Schematic of the temperature disturbance transport in circumferential direction through the stator.

peak-to-trough temperature disturbance at plane T2, given the magnitude and location of the inlet perturbation $\Delta T_{max,T1}$. The thermal reconstruction neglects the heat transfer with the stator vanes, as the residence time is too low, and relies on the conservation of the thermal power between planes T1 and T2.

To obtain an initial estimate of the outlet temperature distribution on a plane perpendicular to the streamwise direction, a Gaussian shape is assumed for the temperature spatial distribution and the *Clean* mass flow distribution is used to solve the power balance. The outcomes of the power balance are the radial ($sigma_r$) and tangential ($sigma_t$) standard deviations of the temperature Gaussian distribution, which are assumed equal at this stage. However, this method results in a distribution that is too elongated in the tangential direction and not physically representative, as $sigma_t$ is higher than the throat dimension and does not account for the contraction of streamlines into the channel due to the acceleration in the vane channel. A better approximation is to calculate $sigma_t$ as the minimum value between the computed $sigma_t$ from the power balance and a value based on the throat dimension (Eq. 6.19).

$$\sigma_t = \min\left\{\frac{\sigma_t}{\cos\left(\alpha_{g,2}\right)}, \frac{o}{2\cos\left(\alpha_{g,2}\right)}\right\} \tag{6.19}$$

To account for approximately 95% of the data, the second term of Eq. 6.19 is halved. The Gaussian distribution, initially defined in a plane perpendicular to the stream-wise direction, is divided by $\cos\left(\alpha_{g,2}\right)$ to project it onto the tangential direction.

After adjusting the tangential standard deviation of the Gaussian distribution using Eq. 6.19, the power balance is re-evaluated to obtain an updated value for the radial standard deviation (σ_r). This calculation takes into account that about 10% of the inlet power is dissipated to other regions of the flow field, including secondary flows and wakes, as evidenced by the measurement campaign described in section 5.2 and depicted in Fig. 6.10 using colored contours.

Figure 6.10 shows the outcomes of the proposed model as line contour along with the experimental data represented by colored contours. The figure includes both injection positions and both EW cases. The model achieves a good agreement with the experimental data for each case, accurately capturing the shape, radial-circumferential extensions, and peak intensity magnitude. This result highlights the dominant effect of streamline contraction in the vane throat on the injected temperature disturbance at plane T2, which is constrained in the pitch-wise direction and extends

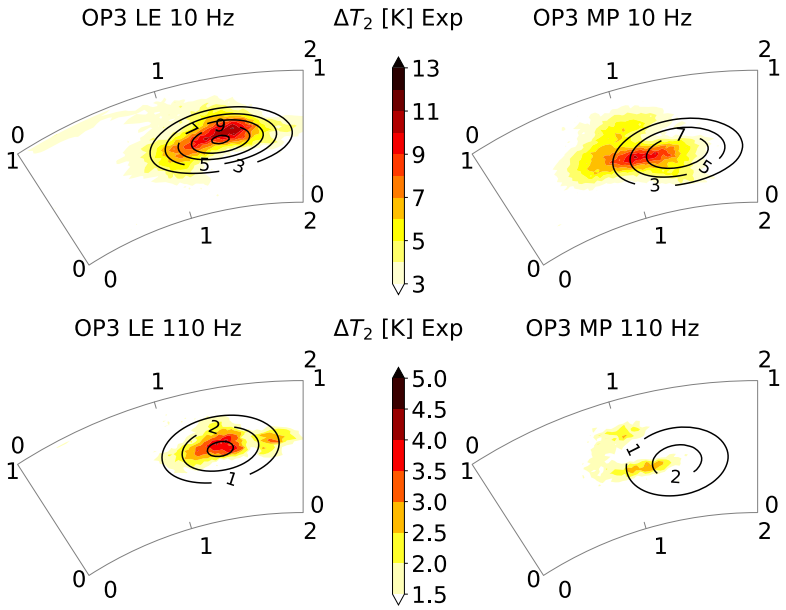

FIGURE 6.10. Peak-to-trough temperature values at plane T2 for OP3 EW cases. Colored contours are the experimental data, line contours are the model results.

in the radial direction. The predicted position is accurately matched for the LE cases, while a small mismatch in the circumferential position is observed for the MP cases, which is considered acceptable given the model simplicity.

The proposed model is utilized to forecast the development of swirling HS, by calculating the maximum temperature variation, ΔT_{max}, as the maximum difference between the grid measured total temperature and the mainstream undisturbed value. The results obtained from applying the model described in this section are presented in Fig. 6.11, where the same features seen in Fig. 6.10 hold also for the HS case. Furthermore, the decay rate derived from the experimental data closely aligns with the decay rate for the HS case, which was not utilized in the determination of the decay rate, providing additional support for the efficacy of the approach at low frequencies.

In terms of maximum peak-to-trough values with respect to the mainstream, the HS case has a value of approximately 9 K for LE and 7 K for MP. These values are lower than the *10 Hz* case, but are consistent with the trends and discussion at plane T1, as shown in Fig. 4.5.

As anticipated in section 5.2, these findings confirm that the HS case shares similarities with the EW cases regarding their maximum temperature and shapes. As a result, it is reasonable to consider swirling EW cases as a sequence of swirling HS cases, similar to the approach taken by Gaetani & Persico (2019) for non-swirling flows.

6.3 Impact of cooling flows

The lack of blade vane cooling necessitates a discussion on the potential influence of cooling flows on the aero-thermal flow field of the blade and the corresponding models presented in this chapter.

Blade cooling can affect the temperature decay downstream of the stator, especially in the LE case where hot-spot and cooling flows interact significantly. Although film cooling can cause additional losses, it has a negligible impact on the velocity field downstream of the vane, according to Jenkins & Bogard (2009). Dorney (1997) also observed that the hot streak temperature has

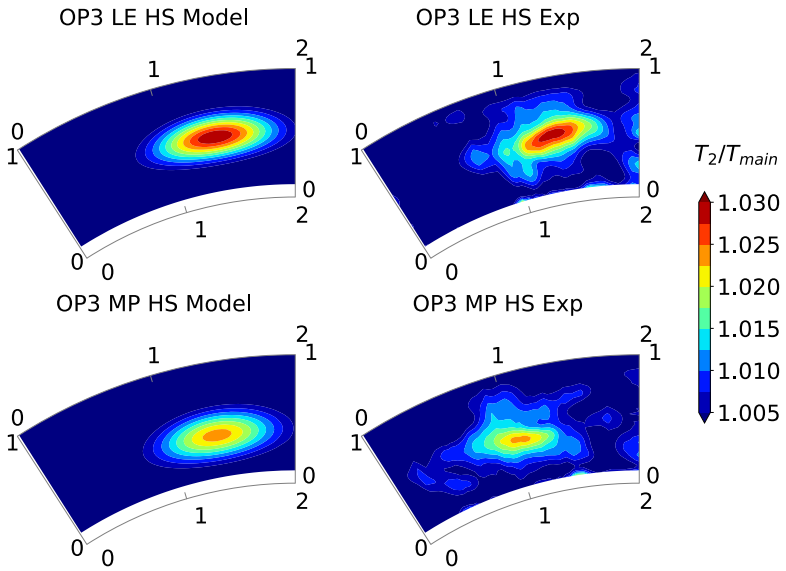

FIGURE 6.11. Non-dimensional mean total temperature at plane T2 for OP3 HS cases. First columns shows the prediction, the second the experiments.

little effect on the downstream velocity magnitude but can alter the flow direction in the rotating frame of reference. This aspect could be impacted by the HS/EW average temperature attenuation due to coolant flows. Furthermore, in the MP case, film cooling on the stator may increase the flow temperature non-uniformities, reducing the blade wake temperature but with little effect on the HS/EW region. On the other hand, in the LE injection, coolant flows decrease the HS/EW temperature, leading to a more uniform temperature at the stator outlet and closer to *Clean* conditions for the rotor.

However, since secondary flows and swirl profile interaction already significantly attenuate the HS/EW temperature at the stator outlet, cooling flows are not expected to affect the rotor aerodynamics significantly. Nevertheless, the superposition method described by Jenkins & Bogard (2009) can be used to estimate the additional temperature decay due to blade cooling flows by applying it to the temperature distribution obtained from the model described in section 6.2.3. The method presented in this thesis is applicable since Jenkins & Bogard (2009) results suggest that film cooling does not significantly affect the displacement of HS/EW.

6.4 Concluding remarks and key findings

This chapter introduces a methodology for predicting and assessing the effects of swirling temperature disturbances, characteristic of the flow field released by a real combustor, on an axial turbine stage.

The methodology presented in this paper utilizes both geometrical data of the turbine and data collected downstream of the combustor simulator to determine the stage inlet conditions required for predicting the transport of EW/HS. This allows for the accurate prediction of the impact of combustor non-uniformities on the turbine, serving as a valuable tool in the design process and helping to reduce the risk of hot spots arising from the combustor. Notably, the model has been validated and can be extended to accommodate any input disturbance and turbine geometry.

To predict the stator outlet flow field, the methodology employs correlations available in the

open literature for axial turbines and some of the experimental observations. The effects of lean geometry are modeled by developing a new correlation based on data available in the literature. This results in a good match with experimental data for both uniform and perturbed inlet conditions.

Furthermore, a model is developed to predict the temperature flow field downstream of the stator when swirling EW or HS are injected at the stage inlet. The model requires only the inlet temperature disturbance distribution and the mass flow distribution of the *Clean* case at plane T2. Using geometrical considerations and power balances, the model determines with good accuracy the location and the circumferential-radial extension of the temperature disturbance. The decay rate of the maximum peak-to-trough through the stator, which is tuned based on experiments for different inlet circumferential positions of the disturbance, is employed to predict the transport and attenuation of the temperature disturbance.

Finally, this chapter compares the impact of swirling EW and HS cases on the thermal flow field of the turbine stage and confirms that EW can be approximated as a series of swirling HS.

CHAPTER 7

FLOW FIELD CHARACTERIZATION AT PLANE T3

This chapter presents the impact of residual non-uniformities on the rotor aero-thermal flow field. The study covers all the operating conditions and the injection cases, with a particular focus on the MP and LE injection positions. Although developing simplified models to predict the aero-thermal flow field is a challenging task that is not pursued, the chapter does propose a model to predict the decay and circumferential movement of the temperature disturbance through the rotor.

Some contents of this chapter are also discussed in:

Notaristefano, A., Gaetani, P., (2022), Impact of Swirling Entropy Waves on a High Pressure Turbine, *ASME Journal of Turbomachinery*, vol. 144(3): 031010, doi:10.1115/1.4052353

Pinelli, L., Marconcini, M., Pacciani, R., Notaristefano, A., and Gaetani, P., (2023), The Effects of Swirling Flows in Entropy Wave Convection Through High-Pressure Turbine Stage, *ASME Journal of Turbomachinery*, vol. 145(3): 031004, doi:10.1115/1.4055613

Notaristefano, A., Gaetani, P., (2023), The Role of Turbine Operating Conditions on Combustor–Turbine Interaction—Part I: Change in Expansion Ratio, *ASME Journal of Turbomachinery*, vol. 145(5): 051001, doi:10.1115/1.4055642

Notaristefano, A., Gaetani, P., (2023), The Role of Turbine Operating Conditions on Combustor–Turbine Interaction—Part II: Change in Expansion Ratio, *ASME Journal of Turbomachinery*, vol. 145(5): 051002, doi:10.1115/1.4055643

Notaristefano, A., Gaetani, P., (2023), Modelling of Combustor Non-Uniformities Evolution through a High-Pressure Turbine Stage, *ASME Turbo Expo 2023*, GT2023-102601, Boston, Massachusetts, United States

Pinelli, L., Giannini, G., Marconcini, M., Pacciani, R., Notaristefano, A., and Gaetani, P., (2023), The Impact of the Off-Design Conditions on the Entropy Wave Interaction with a High-Pressure Turbine Stage, *ASME Turbo Expo 2023*, GT2023-102837, Boston, Massachusetts, United States

7.1 Mean phase-average aerodynamic flow field

Considering the several tested cases, the analysis of the measurements at the rotor outlet is limited to the injection cases MP and LE, which are assumed to be the most representative, as PS and SS are considered intermediate cases.

Measurements downstream of the rotor are obtained using the FRAPP described in section 3.3 and phase-averaging its measurements on the blade passing frequencies.

The analysis is divided into two sections: firstly, the results for the *Clean* case are discussed to understand the main features of the rotor aerodynamics; and secondly, the impact of the residual perturbations at the stator outlet is studied. Within each section, the analysis is further divided based on the effect of a different rotor loading or expansion ratio.

7.1.1 Clean

7.1.1.1 Different expansion ratio

OP2 and OP3 exhibit differences in terms of both expansion ratios and rotor rotational speeds. The description of the aerodynamic flow field is based on the analysis of the deviation angle and the relative total pressure coefficient, defined as 7.1. In this equation, $p_{t,r3}$ represents the absolute and relative total pressure, p_{amb} is the ambient pressure, and $p_{t_1,ref}$ is the mean total pressure at stage inlet. The deviation angle δ is computed as the difference between the measured relative flow angle and the blade geometrical angle of -67.7°.

$$C_{p_{t,r}} = \frac{p_{t,r_3} - p_{amb}}{p_{t_1,ref} - p_{amb}} \tag{7.1}$$

The deviation angle between the two uniform cases (frames C and D of Fig. 7.1) is quite similar, and the Rankine vortex model can be used to identify the secondary structures. These structures include the tip clearance vortex (TCV), the tip passage vortex (TPV), and the hub passage vortex (HPV). The TCV is the dominant structure that generates the highest amount of losses in the region close to the tip casing (lowest $C_{p_{t,r}}$ in Fig. 7.1). In OP2, both the upper and lower branches of the TCV have higher and wider absolute deviations than in OP3. This result is consistent with the higher loading on the blade tip for OP2, and the TCV is the only structure magnified in this case.

Regarding pressure losses, in OP2 they reduce and the wake region is less extended (as shown in Fig. 7.1), which is consistent with the higher Reynolds number and lower total pressure losses measured at plane T2 in section 5.1. Moreover, in OP2, the higher rotational speed centrifuges the boundary layer, thereby weakening the wake and secondary flow structures.

7.1.1.2 Different loading

One important point to note is that OP3, OP3L, and OP3U have different rotational speeds. OP3 represents the reference design condition, OP3L operates at a lower rotational speed resulting in a higher rotor incidence angle, and OP3U operates at a lower incidence angle achieved by reducing the rotational speed.

Figures 7.2 and 7.3 show the flow field downstream of the stator in the absolute and relative frame of reference, respectively. Colored contour plots represent the angles, while labeled contour lines depict pressure coefficient. The sign conventions for angles are displayed in both figures. The absolute and relative total pressure coefficients, C_{p_t} and $C_{p_{t,r}}$, are calculated using Eqs. 7.2 and 7.1, respectively. In these equations, p_{t_3} and $p_{t,r3}$ represent the absolute and relative total pressure,

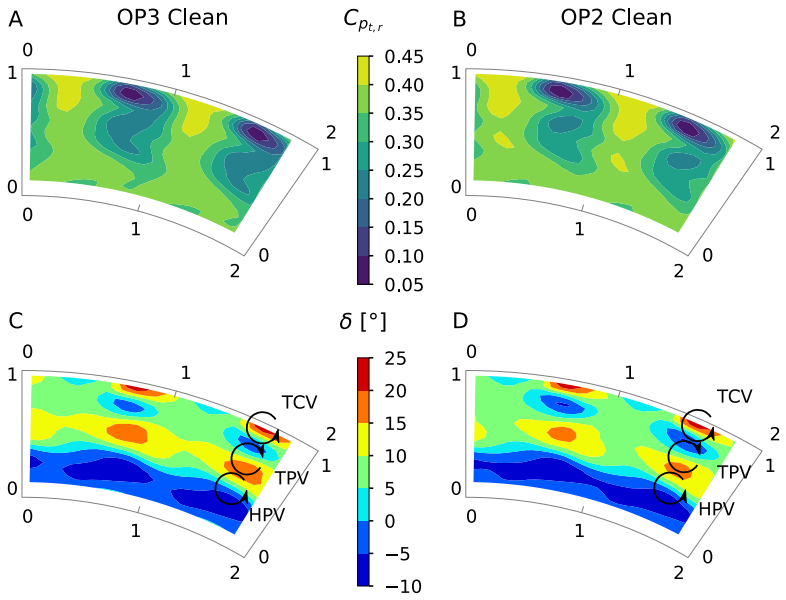

FIGURE 7.1. Relative total pressure coefficient (A-B) and relative flow angle (C-D) at plane T3 for (A-B) OP3 and (C-D) OP2.

$pamb$ is the ambient pressure, and $p_{t_1,ref}$ is the mean total pressure at stage inlet.

$$C_{p,t} = \frac{p_{t_3} - p_{amb}}{p_{t_1,ref} - p_{amb}} \tag{7.2}$$

The total pressure coefficient $C_{p_{t,r}}$ indicates losses in the rotor, while the deviation angle δ reveals the pattern of secondary flows using the Rankine vortex theory, as shown in Fig. 7.1. The good match between experiments and CFD in Fig. 7.2 further validates the numerical methods.

By examining the absolute flow angle and total pressure coefficient together, the blade performance can be understood. The blade work exchange varies along the span and is analyzed with respect to OP3 (frame B of Figs. 7.2). At the tip and mid-span, the positive α_3 and high total pressure coefficient indicate a region of low work extraction. At 80% of the blade span, the tip clearance vortex (TCV) creates a dissipative area characterized by a large absolute angle and low C_{p_t}. Lastly, at the hub, the negative α_3 and low C_{p_t} signify a region of high work extraction. The lack of periodicity in the circumferential direction is due to the presence of the stator wake avenue.

The differences between the three OPs are mainly dominated by changes in incidence angle and rotational speed. In OP3U, the rotor is unloaded due to the negative incidence angle, and the flow is less turned compared to OP3. This results in positive flow angles downstream of the rotor, as the blade velocity is high (Fig. 7.2 A). Additionally, the high blade velocity compensates for the reduction in work caused by the low blade load and flow deflection. To better interpret the work exchange, the Euler work definition (Eq. 7.3) is employed, where u is the mean peripheral velocity (constant in axial machines), and v_{3t} and v_{2t} are the absolute mean tangential velocities at planes T3 and T2, respectively.

$$|l| = u\,|v_{2t} - v_{3t}| \tag{7.3}$$

The minor change in the reaction degree has a negligible effect on v_{2t} in the OPs, while the absolute tangential velocity at plane T3 is close to zero in OP3, positive and larger in OP3U. Although the positive v_{3t} in OP3U decreases the work extraction, the larger rotational speed leads

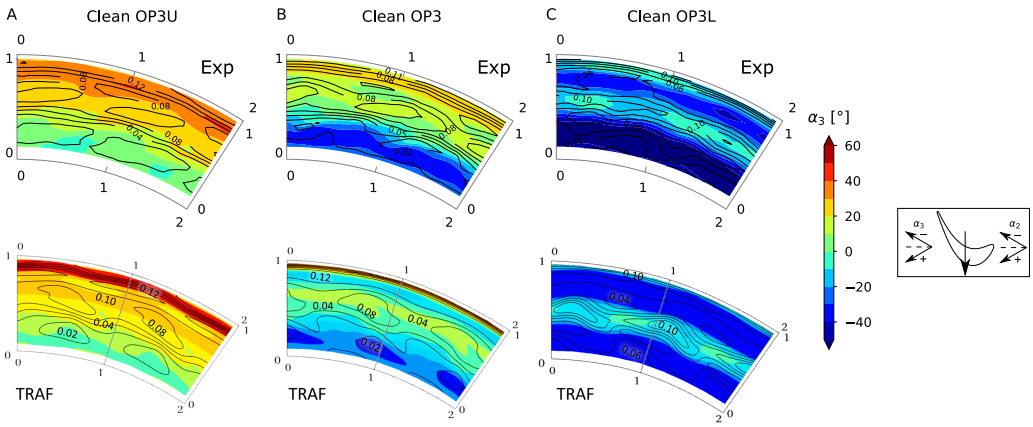

FIGURE 7.2. Absolute flow angle contour at plane T3 for (A) OP3U, (B) OP3 and (C) OP3L Clean cases. The line contours are the absolute total pressure coefficient c_{p_t}. First row experimental results, second row numerical results.

to comparable work extraction. However, the lower blade loading in OP3U reduces the strength of secondary flows, resulting in the least developed wake and lowest deviation angles compared to the other OPs, as shown in Fig. 7.3 A. In contrast, in OP3L, the higher incidence due to the heavily loaded blade results in stronger secondary vortexes. Furthermore, since the mass flow rates are similar for all three operating points, a significant decrease (increase) of the rotational speed brings to a decrease (increase) in the absolute angles at the rotor outlet for OP3L (OP3U) compared to OP3, as shown in Fig. 7.2 C (A). Despite v_{3t} potentially increasing the work extraction according to Eq. 7.3, the lower rotational speed and higher losses in OP3L result in the lowest work extraction. Furthermore, secondary structures become stronger in OP3L, with higher deviation and a more extensive loss region compared to the other OPs (Fig. 7.3). It is worth noting that the relative total pressure coefficient magnitude can be misleading for comparing the three OPs since the relative total pressure at the stator inlet varies. Due to the change in reaction degree, static pressure increases from OP3L to OP3U, resulting in the highest (lowest) Mach number in OP3L (OP3U). However, the higher the rotational speed at plane T2, the lower the relative flow velocity, leading to a lower relative Mach number dominant effect. As a result, the relative total pressure is highest in OP3L and lowest in OP3U at the rotor inlet. To compare the pressure losses, it is more meaningful to look at the reduction of $C_{p_{t,r}}$ across the rotor. After averaging the mass flow over the measuring grids upstream and downstream of the rotor, $C_{p_{t,r}}$ reveals a 42% reduction in OP3U, a 43% reduction in OP3, and a 50% reduction in OP3L, consistent with the earlier discussion of increased pressure losses caused by blade loading.

A discussion of the total temperature measurements, shown in Fig. 7.4 for measurements at the first row and CFD at the second row, would enhance the assessment of the stage working rate for the three OPs. Since the inlet temperature field is identical for all three OPs, the observed downstream temperature differences can be attributed only to varying work extraction. The temperature contours confirm the previously introduced blade working features, with the region of highest work extraction located at the hub where the lowest temperatures are measured/predicted, and the lowest work exchange at mid-span due to a severe underturning region. OP3L generally has the highest temperature as it extracts the least work. The temperature pattern for OP3L is similar to that of OP3, with the exception of the tip region where the experimental data of OP3L have the lowest temperatures among the three OPs. This could be related to the impact of secondary flows

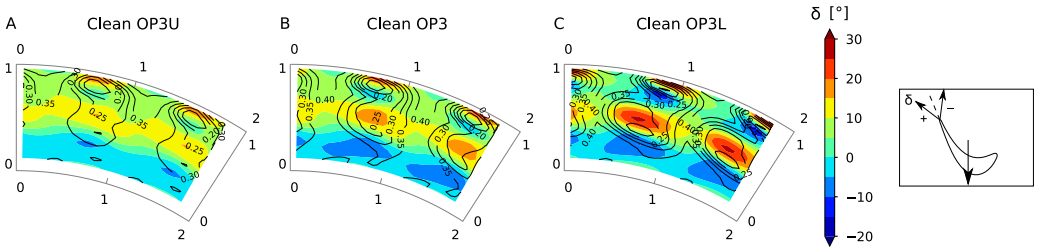

FIGURE 7.3. Relative flow angle contour in the relative frame of reference at plane T3 for (A) OP3U, (B) OP3 and (C) OP3L Clean cases. The line contours are the relative total pressure coefficient c_{p_t}, obtained through a phase-average procedure.

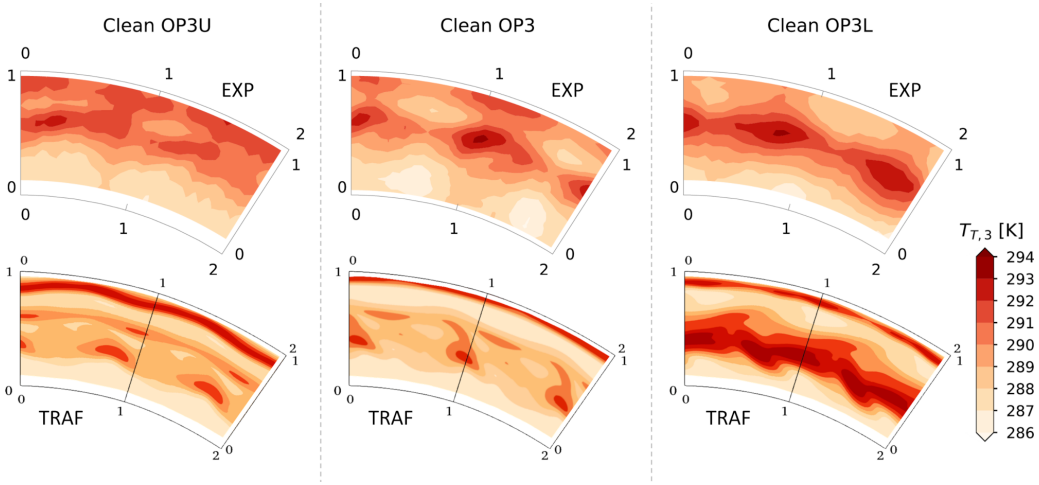

FIGURE 7.4. Total temperature contour at plane T3 for, moving from left to right column, OP3U, OP3 and OP3L Clean cases. First row experimental results, second row numerical results.

on flow mixing and temperature modification, being in OP3L the strongest. This trend is partially confirmed by CFD.

OP3U has the highest temperature at the top casing despite the highest peripheral velocity at the tip region. This is due to severe negative incidence at the tip that stalls the blade (Fig. 2.3), with the Craig & Cox (1970) correlation estimating the negative stalling incidence at approximately -40°, as measured at the tip. In other regions, the results are consistent with OP3 having the highest work extraction and the lowest average temperature, as also confirmed by the turbine torque meter measurements. Finally, OP3U exhibits a more uniform total temperature contour than the other cases, indicating that secondary structures are less developed in this OP.

7.1.2 Perturbed cases

Detailed study of perturbed cases is facilitated by the understanding of the uniform inlet case flow field at the rotor outlet, described in section 7.1.1.

7.1.2.1 Different expansion ratio

The impact of residual combustor non-uniformities on the rotor aerodynamics is addressed looking at span-wise mass-average of absolute flow angle, deviation angle and relative total pressure

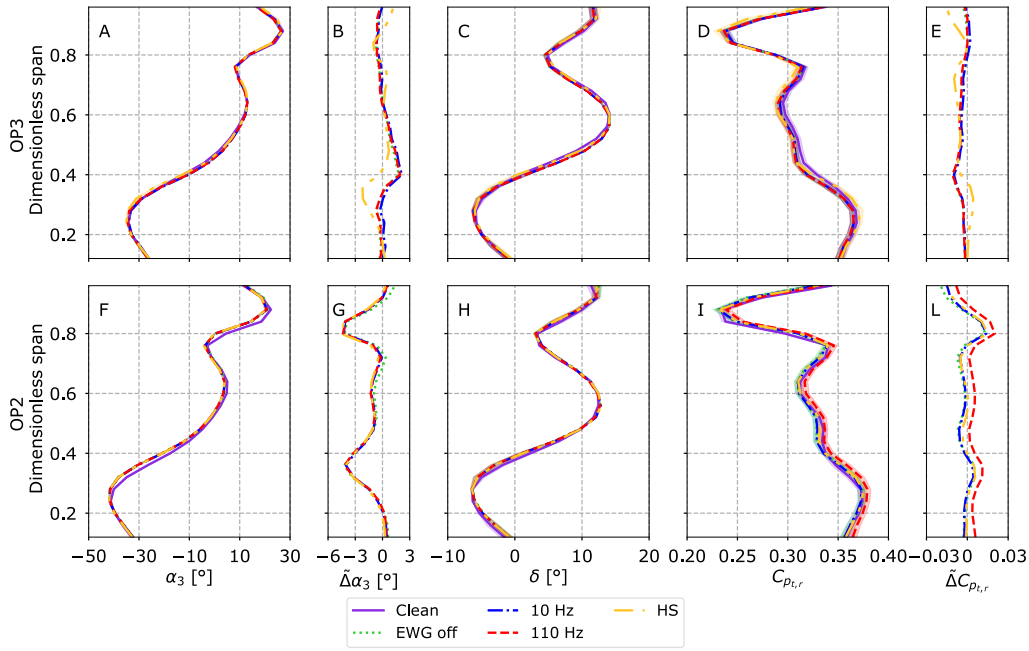

FIGURE 7.5. Circumferential mass-averaged aerodynamic flow field at plane T3 for OP3 (first row) and OP2 (second row) LE injection cases. From left to right: absolute flow angle, flow angle difference between perturbed and Clean cases, deviation angle, relative total pressure coefficient, and relative total pressure coefficient difference between perturbed and Clean cases.

coefficient, shown in Fig. 7.5. Furthermore, the difference between perturbed and uniform cases is shown in the $\widetilde{\Delta}$ plots. To enhance the discussion of this topic, Fig. 7.6 displays the difference between the absolute value of the deviation in the MP and LE *10 Hz* injection cases and the absolute value of the uniform inlet. A positive $\widetilde{\Delta}$ indicates that secondary structures are amplified in the swirling EW cases. The contour lines report the deviation angle of the *Clean* case shown in Fig. 7.1 to highlight the region of secondary flows.

The aerodynamics downstream of the rotor are not considerably affected by the injection position, as revealed by Fig. 7.5. The discrepancies are marginally larger in the MP case than in the LE case, in line with the residual swirl profile observed at plane T2 (see section 5.1).

Focusing on the impact of perturbed injection cases on secondary flows structures, in OP3 the HPV becomes stronger, leading to an increase in angles (Fig. 7.5 A and B) and a decrease in relative total pressure coefficient (Fig. 7.5 D and E) at 40% of the span, compared to the *Clean* case. Figures 7.6 A and B illustrate an enhancement in the deviation angle on both upper and lower branches of the HPV, as well as the TPV (positive $\widetilde{\Delta\delta}$), as a consequence of the interaction between the secondary structures and the swirl profile. The majority of the differences for OP3 in Fig. 7.6 A and B lies below 60% of the span, which is the region of the highest $C_{p_{t,r}}$ reduction (Fig. 7.5 D and E). This result is consistent with the change in rotor incidence due to the residual swirl at the rotor inlet. The TCV is not affected by the injected disturbances as it remains the strongest secondary structure. The mass-average relative total pressure coefficient is not altered in the tip region, see Fig. 7.5 E, as well as the deviation angle shown in Fig. 7.6 A and B.

In OP2, the injected disturbance weakens the HPV, resulting in a lower relative total pressure loss at 35% of the span compared to the *Clean* case (Fig. 7.5 I and L). As a result, the lower branch of the HPV has a negative $\widetilde{\Delta\delta}$ (Fig. 7.6 C and D). The TCV is slightly reduced compared to the

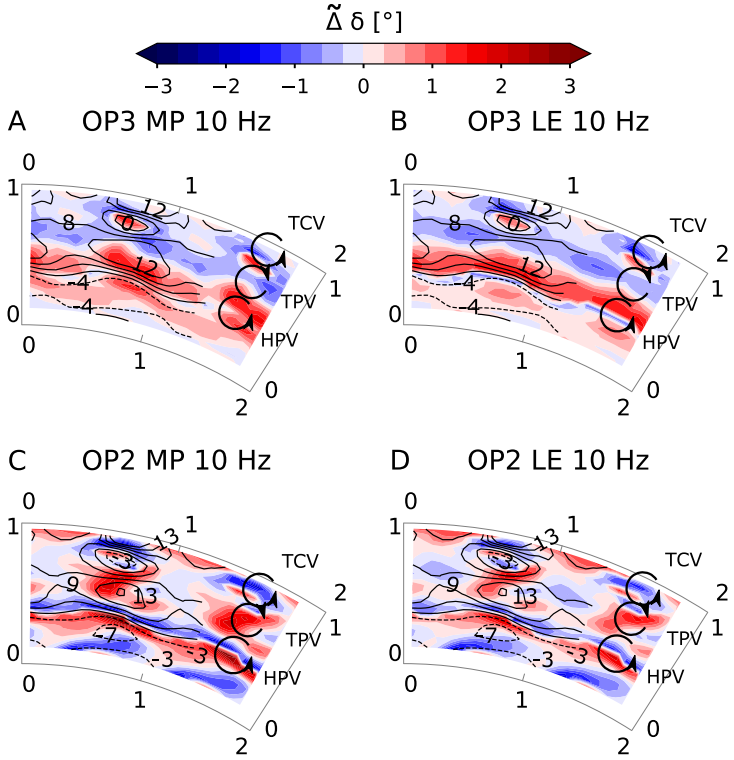

FIGURE 7.6. Deviation angle difference between perturbed and Clean cases at plane T3 for OP3 (first row) and OP2 (second row) MP (first column) and LE (second column) 10 Hz cases. Line contours are the mean phase-average deviation of the Clean case.

Clean case due to its interaction with the swirling EW. In the TCV region, $\widetilde{\Delta\delta}$ is negative (Fig. 7.6 C and D), and $\widetilde{\Delta C}_{p_{t,r}}$ is higher at 80% of the span for the perturbed cases than the *Clean* case (Fig. 7.5 I and L). Although the perturbed injections reduce the TCV intensity compared to the *Clean* case, TCV strength is still higher in OP2 non-uniform inlet cases than in OP3 cases, as shown in Fig. 7.5.

The observed changes in both OPs can be attributed to the swirl profile, as there are negligible differences between the *EWG off* and swirling EW/HS cases. However, there is one exception where the $\widetilde{\Delta C}_{p_{t,r}}$ of the OP2 *110 Hz* case shows a difference from the other injection cases, which may be due to measurement uncertainty (shown as shadow bands in Fig. 7.5 I).

To conclude the section on the impact of combustor non-uniformities on rotor aerodynamics, the residual swirl at the rotor outlet is analyzed using the angle α_3, which can serve as an inlet feature for the following stage. The upper branch of the swirl profile has a positive value, while the lower branch is negative, based on the imposed swirl profile and sign convention used at the rotor outlet. However, as shown in Fig. 7.5 B and G, this structure is not detectable at T3, indicating that the swirl profile is lost at this point. Nevertheless, the swirl still interacts with the rotor secondary structures, altering the rotor incidence and modifying α_3 at 20% and 80% in OP2 (Fig. 7.5 G) and at 40% in OP3 (Fig. 7.5 B).

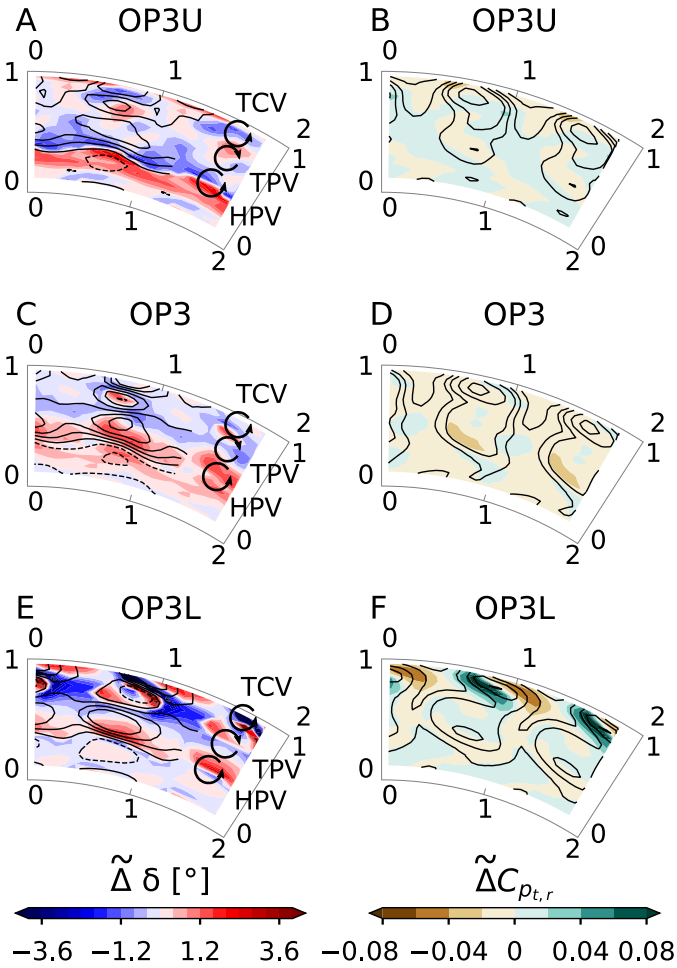

FIGURE 7.7. Deviation angle (first column) and relative total pressure coefficient (second column) difference between perturbed and Clean cases at plane T3 for OP3U (first row), OP3 (second row) and OP3L (third row) MP 10 Hz cases. Contour lines are the Clean values shown in Fig. 7.3.

7.1.2.2 Different loading

A useful method to investigate the influence of flow perturbations on the rotor aerodynamics, as demonstrated in section 7.1.2.1, is to visualize the difference in flow quantities between the perturbed cases and the *Clean* through contour plots. Contour plots of the deviation angle and relative total pressure coefficient, showing the differences between the OP3U, OP3, and OP3L LE *10 Hz* perturbed cases and the *Clean* case, are presented in Fig. 7.7. The contour lines represent the mean values of the *Clean* case and aid in identifying secondary structures and the blade wake. To improve the plot readability, the label values, which were already presented and discussed in Fig. 7.3, are omitted. The MP *10 Hz* case is used as a reference, as the other injection cases and positions do not exhibit significant differences, as it will be discussed in next analysis.

To summarize the discussion of section 7.1.2.1, any change in the incidence angle of OP3 leads to a decline in blade performance, being the design OP. Therefore, the perturbed cases exhibit higher losses across the entire sector in comparison to the *Clean* case, indicated by the negative $\widetilde{\Delta C}_{p_{t,r}}$ in Fig. 7.7 D. The injection of the swirl profile mainly strengthens the HPV and, to a lesser

extent, the TPV, while the TCV remains unaffected and is the most significant secondary structure. The most negative $\widetilde{\Delta C}_{p_{t,r}}$ at the bottom of the wake confirms the magnified HPV in OP3 (Fig. 7.7 D).

To fully comprehend the discussion, the effect of the residual swirl on the rotor blade in OP3L and OP3U is reminded:

- **OP3L** The secondary flows dominate the aerodynamics. In this highly loaded condition, even small changes in the rotor incidence angle can significantly affect the blade operation and secondary flow generation. The swirl incidence plots at the rotor inlet (Fig. 5.12) revealed three distinct regions:
  1. Near the top casing, a low incidence region is generated due to the reduced magnitude of the stator TPV and residual velocity deficit of the injector stem wake.
  2. The swirl profile upper branch further increases the rotor incidence angle above mid-span.
  3. The swirl profile lower branch reduces the rotor incidence angle, unloading the region.
- **OP3U** The upper branch of the swirl profile leads to an increase in the rotor incidence angle, causing a load on a portion of the blade that was previously unloaded in the *Clean* case (Fig. 2.3).

The injection of the swirl profile leads to the creation of an overturning region at approximately 30% of the span, as indicated by the positive values in Fig. 7.7 A, C, and E, which is consistent with the residual swirl profile bottom branch at stator outlet. This overturning is most intense in OP3U and least intense in OP3L, where the secondary structures dominate the aerodynamic flow field. In OP3L, the overturning is only present in the HPV region, which is strengthened in each OP by the injected disturbance. Moreover, in these regions close to the hub, the negative $\widetilde{\Delta C}_{p_{t,r}}$ means that the *Clean* case has a higher $C_{p_{t,r}}$ than the *10 Hz* case, indicating lower losses. It is worth noting that this observation is valid for all OPs.

Off-design conditions can lead to unique features. In OP3L, the perturbed cases result in a lower rotor incidence near the top casing than the *Clean* case, as shown in Fig. 5.12. This feature has been attributed to both the injector stem wake and the reduced strength of the stator TPV due to its interaction with the swirl profile. Consequently, the magnitude of the rotor TCV weakens, leading to a large negative $\widetilde{\Delta\delta}$ in the TCV region (Fig. 7.7 E). Furthermore, in the *10 Hz* case, due to the TCV lower strength, this clearance vortex is located at a higher span position compared to the uniform inlet condition. This displacement causes a positive $\widetilde{\Delta C}_{p_{t,r}}$ at 85% of the span where the TCV is located in the *Clean* case, while at 90% of the span, where the TCV moved in the perturbed case, the $\widetilde{\Delta C}_{p_{t,r}}$ is negative. As for the OP3L, the increase of mean positive incidence at 75% span strengthens the TPV, leading to an increase in deviation angle and a positive $\widetilde{\Delta\delta}$ core in Fig. 7.7 E. This change in TPV leads to a corresponding decrease in $C_{p_{t,r}}$ in the perturbed case, resulting in a negative $\widetilde{\Delta C}_{p_{t,r}}$. Finally, the lower branch of the swirl profile in OP3L reduces the rotor incidence angle in the mid-span region (Fig. 5.12 F), resulting in mainly positive $\widetilde{\Delta C}_{p_{t,r}}$ below mid-span in Fig. 7.7 F.

Another unique feature regards OP3U, where the TCV is weakened as shown by the negative $\widetilde{\Delta\delta}$ value in Fig. 7.7 A and mainly positive $\widetilde{\Delta C}_{p_{t,r}}$ above 60% of the span (Fig. 7.7 B), compared to the *Clean* case. The upper branch of the swirl profile in OP3U increases the incidence on the rotor blade in a region strongly unloaded. As shown in Fig. 2.3, at the tip the blade experiences an incidence angle that is lower than the stalling angle, which is estimated to be -40° using the correlation proposed by Craig & Cox (1970). As a result, the upper branch of the swirl profile increases the load on a portion of the blade that would otherwise operate in a negative stalling condition, thereby improving the overall performance.

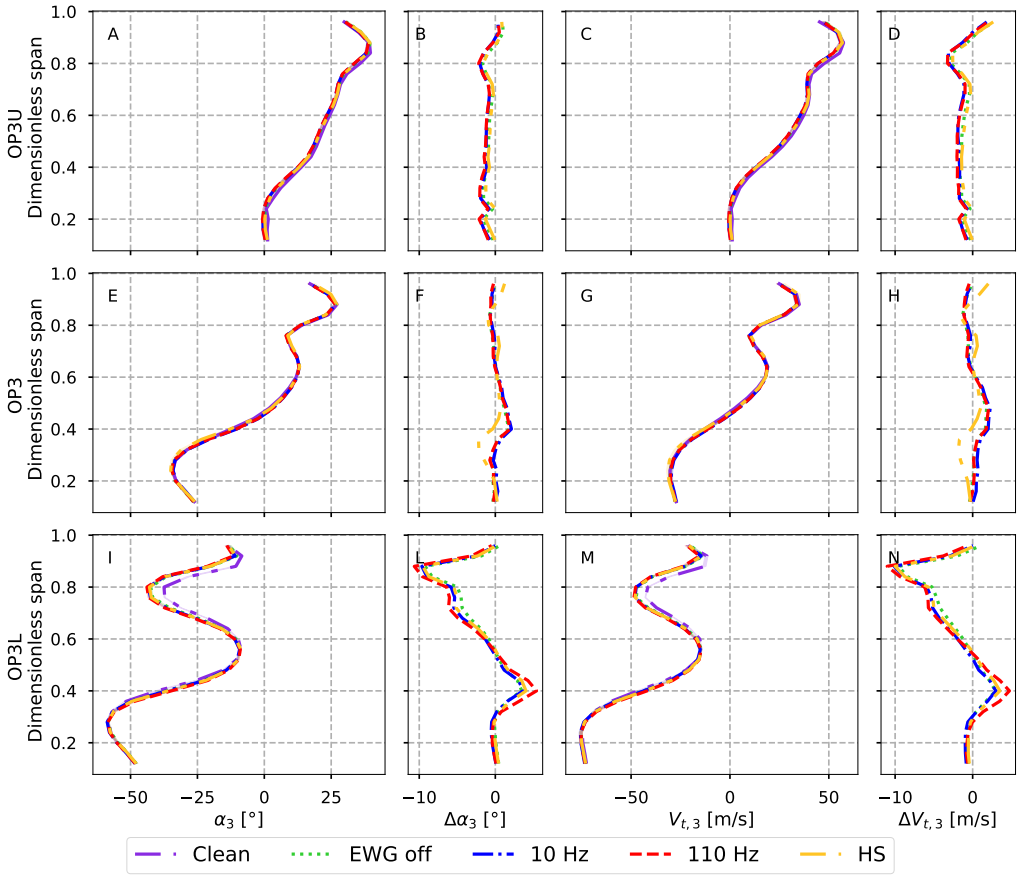

FIGURE 7.8. Circumferential mass-averaged aerodynamic flow field at plane T3 for OP3U (first row), OP3 (second row) and OP3L (third row) LE injection cases. From left to right: absolute flow angle, flow angle difference between perturbed and Clean cases, tangential velocity, and tangential velocity difference between perturbed and Clean cases.

Further analysis is being conducted to investigate the effects of different injection cases on the pitch-wise mass-averaged absolute flow angle and tangential velocity at plane T3. Figure 7.8 shows this analysis for the LE injection position. $\widetilde{\Delta}$ represents the difference in flow quantities between the perturbed cases and the *Clean* case. The differences between the *EWG off* case and the swirling EW/HS cases are negligible, indicating also for these OPs that the swirl profile is the main driver for changes in the steady aerodynamic flow field. The aerodynamics of the rotor remains essentially unaffected by the injection positions. This is clearly demonstrated by the similarity in perturbation effects observed for both the MP injection position in Fig. 7.7 and the LE case in Fig. 7.8. For instance, in OP3L, the swirl profile has a similar impact on the tip region, with a negative average $\widetilde{\Delta}\delta$ at 80-90% span, that leads to negative $\widetilde{\Delta}V_{t,3}$ and strengthens the HPV in all the OPs, as indicated in $\widetilde{\Delta}\alpha_3$ (see Fig. 7.8 L).

Furthermore, the results presented in Fig. 7.8 can be used to estimate the changes in work extraction resulting from combustor non-uniformities. In OP3, the absolute flow angles and tangential absolute velocities of the perturbed cases closely match those of the *Clean* case, resulting in negligible values of $\widetilde{\Delta}\alpha_3$ and $\widetilde{\Delta}V_{t,3}$ (as shown in Fig. 7.8 F and H). However, at 40% of the span,

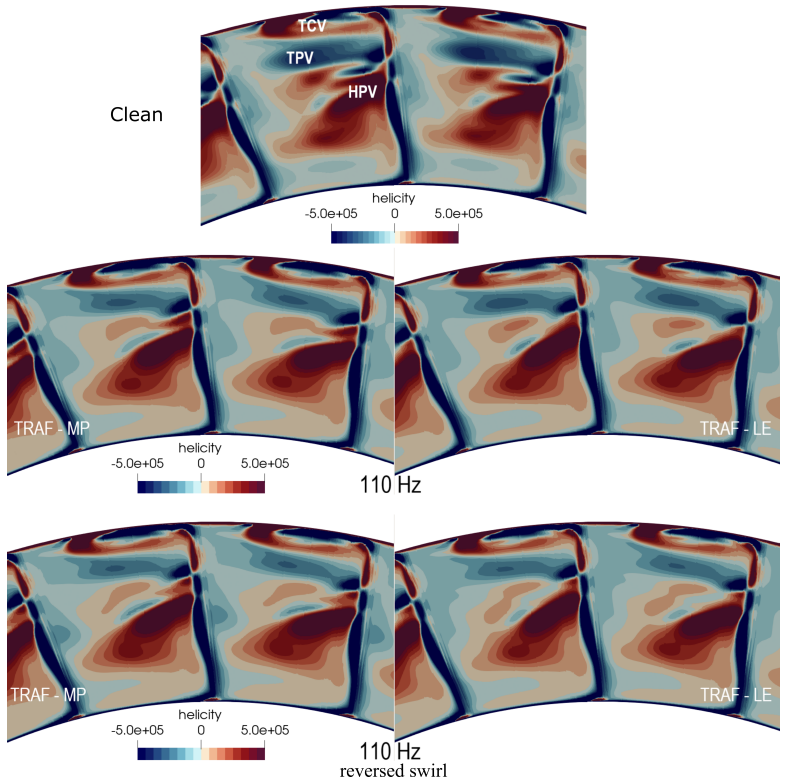

FIGURE 7.9. Stream-wise vorticity plots at plane T3 for OP3 Clean, 110 Hz and 110 Hz reversed swirl.

the *Clean* case has more negative α_3 and $V_{t,3}$ than the perturbed injections, leading to a higher work extraction. In OP3U, the uniform injection produces larger flow angles and tangential velocities compared to the non-uniform cases on most of the span, leading to negative $\widetilde{\Delta}\alpha_3$ and $\widetilde{\Delta}V_{t,3}$ (Fig. 7.8 B and D). As both α_3 and $V_{t,3}$ are positive throughout the span, the *Clean* case exchanges less work compared to the perturbed cases. For OP3L, two opposite effects are observed in Fig. 7.8 L and N: negative differences are measured above 60% of the blade height, while positive differences are observed from 30% to 60%. As the flow angles and absolute tangential velocity are negative across the entire span, a lower absolute tangential velocity results in higher work extraction. Consequently, the perturbed cases for OP3L exhibit higher work extraction above 60% of the blade span compared to the *Clean* case, while the opposite is observed from 30% to 60%.

To conclude, the reversed swirl is analyzed for the OP3 *110 Hz* cases by means of CFD vorticity plots at plane T3 in Fig. 7.9. The injection of the swirling EW causes slight and similar modification of the passage vortexes for both swirl directions, suggesting that the main responsible for this would be the temperature gradient.

7.2 Unsteady aerodynamic flow field

To obtain a comprehensive understanding of the unsteady flow field generated by the rotating blade, it is crucial to perform an unsteady analysis downstream of the rotor in addition to the mean phase-averaged analysis. Such an analysis requires the phase-averaging of the FRAPP measurements based on either the blade passing frequency or the EW frequency. These two types

of analysis are discussed separately in subsections 7.2.1 and 7.2.2, respectively.

7.2.1 Phase average at the blade passing frequency

The unsteadiness introduced at the blade passing frequency is analyzed through the standard deviations of flow parameters at the rotor outlet in the relative reference system. For this purpose, the deviation angle and relative total pressure coefficient standard deviations are displayed in Figs. 7.10 and 7.11 for OP3 and OP3L, respectively, as colored contour plots, with mean values indicated by labeled contour lines. To calculate the standard deviations, various stator-rotor interaction positions are utilized. Two cases are presented: *10 Hz* and *Clean*, the latter serving to highlight the differences.

In both operating conditions, the region with the highest unsteadiness is located close to the blade wake, which extends from 30% of the span to the top casing. This region is characterized by the stator wake avenue, which exhibits a C-shaped pattern near the rotor blade and is the primary cause of the fluctuating flow pattern due to stator-rotor interaction. In particular, the stator wake avenue induces significant unsteadiness in the lower border of the wake region. In OP3 (Fig. 7.10 A and D), the standard deviation indicates fluctuations primarily in the secondary flow regions, particularly in the passage vortices. The tip region shows low standard deviations since the stator-rotor interaction is dominated by the tip clearance. Similarly, due to the strong secondary structures, the rotor blade wake region exhibits almost zero fluctuation in the OP3L *Clean* condition (Fig. 7.11 A and D).

The distribution of standard deviation in OP2 and OP3U is similar to that of OP3, with the only difference being a lower magnitude of the standard deviation. This reduction is consistent with the weakened secondary structures in these operating conditions.

In OP3, as shown in Fig. 7.10, and similarly in OP3U and OP2, the mean flow pattern remains largely unchanged regardless of the injection case or clocking position, as discussed in section 7.1. However, the standard deviation decreases, particularly in the MP injection position, when swirl is injected. The discussion is based on the *10 Hz* case but all the other injection cases share similar features. In Fig. 7.10, the standard deviation peaks decrease by around 30% in the perturbed cases compared to uniform injection. This is because the higher the non-uniformity in the circumferential direction at the rotor inlet, the higher the standard deviation. This behavior is not observed in the uniform inlet, which is characterized by a clear distinction between the wake and isentropic region. Each perturbed condition introduces a loss core around mid-span, which makes the rotor inlet circumferential pattern more uniform at low pressure levels (see contour lines in Fig. 5.1). The perturbation in the LE case is more localized compared to MP, where its influence spreads over the isentropic region. As a result, the standard deviations in the MP case are lower than those in the LE case.

The unsteady flow field at the rotor in OP3L, as seen in Fig. 7.10, is influenced by residual disturbances at the stator outlet, resulting in a reduction of rotor unsteadiness, similar to other OPs. However, an increase in rotor outlet unsteadiness is observed near the region of the TPV, possibly due to the different transport of the stator wake avenue.

Since the standard deviation does not change among the different injection cases, the primary impact is attributed to the additional vorticity injected rather than the temperature disturbance. In conclusion, the study demonstrates the impact of non-uniform turbine inlet conditions on flow parameters at the rotor outlet and emphasizes the importance of considering stator-rotor interaction when designing gas turbines.

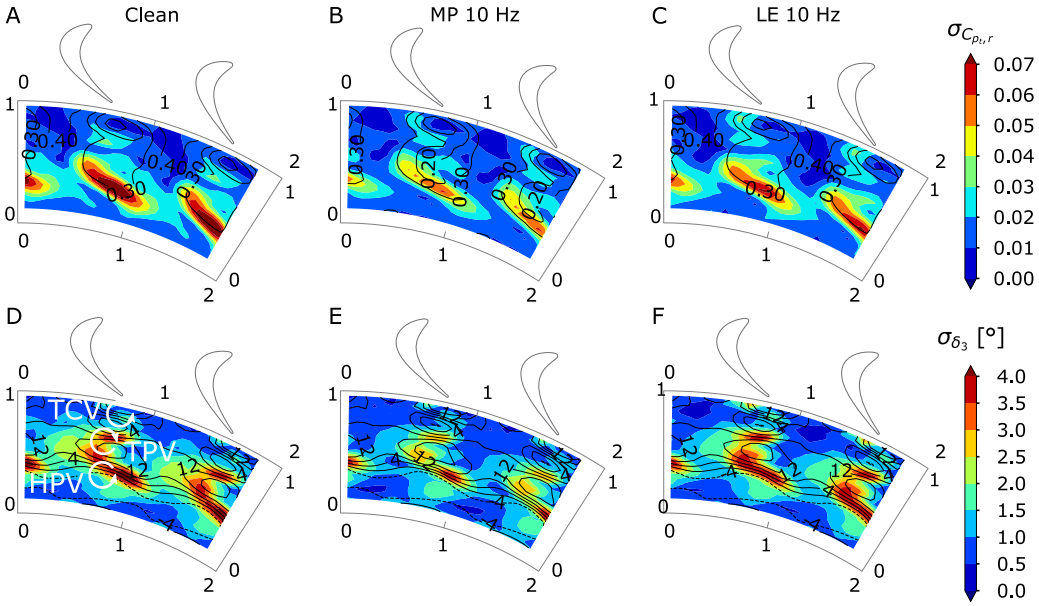

FIGURE 7.10. Standard deviation of relative total pressure coefficient (first row) and deviation angle (second row) at plane T3 for OP3 Clean (first column), MP 10 Hz (second column) and LE 10 Hz (third column). Contour lines are the respective mean phase-averaged values.

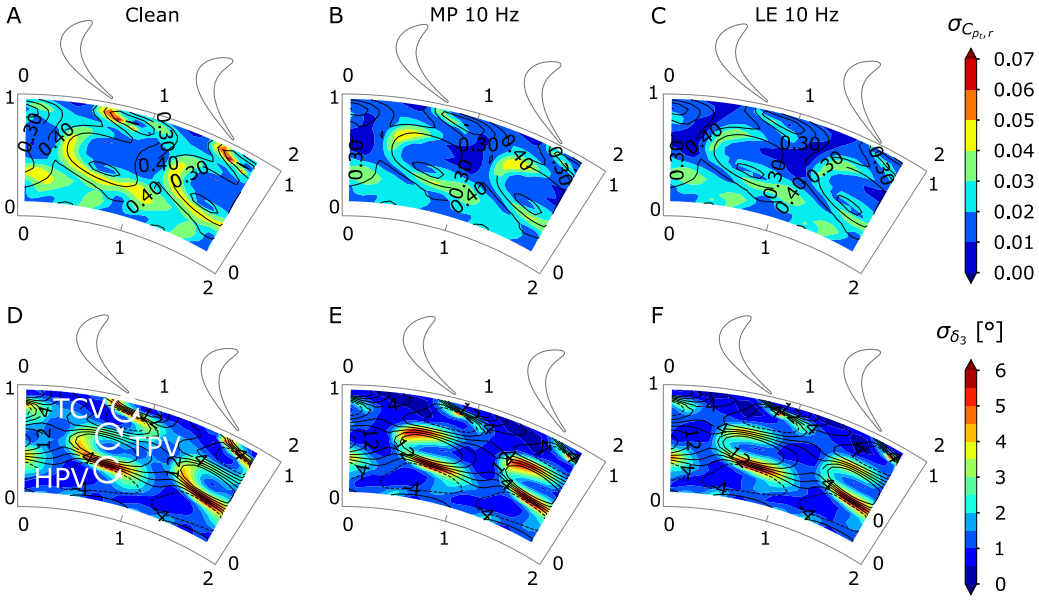

FIGURE 7.11. Standard deviation of relative total pressure coefficient (first row) and deviation angle (second row) at plane T3 for OP3L Clean (first column), MP 10 Hz (second column) and LE 10 Hz (third column). Contour lines are the respective mean phase-averaged values.

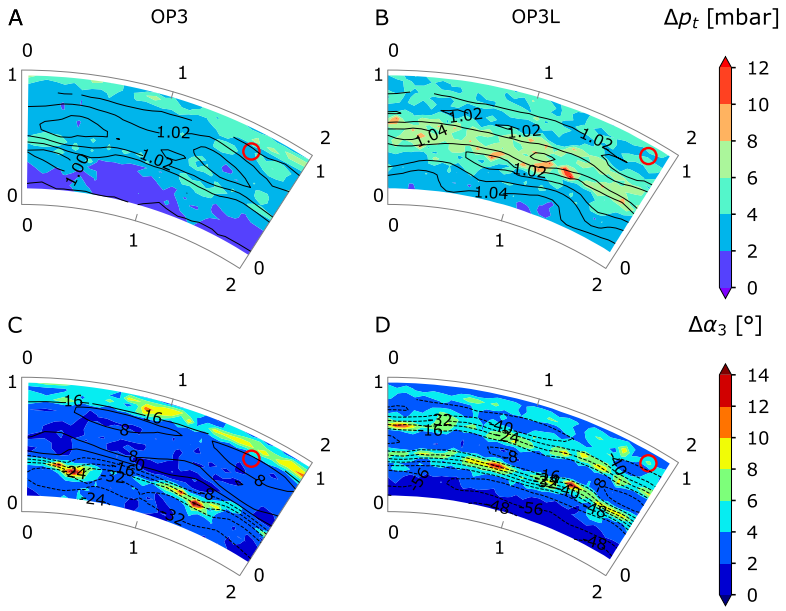

FIGURE 7.12. Peak-to-trough total pressure (first row) and absolute flow angle (second row) at plane T3 for OP3 (first column) and OP3L (second column) LE 10 Hz case. Contour lines are the respective time-average values. The circle highlights the position of the peak temperature.

7.2.2 Phase average on the entropy wave frequency

The analysis of flow parameter fluctuations at the blade passing frequency has shown that the injection of combustor non-uniformity leads to reduced flow unsteadiness, except for in the OP3L case, where the flow in the region near the TPV becomes more unsteady.

Further investigation is conducted by phase-averaging the results at the EW frequency. Figure 7.12 shows the results for the LE *10 Hz* case, which exhibits the highest unsteadiness at the stator outlet, as discussed in section 5.1.2. The MP case is similar, but exhibits lower fluctuations. The figure displays the peak-to-trough total pressure and the flow angle values in the absolute frame of reference, providing insight into the work extraction process. The circle highlights the position of the peak temperature. To ensure phase consistency among the three readings of the virtual 3-hole probe, the reference phase is selected when the trigger signal is maximum (see chapter 2.2).

In OP3, the residual unsteadiness of the EW at plane T2 does not significantly affect the total pressure flow field (Fig. 7.12 A). The regions with the highest levels of flow unsteadiness are not attributable to the EW, but rather to the tip vortex and blade wakes, considering the distance from the circle in both the total pressure and absolute flow angle plots (Fig. 7.12 A-C). However, in the nearby region of the circle, the total pressure unsteadiness and flow angle increase, the latter up to 10°, with a shape and position similar to the peak-to-trough temperature value, as it will be shown in section 7.3.

For OP3U and OP2, the results are similar to OP3, but with reduced fluctuations, similarly as discussed in chapter 7.2.1. In OP3L, the flow field becomes more unsteady, especially the flow angle shown in Fig. 7.12 D, at around 70% of the span in the region identified by the TPV in Fig. 7.11. This could be due to a different blade operation during the hot and cold EW periods.

Overall, the results shown in Fig. 7.12 provide further evidence that accurate flow field predictions require accounting for the unsteadiness induced by the EW at the rotor outlet. As shown in this analysis, the EW can lead to variations of up to 10° in the absolute flow angle and 12

mbar in total pressure, which can significantly impact the overall flow behavior.

7.2.3 Unsteady blade load

The CFD simulations enable the investigation of the unsteady blade load on both stator and rotor blades. The EW is slightly modified to match the rotor frequency, and each *10 Hz* case completes one period when 13 revolutions for OP3U, 12 revolutions for OP3, and 8 revolutions for OP3L are completed. Since the EW period (0.1 s) is much longer than the stage flow-through time (approximately 0.003 s, calculated using an axial stage length of 0.17 m and an average axial velocity of 50 m/s), the EW fluctuation can be considered a quasi-static phenomenon by the stage. This means that once the hot/cold branch is injected at plane T1, the temperature variation is immediately sensed at the leading edges of both stator and rotor blades.

Figures 7.13 and 7.14 illustrate the unsteady stator and rotor loads for OP3U and OP3L, respectively, after subtracting the mean load value to emphasize the fluctuation. The time interval considered is the duration of the EW period, with the hot and cold sub-periods highlighted in the plots. In OP3U, the stator load (Fig. 7.13 a) primarily exhibits the first rotor passing frequency (25 peaks in the rotational period or 325 peaks during the EW period). The EW fluctuation modulates the blade passing frequency fluctuations, as highlighted by the dashed line. Similar considerations can be drawn for the rotor load. During the impingement of the hot branch on the rotor, the unsteady load increases as the incidence locally rises due to the higher acceleration caused by the elevated temperature, as discussed in section 5.1.2.

In OP3L, the amplitude of the load fluctuations increases and a denser harmonic content is observed. The stator load fluctuation (Fig. 7.14 a) is still dominated by the rotor passing frequency, but additional sub-harmonic fluctuations appear, accompanied by modulation at the low frequency of the EW, as indicated by the dashed line. The rotor unsteady load (Fig. 7.14 b) shows even more visible sub-harmonic fluctuations with a frequency about three times the EW frequency. The EW modifies the load cycle generating a load increase during the hot cycle of the EW fluctuation. The appearance of sub-harmonic load fluctuations in OP3L suggests the presence of flow rotating instability caused by the high incidence angle at the rotor tip interacting with tip clearance flow. This phenomenon is clearly observed in the numerical simulations. However, due to the need for further experimental investigations, its detailed discussion is beyond the scope of this thesis.

Figure 7.15 provides a quantitative evaluation of the influence of the injected swirling EW hot branch on rotor load fluctuations. The amplitude of the first EW harmonic for different injection positions and operating conditions is shown in the bars of the plot. The presence of the hot spot increases rotor lift globally, and this effect is more significant at OP3L. For this specific operating point, the rotor experiences a high load and is operating near its positive stall limit. As a result, even minor changes to the incidence angle could have a significant impact on the blade loading. The results from OP3 and OP3U are consistent with each other, indicating no significant differences between the two cases.

The comparison of the two injection positions suggests that the MP case exhibits the highest blade load fluctuations, even though the incoming temperature disturbance of the EW at the rotor inlet has a lower amplitude than that of the LE case. This is likely due to the fact that the EW injected in the MP position is transported through the channel closer to the hub, where the highest work exchange takes place.

Fig. 7.16 shows the pressure fluctuation amplitude at the EW frequency on the rotor suction side for both injection positions and all OPs. Although these fluctuations are lower in magnitude than those caused by the blade passing frequency, they still contribute to the overall unsteady load on the rotor. The MP injection position has higher fluctuations than LE because the EW impacts the rotor closer to the hub, where there is greater work exchange. OP3U and OP3 exhibit similar pressure patterns, although there is a region of more pronounced pressure fluctuations near the LE

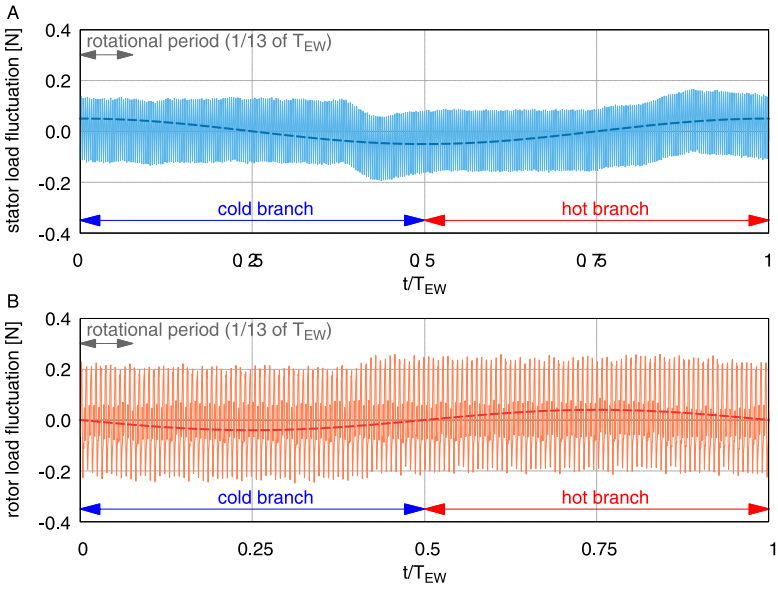

FIGURE 7.13. Unsteady load on stator (first row) and rotor (second row) for OP3U MP 10 Hz.

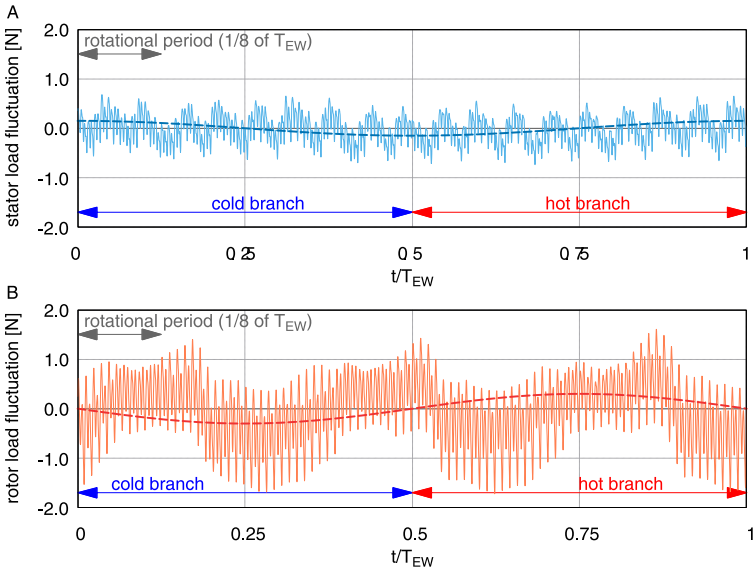

FIGURE 7.14. Unsteady load on stator (first row) and rotor (second row) for OP3L MP 10 Hz.

in OP3U. OP3L has fluctuations around three times higher with respect to the other OPs. This is because even a small variation in incidence angle at the rotor inlet can significantly affect the rotor operation, especially when operating close to stall conditions.

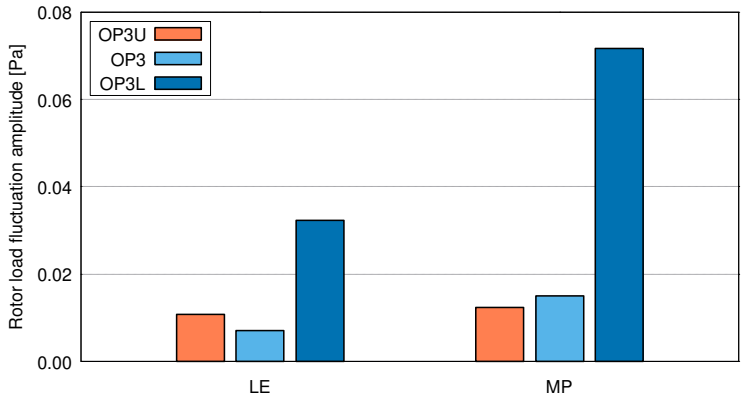

FIGURE 7.15. Rotor load fluctuation amplitude for the 10 Hz cases.

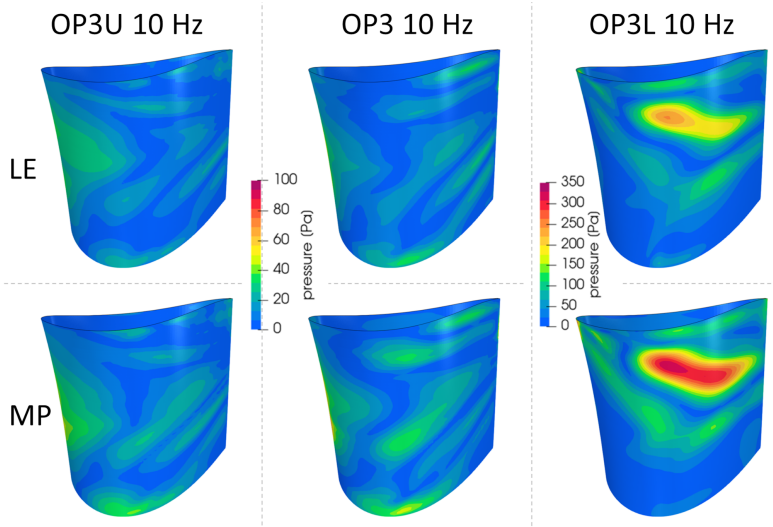

FIGURE 7.16. Pressure distrubution of the unsteady load on the rotor for OP3U (first column), OP3 (second column) and OP3L (third column), LE (first row) and MP (second row) 10 Hz cases.

7.3 Thermal flow field

The residual temperature field downstream of the stage is another important feature investigated. The analysis of peak-to-trough temperature values indicates that the difference in work extraction between OP2 and OP3 does not affect the decay of the EW temperature. However, the temperature difference between the hot and cold EW branches can alter the rotor incidence angle. This effect was discussed in section 5.1.2, where it was found that the maximum change in incidence angle is 8°. This value is not significant enough to cause a modification of the blade loading in design conditions, according to Craig & Cox (1970). Nonetheless, in OP3L, where the blade is close to stalling conditions, this incidence change could have an impact on the blade operation.

The location and magnitude of the EW at the rotor inlet are briefly reviewed before discussing its transport through the rotor. For further details, the reader is directed to section 5.2. In the LE

injection case, the injected perturbation has a larger peak-to-trough value and is positioned at 65% of the span, that is closer to the top casing compared to the MP case, where it is at 50% of the blade span. Despite the lack of measurements at the stator outlet, no significant differences are expected in the transport of EW through the vane in OP2.

The analysis of the peak-to-trough temperature values begins with the 10 Hz case. In the OP3 LE case (Fig. 7.17 A), the EW is concentrated in the tip region and distributed circumferentially across the entire sector. Whereas the MP injection case (Fig. 7.17 B) shows the EW spread over the entire span, but confined azimuthally to a single stator pitch. Additionally, the peak value for the LE case is higher than the MP case. The differences in radial position and magnitude observed between the injection cases are consistent with the inlet rotor features, previously reminded.

At plane T3, OP2 exhibits similarities with the OP3 case. Specifically, in the OP2 LE case (Fig. 7.17 C), the EW mainly affects the tip region and covers the entire circumferential sector, whereas in the MP case (Fig. 7.17 D), the EW is confined to about half of the circumferential sector and is more spread in the radial direction. These findings support the author's view that the transport of EW through the stator is not expected to change significantly between OP2 and OP3. However, differences are observed between OP3 and OP2 at plane T3. First, the radial EW pattern in OP2 is not continuous and breaks at approximately 80% of the span, which could be attributed to the magnified TCV in OP2 that traps a portion of the EW. Furthermore, the high rotational speed confines the EW above mid-span. Finally, the EW fluctuation is higher in OP2 than in OP3, despite the opposite trend observed at stage inlet (see Fig. 4.5). To further investigate this difference in peak values, an entropy transfer function Ξ is defined in Eq. 7.4 similar to Morgans *et al.* (2013). This function is the ratio of the inlet and outlet entropy fluctuations obtained by integrating over the entire measuring grid of two stator pitches. The entropy transfer function, as defined in Eq. 7.4, requires the assumptions of ideal gas, steady pressure flow field and incompressible flow. The incompressible assumption holds true upstream and downstream of the turbine stage where the average absolute Mach numbers are 0.14 and 0.27 in OP2 and even lower in OP3. The pressure steadiness is a very strict condition that is not valid downstream of the rotor. However, since the EW frequencies studied in this research are at least one order of magnitude lower than the blade passing frequency, the phenomenon can be treated as quasi-steady. The pressure steadiness assumption is also supported by the small pressure fluctuations measured in the unsteady analysis in section 7.2.

$$\Xi = \frac{\frac{\Delta T_3}{\overline{\overline{T}}_{t,3}}}{\frac{\Delta T_1}{\overline{\overline{T}}_{t,1}}} \tag{7.4}$$

Table 7.1 displays the values of Ξ. The primary reason for the dissipation of the EW is its interaction with the secondary flows, which accelerates the decay of the EW and increases flow turbulence. These vortical structures have steep gradients that foster mixing between the hot and cold EW branches, which explains why there is a difference between OP3 and OP2, where secondary structures are weaker. Furthermore, in OP2, the faster flow reduces the residence time of the EW, limiting the interaction between hot and cold branches and decreasing shear dispersion. The values of Ξ observed in the present study are lower than those reported by Giusti *et al.* (2017) in ducts, due to the presence of strong secondary structures and turbulent mixing.

This behavior is observed in OP3U as well (Fig. 7.17 E and F), with the same EW shape as in OP3, but with a higher peak-to-trough value. The less intense secondary vortices in OP3U reduce EW mixing, resulting in a higher peak-to-trough temperature value than OP3. The periodic variation of the incidence caused by the EW does not have a significant impact on the blade load (see section 7.2.3) but it does slightly improve the blade operation. This is because the swirling EW increases the incidence in a region that has a negative incidence angle. However, in this region, the flow is less sensitive than OP3L to incidence variations.

TABLE 7.1. Entropy wave transfer function.

OP	Injection position	10 Hz	110 Hz	$\frac{\Xi_{110Hz}}{\Xi_{10Hz}}$
OP3	MP	0.58	0.44	76%
	LE	0.66	0.43	65%
OP2	MP	0.91	0.66	76%
	LE	0.91	0.62	68%

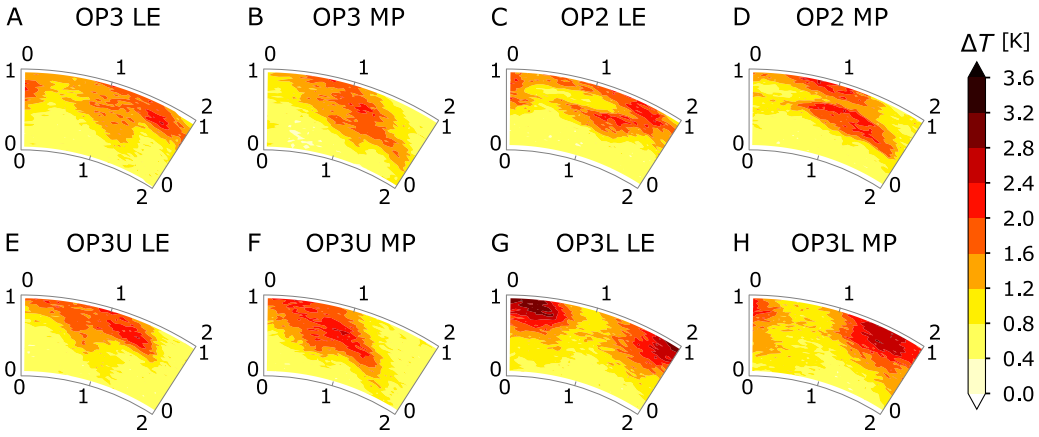

FIGURE 7.17. Peak-to-trough temperature values at plane T3 for 10 Hz injection cases.

The OP3L (Fig. 7.17 G and H) exhibits unique features. For each injection position, the EW is confined to the tip region, and the peak-to-trough values are the highest among the studied OPs. In OP3L MP case, the EW is still more spread radially than LE. The radial position of each OP is consistent with the findings of Prasad & Hendricks (2000), who demonstrated that secondary flows push a hot flow upwards, as it will be further discussed in section 7.6. Despite the strongest secondary flow suggesting the lowest peak-to-trough temperature value in OP3L, this OP exhibits the highest EW magnitude at plane T3. As discussed in sections 7.2 and 7.2.3, the blade load during the EW period changes due to the different incidence angles imposed at the rotor inlet. The incidence increase during the hot period causes the hot branch of the EW to periodically stall the rotor, thereby reducing the work extraction. As a result, due to the unequal work extraction during hot and cold periods, the ΔT is the highest in OP3L.

In the *110 Hz* and *HS* cases, similar thermal flow fields to the *10 Hz* case are observed in Fig. 7.18 and 7.19, respectively. The plot in *110 Hz* (Fig. 7.18) appears granular due to the measurement uncertainty of 0.4 K, which is comparable to the absolute values measured.

In *110 Hz* case, a lower EW transfer function is observed compared to *10 Hz* cases, as shown in Tab. 7.1. This indicates more severe mixing among hot and cold branches at high frequencies, resulting in a percentage reduction of approximately 75% for MP injection and 66% for LE injection (as shown in Tab. 7.1 last column). This difference highlights a more significant shear dispersion in the *110 Hz* case. Specifically, in the LE case, the EW is found closer to the tip casing through the rotor (as seen in Fig. 7.17), and at high frequency, the EW mixes more intensively in the boundary layer.

In the HS case (Fig. 7.19), the continuous hot streak injection increases the injected thermal power and deletes the mixing of hot and cold branches among the causes of ΔT decay. As a result,

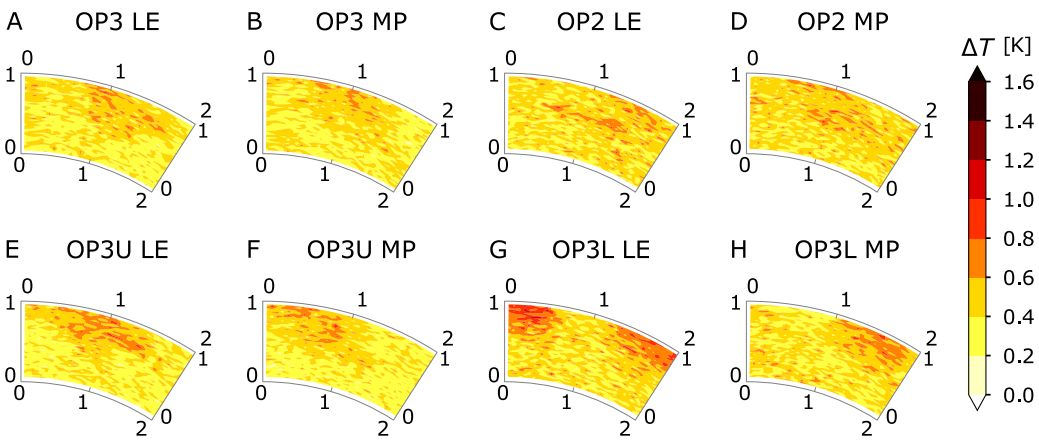

FIGURE 7.18. Peak-to-trough temperature values at plane T3 for 110 Hz injection cases.

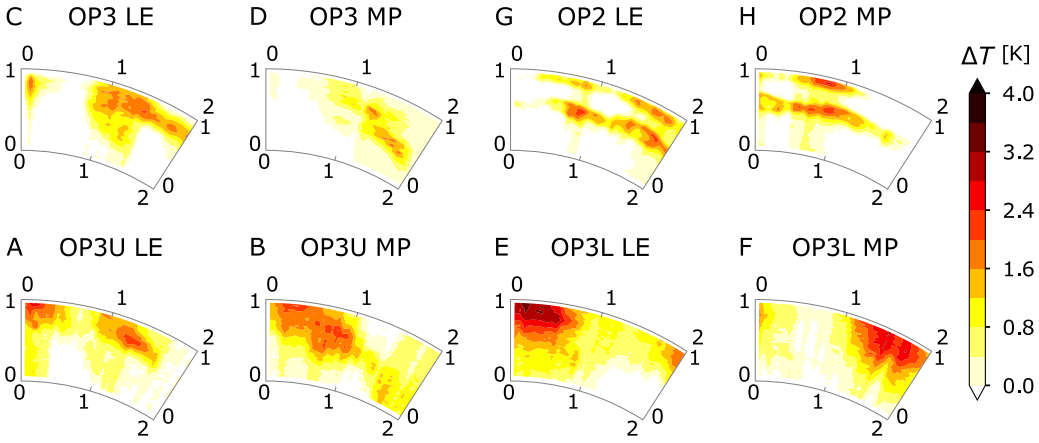

FIGURE 7.19. Peak-to-trough temperature values at plane T3 for HS injection cases.

this injection case exhibits the highest temperature values.

The reversed swirl condition, which is only investigated through CFD for the *110 Hz* cases of OP3 and shown in Fig. 7.20, confines the EW close to the tip region for both injection positions and elongates the EW in the circumferential direction. Peak values are higher than the *110 Hz* case, consistent with the higher values at the rotor inlet.

The CFD validation is shown for *10 Hz* cases for OP3, OP3L and OP3U in Fig. 7.21.

Overall, the maximum peak-to-trough temperature at plane T3 reduces at approximately 4% in EW cases, 5% in HS with respect to the plane T1 values.

7.4 Efficiency

Table 7.2 lists the total-to-total efficiencies for OP3, OP3U and OP3L, which are calculated as the ratio between the Eulerian work (Eq. 7.3) and the isentropic work, based on the measured turbine total-to-total expansion ratio. The Eulerian work is obtained by computing the mass-average velocities at measuring grids. However, it is not possible to calculate the efficiency for OP2 because temperature measurements at plane T2 are missing, and velocities at the stator outlet are unknown.

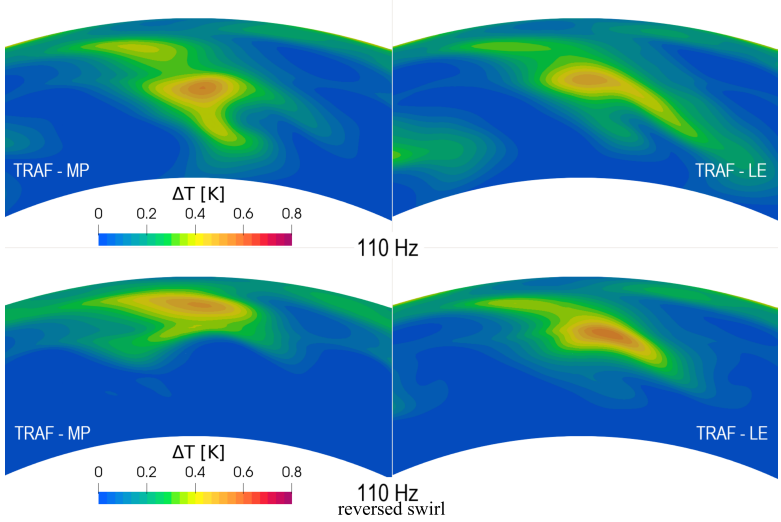

FIGURE 7.20. Peak-to-trough temperature values at plane T3 for OP3 MP (first column) and LE (second column), 110 Hz (first row) and 110 Hz reversed swirl (second row) cases.

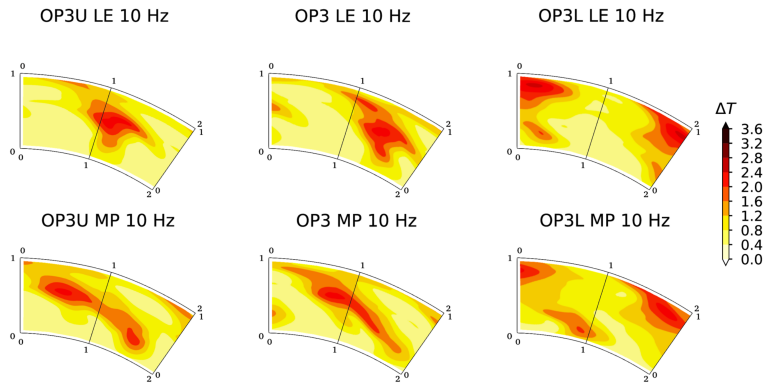

FIGURE 7.21. CFD peak-to-trough temperature values at plane T3 for 10 Hz injection cases.

Furthermore, the experimental efficiencies are compared with the numerical efficiency, which is computed using the mass-flow averaged total pressure and temperature between planes T1 and T3.

In the *Clean* cases, OP3 exhibits the highest experimental efficiency, as it has the design incidence angle to the rotor. The blade is unloaded in OP3U, resulting in a 1.2% decrease in work exchange compared to OP3. In OP3L, where the blade is severely loaded and secondary losses are the strongest, the efficiency drop is 11% compared to OP3.

When combustor non-uniformities are injected, each injection case reduces the efficiency in OP3 due to pressure losses downstream of the stator and residual swirl that acts as a source of off-design to the rotor blade. The swirling EW/HS cases show the highest reduction in efficiency, consistent with the stronger swirl profile generated.

In OP3U, the introduction of the swirling disturbance seems to improve the work exchange, partially recovering the negative incidence. LE injection impacts a zone with a lower incidence than the one impacted by the MP case (see section 5.1), resulting in higher efficiencies in LE injection positions in OP3U. However, the swirl profile introduces losses at the turbine inlet, increases

TABLE 7.2. Total-to-total experimental and numerical efficiency for OP3, OP3U and OP3L. Uncertainty ±0.5%.

		OP3U		OP3		OP3L	
		MP	LE	MP	LE	MP	LE
Clean	Exp	86.8%		88.0%		77.1%	
	CFD	87.4%		87.5%		82.0%	
EWG off	Exp	85.2%	87.0%	87.8%	87.6%	77.9%	77.8%
10 Hz	Exp	86.4%	88.0%	86.8%	87.1%	78.2%	77.4%
	CFD	86.7%	86.7%	88.6%	86.5%	81.3%	81.1%
110 Hz	Exp	87.4%	87.7%	87.1%	87.3%	78.7%	78.9%
	CFD			86.9%	86.7%		
110 Hz counter rotating	CFD			86.7%	86.8%		
HS	Exp	87.1%	87.5%	87.6%	87.7%	78.7%	78.1%

total pressure losses at the stator outlet, and interacts with rotor secondary flows. Therefore, the efficiency is a combination of all the positive/negative effects discussed. Nonetheless, the loading increase due to the swirling EW/HS perturbation is the primary contribution to efficiency improvement compared to *Clean*. This does not apply to *EWG off*, which has a less stable and more dissipative swirl profile.

In OP3L, the injected perturbation could improve the blade operation, particularly considering the lower branch of the swirl profile, which unloads the region close to the hub, where the highest work extraction occurs. Thus, the efficiency in perturbed cases is higher than *Clean*. The *110 Hz* cases have higher efficiencies than *10 Hz* due to smaller temperature fluctuations, reducing the impact of blade stalling. This is also true for the HS case, which has a lower peak temperature than EW at plane T2, as discussed in section 6.2.5. Furthermore, due to the higher temperatures at plane T2, each LE injection position case has a lower efficiency than MP ones.

The comparison between the CFD and experimental outcomes reveals that in OP3, the numerical predictions are in excellent agreement with the experimental results.

The OP3 reversed swirl cases share similarities with their respective *110 Hz* cases. The LE injection position remains practically unchanged, and this is confirmed by the same EW magnitude at the stator outlet for both the swirl direction and by the similar EW transport through the rotor (Fig. 7.20). In the MP case, the counter rotating swirl at plane T2 results in a higher EW magnitude, as seen in Fig. 5.25, which adversely impacts the rotor aerodynamics and reduces efficiency in comparison to the MP *110 Hz* case.

In OP3U, while the levels of efficiency are consistent between the CFD and experiments, the trends are not captured accurately by the numerical simulations. Specifically, the experiments show an increase in efficiency for perturbed cases compared to the uniform inlet condition, which is not observed in the CFD results. In OP3L, the measurements and predictions differ significantly, and the trends are also inconsistent. The primary reason for these discrepancies can be attributed to the limitations of the experimental data due to probe geometrical constraints, which do not cover the entire span. Additionally, the strong non-uniformity under off-design conditions of the flow field could be very sensitive to boundary conditions and increase the discrepancies between CFD and experimental measurements.

TABLE 7.3. Entropy noise emission at the stage inlet p_δ^- and outlet p_δ^+ in dB.

		OP3U		OP3		OP3L	
		MP	LE	MP	LE	MP	LE
10 Hz	p_δ^-	108.9	111.8	109.7	112.8	105.5	110.8
	p_δ^+	114.2	113.5	114.2	112.7	110.6	112.6
110 Hz	p_δ^-			96.2	99.7		
	p_δ^-			98.1	99.4		
110 Hz reversed swirl	p_δ^-			98.2	101.2		
	p_δ^-			101.0	99.5		

7.5 Indirect noise emissions

As discussed in section 1.1.2.4, the acceleration of unsteady temperature disturbance, as well as the unsteady blade load caused by EWs, could generate entropy noise. To analyze this, CFD simulations were performed using the TRAF code, which was validated by Pinelli *et al.* (2022) using experimental data on axial EW cases. Table 7.3 shows the results for the upstream running pressure wave p_δ^- at plane T1 and downstream running pressure waves p_δ^+ at plane T3. The downstream running waves at plane T1 and upstream running waves at plane T3, known as spurious reflections, are less than 6 dB, indicating good non-reflectiveness of the boundary conditions, which are treated as non-reflecting boundary conditions according to Giles (1990).

At plane T1, the upstream running wave is dominated by sound emissions generated due to the acceleration of the hot-spot through the stator. The hot-spot undergoes severe acceleration at the LE injection positions in the frontal part of the stator blade, where the temperature disturbance impinges the vane. Therefore, LE cases have higher upstream running sound emissions than MP. In the MP case, the EW is accelerated more in the rear part of the stator channel, contributing to the downstream running acoustic emissions, which are higher than those in LE cases. The majority of noise generation occurs in the stator due to the higher intensity of the temperature disturbance. The rotor transmits and reflects the sound pressure waves generated by the stator, partially increasing the overall sound accelerating the residual temperature spot, which is already significantly damped through the stator.

OP3 and OP3U cases exhibit similar emissions for the *10 Hz* case, while OP3L cases show lower noise emissions. The difference can be attributed to the dense spectrum of the OP3L case, which interacts with the EW fluctuations and has both amplification and cancellation effects. Additionally, the modified aerodynamics in OP3L change the reflection and transmission coefficients, influencing the pressure waves.

Regarding the effects of the injection cases in OP3, sound generation is related to the EW temperature. The *10 Hz* cases have a higher temperature fluctuation than the *110 Hz* cases, resulting in louder noise emissions with a difference of almost 10 dB.

The reversed swirl case has louder emissions than the *110 Hz* case because the EW disturbance remains more coherent in the stator vane, maintaining its peak-to-trough temperature higher, as shown in Fig. 5.25.

TABLE 7.4. Relative total pressure coefficient reduction (in %) with respect to the Clean case.

	MP				LE			
	EWG off	10 Hz	110 Hz	HS	EWG off	10 Hz	110 Hz	HS
OP3	1.7	2.1	2.0	1.3	1.4	0.9	1.4	1.9
OP3L	1.8	1.5	0.8	1.4	2.1	2.5	0.9	2.0
OP3U	1.8	0.5	0.2	0.1	0.8	1.4	1.2	1.6
OP2	0.8	1.5	1.2	0.6	0.9	0.8	2.0	0.4

7.6 Simplified models

The complexity of the rotor aerodynamics, due to the complex bowed geometry, strong secondary flows, and tip clearance vortex, has hindered attempts to reconstruct the rotor flow field. The assumption of constant radial subdomains throughout the rotor transport is not applicable, as the rotor hub passage vortex moves upwards and interacts with the tip passage vortex, which is pushed downwards by the strong tip clearance vortex. To accurately model this complex evolution, more advanced flow solvers are required.

However, the impact of combustor non-uniformities on rotor aerodynamics is weak, as supported by experimental data shown in this chapter. The highest differences are observed in the OP3L case, which is the OP the most impacted by the combustor-representative disturbances. The residual swirl profile reduces the loading of the rotor in the tip region and the periodically changing rotor operation during the EW period due to an increase in the rotor incidence angle.

The differences of the area-averaged relative total pressure coefficient (Eq. 7.1) listed in Tab. 7.4 are small, indicating that the turbine inlet disturbances have only minimal impact on the rotor aerodynamics.

The lack of a model to accurately predict the aerodynamic flow field at the rotor outlet hinders the development of models for predicting temperature perturbations evolution and decay through the rotor. Nevertheless, attempts have been made to establish correlations between non-dimensional coefficients and the decay of the peak-to-trough temperature value through the rotor or the position of the temperature peak at plane T3, based on the data shown in section 7.3. The blade loading coefficient (λ) is identified as the most representative non-dimensional coefficient since high blade loading leads to a high intensity of the secondary flows, which impacts the radial transport of a temperature disturbance through the rotor, as discussed by Prasad & Hendricks (2000). Stronger secondary flows displace the temperature perturbation towards the top casing (Prasad & Hendricks (2000)), and the peak temperature decreases more due to enhanced turbulent mixing. Therefore, the radial shift and peak-to-trough temperature reduction between planes T2 and T3 are shown in Fig. 7.22 for both MP and LE injection positions as a function of the loading coefficient for the *10 Hz* cases, which are also representative of the *110 Hz* cases. The values are interpolated using a least square polynomial fit to provide a simple correlation for an initial prediction of the two parameters at the early stage of turbine design. The fittings are performed separately for LE and MP cases, and the results are shown as solid lines, with shaded bands representing a 10% error. The uncertainty bars in Fig. 7.22 are shown for completeness, and they are wider than the measurements since the maximum peak-to-trough temperature value at plane T3 is approximately 2 K, and the extended thermocouple uncertainty is 0.3 K.

The trends observed in Fig. 7.22 upper row for the radial displacement are in agreement with the previous discussion, showing a continuous linear increase of the radial position with the loading coefficient for both injection positions. In Fig. 7.22 lower row, where the peak-to-trough ratio is

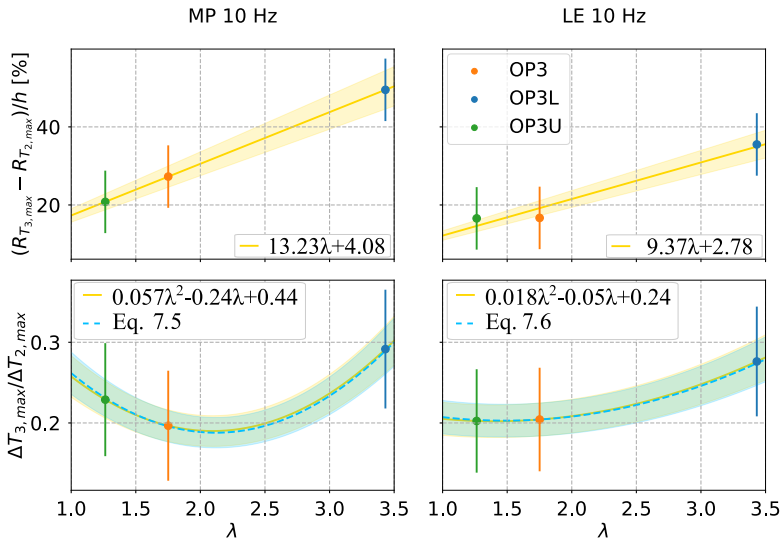

FIGURE 7.22. Radial displacement (upper row) and peak-to-trough temperature reduction (lower row) between planes T2 and T3, 10 Hz case.

shown, OP3U and OP3 follow the expected trend, with weaker secondary flows (OP3U) resulting in a lesser reduction of the maximum peak-to-trough temperature value. However, OP3L does not conform to this trend. Due to the high blade loading in OP3L, the rotor blades operate close to the stalling incidence, and a temperature hot spot further increases the rotor incidence angle. As previously discussed, during the hot period, the blade is closer to stall condition and its work extraction reduces than during the cold period, resulting in the highest maximum peak-to-trough temperature value.

The proposed interpolating functions are validated using the HS case, as shown in Fig. 7.23. The circular bullets represent the HS case results, while solid lines are obtained using the equations reported in Fig. 7.22. The model prediction for the radial displacement is very accurate, as indicated by the excellent agreement between the circular bullets and solid lines. This prediction is also valid for the *110 Hz* case, which suggests that the radial shift of the temperature disturbance is frequency-independent. However, this conclusion does not apply to the peak-to-trough temperature decay of Fig. 7.23, which is a function of the temperature disturbance frequency. The strong rotor secondary flows further amplify the effects of mixing and shear dispersion, which are known to decrease the magnitude of the temperature perturbation at higher frequencies (Giusti *et al.* (2017), Christodoulou *et al.* (2020)). Despite being less satisfactory in predicting the temperature decay, the solid line model still manages to capture the main trends accurately. To account for the effect of frequency and improve the model outcomes, a Helmholtz number is defined as $He = frequency - EW\Delta x_{T2-T3}/v_{1,a}$, where the HS case has a null frequency value. This definition allows to take into account the residence time of the HS/EW. The HS, *10 Hz* and *110 Hz* data are interpolated as a function of both He and λ. The resulting interpolating functions are shown as dashed blue lines in Figs. 7.22 and 7.23, and they can be used to predict the temperature decay through the rotor. The equation details can be found in Eq. 7.5 and 7.6, for the MP and LE injection positions, respectively. The use of this new interpolating function has led to improved predictions for each injection case.

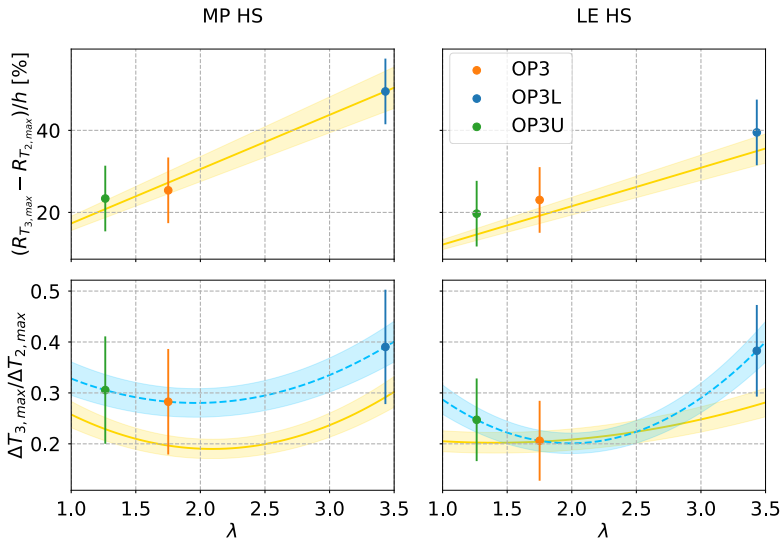

FIGURE 7.23. Radial displacement (upper row) and peak-to-trough temperature reduction (lower row) between planes T2 and T3, HS case. Solid lines are the same of Fig. 7.22, dashed lines are reported in the referenced equations.

$$MP: \ 0.48 - 0.19He - 0.2\lambda + 0.1He^2 + 0.2He^2\lambda - \\ + 0.03He^2\lambda^2 + 0.05\lambda^2 + 0.06He\lambda^2 - 0.36He\lambda \tag{7.5}$$

$$LE: \ 0.55 - 2.2He - 0.35\lambda + 1.25He^2 - 1.2He^2\lambda + \\ + 0.29He^2\lambda^2 + 0.087\lambda^2 - 0.5He\lambda^2 + 2.16He\lambda \tag{7.6}$$

Overall, the comparison of swirling EW and HS yields two main outcomes: firstly, the equations developed can serve as a preliminary estimate for predicting the temperature evolution through the rotor; secondly, this analysis verifies that swirling EW can be regarded as a sequence of steady swirling HS. The obtained trends are similar for both cases, with the main difference being the decay of temperature influenced by the EW frequency.

Regarding the experimental data available downstream of the rotor for OP2, it conforms to the expected trend of OP3, as both operating points exhibit the same flow and loading coefficients. However, no temperature measurements have been performed at plane T2, as discussed in section 5.2.

7.7 Concluding remarks and key findings

This section focuses on the impact of combustor non-uniformities on the aero-thermal flow field of the rotor.

The mean phase-average analysis of the FRAPP measurements revealed that, in each OP, the residual swirling temperature disturbance at the stator outlet interacts with rotor secondary

structures. The interaction between the combustor perturbation and secondary structures is discussed in detail. No evident differences were observed between different injection cases and positions, indicating that the rotor aerodynamics is still dominated by the secondary structures, with a slight modification by the residual swirl.

An unsteady analysis, performed by phase-averaging the FRAPP measurements at the blade passing frequency and then making the standard deviation from the different interaction phases, showed that the perturbed cases in OP3, OP2, and OP3U reduce the aerodynamic unsteadiness at the rotor outlet. This reduction is attributed to the more uniform flow field at stator inlet due to the presence of swirl-induced pressure losses, which breaks the pattern of isentropic-wake regions, making the flow field closer to wake conditions. Based on this analysis, it can be concluded that being the MP pressure field more uniform than the LE field at the stator outlet, the MP cases have lower levels of rotor outlet unsteadiness compared to LE cases.

In OP3L, the introduction of combustor non-uniformities amplifies the unsteadiness in a region adjacent to the TPV. This unsteadiness stems from the altered loading on the rotor blade, which operates near its positive stalling incidence in this operating point. Even a slight increase in the incidence angle could have a significant impact on the aerodynamics of the rotor.

The unsteady analysis is deepened phase-averaging the FRAPP results at the EW frequency. In the OP3 case, representative also of OP2 and OP3U, the peak-to-trough values of the total pressure and absolute flow angle at plane T3 are fluctuating mainly in the regions identified with the secondary flows and partially close to the EW region. In OP3L, these unsteadiness is further magnified and a new region of high flow unsteadiness appears at 70% of the span.

The analysis of the blade loading showed that EW could modulate the unsteady blade load of both the stator and the rotor. This effect is considerably higher in OP3L that experiences great unsteadiness during the EW period.

Peak-to-trough temperature values are strongly dependent on the OP, injection position, and injection case. The highest peak-to-trough values are observed for OP3L because, as the unsteady analysis revealed, the rotor seems to work differently during the EW period. In particular, the higher incidence imposed by the hot disturbance brings the rotor to work closer to its stalling limit, reducing the work extraction.

The efficiency of off-design cases is lower than the design one OP3. In the design case, each injection case reduces the efficiency because it makes the rotor work in conditions different from the design ones. The experimental measurements show that, for off-design cases, the combustor non-uniformities could bring the rotor to work closer to design conditions, improving its performance.

The acceleration of EW and the unsteady loads that they induce on both stator and rotor blades lead to the generation of entropy noise, which is estimated through CFD simulations. The LE case exhibits the highest upstream running pressure waves, while the MP case produces the loudest downstream emissions. These features are associated with the locations where the EW is most accelerated in the stator, resulting in the generation of the majority of the noise. The injection cases that maintain the highest temperature fluctuations also produce the loudest emissions.

To conclude, a simplified model is developed to predict the peak-to-temperature decay through the rotor and the radial shift of the temperature disturbance. The model takes the form of a correlation that depends on the rotor loading coefficient and a Helmholtz number.

CHAPTER 8

CONCLUSION AND OUTLOOK

8.1 Conclusions

This thesis provides a thorough investigation of combustor-turbine interaction in a non-reactive, uncooled turbine stage. To simulate the flow field released by the combustor, a specifically designed combustor simulator is used. The study focuses on four different operating points, two injection positions, and five injection cases, as well as additional cases that are only studied in the OP3 operating condition. In total, more than 40 test cases are comprehensively analyzed in this research. OP3 and OP2 are two design conditions that feature design rotor incidence. In OP3U the rotor incidence angle is negative, while in OP3L is positive and very close to the blade positive stalling threshold.

The flow field generated by the combustor simulator and its impact on the stage aerodynamics are complex, requiring **advanced measurement techniques**. The calibration of the 5-hole probe is extended up to ±45° to fully characterize the swirl profile generated by the combustor simulator. FRAPP measurements are phase-averaged at both rotor passing frequency and EW frequency to provide a better understanding of the unsteady flow field. A fast-thermocouple is dynamically calibrated with high accuracy to ensure it can measure the highest EW frequency of 110 Hz. Uncertainty quantification is applied to all measurements, using a Monte Carlo simulation-based model.

Furthermore, a dedicated **turbulence characterization** is conducted in an atmospheric wind tunnel using a slanted single wire hot-wire anemometer. This campaign aims to quantify the turbulence and flow quantities decay in two measuring planes. The developed procedure shows that this type of probe is capable of measuring the highly swirled flow field generated by the combustor simulator. A phase-averaging technique based on the EW frequency is employed for this probe as well. The results are supported by URANS simulations, providing a better understanding of the main flow physics that cannot be fully comprehended through experiments alone.

The characterization of the **generated perturbations** downstream of the combustor simulator shows the generation of a swirl profile with swirl number of 0.6 and a maximum ratio between the maximum temperature induced by EW/HS and the mainstream of around 1.24. The turbulence intensity reaches peak values of approximately 20%, with an average turbulence value of 6%. These characteristics make the device engine representative considering the literature review conducted in section 1.1. The core of the swirl profile and the location of the maximum peak-to-trough temperature value is at approximately 60-65% at plane T1.

The extensive information obtained on the turbulence parameters and the steady/unsteady aero-thermal flow field will be essential in providing support for high-fidelity CFD simulations of the turbine test case under investigation. This, in turn, will enhance the understanding of the flow and turbulent processes in the context of combustor-turbine interaction experiments.

The impact of combustor non-uniformities on the **stator flow field** is mainly attributed to the swirl profile, which interacts with the secondary flows and changes the stator incidence angle, resulting in increased total pressure losses at the stator outlet. The injection position plays a crucial role in the aerodynamic flow field. In the MP injection case, the swirl profile is transported to the middle of the passage and interacts significantly with the generation of the secondary flows. The injected swirl profile co-rotates with respect to the tip passage vortex. The lower branch of the TPV interacts with the upper branch of the swirl profile and dissipates each other due to their opposite directions. The lean blade geometry of the stator pushes the injected disturbance downwards towards the hub, where it is located downstream of the stator at approximately mid-span.

In the LE case, the swirl profile impinges on the blade leading edge and causes a severe change in incidence angle, leading to high pressure losses. After the disturbance impinges on the blade leading edge, it climbs towards the top casing on the blade vane suction side, where it is transported in its evolution through the stator. The climb compensates for the lean effect, and the disturbance

maintains its radial position between planes T1 and T2.

Despite significant attenuation in both cases, a residual swirl profile persists at the stator outlet. Its intensity is higher, and its impact region is wider in the MP case than in the LE case. In the latter, the weakening effect of the impingement on the blade leading edge and the high flow acceleration during transport through the blade suction side compact the residual swirl in the radial direction and localize its affecting region.

The effects of PS and SS injection positions are investigated for OP3. However, they are found to be intermediate cases with respect to MP and LE and therefore are not considered for further analysis. The PS case exhibits the highest pressure losses due to the high local incidence angle imposed on the blade, similar to the LE case. In the SS case, the swirl is transported closer to the suction side and is more radially confined, similar to the LE case. Both SS and PS cases maintain a swirl intensity at the stator outlet comparable to the MP case and exhibit a shift of the vortex core towards the hub, close to mid-span, due to the pressure field induced by the blade lean.

The flow field at the stator outlet remains unchanged for all injection cases except for the isolate swirl profile case. In this case, the absence of a central flow in the swirler generator results in a swirl profile with lower intensity compared to EW/HS cases. This is reflected in the lower total pressure losses and residual swirl.

The impact of the different expansion ratios is evident in the modification of the stator secondary flows. OP2, characterized by a higher expansion ratio, results in higher Reynolds and Mach numbers, which reduces the strength of the secondary flows. As a consequence, the injected swirl profile undergoes a higher acceleration through the stator, leading to more dissipation. In the MP injection case, the interaction between the TPV and the swirl profile is reduced, resulting in the upper branch of the swirl profile maintaining a higher intensity.

The effect of different rotor rotational speeds on stator aerodynamics is minor, with the main effect being a change in the rotor incidence angle. For example, the rotor in OP3L has an incidence angle that is very close to the stalling incidence.

The CFD investigation shows that the reversed swirl case reduces the interaction with the TPV. This is due to the swirl vorticity adding to the background vorticity generated by the lean geometry, resulting in the bottom branch of the TPV and upper branch of the swirl profile having the same direction and not dissipating each other.

The unsteady analysis reveals that the injection of EWs generates an unsteady flow field that persists at the stator outlet. As the EWs are swirled by the swirler generator, they produce a hot temperature that further increases the rotor incidence angle. This incidence increase is limited and it will not have a significant impact on the blade operation in the design cases (OP3 and OP2). However, this does not apply to OP3L, as the different incidence on the hot and cold EW branches could cause the rotor to work differently during the EW period, because in this OP the blade works closely to its positive stalling incidence.

A residual temperature disturbance is present at the stator outlet as well, and its magnitude depends on the injection case. The MP, SS, and PS cases share the same temperature disturbance shape, but they differ in magnitude due to their interaction with the secondary flows. The LE case has a different temperature perturbation shape, which affects the blade wake and is consistent with its transport discussed above. In the MP, SS, and PS cases, the blade lean pressure field pushes the EW/HS downwards towards the hub casing, while in the LE case, this effect is compensated by the climbing that occurs with the stator leading edge interaction.

The frequency of the EW seems to have no significant effect on the decay rate of the temperature disturbance, as the EW wavelength is at least five times longer than the axial distance between T1 and T2. The primary causes of the decay are the dissipation and mixing imposed by the secondary flows and swirl profile. The swirl profile plays a significant role in reducing the decay rate, as a reduction is observed for swirling EW compared to axial EW cases studied by Pinelli *et al.* (2021).

Furthermore, the presence of the swirl profile changes the temperature disturbance morphology at plane T2. The HS case shares the same features as the EW cases, therefore EW cases can be approximated as a series of swirling HS. This approach significantly reduces the computational time required for CFD simulations.

To conclude, the **rotor outlet flow field** is investigated in terms of steady and unsteady aerothermal flow field. The time-averaged analysis of the FRAPP measurements indicates that the residual swirling temperature disturbance at the stator outlet interacts with the rotor secondary structures. However, there are no significant differences observed between different injection cases and positions, indicating that the rotor aerodynamics is still dominated by the secondary structures with slight modification by the residual swirl.

An unsteady analysis of the FRAPP measurements at the blade passing frequency shows that perturbed cases in OP3, OP2, and OP3U reduce the aerodynamic unsteadiness at the rotor outlet. This reduction is attributed to the presence of swirl-induced pressure losses, which create a more uniform flow field at the rotor inlet that resembles wake conditions. According to this analysis, the MP cases exhibit lower levels of rotor outlet unsteadiness when compared to the LE cases. This is because the MP pressure field is more uniform than the LE field at the stator outlet, where the swirl profile impact is confined to a small region.

However, in OP3L, the introduction of combustor non-uniformities amplifies the unsteadiness in a region adjacent to the TPV due to the altered loading on the rotor blade, which operates near its positive stalling incidence in this operating point. In this OP, an increase in the incidence angle could significantly impact the aerodynamics of the rotor.

The analysis on blade loading shows that the EW can modulate the unsteady blade load of both stator and rotor, and this effect is higher in OP3L due to significant unsteadiness during the EW period.

The peak-to-trough temperature values are dependent on the OP, injection position, and injection case. The highest values are observed for OP3L because the rotor seems to work differently during the EW period, working closer to its stalling limit and reducing the work extraction.

Overall, in design conditions, each perturbed case reduces the **efficiency** compared to the uniform inlet condition because the perturbations make the rotor work in off-design conditions and introduce additional pressure losses. However, in off-design OPs, the inlet perturbations could partially recover the design incidence, and the efficiency can be higher than the uniform inlet condition.

The acceleration of EW and the unsteady loads that they induce on both stator and rotor blades lead to the generation of **entropy noise**, which is estimated through CFD simulations. The LE case produces the highest upstream running pressure waves, while the MP case produces the loudest downstream emissions, associated with the locations where the EW is most accelerated in the stator. Injection cases that maintain the highest temperature fluctuations also produce the loudest emissions.

A **novel methodology** has been developed to predict and evaluate the impact of swirling temperature disturbances on the aerodynamics of an axial turbine stage, with a specific focus on the stator. The rotor features are highly complex, requiring high-order models that are beyond the scope of this research. However, the experimental campaign has conclusively demonstrated that swirling temperature disturbances primarily affect the stator aerodynamics and have a partial impact on the rotor aerodynamics.

The proposed approach leverages both the geometrical data of the turbine and the downstream data collected from the combustor simulator. By enabling the precise evaluation of the impact of combustor non-uniformities on the turbine, this methodology provides a valuable tool for the design process, helping to mitigate the risk of hot spots arising from the combustor. Importantly, the methodology has been validated and can be extended to accommodate any input disturbance

and turbine geometry.

To predict the stator outlet flow field in its span-wise distribution, the methodology combines correlations available in the open literature for axial turbines with some of the experimental observations. To account for the effects of lean geometry, a new correlation based on data available in the literature is developed, resulting in a good match with experimental data for both uniform and perturbed inlet conditions.

Furthermore, the methodology develops a model to predict the temperature flow field downstream of the stator when swirling EW or HS are injected at stage inlet. The model relies solely on the inlet temperature disturbance distribution and the mass flow distribution of the *Clean* case at the stator outlet. By leveraging geometrical considerations and power balances, the model accurately determines the location and circumferential-radial extension of the temperature disturbance.

Finally, a simplified model is developed to predict the peak-to-temperature decay through the rotor and the radial shift of the temperature disturbance, taking the form of a correlation that depends on the rotor loading coefficient and a Helmholtz number. Overall, the analysis provides insights into the impact of combustor non-uniformities on the aero-thermal flow field of the rotor, with significant implications for turbine design and performance.

8.2 Outlooks

The first aspect that requires further investigation is the development of an acoustic post-processing tool that provides reliable results for simulations carried out at DLR. Although all test cases have been simulated, the complex and non-uniform flow field downstream of the rotor has made it difficult to obtain accurate results in terms of aero-acoustics. Further analysis is needed to fully characterize turbine acoustics using the Harmonic Balance code.

Colleagues at the CERFACS have requested the geometry of the combustor simulator to conduct LES simulations on the wind tunnel experiments described in section 4.2, thereby improving the numerical setup. This will facilitate an in-depth study of the generation and decay of turbulence.

Despite the considerable efforts made to create turbine experiments that are as representative of real engines as possible, there is still room for improvement in future work. However, with the extensive data set available, the most straightforward course of action is to validate CFD codes and use them to advance research in the following areas.

The absence of cooling flows in the turbine test section is a crucial limitation as it affects the temperature decay of the perturbation, which in turn can lead to discrepancies when comparing experimental results with real engines. Section 6.3 addresses this topic, highlighting the impact that cooling flows may have on the aero-thermal flow field. This discussion needs to be verified by means of future experimental or numerical studies.

In addition to investigating combustor non-uniformities, an important feature to superimpose is the effect of cavities and purge flows. These flows are inevitably present in real engines and can impact the aero-thermal flow field by altering the aerodynamics, changing the flow patterns, and increasing the overall turbulence. A better understanding of the interaction between cavities and purge flows with combustor non-uniformities could potentially lead to improved designs of real engines.

From an experimental point of view, it would be valuable to evaluate the heat exchange and the resulting local blade temperature increase caused by the impinging temperature disturbances. The transport of these disturbances is crucial in the design of cooling systems, but this information must be coupled with data on local blade temperatures and heat transfer coefficients.

Finally, an investigation of the impact of changing the combustor simulator-vane blade count on the turbine aero-thermal flow field could be conducted to gain a better understanding of the flow behavior.

In addition to conducting CFD on the previously mentioned topics, further future studies are limited to CFD analysis. One of the primary focuses would be to understand the discrepancies observed for turbine efficiency in off-design conditions and the simulations of the entire experimental test cases.

While the frequency of the EW is currently constrained by the available devices, it would be valuable to investigate the effects of increasing the frequency to values approaching the blade passing frequency. This analysis could reveal potential frequency-dependent interactions that may occur.

Furthermore, the extensive measurement campaign conducted downstream of the combustor simulator has provided all the necessary data to carry out high-fidelity CFD simulations on the turbine stage.

To conclude, future CFD investigations should aim to simulate the engine environment as closely as possible by increasing the temperature, maintaining the ratio between temperature disturbances and mainstream, and increasing the inlet pressure. These changes would impact the turbulent diffusion and the non-dimensional numbers in the simulations, providing a more realistic representation of the flow field.

REFERENCES

Adams, M. G., Beard, P. F., Stokes, M. R., Wallin, F., Chana, K. S. & Povey, T. 2021 Effect of a Combined Hot-Streak and Swirl Profile on Cooled 1.5-Stage Turbine Aerodynamics: An Experimental and Computational Study. *Journal of Turbomachinery* **143** (2), 021011, arXiv: https://asmedigitalcollection.asme.org/turbomachinery/article-pdf/143/2/021011/6626881/turbo_143_2_021011.pdf.

Adams, M. G., Povey, T., Hall, B. F., Cardwell, D. N., Chana, K. S. & Beard, P. F. 2020 Commissioning of a Combined Hot-Streak and Swirl Profile Generator in a Transonic Turbine Test Facility. *Journal of Engineering for Gas Turbines and Power* **142** (3), 031008, arXiv: https://asmedigitalcollection.asme.org/gasturbinespower/article-pdf/142/3/031008/6509286/gtp_142_03_031008.pdf.

Aungier, R. H. 2006 *Turbine Aerodynamics: Axial-Flow and Radial-Flow Turbine Design and Analysis*. ASME Press.

Bacci, T., Becchi, R., Picchi, A. & Facchini, B. 2019 Adiabatic Effectiveness on High-Pressure Turbine Nozzle Guide Vanes Under Realistic Swirling Conditions. *Journal of Turbomachinery* **141** (1), 011009, arXiv: https://asmedigitalcollection.asme.org/turbomachinery/article-pdf/141/1/011009/6310498/turbo_141_01_011009.pdf.

Bacci, T., Caciolli, G., Facchini, B., Tarchi, L., Koupper, C. & Champion, J.-L. 2015*a* Flowfield and Temperature Profiles Measurements on a Combustor Simulator Dedicated to Hot Streaks Generation **Volume 5C: Heat Transfer**, v05CT17A001, arXiv: https://asmedigitalcollection.asme.org/GT/proceedings-pdf/GT2015/56734/V05CT17A001/4237694/v05ct17a001-gt2015-42217.pdf.

Bacci, T., Facchini, B., Picchi, A., Tarchi, L., Koupper, C. & Champion, J.-L. 2015*b* Turbulence Field Measurements at the Exit of a Combustor Simulator Dedicated to Hot Streaks Generation. *Turbo Expo: Power for Land, Sea, and Air*, vol. Volume 5C: Heat Transfer. V05CT17A002, arXiv: https://asmedigitalcollection.asme.org/GT/proceedings-pdf/GT2015/56734/V05CT17A002/4237714/v05ct17a002-gt2015-42218.pdf.

Bacci, T., Picchi, A., Babazzi, G., Facchini, B. & Cubeda, S. 2023 Heat Transfer Coefficient and Adiabatic Wall Temperature Measurements on High-Pressure Turbine Nozzle Guide Vanes With Representative Inlet Swirl and Temperature Distortions. *Journal of Turbomachinery* **145** (7), 071010, arXiv: https://asmedigitalcollection.asme.org/turbomachinery/article-pdf/145/7/071010/6979618/turbo_145_7_071010.pdf.

Bach, T., Huet, M., Watson, R., Spence, S. & Mahmoudi, Y. 2021 Effect of film cooling on entropy noise generation in a stator blade row. *AIAA Journal* **59** (8), 3071–3086, arXiv: https://doi.org/10.2514/1.J060077.

Badžek, E., Patinios, M., Farisco, F., Heitmeir, F. & Göttlich, E. 2022 The Influence of Combustor Hot Streaks on the Aerodynamic Performance of a Turbine Center Frame. *Journal of Turbomachinery* **145** (2), 021009, arXiv: https://asmedigitalcollection.asme.org/turbomachinery/article-pdf/145/2/021009/6926924/turbo_145_2_021009.pdf.

Bake, F., Gaetani, P., Persico, G., Neuhaus, L. & Knobloch, K. 2016 *Indirect Noise Generation in a High Pressure Turbine Stage*, arXiv: https://arc.aiaa.org/doi/pdf/10.2514/6.2016-3004.

Bake, F., Richter, C., Mühlbauer, B., Kings, N., Röhle, I., Thiele, F. & Noll, B. 2009 The entropy wave generator (ewg): A reference case on entropy noise. *Journal of Sound and Vibration* **326** (3), 574–598.

Barigozzi, G., Mosconi, S., Perdichizzi, A. & Ravelli, S. 2017 The effect of hot streaks on a high pressure turbine vane cascade with showerhead film cooling. *International Journal of Turbomachinery, Propulsion and Power* **2** (3).

Beard, P. F., Smith, A. & Povey, T. 2013 Impact of Severe Temperature Distortion on Turbine Efficiency. *Journal of Turbomachinery* **135** (1), 011018, arXiv: https://asmedigitalcollection.asme.org/turbomachinery/article-pdf/135/1/011018/6294410/turb_135_1_011018.pdf.

Beard, P. F., Smith, A. D. & Povey, T. 2014 Effect of Combustor Swirl on Transonic High Pressure Turbine Efficiency. *Journal of Turbomachinery* **136** (1), 011002, arXiv: https://asmedigitalcollection.asme.org/turbomachinery/article-pdf/136/1/011002/6296876/turbo_136_01_011002.pdf.

Benner, M. W., Sjolander, S. A. & Moustapha, S. H. 1997 Influence of Leading-Edge Geometry on Profile Losses in Turbines at Off-Design Incidence: Experimental Results and an Improved Correlation. *Journal of Turbomachinery* **119** (2), 193–200, arXiv: https://asmedigitalcollection.asme.org/turbomachinery/article-pdf/119/2/193/5507375/193_1.pdf.

Benner, M. W., Sjolander, S. A. & Moustapha, S. H. 2005 An Empirical Prediction Method For Secondary Losses In Turbines—Part II: A New Secondary Loss Correlation. *Journal of Turbomachinery* **128** (2), 281–291, arXiv: https://asmedigitalcollection.asme.org/turbomachinery/article-pdf/128/2/281/5551059/281_1.pdf.

Boudier, G., Gicquel, L.Y.M., Poinsot, T., Bissières, D. & Bérat, C. 2007 Comparison of les, rans and experiments in an aeronautical gas turbine combustion chamber. *Proceedings of the Combustion Institute* **31** (2), 3075–3082.

Brind, J. & Pullan, G. 2021 Modelling turbine acoustic impedance. *International Journal of Turbomachinery, Propulsion and Power* **6** (2).

Bruun, H. H. 1995 *Hot-Wire Anemometry*. Oxford University Press.

Burberi, C., Ghignoni, E., Pinelli, L. & Marconcini, M. 2018 Validation of an urans approach for direct and indirect noise assessment in a high pressure turbine stage. *Energy Procedia* **148**, 130–137, aTI 2018 - 73rd Conference of the Italian Thermal Machines Engineering Association.

Buresti, G & Di Cocco, N. R. 1987 Hot-wire measurement procedures and their appraisal through a simulation technique. *Journal of Physics E: Scientific Instruments* **20** (1), 87.

Butler, T. L., Sharma, O. P., Joslyn, H. D. & Dring, R. P. 1989 Redistribution of an inlet temperature distortion in an axial flow turbine stage. *Journal of Propulsion and Power* **5** (1), 64–71, arXiv: https://doi.org/10.2514/3.23116.

Cha, C. M., Hong, S., Ireland, P. T., Denman, P. & Savarianandam, V. 2012*a* Experimental and Numerical Investigation of Combustor-Turbine Interaction Using an Isothermal, Nonreacting Tracer. *Journal of Engineering for Gas Turbines and Power* **134** (8), 081501, arXiv: https://asmedigitalcollection.asme.org/gasturbinespower/article-pdf/134/8/081501/5703223/081501_1.pdf.

Cha, C. M., Ireland, P. T., Denman, P. A. & Savarianandam, V. 2012*b* Turbulence Levels are High at the Combustor-Turbine Interface. *Turbo Expo: Power for Land, Sea, and Air*, vol. Volume 8: Turbomachinery, Parts A, B, and C, pp. 1371–1390, arXiv: https://asmedigitalcollection.asme.org/GT/proceedings-pdf/GT2012/44748/1371/4233269/1371_1.pdf.

Cheng, W., Pullin, D. I., Samtaney, R., Zhang, W. & Gao, W. 2017 Large-eddy simulation of flow over a cylinder with re_D from 3.9×10^3 to 8.5×10^5: a skin-friction perspective. *Journal of Fluid Mechanics* **820**, 121–158.

Christodoulou, L., Karimi, N., Cammarano, A., Paul, M. & Navarro-Martinez, S. 2020 State prediction of an entropy wave advecting through a turbulent channel flow. *Journal of Fluid Mechanics* **882**, A8.

Chu, B.-T. & Kovásznay, L. S. G. 1958 Non-linear interactions in a viscous heat-conducting compressible gas. *Journal of Fluid Mechanics* **3** (5), 494–514.

Craig, H. R. M. & Cox, H. J. A. 1970 Performance estimation of axial flow turbines. *Proceedings of the Institution of Mechanical Engineers* **185** (1), 407–424, arXiv: https://doi.org/10.1243/PIME$_P ROC_1 970_1 85_0 48_0 2$.

Cumpsty, N. A., Marble, F. E. & Hawthorne, W. R. 1977 The interaction of entropy fluctuations with turbine blade rows; a mechanism of turbojet engine noise. *Proceedings of the Royal Society of London. A. Mathematical and Physical Sciences* **357** (1690), 323–344, arXiv: https://royalsocietypublishing.org/doi/pdf/10.1098/rspa.1977.0171.

Denton, J. D. & Xu, L. 1998 The exploitation of three-dimensional flow in turbomachinery design. *Proceedings of the Institution of Mechanical Engineers, Part C: Journal of Mechanical Engineering Science* **213**, 125 – 137.

Dorney, D. J. 1997 Investigation of hot streak temperature ratio scaling effects. *International Journal of Turbo and Jet Engines* **14** (4), 217–228.

Dowling, A. P. & Hubbard, S 2000 Instability in lean premixed combustors. *Proceedings of the Institution of Mechanical Engineers, Part A: Journal of Power and Energy* **214** (4), 317–332, arXiv: https://doi.org/10.1243/0957650001537903.

Dowling, A. P. & Mahmoudi, Y. 2015 Combustion noise. *Proceedings of the Combustion Institute* **35** (1), 65–100.

Dowling, A. P. & Stow, S. R. 2003 Acoustic analysis of gas turbine combustors. *Journal of Propulsion and Power* **19** (5), 751–764, arXiv: https://doi.org/10.2514/2.6192.

D'Ippolito, G., Dossena, V. & Mora, A. 2011 The Influence of Blade Lean on Straight and Annular Turbine Cascade Flow Field. *Journal of Turbomachinery* **133** (1), 011013, arXiv: https://asmedigitalcollection.asme.org/turbomachinery/article-pdf/133/1/011013/5845384/011013_1.pdf.

European Commission and Directorate-General for Research and Innovation 2002 *European aeronautics : a vision for 2020*. Publications Office.

European Commission, Directorate-General for Mobility and Transport, Directorate-General for Research and Innovation 2011 *Flightpath 2050 : Europe's vision for aviation : maintaining global leadership and serving society's needs*. Publications Office.

Fitouri, A., Khan, M. K. & Bruun, H. H. 1995 A multiposition hot-wire technique for the study of swirling flows in vortex chambers. *Experimental Thermal and Fluid Science* **10** (1), 142–151.

Flay, R. G. J & Stevenson, D. C. 1986 Integral length scales in an atmospheric boundary-layer near the ground. In *9th Australasian Fluid Mechanics Conference, Auckland*.

Folk, M., Miller, R. J. & Coull, J. D. 2020 The Impact of Combustor Turbulence on Turbine Loss Mechanisms. *Journal of Turbomachinery* **142** (9), 091009, arXiv: https://asmedigitalcollection.asme.org/turbomachinery/article-pdf/142/9/091009/6559796/turbo_142_9_091009.pdf.

Foust, M., Thomsen, D., Stickles, R., Cooper, C. & Dodds, W. 2012 Development of the ge aviation low emissions taps combustor for next generation aircraft engines. In *50th AIAA Aerospace Sciences Meeting including the New Horizons Forum and Aerospace Exposition*, arXiv: https://arc.aiaa.org/doi/pdf/10.2514/6.2012-936.

Gaetani, P. & Persico, G. 2017 Hot streak evolution in an axial hp turbine stage. *International Journal of Turbomachinery, Propulsion and Power* **2** (2).

Gaetani, P. & Persico, G. 2019 Transport of Entropy Waves Within a High Pressure Turbine Stage. *Journal of Turbomachinery* **141** (3), 031006, arXiv: https://asmedigitalcollection.asme.org/turbomachinery/article-pdf/141/3/031006/6310535/turbo_141_03_031006.pdf.

Gaetani, P., Persico, G., Pinelli, L., Marconcini, M. & Pacciani, R. 2020 Computational and Experimental Study of Hot Streak Transport Within the First Stage of a Gas Turbine. *Journal of Turbomachinery* **142** (8), 081002, arXiv: https://asmedigitalcollection.asme.org/turbomachinery/article-pdf/142/8/081002/6553217/turbo_142_8_081002.pdf.

Gicquel, L. Y. M., Staffelbach, G. & Poinsot, T. 2012 Large eddy simulations of gaseous flames in gas turbine combustion chambers. *Progress in Energy and Combustion Science* **38** (6), 782–817.

Giles, M. B. 1990 Nonreflecting boundary conditions for euler equation calculations. *AIAA Journal* **28** (12), 2050–2058, arXiv: https://doi.org/10.2514/3.10521.

Giusti, A., Worth, N. A., Mastorakos, E. & Dowling, A. P. 2017 Experimental and numerical investigation into the propagation of entropy waves. *AIAA Journal* **55** (2), 446–458, arXiv: https://doi.org/10.2514/1.J055199.

Goebel, S. G., Abuaf, N., Lovett, J. A. & Lee, C.-P. 1993 Measurements of Combustor Velocity and Turbulence Profiles. *Turbo Expo: Power for Land, Sea, and Air*, vol. Volume 3A: General. V03AT15A079, arXiv: https://asmedigitalcollection.asme.org/GT/proceedings-pdf/GT1993/78903/V03AT15A079/2403384/v03at15a079-93-gt-228.pdf.

Goldstein, R. J., Lau, K. Y. & Leung, C. C. 1983 Velocity and turbulence measurements in combustion systems. *Experiments in Fluids* **1** (2), 93–99.

Gregory-Smith, D. G. 1982 Secondary Flows and Losses in Axial Flow Turbines. *Journal of Engineering for Power* **104** (4), 819–822, arXiv: https://asmedigitalcollection.asme.org/gasturbinespower/article-pdf/104/4/819/5722188/819_1.pdf.

Greifenstein, M., Heinze, J., Willert, C., Voigt, L., Zedda, M., Richter, C. & Dreizler, A. 2020 Time-resolved temperature profile measurements in the exhaust of a single sector gas turbine combustor at realistic operating conditions. *Experiments in Fluids* **61** (8), 177.

Guzmán-Iñigo, J., Durán, I. & Morgans, A.S. 2021 Scattering of entropy waves into sound by isolated aerofoils. *Journal of Fluid Mechanics* **923**, A10.

Hall, B. F., Chana, K. S. & Povey, T. 2014 Design of a Nonreacting Combustor Simulator With Swirl and Temperature Distortion With Experimental Validation. *Journal of Engineering for Gas Turbines and Power* **136** (8), 081501, arXiv: https://asmedigitalcollection.asme.org/gasturbinespower/article-pdf/136/8/081501/6161761/gtp_136_08_081501.pdf.

Hawthorne, W.R. 1955 *Some Formulae for the Calculation of Secondary Flow Ion Cascades*. Department of Engineering, University of Cambridge.

Hawthorne, W. R. 1951 Secondary circulation in fluid flow. *Proceedings of the Royal Society of London. Series A. Mathematical and Physical Sciences* **206** (1086), 374–387, arXiv: https://royalsocietypublishing.org/doi/pdf/10.1098/rspa.1951.0076.

He, L., Menshikova, V. & Haller, B. R. 2004 Influence of Hot Streak Circumferential Length-Scale in Transonic Turbine Stage. *Turbo Expo: Power for Land, Sea, and Air*, vol. Volume 5: Turbo Expo 2004, Parts A and B, pp. 1117–1126, arXiv: https://asmedigitalcollection.asme.org/GT/proceedings-pdf/GT2004/41707/1117/2608104/1117_1.pdf.

Heitor, M. V. & Whitelaw, J. H. 1986 Velocity, temperature, and species characteristics of the flow in a gas-turbine combustor. *Combustion and Flame* **64** (1), 1–32.

Huet, M. & Geiger, L. 2022 Modeling of indirect combustion noise through a stator. *Journal of Sound and Vibration* **540**, 117296.

Huet, M. & Giauque, A. 2013 A nonlinear model for indirect combustion noise through a compact nozzle. *Journal of Fluid Mechanics* **733**, 268–301.

International Air Transport Association 2019 *Annual Review*.

International Civil Aviation Organization 2010 Committee on aviation environmental protection, eighth meeting. *Tech. Rep.*.

Jacobi, S., Mazzoni, C., Rosic, B. & Chana, K. 2017 Investigation of Unsteady Flow Phenomena in First Vane Caused by Combustor Flow With Swirl. *Journal of Turbomachinery* **139** (4), 041006, arXiv: https://asmedigitalcollection.asme.org/turbomachinery/article-pdf/139/4/041006/6305208/turbo_139_04_041006.pdf.

James, S., Zhu, J. & Anand, M. S. 2006 Large-eddy simulations as a design tool for gas turbine combustion systems. *AIAA Journal* **44** (4), 674–686, arXiv: https://doi.org/10.2514/1.15390.

JCGM 2008 Evaluation of measurement data — supplement 1 to the“guide to the expression of uncertainty in measurement” —propagation of distributions using a monte carlo method. *Tech. Rep.*. JCGM 101:2008.

Jenkins, S., Varadarajan, K. & Bogard, D. G. 2004 The Effects of High Mainstream Turbulence and Turbine Vane Film Cooling on the Dispersion of a Simulated Hot Streak . *Journal of Turbomachinery* **126** (1), 203–211, arXiv: https://asmedigitalcollection.asme.org/turbomachinery/article-pdf/126/1/203/5634703/203_1.pdf.

Jenkins, S. C. & Bogard, D. G. 2005 The Effects of the Vane and Mainstream Turbulence Level on Hot Streak Attenuation . *Journal of Turbomachinery* **127** (1), 215–221, arXiv: https://asmedigitalcollection.asme.org/turbomachinery/article-pdf/127/1/215/5843610/215_1.pdf.

Jenkins, S. C. & Bogard, D. G. 2009 Superposition Predictions of the Reduction of Hot Streaks by Coolant From a Film-Cooled Guide Vane. *Journal of Turbomachinery* **131** (4), 041002, arXiv: https://asmedigitalcollection.asme.org/turbomachinery/article-pdf/131/4/041002/5845604/041002_1.pdf.

Kacker, S. C. & Okapuu, U. 1982 A Mean Line Prediction Method for Axial Flow Turbine Efficiency. *Journal of Engineering for Power* **104** (1), 111–119, arXiv: https://asmedigitalcollection.asme.org/gasturbinespower/article-pdf/104/1/111/5529077/111_1.pdf.

Kaiser, T. L., Noiray, N., Male, Q. & Oberleithner, K. 2022 Modeling the Convection of Entropy Waves in Strongly Non-Parallel Turbulent Flows Using a Linearized Framework. *Turbo Expo: Power for Land, Sea, and Air*, vol. Volume 3B: Combustion, Fuels, and Emissions. V03BT04A039, arXiv: https://asmedigitalcollection.asme.org/GT/proceedings-pdf/GT2022/86007/V03BT04A039/6935235/v03bt04a039-gt2022-82971.pdf.

Kampmann, S., Leipertz, A., Döbbeling, K., Haumann, J. & Sattelmayer, T. 1993 Two-dimensional temperature measurements in a technical combustor with laser rayleigh scattering. *Appl. Opt.* **32** (30), 6167–6172.

Kerrebrock, J. L. & Mikolajczak, A. A. 1970 Intra-Stator Transport of Rotor Wakes and Its Effect on Compressor Performance. *Journal of Engineering for Power* **92** (4), 359–368, arXiv: https://asmedigitalcollection.asme.org/gasturbinespower/article-pdf/92/4/359/5804656/359_1.pdf.

Khanal, B., He, L., Northall, J. & Adami, P. 2013 Analysis of Radial Migration of Hot-Streak in Swirling Flow Through High-Pressure Turbine Stage. *Journal of Turbomachinery* **135** (4), 041005, arXiv: https://asmedigitalcollection.asme.org/turbomachinery/article-pdf/135/4/041005/6295565/turb_135_4_041005.pdf.

Knobloch, K., Neuhaus, L., Bake, F., Gaetani, P. & Persico, G. 2017 Experimental Assessment of Noise Generation and Transmission in a High-Pressure Transonic Turbine Stage. *Journal of Turbomachinery* **139** (10), 101006, arXiv: https://asmedigitalcollection.asme.org/turbomachinery/article-pdf/139/10/101006/6306354/turbo_139_10_101006.pdf.

Koupper, C., Caciolli, G., Gicquel, L., Duchaine, F., Bonneau, G., Tarchi, L. & Facchini, B. 2014 Development of an Engine Representative Combustor Simulator Dedicated to Hot Streak Generation. *Journal of Turbomachinery* **136** (11), 111007, arXiv: https://asmedigitalcollection.asme.org/turbomachinery/article-pdf/136/11/111007/6300400/turbo_136_11_111007.pdf.

Kundu, P. K.; Cohen, I. M. & Dowling, D. R. 2012 *Fluid Mechanics*.

Lakshminarayana, B. & Horlock, J. H. 1973 Generalized expressions for secondary vorticity using intrinsic co-ordinates. *Journal of Fluid Mechanics* **59** (1), 97–115.

Lazik, W., Doerr, T., Bake, S., v. d. Bank, R. & Rackwitz, L. 2008 Development of Lean-Burn Low-NOx Combustion Technology at Rolls-Royce Deutschland. In *Turbo Expo: Power for Land, Sea, and Air*, , vol. Volume 3: Combustion, Fuels and Emissions, Parts A and B, pp. 797–807.

Lefebvre, A. H. 1983 *Gas Turbine Combustion*. Taylor.

Leyko, M., Nicoud, F. & Poinsot, T. 2009 Comparison of direct and indirect combustion noise mechanisms in a model combustor. *AIAA Journal* **47** (11), 2709–2716, arXiv: https://doi.org/10.2514/1.43729.

Liu, Z., Liu, Z. & Feng, Z. 2014 Unsteady Analysis on the Effects of Tip Clearance Height on Hot Streak Migration Across Rotor Blade Tip Clearance. *Journal of Engineering for Gas Turbines and Power* **136** (8), 082605, arXiv: https://asmedigitalcollection.asme.org/gasturbinespower/article-pdf/136/8/082605/6162277/gtp_136_08_082605.pdf.

Lubbock, R. J. & Oldfield, M. L. G. 2018 Turbulent velocity and pressure fluctuations in gas turbine combustor exit flows. *Proceedings of the Institution of Mechanical Engineers, Part A: Journal of Power and Energy* **232** (4), 337–349, arXiv: https://doi.org/10.1177/0957650917732885.

Mansouri, Z. & Jefferson-Loveday, R. 2022 Heat transfer characteristics of a high-pressure turbine under combined distorted hot-streak and residual swirl: an unsteady computational study. *International Journal of Heat and Mass Transfer* **195**, 123143.

Marble, F. E. & Candel, S. M. 1977 Acoustic disturbance from gas non-uniformities convected through a nozzle. *Journal of Sound and Vibration* **55** (2), 225–243.

Massardo, A. & Satta, A. 1985 A Correlation for the Secondary Deviation Angle. *Turbo Expo: Power for Land, Sea, and Air*, vol. Volume 1: Aircraft Engine; Turbomachinery. V001T02A014, arXiv: https://asmedigitalcollection.asme.org/GT/proceedings-pdf/IGT1985/79429/V001T02A014/2477432/v001t02a014-85-igt-36.pdf.

McGuirk, J. J. 2014 The aerodynamic challenges of aeroengine gas-turbine combustion systems. *The Aeronautical Journal* **118** (1204), 557–599.

McKay, M. D., Beckman, R. J. & Conover, W. J. 1979 A comparison of three methods for selecting values of input variables in the analysis of output from a computer code. *Technometrics* **21** (2), 239–245.

Medic, G., You, D., Kalitzin, G., Herrmann, M., Ham, F., Pitsch, H., van der Weide, E. & Alonso, J. 2007 Integrated Computations of an Entire Jet Engine. *Turbo Expo: Power for Land, Sea, and Air*, vol. Volume 6: Turbo Expo 2007, Parts A and B, pp. 1841–1847, arXiv: https://asmedigitalcollection.asme.org/GT/proceedings-pdf/GT2007/47950/1841/2677331/1841_1.pdf.

Miki, K., Wey, T. & Moder, J. 2022 Computational study on fully coupled combustor–turbine interactions. *Journal of Propulsion and Power* **0** (0), 1–14, arXiv: https://doi.org/10.2514/1.B38501.

Moin, P. & Apte, S. V. 2006 Large-eddy simulation of realistic gas turbine combustors. *AIAA Journal* **44** (4), 698–708, arXiv: https://doi.org/10.2514/1.14606.

Mongia, H. 2003 Taps: A fourth generation propulsion combustor technology for low emissions. In *AIAA International Air and Space Symposium and Exposition: The Next 100 Years*, arXiv: https://arc.aiaa.org/doi/pdf/10.2514/6.2003-2657.

Morfey, C. L. 1973 Amplification of aerodynamic noise by convected flow inhomogeneities. *Journal of Sound and Vibration* **31** (4), 391–397.

Morgans, A. S., Goh, C. S. & Dahan, J. A. 2013 The dissipation and shear dispersion of entropy waves in combustor thermoacoustics. *Journal of Fluid Mechanics* **733**, R2.

Moss, R. W. & Oldfield, M. L. G. 1991 Measurements of Hot Combustor Turbulence Spectra. *Turbo Expo: Power for Land, Sea, and Air*, vol. Volume 4: Heat Transfer; Electric Power; Industrial and Cogeneration. V004T09A025, arXiv: https://asmedigitalcollection.asme.org/GT/proceedings-pdf/GT1991/79016/V004T09A025/2401143/v004t09a025-91-gt-351.pdf.

Munk, M. & Prim, R. 1947 On the multiplicity of steady gas flows having the same streamline pattern. *Proceedings of the National Academy of Sciences of the United States of America* **33**, 137–41.

Ong, J. & Miller, R. J. 2012 Hot Streak and Vane Coolant Migration in a Downstream Rotor. *Journal of Turbomachinery* **134** (5), 051002, arXiv: https://asmedigitalcollection.asme.org/turbomachinery/article-pdf/134/5/051002/5851179/051002_1.pdf.

Park, H. D. & Chung, M. K. 1992 Refinement of spanwise distribution models of deviation angle and secondary loss for axial flow turbine. *Mechanics Research Communications* **19** (5), 449–455.

Passmann, M., aus der Wiesche, S., Povey, T. & Bergmann, D. 2021 Effect of Reynolds Number on Five-Hole Probe Performance: Experimental Study of the Open-Access Oxford Probe. *Journal of Turbomachinery* **143** (9), 091003, arXiv: https://asmedigitalcollection.asme.org/turbomachinery/article-pdf/143/9/091003/6737966/turbo_143_9_091003.pdf.

Perdichizzi, A., Ubaldi, M. & Zunino, P. 1990 A hot wire measuring technique for mean velcity and reynolds stress components in compressible flow. In *Proceedings of the X Biannual Symposium on Measuring Techniques in Turbomachinery, Sint-Genesius-Rode, Belgium.*.

Persico, G., Dossena, V. & Gaetani, P. 2010 On the capability of fast response total pressure probes to measure turbulence kinetic energy. In *XX Biannual Symposium on Measuring Techniques in TurbomachineryTransonic and Supersonic Flow in Cascades and Turbomachines*.

Persico, G, Gaetani, P & Guardone, A 2005 Dynamic calibration of fast-response probes in low-pressure shock tubes. *Measurement Science and Technology* **16** (9), 1751.

Persico, G., Gaetani, P. & Paradiso, B. 2008 Estimation of turbulence by single-sensor pressure probes. In *Proceedings of the XIX Biannual Symposium on Measuring Techniques in Turbomachinery Transonic and Supersonic Flow in Cascades and Turbomachines*.

Persico, G., Gaetani, P. & Spinelli, A. 2017 Assessment of synthetic entropy waves for indirect combustion noise experiments in gas turbines. *Experimental Thermal and Fluid Science* **88**, 376–388.

Pinelli, L., Marconcini, M., Pacciani, R., Bake, F., Knobloch, K., Gaetani, P. & Persico, G. 2022 Effect of clocking on entropy noise generation within an aeronautical high pressure turbine stage. *Journal of Sound and Vibration* **529**, 116900.

Pinelli, L., Marconcini, M., Pacciani, R., Gaetani, P. & Persico, G. 2021 Computational and Experimental Study of the Unsteady Convection of Entropy Waves Within a High-Pressure Turbine Stage. *Journal of Turbomachinery* **143** (9), 091011, arXiv: https://asmedigitalcollection.asme.org/turbomachinery/article-pdf/143/9/091011/6696466/turbo_143_9_091011.pdf.

Povey, T., Chana, K. S., Jones, T. V. & Hurrion, J. 2005 The Effect of Hot-Streaks on HP Vane Surface and Endwall Heat Transfer: An Experimental and Numerical Study. *Journal of Turbomachinery* **129** (1), 32–43, arXiv: https://asmedigitalcollection.asme.org/turbomachinery/article-pdf/129/1/32/5942432/32_1.pdf.

Povey, T. & Qureshi, I. 2009 Developments in Hot-Streak Simulators for Turbine Testing. *Journal of Turbomachinery* **131** (3), 031009, arXiv: https://asmedigitalcollection.asme.org/turbomachinery/article-pdf/131/3/031009/5845004/031009_1.pdf.

Prasad, D. & Hendricks, G. J. 2000 A Numerical Study of Secondary Flow in Axial Turbines With Application to Radial Transport of Hot Streaks . *Journal of Turbomachinery* **122** (4), 667–673, arXiv: https://asmedigitalcollection.asme.org/turbomachinery/article-pdf/122/4/667/5842680/667_1.pdf.

Qureshi, I., Beretta, A., Chana, K. & Povey, T. 2012 Effect of Aggressive Inlet Swirl on Heat Transfer and Aerodynamics in an Unshrouded Transonic HP Turbine. *Journal of Turbomachinery* **134** (6), 061023, arXiv: https://asmedigitalcollection.asme.org/turbomachinery/article-pdf/134/6/061023/5851109/061023_1.pdf.

Qureshi, I & Povey, T 2011 A combustor-representative swirl simulator for a transonic turbine research facility. *Proceedings of the Institution of Mechanical Engineers, Part G: Journal of Aerospace Engineering* **225** (7), 737–748, arXiv: https://doi.org/10.1177/0954410011400817.

Qureshi, I., Smith, A. D. & Povey, T. 2013 HP Vane Aerodynamics and Heat Transfer in the Presence of Aggressive Inlet Swirl. *Journal of Turbomachinery* **135** (2), 021040, arXiv: https://asmedigitalcollection.asme.org/turbomachinery/article-pdf/135/2/021040/6298645/turb_135_2_021040.pdf.

Rahim, A. & He, L. 2015 Rotor Blade Heat Transfer of High Pressure Turbine Stage Under Inlet Hot-Streak and Swirl. *Journal of Engineering for Gas Turbines and Power* **137** (6), 062601, arXiv: https://asmedigitalcollection.asme.org/gasturbinespower/article-pdf/137/6/062601/6165953/gtp_137_06_062601.pdf.

Roach, P. E. 1987 The generation of nearly isotropic turbulence by means of grids. *International Journal of Heat and Fluid Flow* **8** (2), 82–92.

Sattelmayer, T. 2003 Influence of the Combustor Aerodynamics on Combustion Instabilities From Equivalence Ratio Fluctuations . *Journal of Engineering for Gas Turbines and Power* **125** (1), 11–19, arXiv: https://asmedigitalcollection.asme.org/gasturbinespower/article-pdf/125/1/11/5565588/11_1.pdf.

Schlichting, H. & Gersten, K. 2017 *Boundary-Layer Theory*.

Schroll, M., Doll, U., Stockhausen, G., Meier, U., Willert, C., Hassa, C. & Bagchi, I. 2016 Flow Field Characterization at the Outlet of a Lean Burn Single-Sector Combustor by Laser-Optical Methods. *Journal of Engineering for Gas Turbines and Power* **139** (1), 011503, arXiv: https://asmedigitalcollection.asme.org/gasturbinespower/article-pdf/139/1/011503/6173305/gtp_139_01_011503.pdf.

Shang, T. & Epstein, A. H. 1997 Analysis of Hot Streak Effects on Turbine Rotor Heat Load. *Journal of Turbomachinery* **119** (3), 544–553, arXiv: https://asmedigitalcollection.asme.org/turbomachinery/article-pdf/119/3/544/5631572/544_1.pdf.

Simone, S., Montomoli, F., Martelli, F., Chana, K. S., Qureshi, I. & Povey, T. 2011 Analysis on the Effect of a Nonuniform Inlet Profile on Heat Transfer and Fluid Flow in Turbine Stages. *Journal of Turbomachinery* **134** (1), 011012, arXiv: https://asmedigitalcollection.asme.org/turbomachinery/article-pdf/134/1/011012/5849707/011012_1.pdf.

Strahle, W. C. 1978 Combustion noise. *Progress in Energy and Combustion Science* **4** (3), 157–176.

Tomasello, S. G., Andreini, A., Meloni, R., Cubeda, S., Andrei, L. & Michelassi, V. 2022 Numerical Study of Combustor-Turbine Interaction by Using Hybrid RANS-LES Approach. *Turbo Expo: Power for Land, Sea, and Air*, vol. Volume 6A: Heat Transfer — Combustors; Film Cooling. V06AT11A005, arXiv: https://asmedigitalcollection.asme.org/GT/proceedings-pdf/GT2022/86038/V06AT11A005/6935713/v06at11a005-gt2022-82139.pdf.

Wang, Z., Wang, D., Wang, Z. & Feng, Z. 2018 Heat transfer analyses of film-cooled hp turbine vane considering effects of swirl and hot streak. *Applied Thermal Engineering* **142**, 815–829.

Wang, Z., Wang, Z., Zhang, W. & Feng, Z. 2021 Numerical study on unsteady film cooling performance of turbine rotor considering influences of inlet non-uniformities and upstream coolant. *Aerospace Science and Technology* **119**, 107089.

Werschnik, H., Schiffer, H.-P. & Steinhausen, C. 2017*a* Robustness of a turbine endwall film cooling design to swirling combustor inflow. *Journal of Propulsion and Power* **33** (4), 917–926, arXiv: https://doi.org/10.2514/1.B36138.

Werschnik, H., Schneider, M., Herrmann, J., Ivanov, D., Schiffer, H.-P. & Lyko, C. 2017*b* The influence of combustor swirl on pressure losses and the propagation of coolant flows at the large scale turbine rig (lstr): Experimental and numerical investigation. *International Journal of Turbomachinery, Propulsion and Power* **2** (3).

Zhang, S., Ding, S., Liu, P. & Qiu, T. 2022 Effect of hot streak on aerothermal performance of high pressure turbine guide vane under different swirl intensities. *Aerospace* **9** (10).

Zimmerman, D. B. 1979 Laser anemometer measurements at the exit of a T63-C20 combustor. Final Report, Sep. 1978 - Apr. 1979 Detroit Diesel Allison, Indianapolis, IN.

NOMENCLATURE

Acronyms/Abbreviations

AR	Aspect ratio
CERFACS	Centre Européen de Recherche et de Formation Avancée en Calcul Scientifique
CFD	Computational fluid dynamics
CFL	Courant–Friedrichs–Lewy number
CS	Cold streak
DLR	Deutsches Zentrum für Luft- und Raumfahrt
DNS	Direct numerical simulation
EW	Entropy Wave
EWG	Entropy wave generator
FRAPP	Fast Response Aerodynamic Pressure Probe
HCV	Hub clearance vortex
HPV	Hub passage vortex
HW	Hot-wire
HS	Hot streak
IP	Injected Perturbation
LE	Leading Edge
LES	Large Eddy Simulation
MP	Mid Pitch
NGV	Nozzle guide vane
OP	Operating point
OTDF	Overall temperature distribution function
PDF	Probability density function
PIV	Particle Image Velocimetry
PWM	Pulse Width Modulation
PS	Pressure side
RANS	Raynolds-averaged Navier-Stokes
RTDF	Radial temperature distribution function
S1, S2	Electrical relays
SN	Swirl number
SS	Suction side
SV	Shed vortex
T1	Traversing plane downstream of the combustor simulator
T2	Traversing plane downstream of the stator
T3	Traversing plane downstream of the rotor
TPV	Tip passage vortex
TCV	Tip clearance vortex
TRAF	UniFi CFD code
URANS	Unsteady Raynolds-averaged Navier-Stokes

Latin alphabet variables

A	Area
C	Total pressure coefficient
c	Chord
D	Diameter
E	Voltage supply
h	Blade height
H	Shape factor
He	Helmholtz number
K	Aerodynamic coefficient
K_1	Kacker and Okapuu acceleration coefficient
M	Mach number
$\dot{m}$	Mass flow rate
n	Rotor rotational speed
o	Throat
p	Pressure
p_δ	Acoustic waves
r	Non-dimensional span
Q	Cooling velocity
q	Fluctuating cooling velocity
$R(T)$	Autocorrelation
Re	Reynolds number
S	Surface
s	Blade channel pitch
t	Time
T	Temperature / Period
T_i	Turbulence intensity
TT	Total-to-total
t_c	Trailing edge thickness
V	Velocity / Hot-wire instantaneous velocity
v	Velocity / Hot-wire fluctuating velocity
y	Spanwise distance from the wall
Y	Total pressure loss
z_{min}	Minimum secondary deviation angle location

Latin alphabet coefficient

A	Coefficient King's law Eq. 3.12
A_i	Coefficients Eq. 3.20
B	Coefficient King's law Eq. 3.12
C_i	Coefficient for radial distribution of pressure losses
k^2	Jorgensen's calibration coefficient Eq. 3.16
h^2	Jorgensen's calibration coefficient 3.16
n	Coefficient King's law Eq. 3.12
R_i	Coefficients Eq. 3.23
Z_i	Coefficients Eq. 3.24

Greek alphabet variables

α	Blade-to-blade angle
β	Total-to-static expansion ratio / Relative blade-to-blade angle
δ	Boundary layer thickness
ϵ	Deviation angle
η	Efficiency
Θ	Blade lean angle
ϑ	Blade deflection
λ	Integral length scale / Stage loading coefficient
Ξ	EW transfer function
Π	Hot-wire pitch angle
ρ	Density
σ	Standard deviation
τ	Time constant
Φ^2	Kinetic energy coefficient
φ	Hot-wire yaw angle
χ	Hot-wire slanted angle
Ψ	Stagger angle

Superscripts (var general variable)

$v\bar{a}r$	Time-mean
$\widehat{var}$	Circumferential average
$+$	Downstream
$-$	Upstream

Subscripts

0	Rest condition
1, 2, 3	Plane T1, T2 or T3 / Components on the wind tunnel reference system
a	Axial
amb	Ambient condition
BL	Boundary layer
C	Clean case
c	Central
$corr$	After temperature correction
d	Down
g	Geometrical
IP	Injected perturbation case
is	Isentropic
l	Left
m	Mid-span
$mean$	Average of lateral pressure taps
min	Minimum
mix	Mixing
MS	Mainstream
p	Pitch / profile
r	Relative, computed in the relative frame of reference / radial
ref	Reference inlet value
rot	Motor rotation

s	Static / secondary
SKE	Secondary kinetic energy
t	Total / tangential
T_i	Turbulence intensity
u	Up
V	Vane
w	Wire
x	Axial
y	Yaw
ϑ	Tangential component of cylindrical reference system

Mathematical symbols

Δ	Peak-to-trough
$\widetilde{\Delta}$	Difference between perturbed and clean cases
$\Delta\vartheta$	Tangential displacement
ΔR	Radial displacement
Δx	Axial positions difference

LIST OF FIGURES

LIST OF TABLES